



**GDAŃSK UNIVERSITY
OF TECHNOLOGY**

Faculty of Chemistry



FACULTY OF
CHEMISTRY

The author of the PhD dissertation: Zuzanna Zarach
Scientific discipline: Chemical Sciences

DOCTORAL DISSERTATION

Title of PhD dissertation: Metal chalcogenide-based electrode materials
for electrochemical energy storage applications

Title of PhD dissertation (in Polish): Materiały elektrodowe na bazie
chalkogenków metali do zastosowań w elektrochemicznym magazynowaniu
energii

Supervisor	Auxiliary supervisor
<i>signature</i>	<i>signature</i>
Ph.D., D. Sc., Assoc. Prof. Andrzej Nowak	Ph.D., Asst. Prof. Mariusz Szkoda

Gdańsk, year 2025



STATEMENT

The author of the PhD dissertation: Zuzanna Zarach

I, the undersigned, agree that my PhD dissertation entitled: Metal chalcogenide-based electrode materials for electrochemical energy storage applications may be used for scientific or didactic purposes.

Gdańsk,.....

.....
signature of the PhD student

Aware of criminal liability for violations of the Act of 4th February 1994 on Copyright and Related Rights (Journal of Laws 2006, No. 90, item 631) and disciplinary actions set out in the Law on Higher Education (Journal of Laws 2012, item 572 with later amendments),² as well as civil liability, I declare, that the submitted PhD dissertation is my own work.

I declare, that the submitted PhD dissertation is my own work performed under and in cooperation with the supervision of Ph.D., D. Sc., Assoc. Prof. Andrzej Nowak, the auxiliary supervision of Ph.D., Asst. Prof. Mariusz Szkoda.

This submitted PhD dissertation has never before been the basis of an official procedure associated with the awarding of a PhD degree.

All the information contained in the above thesis which is derived from written and electronic sources is documented in a list of relevant literature in accordance with art. 34 of the Copyright and Related Rights Act.

I confirm that this PhD dissertation is identical to the attached electronic version.

Gdańsk,.....

.....
signature of the PhD student

I, the undersigned, agree to include an electronic version of the above PhD dissertation in the open, institutional, digital repository of Gdańsk University of Technology, Pomeranian Digital Library, and for it to be submitted to the processes of verification and protection against misappropriation of authorship.

Gdańsk,.....

.....
signature of the PhD student

² Act of 27th July 2005, Law on Higher Education: Chapter 7, Criminal responsibility of PhD students, Article 226.



DESCRIPTION OF DOCTORAL DISSERTATION

The Author of the PhD dissertation: Zuzanna Zarach

Title of PhD dissertation: Metal chalcogenide-based electrode materials for electrochemical energy storage applications

Title of PhD dissertation in Polish: Materiały elektrodowe na bazie chalcogenków metali do zastosowań w elektrochemicznym magazynowaniu energii

Language of PhD dissertation: English

Supervision: Ph.D., D. Sc., Assoc. Prof. Andrzej Nowak

Auxiliary supervision: Ph.D., Asst. Prof. Mariusz Szkoda

Date of doctoral defense:

Keywords of PhD dissertation in Polish: magazynowanie energii, superkondensatory, baterie sodowo-jonowe, chalcogenki metali

Keywords of PhD dissertation in English: energy storage, supercapacitors, sodium-ion batteries, metal chalcogenides

Summary of PhD dissertation in Polish:

Elektrochemiczne systemy magazynowania energii odgrywają kluczową rolę w rozwiązywaniu współczesnych wyzwań związanych z transformacją energetyczną, zmianami klimatu oraz koniecznością ograniczenia wykorzystania paliw kopalnych. Superkondensatory charakteryzują się wyjątkowo dużą gęstością mocy i długą żywotnością, natomiast akumulatory sodowo-jonowe oferują rozwiązania oparte na łatwo dostępnych surowcach. Ich efektywność jest jednak silnie uzależniona od właściwości zastosowanych materiałów elektrodowych. Niniejsza rozprawa doktorska skupia się na badaniu dwóch materiałów z grupy chalcogenków metali: disiarczku molibdenu oraz siarczku cyny, jako nowoczesnych elektrod do superkondensatorów oraz akumulatorów sodowo-jonowych. Przeprowadzone badania obejmują optymalizację syntezy, inżynierię powierzchni oraz modyfikacje strukturalne mające na celu poprawę pojemności, stabilności podczas procesów ładowania/wyładowania i pracy przy dużych gęstościach prądowych. Dodatkowo, zastosowano spektroskopię Ramana w trybie *operando* do obserwacji zmian strukturalnych materiału anodowego podczas pracy półogniwa sodowego, co umożliwiło wgląd w mechanizmy magazynowania energii. Rozprawa ma charakter publikacyjny i uwzględnia trzy rozdziały oparte na recenzowanych artykułach naukowych. Praca stanowi istotny wkład w rozwój skalowalnych i wydajnych materiałów elektrodowych nowej generacji.



Summary of PhD dissertation in English:

Electrochemical energy storage plays a crucial role in addressing global challenges related to sustainable energy, climate change, and the transition away from fossil fuels. Supercapacitors are distinguished by exceptionally high power density and long cycle life, whereas sodium-ion batteries provide widely available raw materials. However, the performance of these systems remains fundamentally limited by the properties of the electrode materials. In this context, the dissertation investigates two metal chalcogenide-based materials molybdenum disulfide and tin sulfide, as advanced electrodes for supercapacitors and sodium-ion batteries. The research focuses on synthesis optimization, surface engineering and structural tailoring of these materials to improve their capacitance (capacity), cycling stability and rate capability. In addition, *operando* Raman spectroscopy is employed to probe tin sulfide electrode transformations during sodium half-cell operation, enabling a deeper understanding of storage mechanisms. The work adopts an article-based format, with three experimental chapters based on peer-reviewed publications. Overall, the dissertation contributes to the development of scalable, high-performance materials for next-generation energy storage devices.

Acknowledgments



The author would like to acknowledge **National Centre for Research and Development (NCBR)** for financial support within the LIDER project no. LIDER/15/0088/L-10/18/NCBR/2019 *“Integrated prototype of a photo-supercapacitor for energy storage obtained as a result of solar radiation conversion”*.



The author would like to acknowledge **National Science Centre (NCN)** for financial support within the PRELUDIUM project no. UMO-2023/49/N/ST5/01794 *“Beyond MoS₂: Unraveling Charge Storage Mechanisms in Transition Metal Dichalcogenides as Anode Materials for Sodium-Ion Batteries through In-situ Raman Measurements”*.



The author would like to acknowledge **Polish National Agency for Academic Exchange (NAWA)** under STER programme, within the project no. PPI/STE/2020/1/00023/U/00001 *“STE(E)R-ING towards International Doctoral School”*, for funding the scientific internship at Technical University of Darmstadt, Germany.

Acknowledgments

I would like to express my deepest gratitude to my supervisor, **Professor Andrzej Nowak**, for his invaluable guidance, encouragement, and for creating inspiring scientific environment in which this work could develop. His optimistic outlook, light-hearted attitude and positive energy greatly shaped the atmosphere in which I was able to grow as a researcher. Under his mentorship I gained new skills, learned to approach challenges with confidence and benefited from opportunities such as my research internship abroad, which significantly influenced my academic path. His scientific advice, openness and trust in my abilities have left a lasting impact on my development.

My sincere appreciation also goes to my co-supervisor, **Dr. Mariusz Szkoda**, who has supported me from the very beginning of my academic career and has always believed in my potential. His dedication, scientific input and generosity in sharing knowledge have significantly contributed to my progress. His trust and encouragement strengthened me not only on the professional level but also on a personal one, giving me the motivation and determination to continue along this demanding path.

I am deeply grateful to my colleagues, in particular Konrad, for his constructive criticism and motivating discussions, which helped me to grow scientifically, and Monika, for her constant support, invaluable scientific assistance and for introducing me to academic circles and respected professors, whose advice and expertise greatly enriched my work and professional opportunities.

I would also like to thank all members of our research group and colleagues from the faculty. In particular, Mariusz, for the daily encouragement, mutual motivation, and the sense of companionship that made the doctoral journey much more bearable, as well as Daria, Anita and Balanand for their collaboration and support throughout the course of this work.

My sincere thanks extend to all collaborators from my research stays abroad. I am especially thankful to Alex and Marco, who not only introduced me to laboratory work during my internship but also created a welcoming environment that made my stay truly rewarding. Our collaboration has grown into a lasting friendship that I deeply value.

I am mostly grateful to Patryk for his constant motivation and support, for sharing both challenges and moments of joy, and for the mutual encouragement that sustained me in the everyday life of my doctoral path.

Finally, I would like to express my heartfelt gratitude to my parents, whose love, sacrifices and belief in me laid the foundation for everything I have achieved. Without their support this dissertation would not have been possible.

Table of Contents

Acknowledgments	7
Table of Contents.....	11
General Introduction.....	13
Research Objectives and Scopes	17
Chapter I Theoretical Background.....	19
1. Introduction to Electrochemical Energy Storage	21
1.1. Global Energy Challenges and the Role of Energy Storage	21
1.2. Electrochemical energy storage systems and electrode materials ..	22
2. Fundamentals of Energy Storage Devices	26
2.1. Electrochemical principles: charge storage, Faradaic vs. non-Faradaic processes	26
2.2. Determination of charge storage mechanisms.....	31
2.3. Key performance metrics: capacitance, capacity, energy density, coulombic efficiency, energy efficiency, power density.....	34
2.4. Comparison between batteries and supercapacitors	37
3. Supercapacitors	39
3.1. Types of supercapacitors: EDLCs vs pseudocapacitors vs hybrid systems	39
3.2. Materials for supercapacitor electrodes	40
3.2.1. Carbon-based materials	40
3.2.2. Metal chalcogenides	45
3.3. Current challenges and perspectives.....	52
4. Sodium-Ion Batteries.....	54
4.1. Basics of SIBs: operating principle and comparison to LIBs	54
4.2. Anode materials for SIBs – energy storage mechanisms	59
4.2.1. Hard carbon and carbon-based materials	60
4.2.2. Metal chalcogenide-based materials.....	63
5. References.....	66

Chapter II <i>The phenomenon of increasing capacitance induced by 1T/2H-MoS₂ surface modification with Pt particles – Influence on composition and energy storage mechanism</i>	83
1. Summary of the publication	85
2. Publication	87
Chapter III <i>Influence of hydrochloric acid concentration and type of nitrogen source on the electrochemical performance of TiO₂/N-MoS₂ for energy storage applications</i>	109
1. Summary of the publication	111
2. Publication	112
Chapter IV <i>A Key to Material's Stability: Tuning Pyrolysis Temperature in SnS_x@C Anodes for Sodium-Ion Batteries</i>	129
1. Summary of the publication	131
2. Publication	133
General conclusions	161
Scientific achievements	165
Author Contribution Statements	177
Copyrights	203

General Introduction

One of the most critical challenges of the twenty-first century is the growing need for scalable, efficient and sustainable energy technologies. Due to the increased industrialization, urbanization and technological breakthroughs, we are now facing two most serious challenges: the depletion of fossil fuel resources and the negative environmental effects that are a consequence of their continuous use. Moreover, countries worldwide are urged to look for cleaner and renewable energy sources due to progressive climate change, which is caused by the continuous emission of greenhouse gases from conventional energy systems.^[1] Nevertheless, despite the growing use of wind, solar and other renewable energy sources, their limitation in the form of periodic use of these sources shapes the direction of further research, indicating that reliable energy storage systems (ESS) must be developed in order to guarantee steady electricity supply and grid stability. Batteries and supercapacitors are examples of electrochemical energy storage devices that are essential to the development of a sustainable energy future. These technologies are crucial for consumer electronics, portable power systems, electric vehicles (EVs), and grid-scale applications. The capability of these systems to store and deliver energy efficiently, safely, and over extended cycles is at the core of this transition.

Lithium-ion batteries (LIBs) currently dominate the energy storage market due to their favorable energy density and mainly because the technology itself has reached full-scale commercial deployment.^[2] However, they are constrained by several issues: limited raw material availability (particularly lithium and cobalt), safety concerns (including thermal runaway), and environmental burdens associated with mining and disposal.^[3] These challenges have prompted growing exploration into alternative energy storage systems, with particular attention to sodium-ion batteries (SIBs) and supercapacitors (SCs). SIBs, in particular, are considered promising replacement for LIBs for stationary applications due to the abundance and geographic diversity of sodium resources, as well as their potential cost advantages.^[4] Although sodium has a larger ionic radius and less negative standard reduction potential than lithium (-2.71 V vs. -3.04 V vs. SHE), ongoing innovations in electrode materials are rapidly narrowing the performance gap. On the other hand, supercapacitors, while offering lower energy density than batteries, are characterized by exceptional power density, long cycle life (up to a million cycles), rapid charge/discharge capabilities, and superior performance at low temperatures.

The performance of both batteries and supercapacitors strictly relies on the choice of electrode materials. The electrode's physical and chemical properties directly influence key performance parameters such as energy and power densities, rate capability, cycling stability, and safety. In both types of devices, carbon-based materials have been widely adopted as electrodes due to their conductivity, stability, and porosity. In the case of supercapacitors,

the goal is to improve the energy density, however, with the carbon-based materials that store the energy mainly by adsorption of ions on the electrode surface, the possibilities of improving this parameter are limited. In the case of LIBs, geopolitical conditions related to the availability of natural graphite and on the other hand the dependence on the supply of petroleum needle coke in synthetic graphite production, motivate the search for alternative anode materials. Finally, in SIBs, despite the replacement of graphite anode with hard carbons, the low initial columbic efficiency caused by irreversible sodium ions intercalation and the insufficient capacity proves problematic. Therefore, to push the boundaries of performance, there is an increasing exploration of new materials, e.g. transition metal compounds.

One such class of materials that has shown considerable promise is metal chalcogenides. These compounds, composed of metals and chalcogen elements (S, Se, or Te), exhibit layered structures, tunable band gaps, and favorable redox properties, making them attractive candidates for use in electrochemical devices. Molybdenum disulfide (MoS_2) as a representative, with its two-dimensional, graphene-like structure provides a large interlayer spacing that facilitates ion intercalation and fast charge transport.^[5–7] Its pseudocapacitive characteristic is beneficial for supercapacitor systems as it is possible to benefit from both surface and redox storage mechanisms, and thus increase energy density of the device. Similarly, a group of tin sulfides, another member of the chalcogenide family, has shown considerable promise as an anode material for SIBs. Its high theoretical capacity and favorable conversion and alloying reaction mechanisms are of great interest. However, like many conversion-type materials, tin sulfides suffer from structural degradation during cycling and ions intercalation/deintercalation.^[8] To reduce this problem, metal chalcogenides are often integrated with materials such as carbon nanotubes or amorphous carbon. These composites enhance structural integrity, improve electronic conductivity, and mitigate volume expansion, leading to enhanced cycle stability and rate performance.^[9]

Apart from focusing on the type of electrode material, recent research trends also emphasize the importance of developing sustainable, scalable, and environmentally conscious material synthesis strategies. The energy storage research is not only focusing on performance metrics like capacitance or energy density, but increasingly incorporates factors such as cost-efficiency, environmental impact, material abundance, and compatibility with industrial fabrication processes. In this broader context, advancing next-generation of electrochemical devices requires a synergistic approach – integrating innovative material design, comprehensive electrochemical evaluation and real-time analysis through *operando* techniques. Considering the composition of electrode materials and its design, binders are quite often an inherent element which does not support the energy storage process, but plays role in improving physical contact. However, their use also contributes to the deterioration of some

parameters of the electrode, resulting in the reduction of volumetric and gravimetric capacitance (in supercapacitors) and capacity (in batteries). Its presence may also contribute to the occurrence of side reactions during charging and discharging processes, and in the case of binders such as polyvinylidene fluoride (PVDF), an additional increase in resistance value may be observed.^[10] Thus, the synthesis approach with simultaneous deposition on current collector may be considered attractive, especially since it is not a limitation in terms of conducting the synthesis on a larger scale. Although the binder-free concept of the direct deposition of active layer on the current collector has proven successful in supercapacitors, in LIBs and SIBs electrode coatings still require a binder to maintain mechanical integrity under repeated volume changes during intercalation/deintercalation processes.^[11]

In parallel with the rapid development of new electrode materials, there is a growing need for advanced characterization techniques capable of capturing structural and chemical changes as they occur. Conventional *post-mortem* analysis, while informative, often fail to reveal the transient phenomena and real-time dynamics governing energy storage mechanisms. To bridge this gap, *in situ* and *operando* techniques – such as operando Raman spectroscopy, X-ray diffraction, and electron microscopy – are getting more and more attention.^[12,13] These tools enable researchers to monitor electrode transformations during charge/discharge processes, providing insights into phase transitions, interfacial reactions, ion intercalation/deintercalation behavior, and degradation mechanisms. In particular, *operando* Raman spectroscopy is a non-destructive tool for probing molecular vibrations and crystalline structures, thus allowing a direct link between structural evolution and electrochemical performance. By applying such techniques, it becomes possible not only to optimize material design but also to uncover fundamental insights into how electrode materials function under real working conditions.

Research Objectives and Scopes

This dissertation aims to explore metal chalcogenide-based electrode materials for electrochemical energy storage, specifically in supercapacitors and sodium-ion batteries (SIBs). The work combines experimental investigations with literature analysis to gain insights into the structure-property relationships of these materials and assess their practical viability. The primary research objectives are:

- (i) MoS₂-based supercapacitor electrodes – with particular emphasis on how different synthesis routes and surface modifications can enhance their capacitance and cycling stability. The investigation also considers phase engineering and the effect of additives on their electrochemical performance.
- (ii) Tin sulfide composite anodes for SIBs – the goal is to improve their reversible capacity, structural robustness during cycling and high-rate capability by optimizing synthesis parameters and by addressing the known issue of cycling stability in metal chalcogenide anodes.
- (iii) *Operando* Raman diagnostics – employing *operando* Raman spectroscopy as a real-time diagnostic tool to monitor structural and compositional changes in electrode materials during galvanostatic charge-discharge cycling. This objective seeks to correlate observed electrochemical behavior with material transformations, providing deeper understanding of the underlying energy storage mechanisms and validating the impact of the aforementioned modifications on performance.

The research is supported by the hypothesis that targeted material engineering will significantly improve the electrochemical performance of metal chalcogenide electrodes in energy storage applications. In particular, it is hypothesized that for MoS₂-based supercapacitor electrodes, controlling the synthesis procedure and introducing surface modifications will overcome inherent limitations, leading to higher capacitance and better long-term stability. For tin sulfide anodes in SIBs, optimizing the synthesis conditions will mitigate an issue of electrode degradation, thereby improving cycling reversibility. *Operando* Raman spectroscopy will provide direct evidence of these improvements by revealing how the material's structure evolves during operation. The real time insights are expected to confirm that the engineered structural features correlate with enhanced charge storage mechanisms and stability.

The dissertation is article-based, meaning the core chapters (Chapters II-IV) are built upon published research papers. **Chapter I** provides a comprehensive literature review that establishes the scientific and technological background of this research. It begins with the fundamentals of electrochemical energy

storage, outlining the operating principles, advantages and limitations of both supercapacitors and sodium-ion batteries. The chapter then explores conventional and emerging electrode materials, with particular emphasis on the structure, properties, and electrochemical behavior of metal chalcogenides.

Chapter II presents the first experimental investigation, based on the research article *“The phenomenon of increasing capacitance induced by 1T/2H-MoS₂ surface modification with Pt particles – Influence on composition and energy storage mechanism”*. This study focuses on MoS₂-based electrodes and examines how phase composition and surface modifications affect capacitance behavior and long-term stability in supercapacitor systems.

Chapter III continues the exploration of MoS₂ in supercapacitor applications, as described in the article *“Influence of hydrochloric acid concentration and type of nitrogen source on the electrochemical performance of TiO₂/N-MoS₂ for energy storage applications”*. This work investigates the impact of synthesis parameters on material structure and capacitive performance, particularly highlighting the effects of nitrogen doping and substrate integration.

Chapter IV shifts focus to sodium-ion batteries and presents findings from the study *“A Key to Material’s Stability: Tuning Pyrolysis Temperature in SnS_x@C Anodes for Sodium-Ion Batteries”*. This chapter explores the synthesis and optimization of tin sulfide-carbon composite anodes, with an emphasis on the utilization of *operando* Raman spectroscopy measurements.

The final chapter summarizes the main findings of this dissertation and reflects on the scientific contributions of each study. It also outlines potential pathways for future research, emphasizing the need for environmentally conscious synthesis methods, advanced material architectures, and the continued integration of *operando* diagnostic tools for real-time insight into electrochemical processes

Chapter I

Theoretical Background

1. Introduction to Electrochemical Energy Storage

1.1. *Global Energy Challenges and the Role of Energy Storage*

Over the past several decades, the world has experienced an unprecedented acceleration in energy demand. Driven by global industrialization, rapid urban growth, digitalization, and the electrification of transport and industry, this trend continues to intensify. According to the International Energy Agency's (IEA) *World Energy Outlook* (New Policies Scenario), global primary energy demand is projected to increase by approximately 25% by 2040, driven in majority by developing economies and the proliferation of energy-intensive technologies.^[14] At the same time, global efforts to limit greenhouse gas emissions and mitigate the effects of climate change have placed energy systems at the center of international environmental policy. However, despite these efforts, fossil fuels still account for the majority of the world's primary energy consumption.^[15] The combustion of coal, oil, and natural gas remains the leading source of carbon dioxide (CO₂) emissions, contributing significantly to global warming, ocean acidification, and air pollution.^[15] The Climate Change 2023 Synthesis Report from the Intergovernmental Panel on Climate Change (IPCC) emphasizes that achieving net-zero emissions within the coming decades is critical to avoiding irreversible environmental damage.^[16] This has led to the introduction of low-carbon energy systems, most notably those based on renewable sources such as solar, wind, and hydropower. However, solar generation, for instance, is not possible at night and may be reduced by cloud cover. Similarly, wind power is inconsistent and geographically constrained. These factors contribute to what is often referred to as the "intermittency problem", which undermines the reliability and predictability of renewable energy supply. In the context of electrical grid, grid operators must therefore contend with the challenge of matching supply and demand in real time, while ensuring power quality and system stability.

To overcome this limitations, energy storage systems (ESS) have become an essential part of modern energy infrastructure. ESS technologies can store the excess of electricity when production outpaces consumption and release it when demand exceeds generation, improving grid reliability and flexibility. In addition to their value for utility-scale applications, energy storage technologies are equally essential for emerging fields such as electric vehicles (EVs), smart grids, and decentralized microgrids. In EVs, for example, the ability to store large amounts of energy in a compact and safe format directly impacts vehicle range, charging time, and performance. In rural or off-grid communities, energy storage facilitates the use of solar home systems and ensures access to electricity without dependence on centralized infrastructure. The strategic role of energy storage is further emphasized by its contribution to energy security and economic resilience. Countries with limited fossil fuel reserves but abundant renewable potential can reduce energy imports and enhance national energy independence through localized generation and storage. Moreover, as global markets shift

toward cleaner energy solutions, energy storage is expected to play a key role in enabling decarbonization pathways across various sectors.

One of the systems that are already playing an essential role is **electrochemical energy storage**, mostly due to its versatility, modularity, and wide range of applications. This category includes batteries and supercapacitors, which store energy via chemical reactions and interfacial charge accumulation mechanisms, respectively. Batteries such as LIBs, SIBs, lead-acid, and redox flow batteries are employed in contexts ranging from consumer electronics to EVs and grid storage. LIBs currently dominate the market owing to their high energy density and efficiency, but concerns over resource scarcity, safety, and recycling are accelerating interest in alternatives such as SIBs.^[17,18] Supercapacitors, which include electric double-layer capacitors (EDLCs) and pseudocapacitors, excel in power density and longevity. Their ability to undergo millions of charge-discharge cycles without significant degradation makes them attractive for applications requiring quick bursts of energy, such as regenerative braking or frequency response in power grids.^[19–21] Hybrid supercapacitors, which blend battery-like and capacitor-like charge storage mechanisms, sometimes referred to as supercapatteries, are also being developed to bridge the gap between energy and power performance.^[22,23]

Each of these technologies presents a unique set of trade-offs. While batteries offer high energy storage capacity, they are often limited by lower power density and cycle life. In contrast, supercapacitors are characterized by high power and durability at the cost of lower energy density. All the distinctions emphasize the necessity of selecting storage technologies that correspond with particular application requirements. In practice, hybrid systems that integrate multiple storage types are becoming increasingly popular, leveraging the strengths of each to meet complex operational needs. Nevertheless, the development of new materials and cell architectures remains the researchers direction, and especially innovations in electrode materials can significantly influence performance characteristics such as energy density, rate capability and cycle life. The next section will present the critical role of the materials that are considered for electrochemical energy storage systems.

1.2. Electrochemical energy storage systems and electrode materials

The performance of each electrochemical storage device depends on how effectively its constituent materials interact within the cell architecture. Considerable attention is usually focused on electrode materials, owing to their direct influence on energy and power performance, however, it is essential to understand the broader view, which also includes electrolytes, separators, binders and current collectors. These components collectively determine the overall efficiency, safety, lifespan and cost of both batteries and supercapacitors.

Electrodes serve as the active sites for energy storage and conversion, and their performance characteristics are fundamental to the system's operation. In rechargeable batteries, the anode (negative electrode) typically

accommodates ion insertion during charging, while the cathode (positive electrode) undergoes the complementary redox process during discharging. In contrast, supercapacitors employ positive and negative electrodes, where energy is stored either through electrostatic charge accumulation at the electrode/electrolyte interface or through rapid and reversible surface redox reactions. Traditional electrode materials such as graphite (anode in LIBs) and activated carbon (supercapacitor electrodes) have long served as reliable benchmarks; however, the ongoing need for improvement has motivated extensive research into advanced materials. Among emerging candidates, metal chalcogenides such as MoS₂, WS₂, SnS₂ and others have demonstrated promising electrochemical behavior. Their layered structures, adjustable band gaps, and redox-active nature make them suitable for both battery-type^[9,24,25] and capacitor-type^[26,27] applications. MoS₂, in particular, combines pseudocapacitive and intercalation characteristics, allowing for fast ion transport and significant charge storage.^[28] Tin sulfides, on the other hand, exhibit high theoretical capacities and favorable reaction mechanisms with sodium, making them attractive for both LIB- and SIB-electrode materials.^[8,29] Nevertheless, chalcogenides also face challenges such as structural instability, large volume changes during cycling, and limited intrinsic conductivity. To address these issues, advanced material engineering techniques have been employed, including nanostructuring to reduce ion diffusion paths,^[30] introducing defects to enhance electronic conductivity and improve interfacial properties,^[31–33] and composite formation with carbon-based matrices to buffer mechanical strain.^[34] Furthermore, the microstructure of electrode materials significantly impacts their electrochemical behavior. Porosity, particle size distribution, and surface area directly influence electrolyte penetration, ion accessibility, and active sites availability.^[33] Optimizing these parameters through tailored synthesis methods, such as hydrothermal processing, electrospinning, or atomic layer deposition, can lead to marked improvements in rate capability and cycling performance.^[34–36]

Beyond the electrodes, in both supercapacitors and rechargeable batteries, the electrolyte plays a vital role in facilitating ion transport between the anode and cathode while maintaining electrochemical stability. Regardless whether it is a supercapacitor or a battery, the electrode/electrolyte interface is the most complex and important region that affects the overall device performance. The selection between aqueous, organic, solid-state, or hybrid electrolyte depends on the desired voltage window, temperature range, and safety profile. Aqueous electrolytes, though limited by a narrow electrochemical stability window, offer low cost and high ionic conductivity, making them suitable for supercapacitors and some low-voltage batteries.^[37,38] On the other hand, organic electrolytes provide higher voltage stability but often suffer from flammability, and their properties hinder long-term supercapacitors' operation,^[39] while their use is a common practice for rechargeable batteries. Solid-state electrolytes, including polymer and inorganic electrolytes, promise enhanced safety and energy density, but are still under development due to interface challenges, low ionic conductivity, but also poor stability at high voltages,

especially for solid polymer electrolytes.^[40] For SIBs, electrolyte choice is essential. The larger ionic radius of Na⁺ ions compared to Li⁺ results in different solvation behavior and interfacial properties.^[41,42] Also, because lithium-ion batteries depend mostly on LiPF₆ electrolytes that begin to decompose at relatively moderate temperatures and trigger strongly exothermic side-reactions that can accelerate thermal runaway. Sodium-ion batteries, in contrast, use NaPF₆ and other sodium salts, which exhibit lower moisture sensitivity and slower decomposition kinetics than LiPF₆, contributing to higher thermal stability. Together with the more inorganic, NaF-rich SEI, this shifts the onset of self-heating upward and markedly reduces total heat release during operation, which is a considerable safety advantage.^[43] Nevertheless, careful control over solvent composition, salt concentration, and the use of additives like fluoroethylene carbonate (FEC) or vinylene carbonate (VC) remains important to enhance SEI formation and ensure stable cycling.^[44,45]

Current collectors, though often overlooked, are crucial for efficient charge transport to and from the electrodes. In batteries, they are typically made from aluminum and copper, whereas for supercapacitors they are usually a thin etched or carbon-coated aluminum foil for both electrodes.^[46–48] Regardless of the device in which they are being used, current collectors must possess high electrical conductivity, corrosion resistance, and good adhesion to the active material. In metal-ion batteries, one notable advantage of SIBs over LIBs is that aluminum foil can be used as the current collector for both the cathode and the anode. For LIBs, aluminum cannot be used on the anode side because lithium tends to alloy with aluminum at low potentials (~0–0.6 V vs. Li/Li⁺), causing electrode degradation, loss of adhesion, and compromising battery stability.^[49] In contrast, sodium does not exhibit such alloying behavior under similar conditions. The substitution offers several benefits: aluminum is lighter, less expensive, and more abundant than copper, making SIBs more cost-effective and sustainable from a materials perspective.^[50,51] Additionally, replacing copper with aluminum can lead to improved gravimetric and volumetric energy density, reduced overall battery weight, and simplified recycling process due to the use of a single material metallic current collector.^[52,53] These advantages support the broader vision of SIBs as a scalable and eco-friendly alternative for large-scale and stationary energy storage applications.

Equally important are binders and conductive additives, which are essential for maintaining electrode integrity and facilitating electronic conductivity within the electrode matrix. However, in high-power applications such as supercapacitors, binders are often considered a limitation. They are electrochemically inactive, and their presence can reduce the available surface area, increase internal resistance, and hinder the full utilization of active materials.^[54] These effects in total may lower the achievable capacitance and rate performance. Apart from most common polyvinylidene fluoride (PVDF), there is also a growing interest in the field of developing green binders to achieve higher sustainability, yet the drawbacks still remain.^[55] To overcome those, a growing number of studies focus on binder-free electrode designs,^[56] particularly those involving direct deposition of active materials onto current

collectors. This approach eliminates the need for binders and conductive additives, thereby improving electrical contact, reducing interfacial resistance and enhancing mechanical adhesion. **In the presented research such strategies are explored for MoS₂-based supercapacitor electrodes, where the active material was synthesized directly on metallic substrates acting as current collectors.** This methodology enables more efficient electron pathways and maximizes the electrochemical interface, contributing to improved capacitive behavior and long-term stability.

In addition to these innovations, traditional binders and conductive additives still continue to play a vital role, especially in battery systems. Binders are polymeric substances that hold the active material particles together and adhere them to the current collector. In LIBs, PVDF is commonly used together with N-methyl-2-pyrrolidone (NMP) as a solvent. PVDF offers strong mechanical properties and chemical stability,^[57] however, due to its reliance on toxic solvent and non-renewable feedstocks, which may likely soon be highly regulated,^[58] there has been a growing push toward water-based binders such as carboxymethyl cellulose (CMC) and styrene-butadiene rubber (SBR), especially in SIB-systems.^[59] These alternatives not only reduce environmental impact, but also improve electrode flexibility.^[60,61] And, even though the use of CMC/SBR binders in lithium-ion batteries has been widely studied, it is not optimal for manufacturers due to several critical challenges, including enhanced hydrogen fluoride (HF) formation due to residual water in aqueous binding systems, aluminum current collector corrosion, and lithium leaching from the cathode.^[62–64] Additionally, conductive additives, such as carbon black (CB), graphene, or carbon nanotubes, are incorporated to improve electronic conductivity of the electrode. Their presence is particularly critical in materials with low intrinsic conductivity, including many metal chalcogenides.^[65] The interplay of all those components determines the full functionality and efficiency of electrochemical energy storage systems. The following sections will provide the fundamentals of electrochemical energy storage and key performance metrics for both supercapacitors and metal-ion batteries.

2. Fundamentals of Energy Storage Devices

2.1. *Electrochemical principles: charge storage, Faradaic vs. non-Faradaic processes*

Electrochemical energy-storage devices comprise two electronically conductive electrodes immersed in an ion-conducting medium, and ionically permeable yet electronically insulating separator. The difference in electrochemical potentials between two electrodes determines the open-circuit voltage, E_{cell} , which drives charge transfer when the circuit is closed. Electrons flow through the external circuit while ions migrate inside the electrolyte to maintain electroneutrality. In practice, additional components like current collectors, binders and the separator introduce physical and transport constraints; yet, the basic idea of coupled electronic and ionic fluxes still applies.

The term *charge storage* encompasses any reversible process that allows the electrode to accumulate an excess of electronic charge during charging and to release it during discharge. Focusing solely on electrode materials, we can divide charge storage into **non-faradaic** and **faradaic**. Non-faradaic processes are governed by classical electrostatic interactions and the resulting capacitance is proportional to the active surface area available for double-layer formation. In contrast, processes that *do* involve redox chemistry are termed **Faradaic**. Their capacity is determined by the number of electrons transferred per active species and by the extent of the electrode material that can participate in this process.

In non-Faradaic storage, the moment a potential is applied, electrons accumulate on the electrode surface, creating excess negative or positive charge. To preserve electroneutrality, the electrolyte reorganizes: counter-ions migrate towards the surface, while same-charged ions are repelled. The outcome is an electrical double layer (EDL), first described by Helmholtz^[66] as a rigid plate-capacitor model comprising a layer of adsorbed ions at a distance d from the electrode, giving a capacitance described by **Equation (1)**:

$$C = \frac{\varepsilon \varepsilon_0 A}{d} \quad (1)$$

where C stands for capacitance, ε is the relative permittivity (dielectric constant) of the medium between the electrodes, ε_0 represents the electric constant (vacuum permittivity), A is the area of the capacitor plates, and d describes the distance between two plates. Subsequent models presented by Gouy,^[67] Chapman^[68] and Stern^[69] introduced more refined interpretations, including ion diffusion and finite ion size, leading to the modern view of a compact inner Helmholtz plane (IHP), a solvated outer Helmholtz plane (OHP), and a diffuse region whose thickness depends on ionic strength. The Helmholtz model, while simple, treats the electrolyte as a structureless continuum and ignores the granular nature of both solvent molecules and ions. Gouy and Chapman overcame this by invoking a Boltzmann distribution of point charges in a thermal field, yielding a diffuse layer with a characteristic thickness of Debye length.^[70]

Stern then finally united the two models, proposing a compact layer of specifically adsorbed ions (capacitance C_s) in series with the diffuse layer capacitance C_D , so that the measured differential capacitance (C) obeys **Equation 2**:

$$C^{-1} = C_s^{-1} + C_D^{-1} \quad (2)$$

The models with the potential profile and ion distribution as a function of distance from the electrode are presented in **Figure 1**.

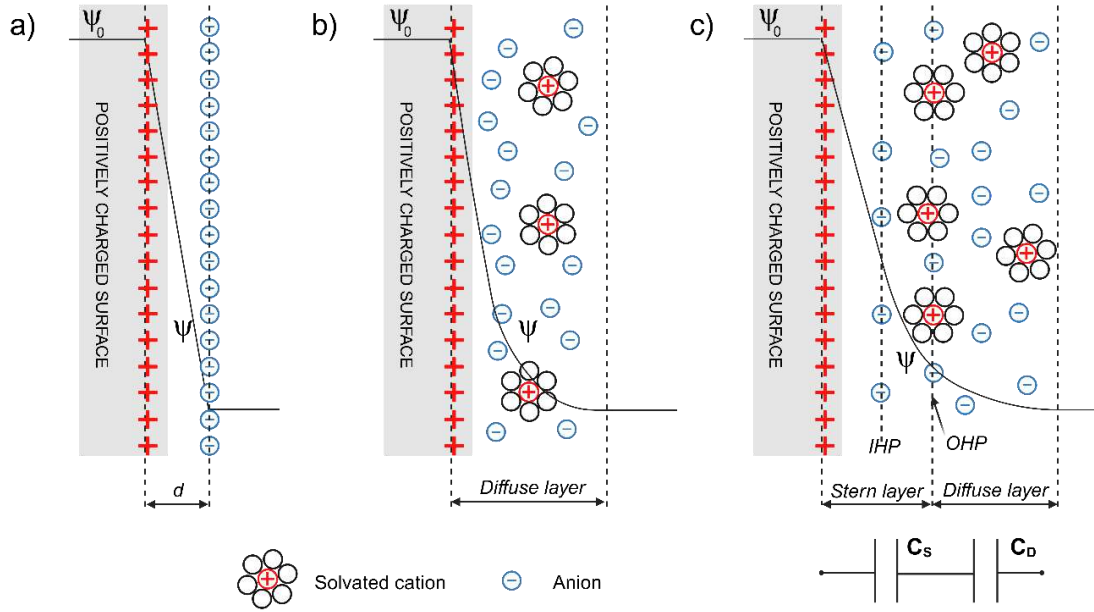


Figure 1. Scheme presenting the electric double layer structure according to the a) Helmholtz model, b) Gouy-Chapman model, and c) Gouy-Chapman-Stern model. Redrawn from Ref.^[71] and created with BioRender.com.

Between the ideal limits of pure EDL and battery-like faradaic reactions lies **pseudocapacitance**, a term firstly introduced by Graham in 1941.^[72] Later on, Conway presented his concept, stating that the capacitance may emerge from two distinct phenomena: namely, the presence of non-specifically adsorbed ions, where charge is induced rather than transferred, and the mechanism of adsorption pseudocapacitance, wherein charge is indeed transferred.^[73] Crucially, both EDL and pseudocapacitive storage are **capacitive** in the sense that the differential capacitance is finite and reversible; battery-type processes, in contrast, are **non-capacitive Faradaic**.^[74,75] Thermodynamically, Faradaic storage is governed by the Nernst equation, which relates the electrode potential to the logarithm of reactant activities. For a general redox couple, charge transfer can be explained by the **Equation 3**:



with the equilibrium potential according to **Equation 4**:

$$E = E^0 + \frac{RT}{zF} \ln \left(\frac{a_{A^{z+}}}{a_A} \right) \quad (4)$$

where E is Nernst potential (V), E^0 stands for standard electrode potential (V), R is universal gas constant ($8.314 \text{ J}\cdot\text{mol}^{-1}\cdot\text{K}^{-1}$), T refers to absolute temperature (K), z is a number of electrons transferred, F stands for Faraday constant ($96485 \text{ C}\cdot\text{mol}^{-1}$), $a_{A^{z+}}$ describes the activity of the oxidized species, a_A is the activity of the reduces species. In a battery electrode, the amount of inserted or extracted ions (e.g., lithium or sodium) changes during cycling, altering the chemical composition of the material. This change in stoichiometry leads to open-circuit voltage steps or plateaus that reflect phase transitions or solid-solution behavior within the electrode. In pseudocapacitance, the concentration of redox-active sites stays essentially constant, yielding a smooth, nearly linear charge-voltage response. However, in practice, the charge storage phenomenon is much more complex. Intercalation-type electrodes accommodate guest ions within crystal sites, while conversion electrodes store charge through bond-breaking and reformation. The reversible capacity therefore, depends on both stoichiometry and the reversibility of associated structural transformations. It is worth mentioning that for metal-ion batteries, a crucial role in energy storage also plays a surface-related phenomenon known as formation of the solid-electrolyte interphase (SEI): it consumes charge on the first cycle yet passivates the anode against further electrolyte decomposition, thereby altering both kinetics and thermodynamics. **Figure 2** presents the cyclic voltammetry (CV) and galvanostatic charge-discharge (GCD) characteristics of an ideal EDL material and other kinds of energy-storage materials, indicating the processes responsible for charge storage.

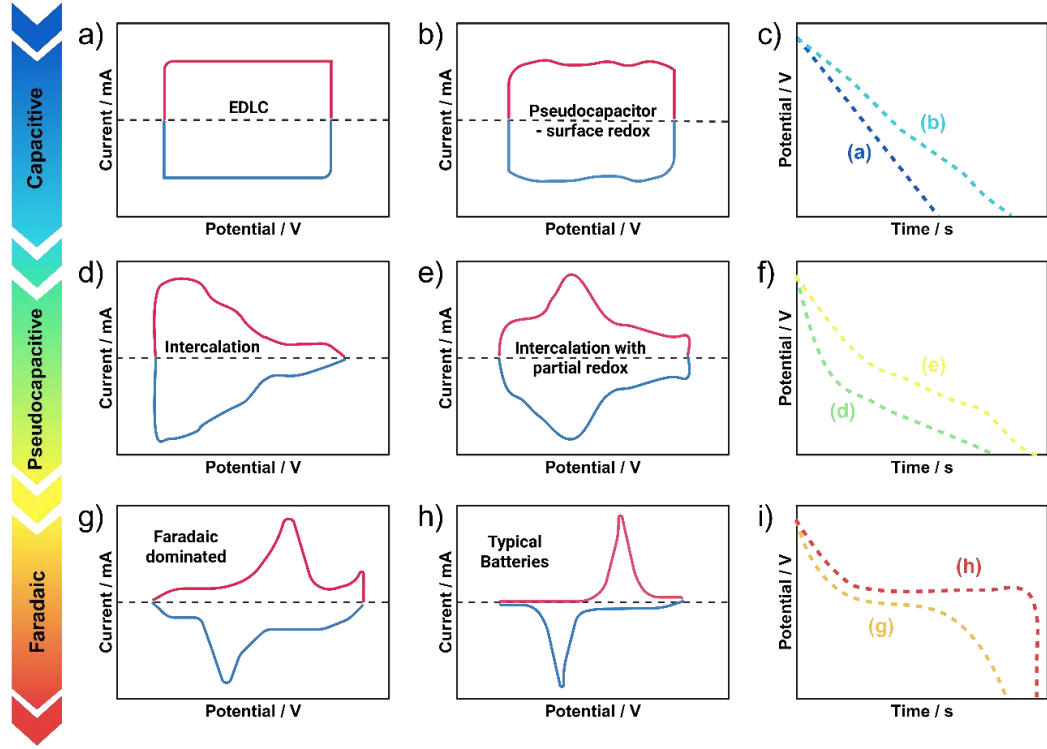


Figure 2. Schematic cyclic voltammetry curves and the corresponding galvanostatic discharge curves (c, f, i) for representative energy-storage mechanisms: **capacitive**: a) electrical double layer capacitor; b) surface-redox pseudocapacitor; **pseudocapacitive**: d) intercalation; e) intercalation with partial redox; **battery-type Faradaic** (g, h) materials. Redrawn from Ref.^[74] and created with BioRender.com.

Having distinguished the three charge-storage families, the next question that may arise is *how fast* each of them can store this charge? This is limited by kinetics, first, at the electrode/electrolyte interface and then inside the porous electrode itself. At the interface, electron transfer obeys Butler-Volmer behavior, and the current density is described by **Equation 5**:

$$j = j_0 \left[\exp\left(\frac{\alpha F \eta}{RT}\right) - \exp\left(\frac{-(1 - \alpha) F \eta}{RT}\right) \right] \quad (5)$$

where j is the current density ($\text{A} \cdot \text{m}^{-2}$), j_0 is the exchange current density ($\text{A} \cdot \text{m}^{-2}$) reflecting the rate of electron transfer at equilibrium, α is the charge-transfer coefficient, F is the Faraday constant ($96\,485 \text{ C} \cdot \text{mol}^{-1}$), η is the overpotential (V), R is the universal gas constant ($8.314 \text{ J} \cdot \text{mol}^{-1} \cdot \text{K}^{-1}$) and T is the absolute temperature (K). In porous electrodes, the local overpotential η varies when the charge is transferred through pores. Consequently, the characteristic time constant of a supercapacitor can be modeled as $\tau = RC$, with R including both the electronic resistance of the electrode and the ionic resistance of the pore electrolyte, while C is the accessible double-layer or pseudocapacitive capacitance. However, in well-designed supercapacitors, the rate-limiting step is almost always ionic transport, not electron transfer. High-surface-area porous carbons may display relaxation time constants on the order of 0.3 – 1s, thanks

to their optimized pore size and conductive networks.^[76,77] On the other hand, layered metal-chalcogenide electrodes such as Ni-Mo selenides^[78] or lithiated SnS₂, benefit from expanded interlayer gaps and short ion-diffusion paths, which can significantly reduce the time constants. Ojha et al.^[79] showed that LiSnS₂ microstructures with wide van-der-Waals gaps achieved fast ionic response and capacitive behavior. It has also been shown that introducing mesopores (2–50 nm) alongside intrinsic van der Waals gaps may reduce ion-transport resistance without compromising capacitance, offering a synergistic pathway for enhanced electrochemical performance.^[80,81]

On the other hand, for Faradaic insertion processes, the controlling step shifts from the ionic conductivity in the electrolyte to solid-state diffusion and associated charge-transfer phenomena. In SIBs and LIBs that employ metal chalcogenide electrodes, the van-der-Waals gaps characteristics of those allow alkali ions to diffuse more easily than in hard carbons – Na⁺ diffusion is up to two orders of magnitude faster than in hard-carbon anodes.^[82] For lithium-ion analogues, a similar enhancement of Li⁺ mobility once the structures are resized to a few nanometers is observed.^[83] However, metal-chalcogenides tend to experience significant volume expansion during deep cycling, which can induce mechanical stress and promote thickening of a solid-electrolyte interphase (SEI). Current strategies to preserve high-rate capabilities therefore combine three elements: 1) reducing lateral crystal dimensions to the few-layer range, which results in shortening ion-diffusion paths; 2) embedding chalcogenides into a conductive carbon matrix, which minimizes ohmic losses; and 3) selecting electrolytes that form an ultrathin, inorganic-rich SEI, thereby limiting interfacial impedance while preventing continuous electrolyte decomposition.^[84]

In practice, electrodes can present several mechanisms at once. Porous carbons may display pure double-layer behavior in their graphitic domains, while introducing heteroatoms into the structure, such as nitrogen or sulfur, can result in additional surface redox sites and thus add an extra pseudocapacitive contribution. One of the studies on N-doped porous carbons confirmed that the additional capacity arises from fast, surface-confined Faradaic reactions rather than bulk ion intercalation.^[85] Also, work by Deng et al.^[86] showed that the extent of this redox contribution depends on both the dopant type and the electrolyte anion, emphasizing the need to decouple ionic transport from redox kinetics when evaluating such materials. On the other hand, metal chalcogenides frequently show a gradual evolution from surface-limited pseudocapacitance during the first cycles to diffusion-controlled intercalation as ions penetrate deeper into the lattice. MoS₂, for example, initially shows capacitive charge storage due to nanoscale heterostructures, but during extended cycling, exhibits bulk-like diffusion such as Warburg impedance and voltage plateaus.^[87,88] Similar transitions have been documented for VS₂ and FeS₂ in Na-ion systems, underlining that the apparent charge storage mechanism evolves with cycling history as ions progressively penetrate deeper into the structure.^[89–91] Recognizing and quantifying the relative contributions of each pathway is essential for rational design, and advanced tools such as *in-situ* electrochemical quartz-crystal microbalance, *operando* synchrotron

X-ray diffraction and time-resolved impedance spectroscopy have become indispensable in this regard.

To sum up, charge can be stored electrostatically in the electric double layer, through fast surface redox (pseudocapacitance), or through bulk Faradaic reactions that accompany ion diffusion in the battery electrode. Electrostatic and pseudocapacitive processes are both truly capacitive – the stored charge scales linearly with voltage – whereas battery-type storage is chemical and shows a voltage plateau. Metal chalcogenides can be placed somewhere at the crossroads: their two-dimensional lattices and rich redox chemistry let them behave like capacitors at short times, but like batteries at longer periods of time.

2.2. Determination of charge storage mechanisms

Energy storage in electrochemical systems often arises from a combination of double-layer capacitance and pseudocapacitance or faradaic non-capacitive processes. While CV and GCD provide valuable insight into materials' electrochemical behavior, interpreting these responses in terms of underlying mechanisms remains a significant challenge. So the question that arises is: can we quantitatively resolve and assign the specific contributions of different charge storage mechanisms in real systems? A key step toward such quantification is recognizing that the structure of the electrochemical interface fundamentally governs the observed charge storage behavior. Depending on whether charge accumulation involves ion adsorption (capacitive), surface redox (pseudocapacitive), or bulk diffusion-limited intercalation, the interface adopts distinct physical and transport characteristics. These regimes can be broadly categorized based on the presence and nature of the diffusion layer, the extent of electron transfer, and the dominant transport mechanism.

The schematic presented in **Figure 3** highlights the connection between interfacial structure and electrochemical response. In diffusion-limited faradaic systems, a distinct concentration gradient and thick diffusion layer develop, and the classic Cottrell or Randles-Ševčík relation applies ($i \propto t^{-1/2}$ and $i_p \propto v^{1/2}$, respectively). In capacitive systems (EDLCs), where no charge transfer occurs, current scales linearly with scan rate, $i \propto v$. However, pseudocapacitive systems exhibit a unique scaling behavior involving combined contributions, expressed by **Equation 6**:

$$|i|_{pseudo} \sim av^{1/2} + bv + cv^{3/2} \quad (6)$$

This expression accounts for the faradaic, capacitive, and pseudocapacitive contributions, respectively, and highlights the hybrid nature of many modern systems – particularly those with nanoconfined or highly porous architecture.^[92]

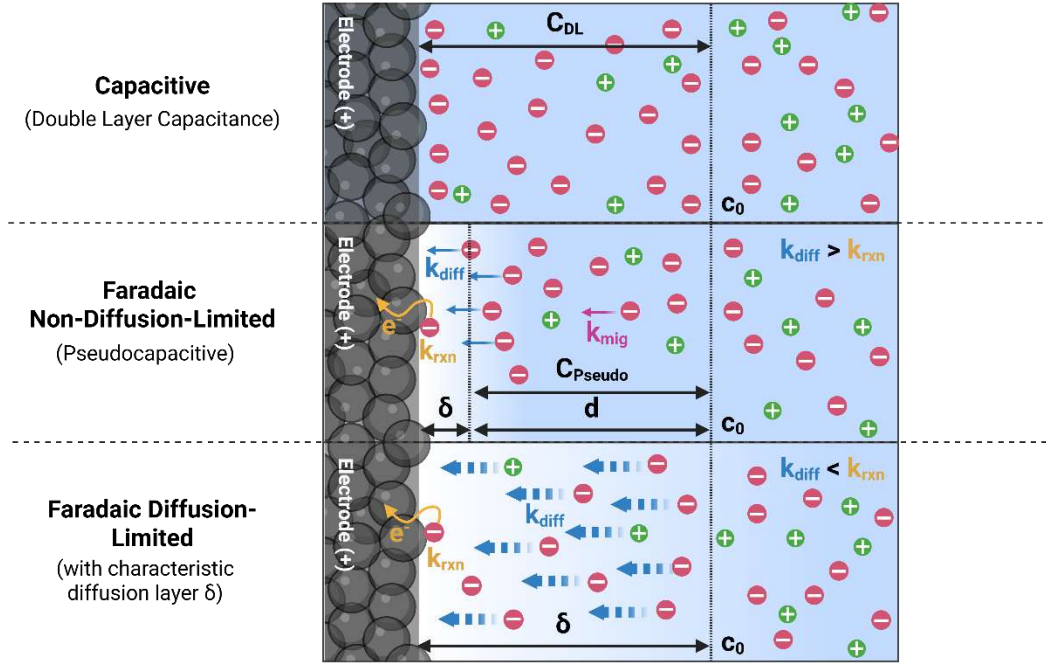


Figure 3. Schematic illustration of the electrochemical interface for different charge storage mechanisms: capacitive electric double layer formation, pseudocapacitive (non-diffusion-limited faradaic) storage, and diffusion-limited faradaic storage. Adapted from Ref.^[92] and created with BioRender.com.

Differentiating between these mechanisms is essential not only for understanding how charge storage occurs, but also for accurate interpretation of performance metrics like specific capacitance, rate capability, and energy density. Among the available tools, cyclic voltammetry remains the most accessible and widely applied method to analyze electrochemical behavior. Within CV analysis, two common quantitative approaches are used to deconvolute the contributions from capacitive and diffusion-limited processes: the methods proposed by Trasatti and coworkers,^[93] and Dunn and coworkers.^[94] These methods, despite their simplifications, offer practical means to interpret CV data and are therefore frequently used – especially in early-stage investigations or when complementary methods (e.g., electrochemical impedance spectroscopy, or *in situ/operando* spectroscopies) are unavailable.

The Trasatti method, first developed in the context of ruthenium oxide systems,^[93] estimates the total capacitance C_T as the sum of a surface-controlled capacitance C_o and a diffusion-controlled component C_i , expressed by **Equation 7**:

$$C_T = C_o + C_i \quad (7)$$

Assuming semi-infinite linear diffusion, the method relies on the scan rate dependence of capacitance, applying the relation according to **Equation 8**:

$$C(v) = \frac{S}{v^{1/2}} + C_o \quad (8)$$

where v is the scan rate and S is a slope related to ion diffusion resistance. The intercept of a plot of $C(v)$ vs. $v^{-1/2}$ yields C_o , while C_i is obtained by subtracting C_o from C_T .^[93] This approach is valuable for distinguishing the dominant mechanism in materials where surface and bulk storage contributions coexist, and it remains a reliable first-pass approximation when applied judiciously.

The method proposed by Dunn and coworkers offers a spatially resolved alternative by quantifying current at each potential as a function of scan rate. It separates the total current $i(V)$ into capacitive and diffusion-controlled components based on their scan rate dependencies (**Equation 9**):

$$i(V) = k_1 v + k_2 v^{1/2} \quad (9)$$

Plotting $i(V)/v^{1/2}$ vs. $v^{1/2}$ allows for the extraction of the constants k_1 and k_2 , which respectively quantify surface and diffusion contributions.^[94] This approach is particularly useful for systems like MoS₂ that exhibit potential-dependent redox features, as it enables mapping of the dominant mechanism across the voltage window.

While both methods are based on simplifications – such as ideal capacitive behavior, semi-infinite diffusion, and negligible ohmic effects – they are widely accepted. In the experimental study presented in Chapter II^[95] and III,^[96] both approaches were employed to analyze the electrochemical response of MoS₂-based electrodes. In such systems, where both surface redox and diffusion-limited intercalation may occur simultaneously, these analyses serve to capture the relative importance of each mechanism with reasonable accuracy. Nevertheless, it is important to be aware of their limitations. Deviations from ideal behavior caused by constant phase element (CPE) behavior or resistive drops at high scan rates can distort the apparent contributions. Modeling studies have demonstrated that even pure EDLC systems can appear diffusion-limited when non-ideal impedance elements or ohmic drops are present, potentially leading to misclassification.^[97]

To overcome such limitations, more sophisticated methods have emerged. One of the presented strategies is electrochemical modeling that integrates circuit parameters such as resistors, capacitors, and CPEs into a physics-based simulation. Pholauyphon et al.^[97] developed such a framework, allowing simulation of CV behavior under varied scan rates, resistances and CPE exponents. Their results showed that both the Trasatti and Dunn methods significantly overestimate diffusion-controlled contributions when interfacial effects or slow ion transport dominate the response. The modelling approach, in contrast, correctly isolates surface-controlled currents even in complex systems.

Beyond cyclic-voltammetry-based approaches such as the Dunn and Trasatti analyses, several complementary experimental approaches have been developed to quantify and to distinguish between double layer capacitance, surface pseudocapacitive redox and diffusion-limited insertion that are responsible

for energy storage in batteries and supercapacitors. For example, by fitting Nyquist or Bode plots with transmission-line or porous-electrode models, one can extract individual contributions from solution resistance, double layer capacitance, charge transfer kinetics and semi-infinite diffusion. Mei et al. showed that these parameters evolve systematically with state of charge in $\text{LiNi}_{0.6}\text{Co}_{0.2}\text{Mo}_{0.2}\text{O}_2$ and MoS_2 electrodes, allowing the capacitive fraction to be distinguished from insertion-controlled processes across several decades of frequency.^[98] Another example is the application of electrochemical quartz-crystal microbalance (EQCM) that couples gravimetry with electrochemistry. When applied to highly microporous carbons, EQCM revealed partial desolvation of Li^+ during adsorption, directly separating pure double layer storage from solvated-ion intercalation.^[99] In hydrous RuO_2 thin films the same technique resolved mass gains and losses associated with proton-coupled redox, quantitatively distinguishing surface pseudocapacitance from deeper insertion pathways.^[100]

Transient titration methods, most widely the galvanostatic intermittent titration technique (GITT), determine the chemical diffusion coefficient as a function of potential. The resulting diffusion coefficient values indicate the mechanism: a high, potential-dependent D points to diffusion-limited (battery-type) behavior, whereas potential-independent D supports capacitive storage. Moreover, a recent refinement – the intermittent current-interruption (ICI) method – delivers the same information within minutes, making *operando* coupling feasible.^[101] Finally, a wide group of *operando* spectroscopy measurements may provide significant information, as well. *Operando* Raman spectroscopy, exemplified by Chen et al. for birnessite-type MnO_2 , tracked potential-dependent phonon shifts that correlate with cation ($\text{Li}^+/\text{Na}^+/\text{K}^+$) insertion depth, thereby separating near-surface redox from bulk intercalation in real time.^[102] Complementarily, *in situ* X-ray absorption spectroscopy (XAS) has been used by lamprasertkun et al.^[103] to follow Mn K -edge shifts in layered MnO_2 nanosheets and to quantify the relative proportions of double layer, surface redox and intercalation contributions during fast cycling.

Taken together, these advanced tools complement traditional CV-based approaches by probing different aspects of the system. And, while the Trasatti and Dunn analyses may be limited in their assumptions, they remain valuable and justified tools where their application enables differentiation of storage mechanisms, especially when used alongside or validated by more comprehensive techniques.

2.3. *Key performance metrics: capacitance, capacity, energy density, coulombic efficiency, energy efficiency, power density*

Capacitance, the defining metric of a capacitor, describes the amount of charge stored per unit of potential difference. Mathematically, it is expressed as the differential change in stored charge with potential (**Equation 10**):

$$C = \frac{dQ}{dV} \quad (10)$$

In laboratory practice, it is commonly reported as an average value over a defined potential difference ΔV . To facilitate comparison across materials, capacitance is normalized either to mass (specific capacitance, C_S in $\text{F}\cdot\text{g}^{-1}$), geometric area (areal capacitance, C_A in $\text{F}\cdot\text{cm}^{-2}$) or volume (volumetric capacitance, C_V in $\text{F}\cdot\text{cm}^{-3}$). For porous electrodes – where only a fraction of the material may be wetted at high scan rates – these different normalizations can highlight kinetic limitations and ion accessibility.^[104] In the battery literature, the counterpart to capacitance is **capacity**, expressed in coulombs or more commonly in milliampere-hours per gram ($\text{mAh}\cdot\text{g}^{-1}$). Capacity measures the total charge that can be extracted when the electrode undergoes a complete insertion or conversion reaction. The numerical connection between the two metrics is straightforward: $1 \text{ F} = 1 \text{ C}\cdot\text{V}^{-1}$, so an electrode delivering $200 \text{ mAh}\cdot\text{g}^{-1}$ across 3 V equates to $720 \text{ C}\cdot\text{g}^{-1}$ or $240 \text{ F}\cdot\text{g}^{-1}$. However, the underlying charge storage mechanisms differ fundamentally: in batteries the energy is stored chemically, whereas for EDLC capacitors, it is stored electrostatically.^[105]

Energy density (E) quantifies the amount of work a device can perform per unit mass or volume. For an EDLC, it is expressed in Wh kg^{-1} , and given by **Equation 11**:

$$E = \frac{C_S(\Delta V)^2}{2 \cdot 3600} \quad (11)$$

where C_S is specific capacitance and ΔV refers to voltage window. The factor of $\frac{1}{2}$ originates from the linear charge-voltage relationship in an ideal capacitor, meaning that the average charging voltage equals half of the maximum voltage. Pseudocapacitors obey the same relation so long as the q - V curve remains quasi-linear. In contrast, for batteries, the energy is more appropriately obtained by integrating the voltage-capacity curve $V(Q)$, or equivalently by taking the product of the average operating voltage and the capacity. Device-level energy density must subtract the mass of inactive components – current collectors, binders, separators, and electrolyte – which can halve the gravimetric value relative to active material alone. Energy that can be stored scales quadratically with voltage, yet the electrochemical stability window is constrained by electrolyte stability.^[106] Aqueous electrolytes decompose above $\sim 1.23 \text{ V}$ vs. SHE (standard hydrogen electrode); organic carbonate mixtures extend this window to 2.5 – 3 V , while ionic liquids can, in principle, withstand 4 – 5 V , although in practice they are limited by impurities and catalytic degradation. As a result, significant research is dedicated to widening the voltage window via electrolyte formulation and electrode surface passivation.^[105]

The **coulombic efficiency** serves as a key metric for quantifying parasitic processes, according to the **Equation 12**. While a theoretically ideal capacitor would return every electron during discharge, in reality, side reactions such as electrolyte decomposition, surface redox, and corrosion can cause irreversible charge loss. Non-Faradaic devices can achieve coulombic efficiencies approaching 99.9% over a million cycles, whereas even state-of-the-art lithium-ion batteries rarely exceed 99.7% over a few thousand cycles.^[105]

$$\eta_c = \frac{Q_{dis}}{Q_{ch}} \quad (12)$$

In contrast, the **energy efficiency** is the time-integrated ratio of discharge to charge energy and is evaluated on IR-corrected galvanostatic curves. Unlike the coulombic efficiency, energy efficiency penalizes every source of energy loss: ohmic drop, voltage hysteresis and irreversible Faradaic processes. Therefore becomes indispensable whenever the voltage profile deviates from the ideal linear capacitor.^[107] For high-power applications, even small increases in equivalent series resistance (ESR) reduce energy efficiency, driving research into low-resistivity electrolytes, highly conductive carbon or chalcogenide composites, but also three-dimensional current-collector architectures.^[108]

The rate at which that energy is delivered is defined by **power density**, expressed in W kg^{-1} . For ideal capacitors, power density can be extremely high due to the absence of solid-state diffusion limits. However, in practice the maximum power is constrained by the device's ESR, according to **Equation 13**:^[109]

$$P = \frac{(\Delta V)^2}{4 \cdot ESR \cdot m} \quad (13)$$

where P is the power density ($\text{W} \cdot \text{kg}^{-1}$), ΔV is the operating voltage window (V), ESR is the equivalent series resistance (Ω) and m is the mass of active electrodes material, unless otherwise specified. In commercial device specifications, m typically refers to the total mass of the device, which leads to lower but more practical power density values. The factor of 4 originates from the condition that maximum power output is achieved when the external load resistance matches the ESR, resulting in only half the voltage being applied across the load. ESR itself includes contributions from electronic conductivity, ionic transport, interfacial impedance, and even inductance at high frequencies. Minimizing any one of these requires balancing conductivity, porosity, and electrode architecture. Plotting energy density against power density on logarithmic axes is a Ragone plot – a visual summary of performance across timescales. Pure supercapacitors dominate the high-power, moderate-energy domain; batteries occupy the bottom-right (high energy, moderate power); and fuel cells extend toward low power but practically infinite energy due to the continuous supply of fuel. It is worth mentioning that kinetically enhanced pseudocapacitors aim to push the locus of points diagonally upward, encroaching upon battery territory without abandoning their intrinsic capacitive nature. **Figure 3** presents the Ragone plot for the aforementioned devices.

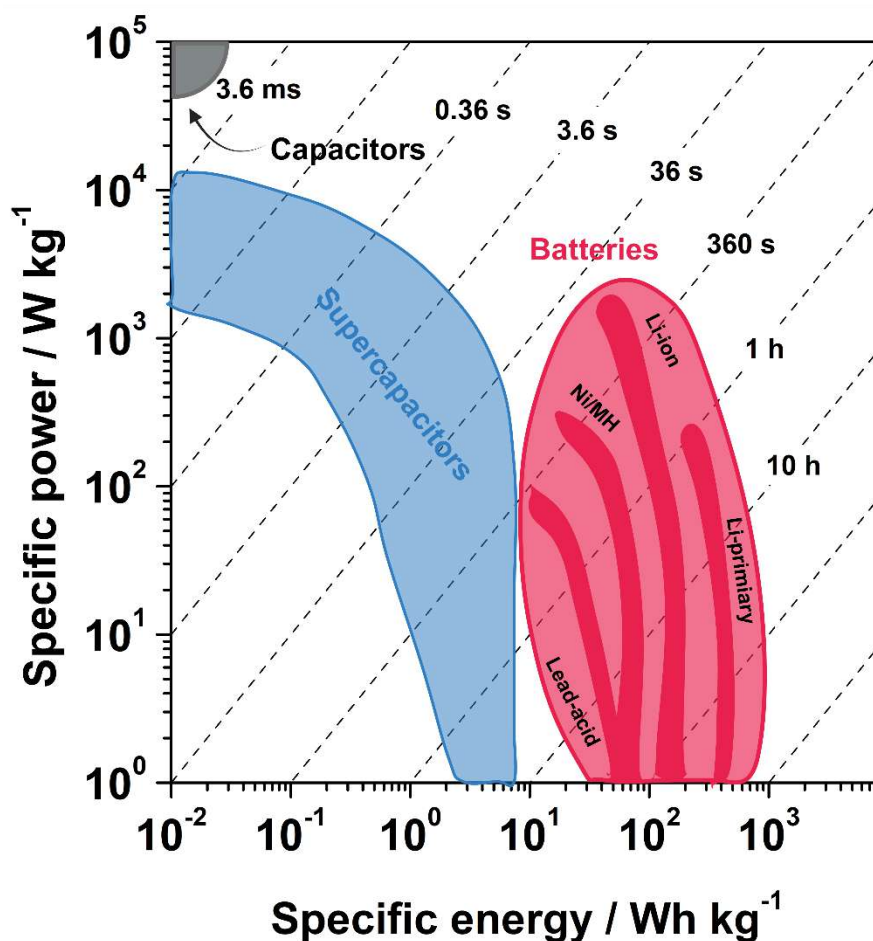


Figure 3. Electrochemical energy storage systems' energy and power relation depicted in a Ragone plot, along with the corresponding time constant regimes. Redrawn from Ref.^[110] and created with BioRender.com.

Another factor is **longevity**, which can be described by **cycle life** and **calendar life**. The former measures how many charge-discharge cycles a device can sustain before its capacity falls below a prescribed threshold, typically 80% of its initial value. Calendar life on the other hand captures the same degradation processes in an inactive state (storage) and is mostly influenced by temperature, state of charge and electrolyte purity.^[111]

2.4. Comparison between batteries and supercapacitors

Although both batteries and supercapacitors rely on the same processes when we take into account movement of electrons and ions, the manner in which those charges are stored differs profoundly. In batteries, energy is stored via bulk redox reactions in the active material, where charge-discharge processes require ionic diffusion across microns of solid and are limited by stoichiometric redox capacity. In contrast, supercapacitors store energy electrostatically at the surface or in a near-surface redox layer, and charge storage is primarily governed by accessible surface area, dielectric environment, and electrolyte structure, not stoichiometry.^[112] This distinction is reflected in industry-standard performance metrics. Commercial lithium-ion cells typically deliver $150\text{--}250 \text{ Wh}\cdot\text{kg}^{-1}$ of energy

density, yet rarely exceed $1 \text{ kW}\cdot\text{kg}^{-1}$ of continuous power and $\sim 10 \text{ kW}\cdot\text{kg}^{-1}$ of pulse power. In contrast, state-of-the-art EDLC supercapacitors provide only $5\text{--}10 \text{ Wh}\cdot\text{kg}^{-1}$, but can effortlessly supply $10\text{--}15 \text{ kW}\cdot\text{kg}^{-1}$ with millisecond response times.^[113] Pseudocapacitors and hybrid devices narrow the energy gap, delivering $30\text{--}100 \text{ Wh}\cdot\text{kg}^{-1}$ under favorable conditions.^[114,115]

Cycle life is another differentiator. Supercapacitors frequently survive beyond one million cycles with less than 20% degradation, whereas even the most advanced lithium-ion batteries seldom exceed 5 000 cycles under identical depth-of-discharge conditions. This supercapacitors' longevity is due to the absence of crystallographic rearrangement, whereas mechanical and chemical degradation accumulates in battery electrodes over time. From a safety perspective, supercapacitors store less energy per unit volume, so even in the event of a failure, the consequences are typically mild and the heat released is minimal. In contrast, batteries that hold large chemical energy, demand elaborate management systems to mitigate thermal runaway. Moreover, the absence of phase transitions grants supercapacitors superior low-temperature performance, although electrolyte viscosity still imposes limits below $-40 \text{ }^{\circ}\text{C}$.^[116] An important nuance is that the high gravimetric energy density at the cell level is partly reduced at the system level, since battery packs require additional mass and volume for thermal management, safety features and protective enclosures. Supercapacitor modules, in contrast, generally demand less active cooling due to their intrinsic tolerance to high currents and overcharging. However, their low cell voltage necessitates series configurations, and the accompanying cell-balancing electronics can lower volumetric energy density.

These complementary strengths indicate distinct application domains: batteries dominate wherever long-duration energy supply is paramount – electric vehicles, portable electronics, grid-level storage, whereas supercapacitors are ideal for high-power, short-burst applications such as regenerative braking, wind turbine pitch control, fuel-cell buffering and emergency backup systems.^[117] Hybrid energy-storage systems combining both technologies in parallel are increasingly adopted, capitalizing on the high energy of batteries and the high power of electrochemical capacitors.^[118] As the two technologies mature, their design strategies are crossing each other. Batteries are being engineered with nanostructured electrodes to shorten diffusion paths and boost rate capability, effectively borrowing from supercapacitor strategies. On the other hand, supercapacitors incorporate redox-active materials to improve energy density. The boundaries are even more blurred when concepts like *intercalation pseudocapacitance* appear, where classical battery mechanisms occur within a capacitive response time. Understanding and exploiting this trend, rather than treating batteries and capacitors as binary categories, may be the frontier of modern research.

3. Supercapacitors

3.1. *Types of supercapacitors: EDLCs vs pseudocapacitors vs hybrid systems*

Supercapacitors are typically categorized into three working families. The first one, electrical double-layered capacitors (EDLCs), stores charge by physical adsorption and rearrangement of ions at the surface of a conductive electrode. There is no charge transfer across the interface, so the process is fast and highly reversible. EDLCs most commonly use activated carbon due to its high surface area, conductivity, and affordability. The concept was first introduced by General Electric in 1957,^[119] but practical devices emerged in the 1970s when Standard Oil of Ohio Research Center developed porous carbon electrodes^[120,121] and licensed the technology to Nippon Electric Company, which began selling the first commercial EDLCs under the name “Super Capacitor” in 1971.^[122] Since then hundreds of papers have nudged that figure up or improved the rate capability, but the basic picture has not changed: EDLCs trade enormous cycle life for modest energy density.

In the second group, known as pseudocapacitors, charge storage is governed by fast and reversible Faradaic reactions at or near the surface of the electrode. Unlike EDLCs, pseudocapacitors involve electron transfer across the electrode-electrolyte interface, yet the reactions occur without bulk phase changes or long-range ion diffusion, preserving the high-rate capability typical of capacitive systems. The concept of pseudocapacitance emerged from early electrochemical investigations into surface-bound redox phenomena at 1960s. At that time, studies revealed that certain adsorbed/deposited species (on the electrode) could undergo rapid and reversible electron transfer without traditional bulk diffusion, hinting at capacitive-like charge storage behavior.^[123] An essential step forward was in 1971, when ruthenium dioxide (RuO_2) was reported to exhibit cyclic voltammetry profiles resembling those of ideal capacitors – the rectangular-shaped curves – even though the charge storage involved Faradaic processes.^[124] This was one of the first demonstrations that redox-active materials could mimic the behavior of capacitors, thereby challenging the conventional separation between capacitive and battery-type systems. On the following decades, similar electrochemical behavior was observed in various conducting polymers,^[125] as well as in a range of transition metal oxides like manganese dioxide, cobalt oxide, and nickel oxide.^[126–129] Despite these early findings, the use of such materials in the context of supercapacitors was not widely adopted until the 1990s, when the term pseudocapacitance began to gain traction in the scientific literature. More recently, metal chalcogenides such as sulfides and selenides of molybdenum, cobalt, and nickel have attracted significant attention as pseudocapacitive materials.

Yet, pseudocapacitance is not the only mechanism bridging the gap between batteries and capacitors. In terms of device architecture, hybrid supercapacitors are constructed by combining two different types of electrodes – typically one battery-type Faradaic electrode and one capacitor-type electrode.^[130] These devices aim to unify the high energy density of batteries with the high power

density and long cycle life of capacitors. A well-known example is the lithium-ion capacitor (LIC), originally patented by Amatucci et al.,^[131] which pairs a nanostructured $\text{Li}_4\text{Ti}_5\text{O}_{12}$ anode with an activated carbon cathode, achieving working voltages close to 4 V in organic electrolytes. Similarly, sodium-ion capacitors (NICs) have gained attention by using analogous configurations, such as hard carbon/activated carbon systems, capable of delivering much greater energy density than supercapacitors and enhanced performance in power density in comparison with traditional sodium ion batteries.^[132,133]

A separate but important distinction in supercapacitors design is whether the two electrodes are chemically the same. Symmetric cells, which use the same material for both electrodes (typically activated carbon), are simple to balance and diagnose, but their operational voltage is restricted by that single material's stability window.^[134] On the other hand, asymmetric supercapacitors combine different materials for anode and cathode electrode, with different stability windows. This configuration allows the cell to operate over a wider voltage range, leading to a substantial improvement in energy density.^[135,136] For instance, Fan et al.^[137] demonstrated an asymmetric cell using a graphene/ MnO_2 composite as the cathode and activated carbon nanofibers as the anode, achieving a voltage of 1.8 V and energy density of $51.1 \text{ Wh}\cdot\text{kg}^{-1}$. Another study by Wen et al.^[138] used a MnO_2 @carbon spheres composite and nitrogen-doped carbon as the negative electrode to reach 1.9 V in a Na_2SO_4 electrolyte. Crucially, in asymmetric design, achieving an appropriate mass balance between the two electrodes is essential to maintain capacity matching and stability, which adds design complexity but is often justified by the significant gain in energy output.

3.2. *Materials for supercapacitor electrodes*

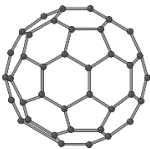
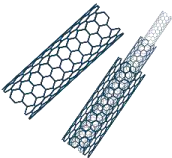
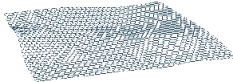
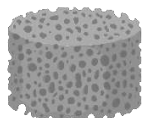
3.2.1. Carbon-based materials

In general, electrochemical capacitors derive their exceptional power performance from surface-confined charge storage processes. While electrolyte selection defines the operational voltage window and ionic transport properties of the device, the architecture of the electrode material ultimately govern accessible surface area, electronic/ionic transport pathways, and long-term stability under multiple cycles of polarization. In practice, nearly all commercial ECs utilize carbonaceous electrodes – most commonly these are activated carbon (AC)-based materials processed into films or pressed powders. This is because carbons combine broad electrochemical stability, tunable porosity, good electrical conductivity, low cost, and scalability from diverse feedstocks.^[139,140] Early broad research reviews by Conway,^[73] Frackowiak and Béguin,^[141] but also Simon and Gogotsi^[142,143] established the structure-charge storage relationships that continue to guide material development, emphasizing the importance of accessible surface area for double-layer charge, the influence of pore size distribution relative to solvated ion dimensions. They also point out the opportunities to couple EDL capacitance with pseudocapacitance that may be introduced by heteroatoms or composite phases.

One of the ways to organize the highly diverse field of carbon materials is by their **structural dimensionality**: zero-dimensional (0D) with fullerenes, **carbon (CQD)** and **graphene (GQD) quantum dots** as representatives; one-dimensional (1D) like **carbon nanotubes (CNTs)**; two-dimensional (2D) with a classical example of **graphene** or **reduced graphene oxide (RGO)**; and three-dimensional (3D) structures such as **aerogels** or **AC**. Dimensionality is more than just a way to classify these materials – it constrains electron percolation paths length, determines ion transport, controls packing density, influences mechanical integrity at the electrode/collector interface, and affect the overall electrochemical performance.^[144,145]

There are several physicochemical properties that are relevant to electrochemical capacitors' performance that include Brunauer-Emmet-Teller (BET) specific surface area (SSA), pore size distribution with its micro-, meso- and macroporosity, but also as much important a degree of graphitization (sp^2) which determine electrical conductivity, and accessible crystallographic edges or defect sites that host heteroatom functionalities.^[145] **Table 1** summarizes characteristics reported in the literature for various carbon materials in relation to their dimension, with representative carbons that will be described in detail in this chapter – activated carbons, carbon nanotubes, graphene-based carbons, and 3D carbon architectures.

Table 1. Physicochemical and electrochemical characteristics of carbonaceous materials used for electrochemical capacitors. Structures created with BioRender.com.

Dimension	0D	1D	2D	3D
Representative Materials	CQD, Fullerene	Single-walled/ Multi-walled CNTs	Graphene, RGO	AC, aerogels
SSA [m ² g ⁻¹]	100–800	200–1300	500–2000	800–3500
Capacitance [F g ⁻¹]	50–200	150–420	150–300	250–300
Conductivity [S m ⁻¹]	10–100	10 ² –10 ⁷	10 ² –10 ⁸	10 ² –10 ³
Structure				
Reference	[146,147]	[148]	[148,149]	[150,151]

Activated carbon has established itself as the industrial standard for supercapacitor electrode materials, largely due to its accessibility and favorable electrochemical properties that can be easily tuned. Its production relies on thermochemical conversion of carbon-rich precursors through pyrolysis

followed by an activation step that allows for obtaining highly porous structures. A broad spectrum of feedstocks can be used, ranging from conventional fossil-derived sources like coal and petroleum coke to sustainable biomass wastes such as coconut shells, sawdust, nutshells, or even sewage sludge.^[152–154] The activation procedure, which typically involves physical agents such as steam or carbon dioxide, or chemical agents like KOH or eutectic salt melts, can induce extensive etching of the disordered carbon structure and generate a network of pores from micro- to mesoporosity.^[155–157] These pores form through partial removal of amorphous carbon domains and lead to specific surface areas that often exceed $2000 \text{ m}^2 \text{ g}^{-1}$, and in optimized systems, even reaching up to $3500 \text{ m}^2 \cdot \text{g}^{-1}$.^[158] The resulting morphology typically consists of a turbostratic carbon^[159] with randomly oriented graphene-like sheets, creating pores and interconnected tunnels that allow for fast electrolyte diffusion during charge/discharge cycles.

While ACs primarily store charge through non-faradaic electric double layer capacitance, their electrochemical performance can be significantly enhanced by tailoring the surface chemistry. Post-synthesis functionalization or heteroatom doping may introduce redox-active groups, and as a result a material that can also support pseudocapacitive behavior is obtained.^[160] Nitrogen and oxygen are the most commonly introduced heteroatoms, as they can increase wettability and can participate in faradaic reactions.^[161–165] For example, oxygenated groups like quinones and carbonyls contribute redox activity in acidic media.^[166,167] On the other hand, phenols, lactones and carboxylic acids tend to be active in alkaline electrolytes, allowing specific capacitance values to increase substantially beyond what can be achieved only with EDL contribution.^[168,169] Nitrogen functionalities, e.g. pyridinic, pyrrolic, or graphitic nitrogen, can be introduced by thermal treatment in the presence of nitrogen-rich precursors like melamine or urea, and according to the literature they improve electrical conductivity, cycling stability and electrochemical stability window.^[170–172] Moreover, the wettability of the carbon surface, which is crucial for electrolyte penetration and pore accessibility, has been shown to improve with the introduction of hydrophilic oxygen functionalities such as carboxyl, phenol, and hydroxyl groups. This enhancement facilitates faster ion transport and improved capacitance, especially in aqueous media.^[173–175]

Nevertheless, the use of AC-based electrode materials is not without limitations. Their energy density is restricted by the capacitive mechanisms of energy storage and the typically narrow voltage window, especially when aqueous electrolytes are used. The integration of pseudocapacitive elements and the development of advanced hybrid materials, e.g. AC combined with metallic compounds^[176,177] or conductive polymers,^[178] are among the strategies being explored to improve the performance beyond that of classical double layer systems. For instance, Kour et al.^[179] synthesized MnO_2 nanorods via hydrothermal processing and incorporated them onto activated carbon using a simple sol-gel approach.

The resulting MnO₂/AC composite exhibited a specific capacitance of 398.5 F·g⁻¹ at 1 A·g⁻¹, more than double than pristine MnO₂, and achieved an impressive energy density of 105.2 Wh·kg⁻¹, which they attributed to the synergy between the faradaic redox activity of MnO₂ and the high surface area of AC.^[179] Similarly, Liao et al.^[180] reported the fabrication of Fe₂O₃-AC and MnO₂-AC hybrid electrodes using oxidative potassium salts and *in situ* growth techniques. These composites showed specific capacitance of 645 and 548 F·g⁻¹, respectively, and exhibited 90.2% retention over 10 000 cycles in alkaline electrolytes.^[180] Polymer-based composites are also reported to present impressive electrochemical performance. Dubey et al.^[181] developed a hybrid electrode by depositing conductive polypyrrole on porous AC derived from human hair, using an *in situ* oxidative polymerization that takes advantage of the 3D carbon network as a scaffold. The presented composite was characterized by capacitance enhancement (358 F·g⁻¹ in 1 M H₂SO₄) due to the pseudocapacitive contribution of polypyrrole, but also improved ion access and electrical conductivity.^[181] Despite these advances and researchers searching for new solutions, AC continues to serve as the foundational material in commercial supercapacitor devices due to its processability, low cost, long cycle life, and fast charge-discharge capabilities. Its enduring relevance is sustained by ongoing innovations in surface functionalization, hierarchical porosity control, and electrolyte studies, all aimed at pushing the boundaries of capacitive energy storage.

In contrast to the highly amorphous and disordered nature of activated carbon, **carbon nanotubes** offer a structurally ordered, graphitic alternative that shows several advantages to supercapacitor electrodes design. CNTs are typically categorized into single walled (SWCNTs) and multi-walled (MWCNTs) nanotubes, depending on the number of graphene layers. Their synthesis can be approached in several ways, e.g. by arc discharge, laser ablation, or even more commonly used chemical vapor deposition (CVD) technique. However, although the synthesis results in crystalline materials, it is often accompanied by metallic catalyst residues and amorphous carbon byproducts that require post-synthesis purification.^[182,183] CNTs stands out when it comes to their exceptional electrical conductivity.^[148] This makes them ideal for reducing charge transfer resistance in electrode structures, especially when incorporated as conductive scaffolds.^[184,185]

However, despite their superior electrical properties, pristine CNTs are generally characterized by moderate surface areas, ranging from 200 to 1300 m² g⁻¹ for SWCNTs, and considerably lower for MWCNTs, but this depends on tube diameter, wall number and degree of aggregation.^[186] This limitation in accessible surface area restricts their double layer capacitance compared to highly porous materials like ACs. Additionally, the smooth graphitic surface of CNTs results in poor wettability and limited ion accessibility if no surface functionalization is applied.^[187,188] Strategies to enhance their capacitive performance have thus

focused on surface modification and composite formation. For example, functionalization with oxygen-containing groups through acid treatments or plasma oxidation not only improves electrolyte access but also introduces redox-active sites capable of introducing the pseudocapacitive contribution in energy storage.^[189–192]

More commonly, CNTs serve as high-conductivity frameworks as part of composite electrodes. Their 1D morphology facilitates percolating networks and they are usually integrated with electrochemically active materials such as transition metal oxides^[193,194] and conductive polymers^[195–197] to form hybrid electrodes with enhanced energy storage capacity and rate performance. In such composites, CNTs not only provide electronic pathways but also provides mechanical stability that hinder structural degradation during cycling. Notably, CNT-based composites have demonstrated specific capacitance values exceeding $300 \text{ F} \cdot \text{g}^{-1}$ depending on the composite material. Apart from performance enhancement, the incorporation of CNTs into 3D structures such as aerogels, offers scalable solutions for flexible and wearable energy storage devices, which is an emerging area where conventional AC-based electrodes fall short.^[198–200] Therefore, CNTs may not compete with AC in terms of active surface area, but their electrical conductivity and structural order make them an attractive choice in the development of next-generation supercapacitor technologies.

The third representative material is **graphene**, which is a two-dimensional structure, consisting of a single layer of sp^2 -bonded carbon atoms arranged in a honeycomb lattice. It was first isolated in 2004 through mechanical exfoliation, which at this time was a breakthrough that underscored its exceptional physicochemical properties and led to the 2010 Nobel Prize in Physics for Andre Geim and Kostya Novoselov. Its theoretical specific surface area reaches $\sim 2630 \text{ m}^2 \cdot \text{g}^{-1}$ and is one of the reasons for its potential in double layer charge storage.^[149,201] Also, its electrical conductivity is close to and even exceeds that of CNTs, with values approaching 10^8 S m^{-1} .^[148] In context of energy storage applications, it can facilitate ultrafast electron transport and support high charge/discharge rates, making it an attractive candidate for electrode material.

However, the practical implementation of graphene in supercapacitors remain challenged by issues of synthesis, but also structural aggregation. Conventional methods for producing graphene, such as CVD, chemical exfoliation and thermal reduction of graphene, often result in multilayer stacks or restacking of single layers due to van der Waals forces. And, although strategies such as heteroatom doping,^[202–204] surface functionalization,^[205–207] and three-dimensional structuring (e.g. aerogels or foams)^[208–210] have been studied to mitigate these effects, the material's theoretical advantages are often not fully realized in practical devices. As with CNTs, graphene is most effective when used as a conductive counterpart for pseudocapacitive or battery-type materials.^[211–213] Composites incorporating graphene with transition metal oxides or sulfides have

demonstrated notable improvements in specific capacitance and energy density. For instance, Dong et al.^[214] synthesized a NiCo₂S₄/graphene, where nickel-cobalt sulfide nanoneedles were embedded into a graphene framework to prevent aggregation and maximize interfacial contact. The asymmetric supercapacitor device constructed with this composite delivered a specific capacitance of 199.3 F·g⁻¹ at 2 A·g⁻¹ and retained 90.4% after 10 000 cycles ($j = 10 \text{ A} \cdot \text{g}^{-1}$), proving excellent cycling stability and rate performance.^[214] In another study, Qian et al.^[215] prepared a surfactant-free graphene Mn₃O₄ hybrid electrode using simple solvothermal synthesis. The composite reached specific capacitance of 239.6 F·g⁻¹, and there was no need of addition of conducting fillers due to the high graphene conductivity. The enhancement of capacitance in comparison with pristine graphene and pure Mn₃O₄ was due to the uniform distribution of oxide nanoparticles and large surface area and high conductivity of graphene counterpart.^[215] Additionally, Liu et al.^[216] designed a Co_{0.33}Fe_{0.67}S₂/graphene composite using a one-step hydrothermal method, forming a sandwich-like structure where sulfide nanoparticles were embedded between graphene nanosheets. Authors stated that this design promoted high electronic conductivity and redox activity, at the same time suppressing volume changes. The asymmetric supercapacitor device constructed with this composite achieved an energy density of 63 Wh·kg⁻¹ at a power density of 300.5 W·kg⁻¹.^[216]

In summary, carbon-based materials, from the disordered yet highly porous activated carbon to the structurally defined CNTs and graphene, are definitely background for supercapacitor electrode development.^[217] While each of these materials offers distinct advantages in terms of surface area, conductivity and tunable chemistry, they are fundamentally limited by the non-faradaic nature of electric double layer capacitance and, sometimes, by practical synthesis constraints. These limitations have driven research toward alternative types of materials that can provide high energy density thanks to the pseudocapacitive behavior. In this context, metal chalcogenides (particularly sulfides and selenides of transition metals) are standing out as promising candidates.

3.2.2. Metal chalcogenides

The past decade has seen a considerable interest in the exploration of two-dimensional materials beyond graphene, prompted by the need to overcome its inherent limitations in energy storage applications. Among the most promising of these 2D materials are the transition metal dichalcogenides (TMDs), which follow the general formula MX₂, where *M* is a transition metal (e.g., Mo, W, V) and *X* is a chalcogen atom (S, Se, Te),^[26] see **Figure 4a**. Structurally, TMDs consist of a layer of metal atoms sandwiched between two chalcogen layers. Within layers those atoms are held together by strong covalent bonds, whereas between the layers weak van der Waals interactions may be distinguished. This layered structure facilitates both ion intercalation and surface reactions, making TMDs particularly attractive for electrochemical energy storage devices such as supercapacitors.^[218]

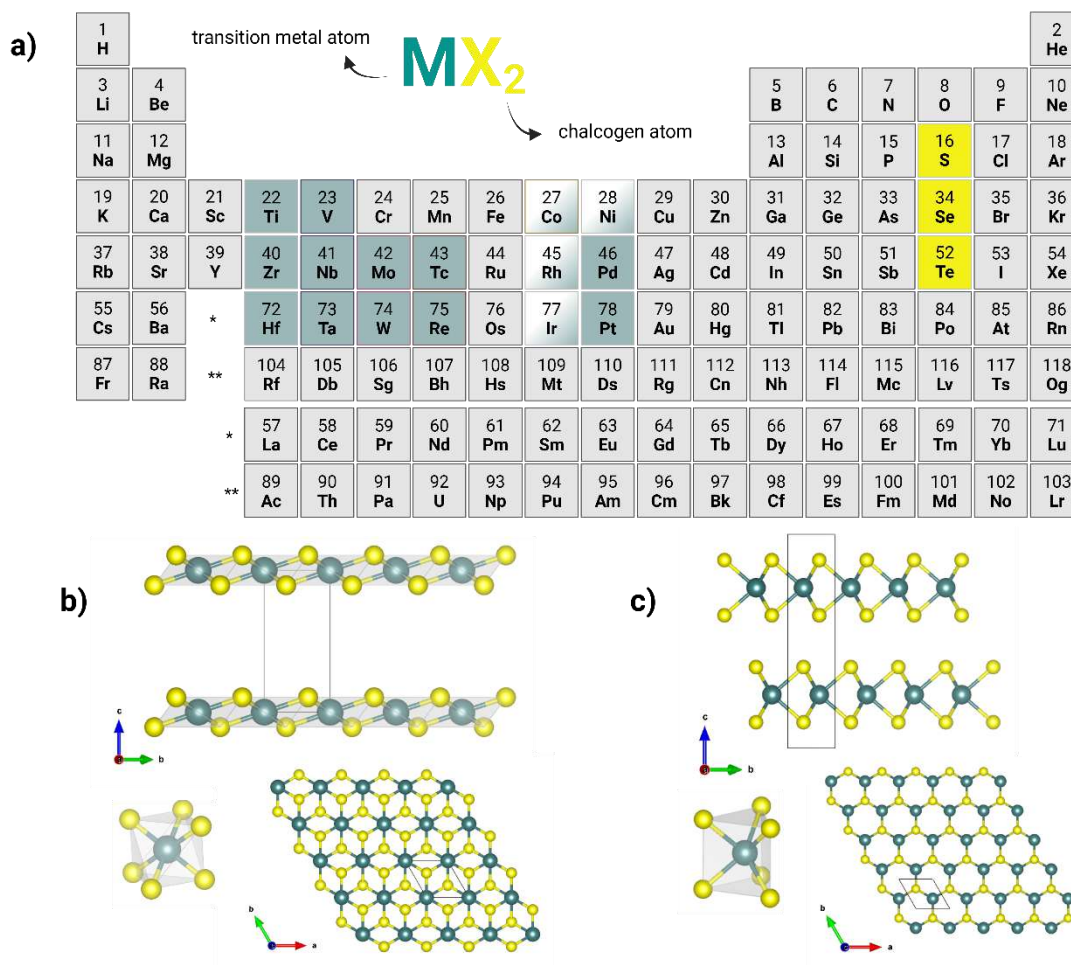


Figure 4. a) Periodic table with transition metal elements and chalcogen elements forming layered structures; side and top views of b) 1T (octahedral coordination) and c) 2H (trigonal prismatic coordination) structures of MoS₂. Adapted from Ref.^[219] and Ref.^[95], created with BioRender.com. Crystal structures were created using VESTA 3 software.^[220]

Among TMDs, molybdenum sulfide (MoS₂) is one of the most studied. MoS₂ can exist in different crystallographic phases, most notably the 2H (**Figure 4c**) semiconducting phase, with a band gap of ~1.9 eV in monolayer form, and the 1T phase (**Figure 4b**), which exhibits metallic behavior and enhanced electrical conductivity, up to five orders of magnitude higher than 2H MoS₂.^[221,222] However, MoS₂ naturally crystallizes in the 2H phase, which is more thermodynamically stable under ambient conditions.^[223] In contrast, the 1T phase is metastable and thus more challenging to obtain and maintain over time. It also tends to revert to the 2H form unless stabilized by defects, dopants, or structural confinement.^[224] Several studies have attempted to overcome this imitation through phase engineering strategies. For example, Li et al.^[225] demonstrated that incorporating –COOH groups during a one-step hydrothermal synthesis allowed for the controlled stabilization of high-purity 1T MoS₂, achieving a specific capacitance of 180 F·g⁻¹ and 84.6% retention over 10 000 cycles.^[225] Similarly, Xuyen and Ting^[226] developed MoS₂ nanoflowers with tunable 1T/2H phase ratios

using a microwave-assisted hydrothermal route. They showed that increasing the 1T content from 40% to 73% was performed by adjusting the ratio of precursors, which directly enhanced capacitance from $\sim 150 \text{ F} \cdot \text{g}^{-1}$ to $259 \text{ F} \cdot \text{g}^{-1}$, pointing out the advantages of the metallic phase.^[226] Nevertheless, achieving stable and high-yield 1T-phase MoS_2 remains difficult. The interconversion between phases and the engineering of mixed phase structures has therefore emerged as a practical compromise. In the mixed structures, the 2H may stabilize the 1T phase, allowing the composite to retain improved conductivity while preserving chemical robustness.^[224] This has important implications for applications in supercapacitors, where the increased number of redox active sites in 1T MoS_2 can significantly increase specific capacitance, particularly in hybrid architectures or on direct-on-substrate growth.

The synthesis of MoS_2 and other TMDs can be broadly categorized into top-down and bottom-up strategies, each offering distinct advantages depending on the intended application. Top-down methods typically involve exfoliating bulk layered crystals into few- or single-layer nanosheets, using techniques such as mechanical cleavage, liquid-phase exfoliation, chemical exfoliation, or electrochemical delamination.^[227] While mechanical exfoliation, which is inspired by the “Scotch tape” method for graphene production, yields high-quality monolayers, it is not scalable.^[228] Liquid-phase exfoliation on the other hand offers higher yield and can be tuned using surfactants or solvents such as N-methyl-2-pyrrolidone (NMP) or dimethylformamide (DMF), which promotes better delamination. However, this approach often results in structural defects and restacking, limiting electrochemical performance.^[229] In contrast, bottom-up methods such as chemical vapor deposition (CVD) and hydrothermal and solvothermal synthesis allow for better control over material composition, morphology and crystalline phase.^[230] CVD typically produces uniform monolayer films on substrates under tightly regulated conditions, but requires high temperatures ($> 600 \text{ }^\circ\text{C}$), multiple gas lines, and precise control of precursors.^[221] All of this make this process costly and technically demanding. Hydrothermal and solvothermal syntheses, on the other hand, are solution-based processes that take place in sealed autoclave at moderate temperatures (up to $220 \text{ }^\circ\text{C}$), using aqueous or organic solvents, respectively.^[230] These methods enable scalable production of nanostructured chalcogenides in various morphologies: nanosheets,^[231] nanoflowers^[232,233] or hollow spheres.^[234,235] This can be achieved by varying reaction time, temperature, precursors and additives.^[236–239] Also, the possibility to tune phase and porosity makes hydrothermal synthesis especially attractive for electrochemical energy storage.^[240–243] However, they are not without limitations. The resulting materials may often exhibit variability between batches, residual impurities, or inconsistent crystallinity, and a lot of misconceptions in the literature, especially when characterizing hydrothermally obtained 1T phase MoS_2 .^[244]

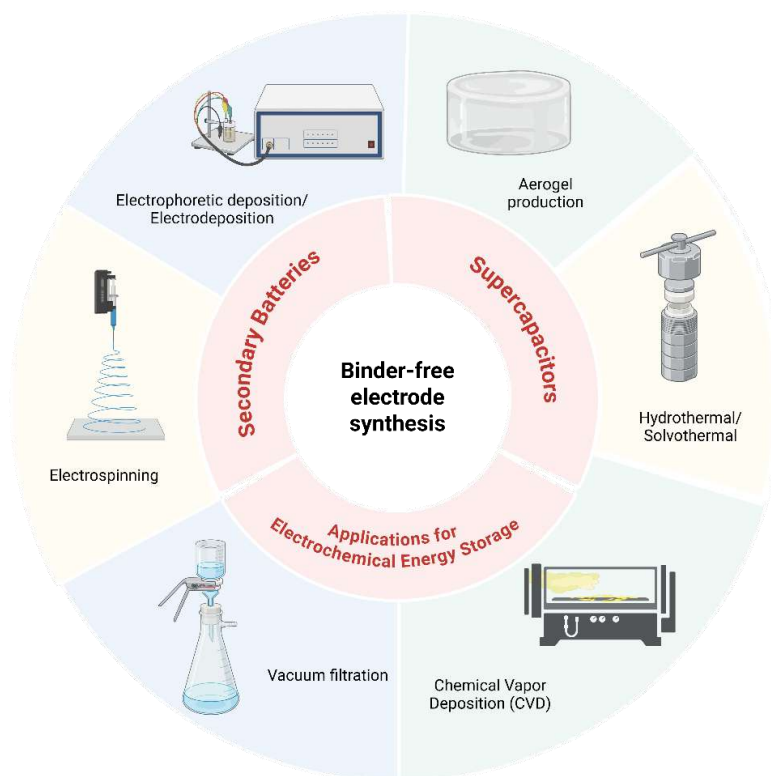


Figure 5. Binder-free synthesis approaches for electrochemical energy storage applications. Adapted from Ref.^[245] and created with BioRender.com.

A particularly promising approach in the development of electrode materials for supercapacitors is the binder-free growth of active materials directly on conductive substrates. Traditional electrode fabrication involves casting slurries of active material, conductive additives and polymeric binders (e.g., PDVF). However, this approach can introduce interfacial resistance or reduce active surface exposure, but most of all binders presence increases “dead mass” and as a result influence the electrochemical performance.^[246,247] Binder-free strategies bypass these issues by facilitating close contact between the electroactive material and current collector, which may improve charge transfer kinetics and mechanical stability.^[245,248–252] Various methods have been explored for binder-free electrodes, which are presented in **Figure 5**. For instance, Ren et al.^[253] used a CVD technique to deposit amorphous FePO_4 onto carbon nanotubes fibers, creating flexible, binder-free electrodes with excellent mechanical strength and sodium-ion battery performance. Similarly, Yao et al.^[254] synthesized nitrogen-doped carbon-coated Ni_3S_2 nanowires directly on nickel foam, improving electronic conductivity and cycling stability in Li-ion batteries. However, CVD, while enabling atomic-scale control and high material purity, typically requires high temperatures and sophisticated equipment. Other technique is electrochemical deposition which, on the other hand, allows fine control over film thickness and uniformity, but may not yield the desired nanostructures for high surface area.^[245] In contrast, hydrothermal synthesis stands out for its simplicity and ability to directly grow nanostructured materials on a wide variety of substrates, including carbon cloth, nickel foam, graphene-

based films, and also metallic foils. Pazhamalai et al.^[255] demonstrated hydrothermal growth of vertically oriented copper tungsten sulfide nanostructures on Ni foam. The resulting binder-free electrode offered efficient ion transport pathways and reached specific capacitance of $107.9 \text{ F}\cdot\text{g}^{-1}$ with high cycling stability over 10 000 cycles.^[255] A similar strategy was used by Ma et al.,^[256] who fabricated hollow CoMoS_4 nanotubes on carbon cloth by combination of hydrothermal synthesis and sulfidation. As a result, the asymmetric supercapacitor with the assembled electrode delivered high energy density ($49.1 \text{ Wh}\cdot\text{kg}^{-1}$ at $800 \text{ W}\cdot\text{kg}^{-1}$) and maintained 90% capacity over 10 000 cycles.^[256] Together, all of those examples illustrate the variety of methods available to synthesize binder-free electrode. From high-temperature vapor-based processes to wet chemistry techniques and electrochemical deposition, the choice of method is often guided by the desired material morphology, substrate, and the application.

Pristine transition metal chalcogenides such as MoS_2 possess layered structures and promising redox activity, however, their full potential in supercapacitor electrodes may be compromised by low intrinsic conductivity and poor ion accessibility on the inert basal planes. To overcome these limitations, researchers have developed tailored strategies including heteroatom doping, metallic substitution, and defect engineering. Each of those strategies enforces interlayer expansion, enhanced charge carrier density and improvement of surface properties in order to elevate both double layer and pseudocapacitive contributions. Nitrogen doping, for example, introduces localized electron donating sites that increase the conductivity of MoS_2 while modifying its electronic band structure. This can also activate redox sites even in the basal plane, traditionally considered electrochemically inactive.^[257] Le et al.^[258] employed a low-temperature N_2 plasma process to introduce nitrogen atoms into a 1T/2H MoS_2 heterostructure, preserving the beneficial metallic character of the 1T phase and simultaneously increasing the number of electrochemically active sites. The presented material achieved a specific capacitance of $410 \text{ F}\cdot\text{g}^{-1}$ at $1 \text{ A}\cdot\text{g}^{-1}$, outperforming pure MoS_2 , and displayed superior mechanical stability in a flexible solid-state supercapacitor.^[258] In other research, co-doping with nitrogen and phosphorus into MoS_2 -graphene composites not only induced lattice distortion but also improved interfacial charge transport.^[259] Electrode material was characterized by specific capacitance of $588 \text{ F}\cdot\text{g}^{-1}$ at $1 \text{ A}\cdot\text{g}^{-1}$ in 1 M Na_2SO_4 aqueous electrolyte, and symmetric supercapacitor with energy density of $24.34 \text{ Wh}\cdot\text{kg}^{-1}$.^[259]

Another problem, especially associated with sulfides, is that this class of materials is prone to oxidation. Transition metal sulfides such as MoS_2 are particularly sensitive to ambient oxygen and moisture, which can trigger not only a gradual conversion of Mo species to higher oxidation states, but also an irreversible structural transformation from the metastable 1T phase to the thermodynamically stable phases or even to molybdenum oxides like MoO_3 .^[260,261] This susceptibility to oxidation is not merely a challenge for long-term material stability – it also introduces considerable ambiguity in structural characterization, especially in hydrothermally synthesized samples. Among the most widespread issues

is the misidentification of oxidation products in Raman spectroscopy. Because 1T MoS₂ has a characteristically broad and low-signal Raman bands, it can be difficult to detect them, especially when overlapped by the sharper bands of the 2H phase or MoO₃ (see the modes presented in **Table 2**).^[244] Alarmingly, many studies assign spectra to 1T MoS₂ without showing the full spectral range, often cutting off the range above 700 cm⁻¹, and thereby missing the characteristic high-wavenumber MoO₃ peaks above 800 cm⁻¹ that would clearly reveal surface oxidation.^[244] This is further complicated by the use of high laser powers that can locally induce oxidation or phase transition during measurement, especially in thin or poorly crystalline samples.^[262] Furthermore, electrochemical impedance studies have shown that 1T MoS₂ exhibits significantly lower charge transfer resistance compared to the 2H phase, a property that is lost when oxidation reverts the material back to the less conductive 2H form.^[263] While storing materials under inert atmospheres is essential to preserve the 1T phase, other stabilization strategies have also emerged. These include intercalation of alkali ions such as Li⁺ or NH₄⁺ that help stabilize the 1T lattice,^[264] as well as heteroatom doping with elements like P or Ni, which can enhance electronic conductivity and reduce susceptibility to oxidation by modifying the electronic structure.^[260] These approaches, combined with careful synthesis control and post-synthetic handling, are critical for preserving the functional properties of 1T MoS₂.

Table 2. Raman bands of 1T MoS₂, 2H MoS₂ and MoO₃. Adapted from Ref.^[244]

1T MoS ₂ ^[265–267]		2H MoS ₂ ^[265,268]		MoO ₃ ^[269–271]	
/ cm ⁻¹	mode	/ cm ⁻¹	mode	/ cm ⁻¹	mode
				116	B _{3g}
				128	B _{1g}
147					
151	J ₁			159	B _{2g}
226	J ₂			219	A _g
286	E _{1g}			283	B _{1g}
333	J ₃			338	A _g
		383	E _{2g}		
412	A _{1g}	409	A _{1g}		
				666	B _{3g}
				820	A _g

Transition-metal doping/functionalization may also be an alternative route for structural and electronic modification. Hanifehpour et al.^[272] presented iron-doped MoS₂ nanosheets synthesized via hydrothermal method demonstrated improved morphology and electrochemical performance relative to pristine MoS₂. Authors observed improved specific capacitance, accompanied by lower charge-transfer resistance and enhanced cycling stability.^[272] A similar hydrothermal approach with cobalt as a dopant resulted in Co-MoS₂ nanoflowers with specific capacitance values reaching 453 F·g⁻¹ in comparison with undoped MoS₂, and the symmetric supercapacitors excellent cycling stability of 98.5% after 10 000 cycles.^[273] Similarly, Ni-doped MoS₂ nanosheets, prepared through

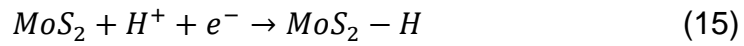
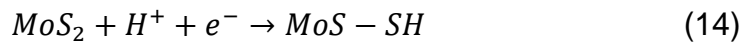
controlled solvothermal synthesis, demonstrated improved wettability and enhanced ion diffusion kinetics. In a flexible solid-state supercapacitor configuration, the Ni-MoS₂ electrodes delivered a capacitance of 528.7 F·g⁻¹ and retained 85% of initial capacitance after 10 000 cycles ($j = 5 \text{ A} \cdot \text{g}^{-1}$).^[274] Another approach is to use rare-earth metal dopants, which can introduce multivalent redox activity and modulate the crystallinity of MoS₂. In a recent study, Gd- and Nd-doped MoS₂ nanosheets prepared via hydrothermal synthesis exhibited a specific capacitance of 357 F·g⁻¹ at 10 mV s⁻¹, with over 81% capacitance retention after 5 000 cycles.^[275] Electrochemical impedance spectroscopy also confirmed that rare-earth doping reduced both solution and charge-transfer resistance, enabling more efficient ion transport and enhancing the long-term cycling stability.^[275] Even noble metal dopants, though costly, have been used to further improve electrochemical performance. Shao et al.^[276] introduced Pt nanoparticles into MoS₂ nanosheets grown on carbon cloth using hydrothermal synthesis. The Pt-doped electrodes exhibited nearly twice the specific capacitance of pristine MoS₂, reaching ~250 F·g⁻¹ at 0.5 A·g⁻¹, and in the asymmetric supercapacitor configuration the reported capacitance was 42 F·g⁻¹.^[276] Pt functionalization of 2H-MoS₂ was also presented by Wang et al.,^[277] with the specific capacitance of 284 F·g⁻¹ at 5 mV·s⁻¹ in 1 M KOH electrolyte solution. Taken together, these examples illustrate how heteroatom and transition metal doping, defect engineering, and noble metal functionalization may enhance the electrochemical performance of transition metal chalcogenides, especially MoS₂.

In general, the investigation of layered chalcogenides for electrochemical energy storage can be traced back to the work of Whittingham, who in the 1970s identified TiS₂ as a viable host for lithium intercalation due to its metallic 1T phase and van der Waals gaps conducive to reversible insertion reactions.^[278] Its capability to store charge through intercalation without phase change offered a model framework for early battery cathode design.^[278,279] In contrast, MoS₂ which crystallizes in the semiconducting 2H phase, presents a more intricate case. While extensively explored in lithium-ion systems, where a phase transition to 1T occurs upon lithiation,^[280–282] the charge storage mechanisms of MoS₂ in electrochemical capacitors, particularly in aqueous environments, remain less clearly defined. Despite its structural similarity to TiS₂, MoS₂ exhibits notably different behavior when applied to capacitive systems.

The dominant hypothesis in aqueous electrolytes assumes that charge is predominantly stored via surface adsorption of hydrated ions at the basal planes of 2H-MoS₂, as the potential required to induce a phase transition or intercalation exceeds the thermodynamic window limited by water electrolysis.^[283] Studies on bulk MoS₂ confirm its limited capacitance in neutral media (typically below 20 F g⁻¹),^[284] a value far below what would be expected if intercalation processes contributed. This observation supports the view that basal-plane adsorption, rather than interlayer intercalation, governs charge storage. Nonetheless, morphological and compositional modifications complicate this picture. For instance, introduction of structural defects, phase engineering toward metallic 1T-MoS₂, or incorporation into conductive heterostructures

enables redox activity involving proton-coupled electron transfer at Mo centers, suggesting faradaic contributions may be non-negligible.^[88,285–287] Furthermore, interlayer expansion through exfoliation or ionic pre-treatment can promote a solid-solution-like insertion of small cations, evidenced by changes in interlayer spacing under cycling, although this remains highly system-specific.^[288–290]

Despite growing evidence for such mechanisms, a unified understanding has yet to emerge. Some studies argue for nearly pure electric double layer behavior in neutral aqueous media,^[291] while other suggest hybrid storage involving both ion adsorption and proton intercalation,^[88] potentially described by proton-coupled reactions at MoS₂ surfaces. Two representative reactions are commonly proposed: protonation of surface sulfur atoms to form thiol-like groups (**Equation 14**) and proton incorporation into the MoS₂ lattice, leading to hydrogenated MoS₂ species (**Equation 15**):



This inconsistency is probably because MoS₂'s behavior depends strongly on its structure, number of defects, phase, and the type of electrolyte used. As such, the classification of MoS₂ as a pseudocapacitive or double layer material remains system-dependent, with aqueous charge storage mechanisms best described as a continuum of surface and interlayer processes modulated by structural design.

3.3. *Current challenges and perspectives*

Transition metal chalcogenides, particularly in their two-dimensional layered architectures, have demonstrated immense potential as supercapacitor electrode materials due to their high surface area, tunable electronic structures, and possibility to improve capacitance by pseudocapacitance contribution. However, despite their attractive properties, the journey from lab-scale to practical application is still hindered by persistent challenges.

One of the primary limitations lies in their intrinsic low electrical conductivity and tendency for restacking, which suppresses ion accessibility and active surface area. Additionally, issues such as structural instability, susceptibility to oxidation and volumetric changes during cycling pose significant hurdles to achieving long-term electrochemical durability. To overcome these obstacles, recent research has highlighted the value of defect engineering, phase tuning, heterostructure functionalization and composite formation with conductive matrices. Nevertheless, many of these strategies are still constrained by synthesis complexity, limited scalability, and cost.

Looking ahead, the future of TMD-based supercapacitors will depend on the development of scalable, controllable synthesis methods, better understanding of structure-performance relationship and energy storage mechanisms, as well as integration of TMDs into hybrid systems that leverage synergistic effects. Multidisciplinary approaches combining materials science,

computational modeling and advanced characterization will be essential to bridge the gap between theoretical potential and real-world application.

In this context, continued exploration of metal chalcogenides is not only justified but necessary, both for advancing the high-performance electrode materials and for enabling the next generation of efficient, durable and versatile energy storage devices.

4. Sodium-Ion Batteries

4.1. Basics of SIBs: operating principle and comparison to LIBs

Sodium-ion batteries are not a new concept, but their return to the spotlight is closely tied to the evolving demands of our global energy systems. Over the past three decades, LIBs have played a central role in powering devices ranging from phones and laptops to electric vehicles and solar storage units. Their high energy density and long cycle life made them the dominant energy storage technology, and in many applications, they remain the best option available. However, the rapid growth of the LIBs market has also exposed several significant limitations. Lithium, along with cobalt and nickel, is not only expensive, but also unevenly distributed across a small number of countries. As global demand keeps growing, concerns over long-term supply and rising costs are becoming more serious.^[292,293]

This is where SIBs begin to make renewed sense. Sodium is inexpensive, widely available and abundant. In fact, it is the sixth most abundant element on Earth,^[294] meaning there is much less risk of running into supply shortages or price spikes. Although SIBs cannot yet compete with LIBs in terms of gravimetric energy density, they offer strong advantages in terms of sustainability and resource accessibility, particularly in large-scale applications such as stationary energy storage and short range transportation systems.^[295] Although SIBs have only recently attracted widespread attention, their development traces back more than half a century. The earliest known effort to harness sodium for rechargeable battery systems began in the 1960s, when researchers at Ford Motor Company, namely Kummer and Weber, developed the high-temperature sodium-sulfur (Na-S) battery in w 1966 for electric vehicle applications.^[296] Despite its promise, the Na-S system was constrained by severe safety issues and operational complexities due to its required operating temperatures near 300 °C, leading to limited commercial uptake.

Research on room-temperature sodium systems was already ongoing in parallel to early lithium-ion work. In the early 1980s, sodium intercalation into layered chalcogenides such as TiS_2 was demonstrated, paralleling similar developments in lithium chemistry.^[297,298] However, the discovery that sodium ions could not intercalate efficiently into graphite caused research momentum to shift toward lithium, especially after commercial LIBs were introduced in 1991. And it wasn't until 2000 that interest in SIBs was revived, largely due to the successful demonstration of sodium storage in hard carbon by Dahn's group.^[299,300] The 2010s marked a major turning point. Faradion, founded in the UK in 2011, became the first company dedicated to commercializing SIB technology, using Prussian blue analogues (PBAs) and organic electrolytes.^[301] In 2013, Natron Energy focused on aqueous SIBs for high-safety, long-life applications.^[302] This was followed by a notable technical milestone, which was the launch of the first 18650-format sodium-ion cell in France (RS2E) in 2015, using

$\text{Na}_3\text{V}_2(\text{PO}_4)_2\text{F}_3$ cathode.^[303] Currently, China has become a global leader in sodium battery development. Companies like HiNa Battery and NaTRIUM Energy have developed pouch cells with layered oxide cathodes and hard carbon anodes, achieving energy densities up to 150 Wh/kg and cycle life exceeding 4 000 cycles.^[303] More recently, CATL, the world's largest battery manufacturer, presented its first-generation commercial SIBs featuring PBA cathodes and biomass-derived hard carbon, delivering ~160 Wh/kg.^[304] This milestone highlights how decades of scientific development are now converging with industrial momentum, making it timely to revisit sodium-ion batteries actually work at the fundamental level.

In terms of operating principle, SIBs work in much the same way as LIBs. During charging, sodium ions are extracted from the cathode through the electrolyte to the anode. Upon discharge, the process reverses and the ions flow back, releasing energy. This “rocking-chair” mechanism mirrors the lithium-ion process quite closely, however, despite this similarity in principle, there are fundamental differences that make sodium-ion systems more challenging to design. The most significant of these differences lies in the size of the sodium ion. Sodium ions are considerably larger than lithium ions (1.02 Å vs. 0.76 Å),^[305] which affects both their mobility and their ability to fit within the structural frameworks of common electrode materials. For example, graphite, which serves as the standard anode material in LIBs, simply does not work for sodium. In sodium systems, graphite fails to intercalate sodium effectively due to its insufficient interlayer spacing and less favorable thermodynamics.^[306] To overcome this, researchers have turned to hard carbon as the preferred anode material, which, with its disordered microstructure and wider interlayer spacing, provides more favorable conditions for sodium storage.^[307] Despite these material differences, the overall design of SIBs is very similar to lithium-ion cells. Both use a cathode, an anode, an electrolyte, and a separator (**Figure 6**). In fact, many of the same solvents and additives used in LIB electrolytes (such as ethylene carbonate (EC) or dimethyl carbonate (DMC)) can also be used in SIBs, though with sodium salts like NaPF_6 or NaClO_4 .^[308,309] One small but important difference is the choice of current collector. While LIBs typically require copper foil on the anode side, sodium-ion systems can use aluminum on both sides. This is possible because aluminum does not form problematic alloys with sodium, as it does with lithium, simplifying the manufacturing process and lowering cost.^[310,311]

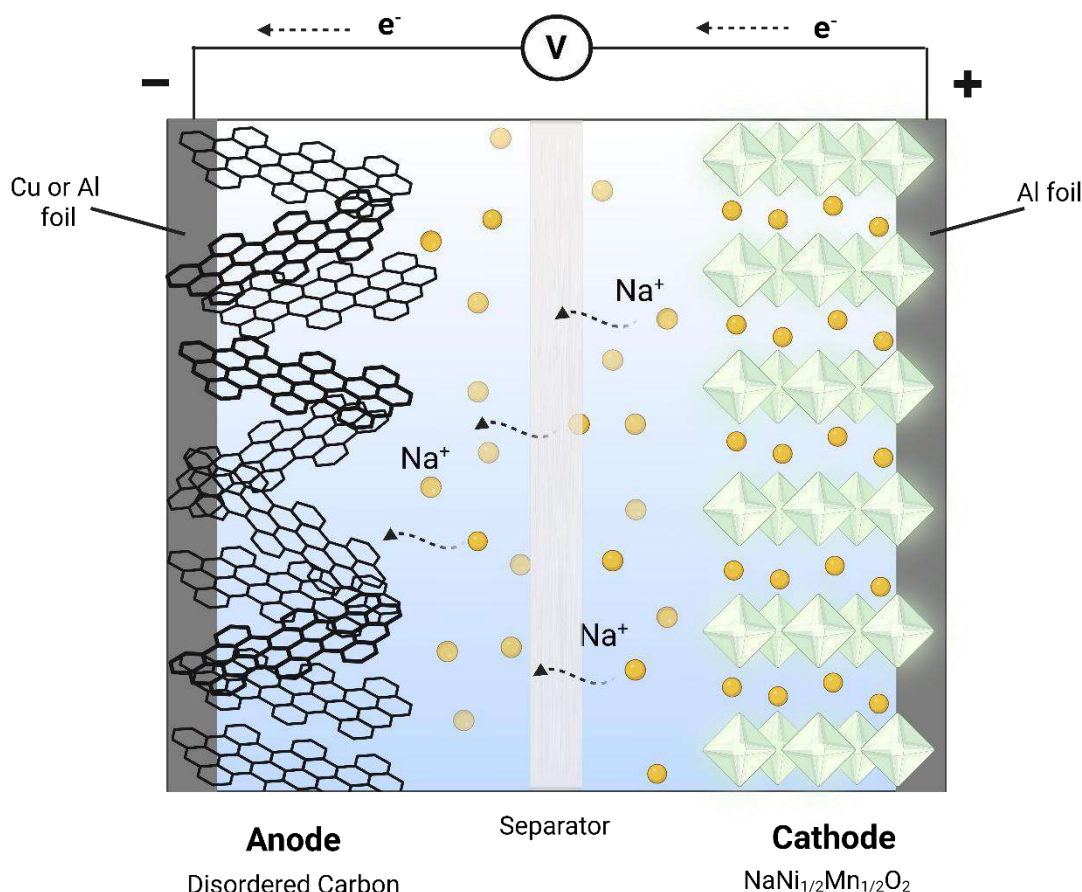


Figure 6. Schematic representation of sodium-ion battery cell with disordered carbon anode and layered transition metal cathode. Adapted from Ref.^[312] and created with BioRender.com.

Moreover, the economic case for SIBs extends well beyond individual component choices like aluminum current collectors. A deeper look at system-level cost modeling reveals that SIBs could become a competitive or even preferable alternative to LIBs in certain markets. Vaalma et al.^[4] conducted one of the earliest comprehensive resource and cost assessments, noting that sodium's global availability and stable supply outlook offer a distinct long-term advantage over lithium, especially as demand across the lithium supply chain continues to intensify.^[4] More recently, Yao et al.^[17] analyzed over 6 000 possible development scenarios using techno-economic modeling and found that, although SIBs currently trail behind lithium iron phosphate (LFP) batteries in cost-per-kWh, moderate improvements in specific capacity and energy density could close this gap by the early 2030s. Notably, the study emphasizes that price advantage is not guaranteed by raw material costs alone. In high-lithium-price scenarios (e.g. > \$ 50 000/tonne for lithium carbonate equivalent (LCE)), over half of the modeled SIB pathways achieve cost parity or better, but if lithium prices remain low (e.g. around \$ 10 000/tonne LCE), more intensive cathode innovation or disruptions in LIB supply chains (e.g. for graphite) would be required to tilt the balance.^[17] Supporting this trend, Peters et al.^[313] compared the cost

of commercial-format SIB cells with both NMC and LFP lithium-ion cells, finding that current SIB production already approaches cost parity with LFP-based systems (€ 223/kWh vs € 229/kWh), especially when using hard carbon from fossil coke or waste biomass. Similar conclusions were reached by Trotta et al.,^[314] who showed that sodium-ion half-cells built with glucose-derived hard carbon anodes were 18% cheaper than lithium equivalents, and had a lower environmental impact across nearly every life-cycle category.

Still, multiple studies agree that raw material costs alone are not enough to guarantee economic success. Sodium-ion cells must improve in materials intensity, that is, the amount of active material required per kWh of energy stored. Lower energy density means more bulk, more cost per unit energy and more complex system-level integration.^[17] So, unless sodium-ion energy densities are significantly improved, the total pack cost (including housing and thermal management) may remain higher than comparable lithium-based systems, even if raw materials are cheaper.^[293]

While sodium-ion and lithium-ion batteries share similar working principles, their safety profiles differ significantly due to intrinsic materials properties and failure mechanisms. LIBs have long been associated with risks of thermal runaway, fires, and explosions, which is due to high energy density and the flammability of organic electrolytes.^[315] On the other hand, sodium-ion systems offer several inherent safety advantages. Aluminum current collectors, used on both electrodes in SIBs provide better thermal stability and enable safe storage in a fully discharge state, which is an important factor in shipping and transportation.^[315] In general, thermal runaway in both systems proceeds through similar stages – SEI decomposition, anode-electrolyte reactions, and cathode breakdown (**Figure 7**), however, several studies suggest that SIBs may have slightly lower thermal abuse severity. For example, the self-heating rate and peak temperatures observed in sodium-ion cells are generally lower than in comparable LIBs, implying that SIBs generate less heat during exothermic failure.^[316] Also, which was indicated by Passerini et al.,^[317] pure sodium salts present better thermal stability than lithium salts, which also results in improved safety. The onset temperature for SEI decomposition in Na-ion cells is also higher in certain configurations, and some sodium cathodes like Na_{0.5}CrO₂ exhibit greater thermal stability at elevated temperatures than typical lithium counterparts such as LiFePO₄.^[318]

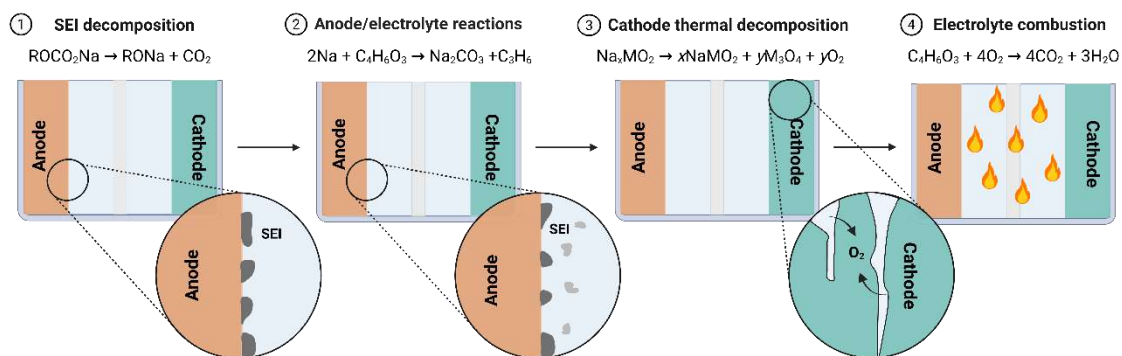


Figure 7. Schematic representation of thermal runaway pathways in SIBs. Adapted from Ref.^[319] and created with BioRender.com.

However, these advantages are not absolute. As highlighted by some studies,^[320,321] the larger ionic radius of sodium leads to more pronounced volume changes during cycling, which can induce mechanical stress, structural collapse or phase transitions in cathodes, thereby accelerating heat accumulation. Moreover, the SEI layer in SIBs is often less stable and more soluble than in LIBs, resulting in earlier decomposition, pronounced side reactions, and flammable gas generation at lower temperatures.^[319] Also, although Na dendrites are mechanically weaker and less likely to penetrate separators than Li dendrites,^[322,323] they are chemically less stable, increasing the chance of violent exothermic reactions once exposed to electrolyte.^[319] Nevertheless, the safety of both systems depends not only on materials selection but also on cell design, electrolyte formulation, and thermal management. And, it has to be borne in mind, that although SIBs show promising safety features, the technology still faces challenges which must be addressed.

A major part of these challenge lies in the fundamental components of the battery cell, which directly govern the cell's ionic transport, electrochemical stability, thermal tolerance, and long-term performance. One of those components is the separator, which once viewed as a passive barrier, is now increasingly recognized as a multifunctional component in battery design. For SIBs, safety-aware separator engineering has become critical due to the high chemical reactivity of metallic sodium and the growing emphasis on thermal abuse resistance. As shown by Zhang et al.,^[324] and more recently by Xue et al.,^[325] separators tailored for SIBs incorporate ceramic coatings, high-porosity membranes, but also hybrid composites to suppress dendritic growth and enhance flame retardancy.^[326] Polymer membranes are often modified by inorganic filler doping or layered designs to balance thermal shrinkage, mechanical integrity and electrolyte wettability, which are the properties crucial for improved performance of battery cells.^[326–330]

Electrolytes, meanwhile, play a dual role – conducting sodium ions and mediating electrode/electrolyte interphases. Conventional carbonate-based electrolytes such as NaPF_6 in EC/PEC remain widespread due to their availability and conductivity, but they are often incompatible with high voltage cathodes

or low temperature working conditions.^[331] Recent trends are shifting toward localized high-concentration electrolytes (LHCEs), ether-based solvents, and fluorinated additives to regulate solvation structures and stabilize SEI and CEI (cathode electrolyte interface) layers.^[44,308,332] All of the strategies are utilized in order to help suppress gas evolution, solvent co-intercalation and dendrite formation. They also play a significant role in the process of SEI formation and preserving its stability during multiple charge/discharge cycles.^{[331][333–336]}

Cathode materials, which are the energy-limiting component of the system, remain the most intensively studied and compositionally diverse part of SIB cell. They are typically classified into three main categories: layered transition metal oxides, polyanionic compounds, and Prussian blue analogues (PBAs).^[337]

Layered oxides (NaMO₂-type, where M = Ni, Mn, Fe, etc.) have high theoretical capacities (up to ~200 mAh g⁻¹) and relatively high working voltages. However, their structural integrity is often compromised by Na/vacancy ordering, phase transitions and oxygen evolution at high voltage or deep cycling.^[338] Strategies to mitigate these issues include dual-phase engineering,^[339] surface coatings or doping with elements like Mg or Ti^[340,341] to enhance structural coherence and suppress migration of transition metal ions.^[342] **Polyanionic cathodes**, such as **NASICON-type Na₃V₂(PO₄)₃** and fluorophosphate Na₃V₂(PO₄)₂F₃, exhibit exceptional structural stability and thermal robustness, owed to strong covalent P–O bonds.^[343] These frameworks support high-voltage plateaus (up to 3.8 V), excellent cycling life and high thermal decomposition thresholds, making them ideal for applications demanding durability over raw energy density.^[344,345]

Prussian blue analogues (PBAs) are the class of materials which are open-framework cyanometalates with high Na⁺ diffusivity, and they stand out mostly because of their cost-efficiency and rapid rate capability.^[346,347] Their structural openness supports fast kinetics, and its moisture-tolerant analogues, with an example of Prussian white, have already been scaled up in commercial prototypes.^[348,349] However, their performance can be hindered by structural defects (Fe(CN)₆ vacancies), coordinated water and reduced volumetric energy density.^[338,350]

In summary, the balance between safety, energy and cost in sodium-ion systems is deeply rooted in these component-level material choices. But perhaps the most critical bottleneck remains on the anode side, where sodium's size, reactivity and sluggish kinetics present several challenges in achieving stable cycling and high coulombic efficiency. Thus, the next chapter will turn to a detailed analysis of anode materials and sodium storage mechanism, which is one of the focuses of this thesis.

4.2. Anode materials for SIBs – energy storage mechanisms

As SIBs move closer to real-world applications, the role of the anode becomes increasingly important. While progress on cathode materials has brought the technology closer to commercialization, many of the key limitations still lie on the anode side. Unlike lithium, sodium's larger ionic radius and different electrochemical behavior pose significant challenges for anode design, especially

in terms of volume change, diffusion kinetics and electrode integrity. These issues are further amplified by the fact that traditional graphite, which functions well in lithium-ion batteries, fails to provide reversible sodium storage due to unfavorable interlayer spacing and weak interaction with sodium ions.^[351]

This has led to the exploration of a wide range of alternative anode materials, broadly categorized based on their sodium storage mechanisms: **intercalation**,^[352] **alloying**,^[353] **conversion**,^[354] and combination **conversion-alloy** materials.^[355] Intercalation-type materials typically offer good structural reversibility and cycling stability, though their capacities are often limited. Carbon-based anodes, especially hard carbon, remain the most widely studied intercalation materials for SIBs.^[307] Their sodium storage behavior is generally explained by a dual mechanism involving Na⁺ adsorption and pores filling.^[356] Despite moderate capacity values, their stability and cost-effectiveness make them strong candidates for practical use. On the other hand, alloying-type anodes, such as those based on tin,^[357,358] antimony^[359,360] or phosphorus,^[361,362] exhibit much higher theoretical capacities due to multi-electron redox reactions. However, the significant volume expansion during alloying and dealloying leads to particle pulverization, loss of electrical contact and rapid capacity fading.^[363] Recent efforts have focused on nanoscale structuring, carbon buffering matrices and surface coatings to mitigate these effects and improve cycling stability.^[364,365] Moreover, classes of conversion and conversion-alloying materials offer even higher capacities by leveraging redox reactions with transition metal compounds, but often faces issues with reaction reversibility and kinetic sluggishness.^[354] Nevertheless, such systems, including metal chalcogenides, show promising performance when carefully engineered to accommodate structural changes and maintain electronic pathways during cycling.

In short, while no universal anode material has yet emerged for SIBs, the diversity of available storage mechanisms provide a wide design space. Intercalation materials like hard carbon offer safety and reliability, while alloying and conversion-type anodes bring much higher capacities, at the cost of more complex mechanical and electrochemical challenges. The following sections will explore both directions in more detail, beginning with hard carbon and its sodium storage mechanisms, followed by the alloy-conversion systems, with a particular focus on metal chalcogenides.

4.2.1. Hard carbon and carbon-based materials

Carbon-based materials have long been explored as negative electrodes in rechargeable battery systems due to their structural versatility, chemical tunability, and stability. In SIBs, carbonaceous materials are of particular interest because of their natural abundance, low cost, and electrochemical stability. However, the suitability of different carbon allotropes for sodium storage varies widely, driven by the distinct interaction of Na⁺ ions with carbon structures, which differ fundamentally from their lithium counterparts.

Graphite, the most common standard for LIBs, demonstrates poor performance in conventional SIB electrolytes, with a theoretical reversible capacity of just

35 mAh·g⁻¹ due to the inability of Na⁺ to intercalate efficiently into its tightly packed graphitic layers.^[366] Although the capacity can be enhanced by using ether-based electrolytes that facilitate co-intercalation mechanism,^[367,368] this approach brings limitations related to energy density and long-term stability, making graphite less attractive for SIBs under typical operating conditions. Soft carbon, also referred to as low-temperature or graphitizable carbon, offers somewhat improved performance due to its larger interlayer distance. However, Na⁺ intercalation is still limited and thus this group of materials offers low sodium storage capacity, keeping it from being a practical choice.^[369,370] Moreover, materials such as graphene and carbon nanotubes exhibit high conductivity and tunable surface chemistry, but their extremely high surface area leads to substantial irreversible capacity losses especially in the first cycle (low initial coulombic efficiency, ICE) through excessive SEI formation and electrolyte decomposition.^[371,372]

Among all carbon-based candidates, hard carbon (HC) has emerged as the most promising and widely studied anode material for SIBs, reaching capacity values around 300 mAh·g⁻¹. Hard carbon is typically prepared by pyrolyzing carbon-rich precursors such as biomass, polymer, or pitch at high temperatures.^[373] Its structure, often described as a “house-of-cards”, consists of short-range ordered graphene-like domains mixed with amorphous regions and enclosed nanopores. The model was originally proposed by Stevens and Dahn,^[299] who also linked the observed charge/discharge profile, featuring a sloping region at higher voltages and a flat plateau below ~0.1 V, to alkali metal insertion and adsorption into nanopores, respectively.

Several models have been proposed since to explain how sodium ions are stored in hard carbon (see **Figure 8**).^[374] Given that the mechanism of Na⁺ storage in hard carbon exhibits similarities to the Li⁺ storage process in graphite, Cao et al.^[375] linked the sloping region of the voltage profile to Na⁺ adsorption on defect sites and heteroatom functional groups at the surface of carbon. These defects may include edge planes, vacancies, and oxygen-containing groups. The plateau region, meanwhile, was attributed to the insertion or intercalation of Na⁺ into the graphitic-like domains. Later on, Ding et al.^[376] also confirmed this interpretation, using *ex situ* XRD analysis, indicating that the intercalation of Na⁺ happens below 0.2 V. However, this simple dual-mechanism model evolved over time. In 2015 Bommier et al.^[377] proposed that a significant portion of the plateau capacity actually arises from pore-filling processes in closed nanopores or nanovoids, where Na⁺ is deposited in quasi-metallic clusters, leading to a two-step storage mechanism involving adsorption/intercalation and subsequent pore filling.

More recent *in situ* and *operando* studies have shed new light on the complexity of these mechanisms. Using synchrotron-based small- and wide-angle X-ray scattering (SAXS/WAXS), researchers have shown that sodium insertion begins with adsorption at surface defects and limited intercalation between disordered graphene layers, but the dominant contribution to capacity arises from low-voltage filling of closed nanopores.^[378,379] Operando scattering and spectroscopy

studies further confirm that this low-voltage capacity corresponds to sodium cluster-like states confined in nanopores, with the degree of pore filling strongly dependent on pore size and accessibility.^[380] Similarly, detailed structural and spectroscopic analyses have emphasized the critical role of nanoporosity, showing that sodium storage is divided by a high-voltage domain dominated by surface adsorption/intercalation and a low-voltage domain where quasi-metallic sodium clusters form inside sub-nanometer pores.^[381–383]

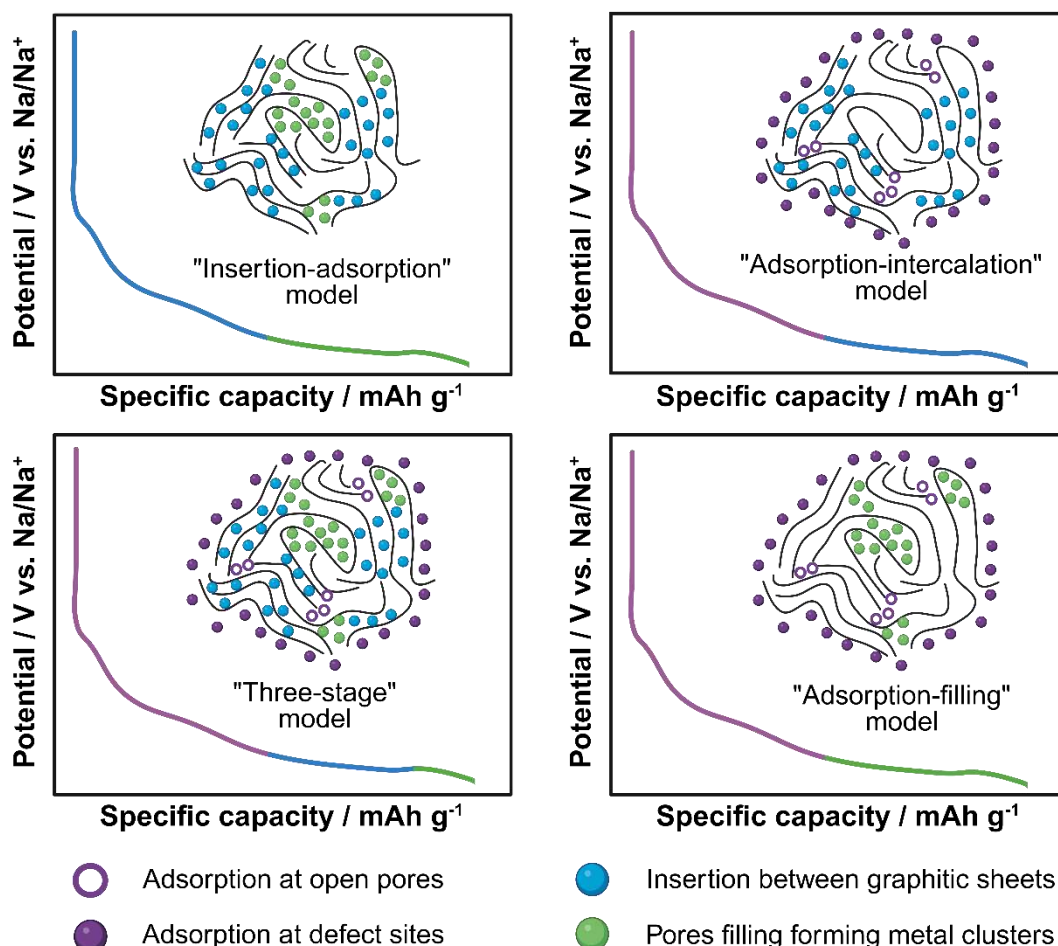


Figure 8. Sodium storage models, adapted from Ref.^[374] and created with BioRender.com.

Recent advances point toward the view that a large fraction of the low-voltage capacity originates from the filling of closed pores, while adsorption and limited insertion account for the higher-voltage processes. Yet, because hard carbons are structurally diverse and difficult to characterize with a single probe, no universal mechanism has been agreed upon, and the true nature of sodium storage remains actively debated.^[384] Nevertheless, all studies make clear that a wide range of physical properties like surface area, interlayer spacing, porosity and functional groups affect how sodium ions interact with hard carbon. For instance, a too-high surface area leads to large irreversible capacity losses during initial cycling, due to uncontrolled SEI formation and electrolyte decomposition.^[385] Meanwhile, a narrow distribution of pore sizes in the range

of 0.5–2 nm has identified as critical for maximizing the low-voltage plateau capacity.^[386] The role of heteroatom doping (such as N, O, or S) is also being actively explored. While certain dopants improve electronic conductivity and wettability, yet sometimes it can block access to internal pores or affect interface stability.^[387,388] Also, synthesis conditions strongly influence these structural properties. Pyrolysis temperature, for example, controls the balance between disorder and graphitic order.^[389] At lower temperatures (~1000 °C), hard carbon retains many functional groups and exhibits higher microporosity but lower electrical conductivity. Higher temperature may enhance graphitic ordering and improve conductivity but also may collapse smaller pores, reducing sodium storage capacity.^[390] The results indicate that a careful balance must be achieved. It is also an advantage that biomass-derived hard carbon may offer a sustainable approach, though its composition and structure are often less uniform. For instance, agricultural waste, starch-, and glucose-derived HCs display widely varying surface areas, porosities, and impurity contents, which translate into significant differences in performance and efficiency.^[391,392]

In conclusion, while carbon-based materials offer a broad toolbox for sodium-ion storage, hard carbon continues to attract the most attention due to its performance consistency and adaptability to large-scale synthesis. However, it is important to recognize that the reversible capacity of hard carbons, while reasonable, are still limited when compared to theoretical targets for next-generation batteries. Moreover, challenges such as low ICE, rate performance, and large voltage hysteresis remain active areas of research. To address these limitations, hard carbon is often combined with other active materials, especially alloying or conversion-type compounds, to form hybrid or composite electrodes that link the strengths of both components. One such group of materials, metal chalcogenides, has shown particular promise and they will be the focus of the next chapter.

4.2.2. Metal chalcogenide-based materials

Metal chalcogenides, compounds formed between metals and group 16 elements (S, Se, Te), have emerged as one of the most compelling classes of anode materials for SIBs. Unlike intercalation-type materials, which store sodium ions through insertion into existing frameworks, chalcogenides typically undergo alloying and/or conversion reactions. These mechanisms allow for the storage of multiple sodium ions per metal atom, offering theoretical capacities significantly higher than those of carbon-based anodes like hard carbon. However, the appeal of metal chalcogenides lies not only in their high theoretical capacities, but also in their ability to undergo structural transformations during cycling. Upon sodiation, these materials often transform through a two-step process: a conversion reaction, where the metal sulfide breaks into metallic nanoparticles and sodium sulfide (Na₂S), followed by an alloying reaction between sodium and the metal.^[355] These processes can reversibly store large amounts of sodium, often exceeding 500 mAh·g⁻¹.^[393–395] However, they also present challenges, particularly due to the significant volume changes associated

with sodiation/desodiation cycles. These expansions can result in particle pulverization, electrode disintegration and rapid capacity fading over time.^[36]

Among metal chalcogenides, tin-based sulfides have drawn particular interest due to their abundant resources and rich sodium chemistry. Tin sulfides (SnS_x) stand out due to their unique combination of high theoretical capacity (for SnS $\sim 1022 \text{ mAh}\cdot\text{g}^{-1}$) and relatively low working potential ($\sim 0.5\text{--}1.0 \text{ V vs. Na/Na}^+$).^[396] Upon initial discharge, SnS converts into metallic Sn and Na_2S . In a second step, the Sn reacts with additional Na^+ to form Na-Sn alloys. On charging, this sequence ideally reverses. However, the reversibility of the Na_2S phase and the degree of reformation of the SnS structure remain major concerns. The nanostructuring of SnS and related chalcogenides plays a crucial role in addressing these issues. Designing ultrathin nanosheets, hollow spheres or core-shell structures can accommodate the strain generated during cycling and enhance sodium diffusion kinetics.^[397–399] For example, Zhang et al.^[400] designed a nanocomposite consisting of ultrathin SnS nanosheets embedded within a 3D graphene and hollow mesoporous carbon sphere network. This architecture shortened Na^+ diffusion paths and provided a conductive, strain-absorbing matrix. As a result, the composite delivered $524 \text{ mAh}\cdot\text{g}^{-1}$ at $0.1 \text{ A}\cdot\text{g}^{-1}$ after 100 cycles and showed enhanced ion/electron transport.^[400] Similarly, Guo et al.^[399] developed SnS@C yolk-shell spheres, where the internal void buffered volume changes and the carbon shell ensured conductivity and mechanical stability during cycling. Moreover, beyond structural design, the presented examples show that compositing metal chalcogenides with conductive carbon matrices has proven especially effective. These hybrid structures buffer the mechanical stress of sodiation, suppress particle aggregation and enhance electron transport. For instance, Qu et al.^[401] synthesized a layered SnS_2 -reduced graphene oxide composite using a hydrothermal route. The material delivered an initial specific capacity of $630 \text{ mAh}\cdot\text{g}^{-1}$ at $0.2 \text{ A}\cdot\text{g}^{-1}$, retained $500 \text{ mAh}\cdot\text{g}^{-1}$ after 400 cycles at $1 \text{ A}\cdot\text{g}^{-1}$, and maintained high coulombic efficiency, demonstrating that the graphene matrix effectively buffered mechanical stress and enhanced electron transport.^[401] Similarly, Liu et al.^[402] created a flexible SnS_2 -graphene nanoribbon paper electrode, achieving $334 \text{ mAh}\cdot\text{cm}^{-3}$ after 1500 cycles at $1 \text{ A}\cdot\text{g}^{-1}$. The composite utilized ultrafine SnS_2 nanocrystals uniformly dispersed within a compact graphene network, which enhanced structural stability of the composite.^[402] Finally, a sandwich-like SnS_2 /graphene/ SnS_2 heterostructure, reported by Jiang et al.^[403], expanded the interlayer spacing of SnS_2 , facilitating Na^+ diffusion and improving rate performance. The material delivered $765 \text{ mAh}\cdot\text{g}^{-1}$ at $10 \text{ A}\cdot\text{g}^{-1}$, maintaining its structure after 200 cycles.^[403] Together, these studies confirm that rational design of tin sulfide-carbon hybrid structures through nanoscale control, interlayer spacing optimization, and 3D architecture can significantly improve sodium storage performance.

Nevertheless, despite significant progress in designing advanced chalcogenide-based anodes, key limitations continue to hinder their practical application in sodium-ion batteries. One of the most pressing challenges is the low initial coulombic efficiency (ICE), which is often attributed to a combination

of irreversible reactions during the first sodiation and incomplete reformation of the original structure upon desodiation. These effects arise from sluggish reaction kinetics, nanograin coarsening and side reactions including electrolyte decomposition.^[355] While some chalcogenide systems exhibit ICE values close to 80%, this remains insufficient for commercial viability and the value is usually in the range of 30% - 70%.^[404,405] Approaches such as pre-sodiation and the use of sacrificial sodium-containing salts have been proposed to mitigate this loss by compensating for initial sodium consumption.^[405]

In parallel, voltage hysteresis represents another major bottleneck. Conversion-alloying anodes frequently exhibit hysteresis exceeding 0.5 V, a level that significantly undermines energy efficiency and complicates battery management.^[355] According to several hypotheses, hysteresis originates from multiple sources including kinetic asymmetry between the sodiation and desodiation pathways, differences in ion mobility (e.g., faster Na⁺ vs. sluggish metal cations), structural rearrangements and mechanical stress induced by large volume changes.^[406–408] In general, alloying steps tend to generate lower hysteresis than conversion reaction, yet it is suggested that kinetically induced polarization can be mitigated by operating at lower current densities. However, under slow charge-discharge conditions, hysteresis related to phase transitions may become more pronounced, indicating that both kinetic and thermodynamic factors play a role depending on the cycling regime.^[355]

Altogether, these interconnected challenges underline the urgent need for continued research aimed at improving the reversibility, efficiency and electrochemical stability of metal chalcogenide anodes. In this context, the investigation of SnS_x@C composites presented in this thesis aims to shed light on material- and synthesis-level strategies to mitigate these barriers.

5. References

- [1] H. Ritchie, P. Rosado, M. Roser, *CO₂ and Greenhouse Gas Emissions. Our World in Data*, **2023**. <https://ourworldindata.org/co2-and-greenhouse-gas-emissions> (accessed 06.06.2025)
- [2] International Energy Agency (IEA), *Batteries and Secure Energy Transitions*, IEA: Paris, **2024**.
- [3] Y. Miao, L. Liu, K. Xu, J. Li, *Environ. Sci. Pollut. Res.* **2023**, 30, 65558-65571.
- [4] C. Vaalma, D. Buchholz, M. Weil, S. Passerini, *Nat. Rev. Mater.* **2018**, 3, 18013.
- [5] H. Dai, M. Tang, J. Huang, Z. Wang, *ACS Appl. Mater. Interfaces* **2021**, 13, 10870-10877.
- [6] X. Ren, Q. Zhao, W. D. McCulloch, Y. Wu, *Nano Res.* **2017**, 10, 1313-1321.
- [7] D. Sarkar, D. Das, S. Das, A. Kumar, S. Patil, K. K. Nanda, D. D. Sarma, A. Shukla, *ACS Energy Lett.* **2019**, 4, 1602-1609.
- [8] Y. Shan, Y. Li, H. Pang, *Adv. Funct. Mater.* **2020**, 30, 2001298.
- [9] X. Yue, B. Qiao, J. Wang, Z. Xie, Z. Liu, Z. Yang, A. Abudula, G. Guan, *Renew. Sustain. Energy Rev.* **2023**, 185, 113592.
- [10] O. Gerard, A. Numan, S. Krishnan, M. Khalid, R. Subramaniam, R. Kasi, *J. Energy Storage* **2022**, 50, 104283.
- [11] P. Zhu, P. R. Slater, E. Kendrick, *Mater. Des.* **2022**, 223, 111208.
- [12] C. Meng, P. Das, X. Shi, Q. Fu, K. Müllen, Z. S. Wu, *Small Sci.* **2021**, 1, 2000076.
- [13] J. N. Weker, M. F. Toney, *Adv. Funct. Mater.* **2015**, 25, 1622-1637.
- [14] International Energy Agency (IEA), *World Energy Outlook 2018*, IEA: Paris, **2018**.
- [15] Energy Institute, *Statistical Review of World Energy 2025*, Energy Institute: London, **2025**.
- [16] IPCC, *Climate Change 2023: Synthesis Report. Contribution of Working Groups I, II and III to the Sixth Assessment Report of the Intergovernmental Panel on Climate Change*, IPCC: Geneva, **2023**.
- [17] A. Yao, S. M. Benson, W. C. Chueh, *Nat. Energy* **2025**, 10, 404-416.
- [18] M. G. M. Abdolrasol, S. Ansari, I. A. Sarker, S. K. Tiong, M. A. Hannan, *Prog. Energy* **2025**, 7, 022007.
- [19] K. Dissanayake, D. Kularatna-Abeywardana, *J. Energy Storage* **2024**, 96, 112563.
- [20] T. Ariyaratna, N. Kularatna, K. Gunawardane, D. Jayananda, D. A. Steyn-Ross, *IEEE J. Emerg. Sel. Top. Ind. Electron.* **2021**, 2, 267-276.
- [21] A. Fatih Guven, A. Y. Abdelaziz, M. Mahmoud Samy, S. Barakat, *Energy Convers. Manag.* **2024**, 312, 118560.
- [22] M. Z. Iqbal, U. Aziz, *J. Energy Storage* **2022**, 46, 103823.
- [23] S. Seenivasan, S. Adhikari, A. T. Sivagurunathan, D. H. Kim, *Energy Environ. Sci.* **2025**, 18, 1054-1095.
- [24] H. Tan, Y. Feng, X. Rui, Y. Yu, S. Huang, *Small Methods* **2020**, 4, 1900563.
- [25] Y. Zhang, L. Zhang, T. Lv, P. K. Chu, K. Huo, *ChemSusChem* **2020**, 13, 1114-1154.
- [26] E. S. Sowbakkiyavathi, S. P. Arunachala Kumar, D. K. Maurya, B. Balakrishnan, J. Z. Guo, A. Subramania, *Adv. Compos. Hybrid Mater.* **2024**, 7, 1-66.
- [27] K. P. Shwetha, Y. Athreya, L. Suraj, C. Kumar Rastogi, M. K. Sudha

- Kamath, K. Natarajan, A. Khosla, C. Manjunatha, *Mater. Today Proc.* **2023**, 73, 274-285.
- [28] Y. Jiao, A. M. Hafez, D. Cao, A. Mukhopadhyay, Y. Ma, H. Zhu, *Small* **2018**, 14, 1800640.
- [29] X. Rui, H. Tan, Q. Yan, *Nanoscale* **2014**, 6, 9889-9924.
- [30] Y. Zhang, Q. Zhou, J. Zhu, Q. Yan, S. X. Dou, W. Sun, *Adv. Funct. Mater.* **2017**, 27, 1702317.
- [31] A. M. Patil, S. Moon, S. B. Roy, J. Ha, N. R. Chodankar, D. P. Dubal, A. A. Jadhav, G. Guan, K. Kang, S. C. Jun, *Small* **2023**, 19, 2301153.
- [32] S. Kaladi Chondath, L. Bansal, B. Sahu, R. Kumar, *ACS Appl. Energy Mater.* **2025**, 8, 8680-8709.
- [33] Y. Li, F. Wu, J. Qian, M. Zhang, Y. Yuan, Y. Bai, C. Wu, *Small Sci.* **2021**, 1, 2100012.
- [34] Z. Deng, H. Jiang, C. Li, *Small* **2018**, 14, 1800148.
- [35] Z. Li, R. Sun, Z. Qin, X. Liu, C. Wang, H. Fan, Y. Zhang, S. Lu, *Mater. Chem. Front.* **2021**, 5, 4401-4423.
- [36] S. Dai, L. Wang, M. Cao, Z. Zhong, Y. Shen, M. Wang, *Mater. Today Energy* **2019**, 12, 114-128.
- [37] T. S. Bhat, P. S. Patil, R. B. Rakhi, *J. Energy Storage* **2022**, 50, 104222.
- [38] H. Zhang, X. Liu, H. Li, I. Hasa, S. Passerini, *Angew. Chemie Int. Ed.* **2021**, 60, 598-616.
- [39] M. Saha, A. Kumar, R. Kanaoujiya, K. Behera, S. Trivedi, *Energy Fuels* **2024**, 38, 8528-8552.
- [40] Q. Zhao, S. Stalin, C. Z. Zhao, L. A. Archer, *Nat. Rev. Mater.* **2020**, 5, 229-252.
- [41] W. Zhao, M. Wang, H. Lin, K. Kim, R. He, S. Feng, H. Liu, *Prog. Nat. Sci. Mater. Int.* **2024**, 34, 263-273.
- [42] H. Darjazi, M. Falco, F. Colò, L. Balducci, G. Piana, F. Bella, G. Meligrana, F. Nobili, G. A. Elia, C. Gerbaldi, *Adv. Mater.* **2024**, 36, 2313572.
- [43] A. Ponrouch, D. Monti, A. Boschini, B. Steen, P. Johansson, M. R. Palacín, *J. Mater. Chem. A* **2014**, 3, 22-42.
- [44] Z. Tian, Y. Zou, G. Liu, Y. Wang, J. Yin, J. Ming, H. N. Alshareef, *Adv. Sci.* **2022**, 9, 2201207.
- [45] L. Liu, L. Xiao, Z. Sun, S. Bashir, R. Kasi, Y. Gu, R. Subramaniam, *J. Energy Chem.* **2024**, 94, 414-429.
- [46] A. Abdisattar, M. Yeleuov, C. Daulbayev, K. Askaruly, A. Tolynbekov, A. Taurbekov, N. Prikhodko, *Electrochem. commun.* **2022**, 142, 107373.
- [47] L. Liu, H. Zhao, Y. Lei, *Small Methods* **2019**, 3, 1800341.
- [48] N. Kumar, L. Pradhan, B. K. Jena, *Wiley Interdiscip. Rev. Energy Environ.* **2022**, 11, e415.
- [49] P. Zhu, D. Gastol, J. Marshall, R. Sommerville, V. Goodship, E. Kendrick, *J. Power Sources* **2021**, 485, 229321.
- [50] L. Otaegui, E. Goikolea, F. Aguesse, M. Armand, T. Rojo, G. Singh, *J. Power Sources* **2015**, 297, 168-173.
- [51] F. Tang, Y. Yang, C. Liu, S. Yang, S. Xu, Y. Yao, H. Yang, Y. Yang, S. He, H. Pan, X. Rui, Y. Yu, *Nat. Commun.* **2025**, 16, 2280.
- [52] J. F. Peters, M. Baumann, J. R. Binder, M. Weil, *Sustain. Energy Fuels* **2021**, 5, 6414-6429.
- [53] J. Peters, D. Buchholz, S. Passerini, M. Weil, *Energy Environ. Sci.* **2016**, 9, 1744-1751.

- [54] N. A. Salleh, S. Kheawhom, N. Ashrina A Hamid, W. Rahiman, A. A. Mohamad, *J. Mater. Res. Technol.* **2023**, 23, 3470-3491.
- [55] A. Joseph, A. Mathew, S. Perikkathra, T. Thomas, *Eur. Polym. J.* **2024**, 210, 112941.
- [56] N. Zhang, M. Wang, Y. Quan, X. Li, X. Hu, J. X. Yan, Y. Wang, M. Sun, S. Li, *J. Ind. Eng. Chem.* **2025**, 141, 1-31.
- [57] S. Sudhakaran, T. K. Bijoy, *ACS Appl. Energy Mater.* **2023**, 6, 11773-11794.
- [58] D. Corzo, D. Rosas-Villalva, C. Amruth, G. Tostado-Blázquez, E. B. Alexandre, L. H. Hernandez, J. Han, H. Xu, M. Babics, S. De Wolf, D. Baran, *Nat. Energy* **2023**, 8, 62-73.
- [59] Y. Yu, Chapter: Binders for Sodium-Ion Batteries in *Sodium-Ion Batteries* (Ed.: Y.Yu), Wiley-VCH GmbH, **2022**, 449–466.
- [60] W. J. Chang, G. H. Lee, Y. J. Cheon, J. T. Kim, S. Il Lee, J. Kim, M. Kim, W. Il Park, Y. J. Lee, *ACS Appl. Mater. Interfaces* **2019**, 11, 41330-41337.
- [61] R. Gordon, R. Orias, N. Willenbacher, *J. Mater. Sci.* **2020**, 55, 15867-15881.
- [62] S. Radloff, R. G. Scurtu, G. Carbonari, M. Hölzle, T. Diemant, M. Bozorgchenani, F. Klein, M. Wohlfahrt-Mehrens, *J. Power Sources* **2023**, 580, 233314.
- [63] Y. Liu, R. Zhang, J. Wang, Y. Wang, *iScience* **2021**, 24, 102332.
- [64] A. C. Rolandi, I. de Meatza, N. Casado, M. Forsyth, D. Mecerreyes, C. Pozo-Gonzalo, *RSC Sustain.* **2024**, 2, 2125-2149.
- [65] X. Lu, G. J. Lian, J. Parker, R. Ge, M. K. Sadan, R. M. Smith, D. Cumming, *J. Power Sources* **2024**, 592, 233916.
- [66] H. Helmholtz, *Ann. Phys.* **1853**, 165, 353-377.
- [67] M. Gouy, *J. Phys. Théorique Appliquée* **1910**, 9, 457-468.
- [68] D. L. Chapman, *London, Edinburgh, Dublin Philos. Mag. J. Sci.* **1913**, 25, 475-481.
- [69] O. Stern, *Zeitschrift für Elektrochemie und Angew. Phys. Chemie* **1924**, 30, 508-516.
- [70] E. Gongadze, U. van Rienen, A. Iglič, *Cell. Mol. Biol. Lett.* **2011**, 16, 576.
- [71] A. González, E. Goikolea, J. A. Barrena, R. Mysyk, *Renew. Sustain. Energy Rev.* **2016**, 58, 1189-1206.
- [72] D. C. Grahame, *J. Am. Chem. Soc.* **1941**, 63, 1207-1215.
- [73] B. E. Conway, Chapter: The Double Layer and Surface Functionalities at Carbon in *Electrochemical Supercapacitors, Scientific Fundamentals and Technological Applications* (Ed.: B. E. Conway), Springer New York, **1999**, 183–220.
- [74] Y. Gogotsi, R. M. Penner, *ACS Nano* **2018**, 12, 2081-2083.
- [75] L. Guan, L. Yu, G. Z. Chen, *Electrochim. Acta* **2016**, 206, 464-478.
- [76] R. Shao, J. Niu, J. Liang, M. Liu, Z. Zhang, M. Dou, Y. Huang, F. Wang, *ACS Appl. Mater. Interfaces* **2017**, 9, 42797-42805.
- [77] L. Jiang, L. Sheng, X. Chen, T. Wei, Z. Fan, *J. Mater. Chem. A* **2016**, 4, 11388-11396.
- [78] S. Ghosh, P. Samanta, W. Jang, C. M. Yang, N. C. Murmu, T. Kuila, *ACS Appl. Energy Mater.* **2022**, 5, 1528-1541.
- [79] M. Ojha, S. Naskar, B. Kaur, A. Kolay, M. Deepa, *J. Energy Storage* **2021**, 44, 103463.
- [80] T. Brezesinski, J. Wang, S. H. Tolbert, B. Dunn, *Nat. Mater.* **2010**, 9, 146-

- 151.
- [81] S. Rudra, R. Chakraborty, P. K. Maji, S. Koley, A. K. Nayak, D. Paul, M. Pradhan, *Electrochim. Acta* **2019**, *324*, 134865.
- [82] C. Wang, L. Zhang, Z. Zhang, R. Zhao, D. Zhao, R. Ma, L. Yin, *Prog. Mater. Sci.* **2021**, *118*, 100763.
- [83] T. Chen, L. Xue, Z. Shi, C. Qiu, M. Sun, Y. Zhao, J. Liu, M. Ni, H. Li, J. Xu, H. Xia, *ACS Appl. Mater. Interfaces* **2022**, *14*, 54369-54388.
- [84] B. Yang, A. G. Tamirat, D. Bin, Y. Yao, H. Lu, Y. Xia, *Adv. Funct. Mater.* **2021**, *31*, 2104543.
- [85] E. Zhang, Y. C. Wu, H. Shao, V. Klimavicius, H. Zhang, P. L. Taberna, J. Grothe, G. Buntkowsky, F. Xu, P. Simon, S. Kaskel, *J. Am. Chem. Soc.* **2022**, *144*, 14217-14225.
- [86] J. Deng, J. Li, S. Song, Y. Zhou, L. Li, *Nanomaterials* **2020**, *10*, 353.
- [87] V. Shrivastav, Mansi, P. Dubey, V. Shrivastav, A. Kaur, M. Hołdyński, A. Krawczyńska, U. K. Tiwari, A. Deep, W. Nogala, S. Sundriyal, *Sci. Rep.* **2023**, *13*, 20675.
- [88] Q. Mahmood, S. K. Park, K. D. Kwon, S. J. Chang, J. Y. Hong, G. Shen, Y. M. Jung, T. J. Park, S. W. Khang, W. S. Kim, J. Kong, H. S. Park, *Adv. Energy Mater.* **2016**, *6*, 1501115.
- [89] J. Hong, X. Liang, C. Shi, X. Li, J. Lu, S. Liu, J. Ding, W. Wang, *J. Energy Storage* **2025**, *127*, 117101.
- [90] Y. Zhao, D. Yang, T. He, J. Li, L. Wei, D. Wang, Y. Wang, X. Wang, G. Chen, Y. Wei, *Chem. Eng. J.* **2021**, *421*, 129715.
- [91] Z. Lu, W. Wang, J. Zhou, Z. Bai, *Chinese J. Chem. Eng.* **2020**, *28*, 2699-2706.
- [92] P. Ghasemihangarani, G. Farhan, D. del Mundo, T. Schoetz, *Adv. Energy Mater.* **2025**, *15*, 2404704.
- [93] S. Ardizzzone, G. Fregonara, S. Trasatti, *Electrochim. Acta* **1990**, *35*, 263-267.
- [94] J. Wang, J. Polleux, J. Lim, B. Dunn, *J. Phys. Chem. C* **2007**, *111*, 14925-14931.
- [95] Z. Zarach, M. Szkoda, K. Trzciński, M. Łapiński, G. Trykowski, A. P. Nowak, *Electrochim. Acta* **2022**, *435*, 141389.
- [96] Z. Zarach, A. P. Nowak, K. Trzciński, G. Gajowiec, G. Trykowski, M. Sawczak, M. Łapiński, M. Szkoda, *Appl. Surf. Sci.* **2023**, *608*, 155187.
- [97] W. Pholauyphon, P. Charoen-amornkitt, T. Suzuki, S. Tsushima, *Electrochem. commun.* **2024**, *159*, 107654.
- [98] B. A. Mei, J. Lau, T. Lin, S. H. Tolbert, B. S. Dunn, L. Pilon, *J. Phys. Chem. C* **2018**, *122*, 24499-24511.
- [99] M. D. Levi, N. Levy, S. Sigalov, G. Salitra, D. Aurbach, J. Maier, *J. Am. Chem. Soc.* **2010**, *132*, 13220-13222.
- [100] S. Sopčić, M. K. Roković, Z. Mandić, A. Róka, G. Inzelt, *Electrochim. Acta* **2011**, *56*, 3543-3548.
- [101] Y. C. Chien, H. Liu, A. S. Menon, W. R. Brant, D. Brandell, M. J. Lacey, *Nat. Commun.* **2023**, *14*, 2289.
- [102] D. Chen, D. Ding, X. Li, G. H. Waller, X. Xiong, M. A. El-Sayed, M. Liu, *Chem. Mater.* **2015**, *27*, 6608-6619.
- [103] P. Iamprasertkun, C. Tangarnjanavalukul, A. Krittayavathananon, J. Khuntilo, N. Chanlek, P. Kidkhunthod, M. Sawangphruk, *Electrochim. Acta* **2017**, *249*, 26-32.

- [104] M. J. Pinzón C., J. M. de Aquino, R. G. Freitas, G. A. Pereira, L. M. Da Silva, H. Zanin, *J. Energy Storage* **2023**, 62, 106858.
- [105] P. Simon, Y. Gogotsi, *Nat. Mater.* **2020**, 19, 1151-1163.
- [106] C. Liu, X. Yan, F. Hu, G. Gao, G. Wu, X. Yang, *Adv. Mater.* **2018**, 30, 1705713.
- [107] A. Laheäär, P. Przygocki, Q. Abbas, F. Béguin, *Electrochem. commun.* **2015**, 60, 21-25.
- [108] M. Y. Adel, O. B. Mohammed, A. T. Younis, *ChemistryOpen* **2025**, 14, e202400444.
- [109] W. Li, Q. A. Huang, Y. Li, Y. Bai, N. Wang, J. Wang, Y. Hu, Y. Zhao, X. Li, J. Zhang, *J. Energy Chem.* **2023**, 77, 384-405.
- [110] P. Simon, Y. Gogotsi, *Nat. Mater.* **2008**, 7, 845-854.
- [111] T. S. Mathis, N. Kurra, X. Wang, D. Pinto, P. Simon, Y. Gogotsi, *Adv. Energy Mater.* **2019**, 9, 1902007.
- [112] A. Dutta, S. Mitra, M. Basak, T. Banerjee, *Energy Storage* **2023**, 5, e339.
- [113] A. Noori, M. F. El-Kady, M. S. Rahmanifar, R. B. Kaner, M. F. Mousavi, *Chem. Soc. Rev.* **2019**, 48, 1272-1341.
- [114] M. Z. Iqbal, M. M. Faisal, S. R. Ali, *Int. J. Energy Res.* **2021**, 45, 1449-1479.
- [115] A. Maćkowiak, A. Beda, P. Jeżowski, P. Bujewska, K. Fic, C. Matei-Ghimbeu, **2025**. <https://ssrn.com/abstract=5293754> (accessed 03.08.2025)
- [116] N. R. Chodankar, S. J. Patil, S. K. Hwang, S. V. Karekar, K. Jayaramulu, W. Zhang, D. P. Dubal, Y. S. Huh, Y. K. Han, *J. Mater. Chem. A* **2021**, 9, 26603-26627.
- [117] S. Rudra, H. W. Seo, S. Sarker, D. M. Kim, *Molecules* **2024**, 29, 243.
- [118] L. Yu, G. Z. Chen, *Electrochem. Energy Rev.* **2020**, 3, 271-285.
- [119] H. J. Becker, *US Patent* 2,800,616, **1957**.
- [120] R. A. Rightmire, *US Patent* 3,288,641, **1966**.
- [121] D. L. Boos, *US Patent* 3,536,963, **1970**.
- [122] M. Endo, T. Takeda, Y. J. Kim, K. Koshiba, K. Ishii, *Carbon Sci.* **2000**, 1, 117-128.
- [123] B. E. Conway, E. Gileadi, *Trans. Faraday Soc.* **1962**, 58, 2493-2509.
- [124] B. E. Conway, *J. Electrochem. Soc.* **1991**, 138, 1539.
- [125] Y. Wang, Y. Song, Y. Xia, *Chem. Soc. Rev.* **2016**, 45, 5925-5950.
- [126] T. C. Liu, W. G. Pell, B. E. Conway, *Electrochim. Acta* **1999**, 44, 2829-2842.
- [127] T. F. Yi, T. T. Wei, J. Mei, W. Zhang, Y. Zhu, Y. G. Liu, S. Luo, H. Liu, Y. Lu, Z. Guo, *Adv. Sustain. Syst.* **2020**, 4, 1900137.
- [128] H. Jeong Lee, J. iHoon Lee, S.-Y. Chung, J. Wook Choi, H. J. Lee, J. H. Lee, S. hung, J. W. Choi, *Angew. Chemie Int. Ed.* **2016**, 55, 3958-3962.
- [129] M. K. Song, S. Cheng, H. Chen, W. Qin, K. W. Nam, S. Xu, X. Q. Yang, A. Bongiorno, J. Lee, J. Bai, T. A. Tyson, J. Cho, M. Liu, *Nano Lett.* **2012**, 12, 3483-3490.
- [130] G. Z. Chen, *Int. Mater. Rev.* **2017**, 62, 173-202.
- [131] G. G. Amatucci, F. Badway, A. Du Pasquier, T. Zheng, *J. Electrochem. Soc.* **2001**, 148, A930.
- [132] P. Cai, K. Zou, X. Deng, B. Wang, M. Zheng, L. Li, H. Hou, G. Zou, X. Ji, *Adv. Energy Mater.* **2021**, 11, 2003804.
- [133] J. Ding, W. Hu, E. Paek, D. Mitlin, *Chem. Rev.* **2018**, 118, 6457-6498.
- [134] J. Cherusseri, D. Pandey, J. Thomas, *Batter. Supercaps* **2020**, 3, 860-875.
- [135] S. Roldán, D. Barreda, M. Granda, R. Menéndez, R. Santamaría, C. Blanco, *Phys. Chem. Chem. Phys.* **2015**, 17, 1084-1092.

- [136] J. Sun, C. Wu, X. Sun, H. Hu, C. Zhi, L. Hou, C. Yuan, *J. Mater. Chem. A* **2017**, 5, 9443-9464.
- [137] Z. Fan, J. Yan, T. Wei, L. Zhi, G. Ning, T. Li, F. Wei, *Adv. Funct. Mater.* **2011**, 21, 2366-2375.
- [138] J. Wen, X. Chen, M. Huang, W. Yang, J. Deng, *J. Chem. Sci.* **2020**, 132, 6.
- [139] Y. Zhai, Y. Dou, D. Zhao, P. F. Fulvio, R. T. Mayes, S. Dai, *Adv. Mater.* **2011**, 23, 4828-4850.
- [140] E. Frackowiak, F. Béguin, *Carbon* **2001**, 39, 937-950.
- [141] E. Frackowiak, F. Béguin, *Carbon* **2002**, 40, 1775-1787.
- [142] P. Simon, Y. Gogotsi, *Acc. Chem. Res.* **2013**, 46, 1094-1103.
- [143] Y. Gogotsi, *MRS Bull.* **2015**, 40, 1110-1121.
- [144] Y. Zhao, Y. Zhang, Y. Wang, D. Cao, X. Sun, H. Zhu, *Carbon Energy* **2021**, 3, 895-915.
- [145] J. Xiao, J. Han, C. Zhang, G. Ling, F. Kang, Q. H. Yang, *Adv. Energy Mater.* **2022**, 12, 2100775.
- [146] F. ul Nisa, M. Tahir, S. Khalid, N. Amin, H. Yin, Y. Long, H. Tang, K. Ijaz, A. U. Khan, M. Naseem, Z. Peng, Z. Ma, L. Wu, M. F. Uddin, A. J. Khan, L. Qu, W. Ahmad, L. He, *Adv. Funct. Mater.* **2025**, 35, 2418053.
- [147] S. Yadav, S. Daniel, *Energy Storage* **2024**, 6, e500.
- [148] Y. Wang, G. J. Weng, Chapter: Electrical conductivity of carbon nanotube and graphene-based nanocomposites in *Micromechanics and Nanomechanics of Composite Solids* (Ed.: S. Meguid, G. Weng), Springer International Publishing, **2017**, 123–156.
- [149] P. K. Sahoo, N. Kumar, A. Jena, S. Mishra, C. P. Lee, S. Y. Lee, S. J. Park, *RSC Adv.* **2024**, 14, 1284-1303.
- [150] H. Jiang, P. S. Lee, C. Li, *Energy Environ. Sci.* **2012**, 6, 41-53.
- [151] Z. Sun, S. Jin, H. Ji, *ACS Appl. Energy Mater.* **2023**, 6, 1-11.
- [152] M. T. Gari, B. T. Asfaw, S. K. Arumugasamy, L. D. Abo, M. Jayakumar, Chapter: Natural Resources-Based Activated Carbon Synthesis in *Encycl. Green Mater.* (Ed.: C. Baskar, S. Ramakrishna, A.D.L. Rosa), Springer, **2025**, 1520-1530.
- [153] P. González-García, *Renew. Sustain. Energy Rev.* **2018**, 82, 1393-1414.
- [154] D. Bergna, T. Varila, H. Romar, U. Lassi, *Biomass and Bioenergy* **2022**, 159, 106387.
- [155] J. M. Juárez-Galán, A. Silvestre-Albero, J. Silvestre-Albero, F. Rodríguez-Reinoso, *Microporous Mesoporous Mater.* **2009**, 117, 519-521.
- [156] Z. Heidarinejad, M. H. Dehghani, M. Heidari, G. Javedan, I. Ali, M. Sillanpää, *Environ. Chem. Lett.* **2020**, 18, 393-415.
- [157] H. Liu, C. Cheng, H. Wu, *Sci. Total Environ.* **2021**, 790, 148214.
- [158] G. Li, A. Iakunkov, N. Boulanger, O. A. Lazar, M. Enachescu, A. Grimm, A. V. Talyzin, *RSC Adv.* **2023**, 13, 14543-14553.
- [159] P. Toth, *Carbon* **2021**, 178, 688-707.
- [160] N. Noor, A. Rego, A. Plavniece, K. Kaare, A. Schouten, A. I. Espinoza, A. Volperts, I. Kruusenburg, D. Higgins, *ChemistrySelect* **2025**, 10, e202404561.
- [161] T. X. Shang, R. Q. Ren, Y. M. Zhu, X. J. Jin, *Electrochim. Acta* **2015**, 163, 32-40.
- [162] K. Dujearic-Stephane, M. Gupta, A. Kumar, V. Sharma, S. Pandit, P. Bocchetta, Y. Kumar, *J. Compos. Sci.* **2021**, 5, 66.

- [163] D. Hulicova-Jurcakova, M. Seredych, G. Q. Lu, T. J. Bandosz, *Adv. Funct. Mater.* **2009**, *19*, 438-447.
- [164] J. Chen, C. Li, Y. Lian, Y. Chen, T. Chen, X. Hu, *Mater. Today Chem.* **2021**, *19*, 100414.
- [165] H. Liu, H. Song, X. Chen, S. Zhang, J. Zhou, Z. Ma, *J. Power Sources* **2015**, *285*, 303-309.
- [166] C. T. Hsieh, H. Teng, *Carbon* **2002**, *40*, 667-674.
- [167] L. K. Shrestha, L. Adhikari, R. G. Shrestha, M. P. Adhikari, R. Adhikari, J. P. Hill, R. R. Pradhananga, K. Ariga, *Sci. Technol. Adv. Mater.* **2016**, *17*, 483-492.
- [168] B. Réty, H. Y. Yiin, C. Matei Ghimbeu, *Energy Storage Mater.* **2025**, *74*, 103963.
- [169] D. S. Dmitriev, A. V. Nashchekin, V. I. Popkov, *Appl. Surf. Sci.* **2020**, *501*, 144216.
- [170] K. Jurewicz, R. Pietrzak, P. Nowicki, H. Wachowska, *Electrochim. Acta* **2008**, *53*, 5469-5475.
- [171] G. Liu, X. Chen, S. F. Ahmed, W. Ma, *J. Power Sources* **2025**, *640*, 236652.
- [172] H. Rustamaji, T. Prakoso, H. Devianto, P. Widiatmoko, W. H. Saputera, *J. Energy Storage* **2022**, *52*, 104724.
- [173] Y. Qiu, Z. Cheng, B. Guo, H. Fan, S. Sun, T. Wu, L. Jin, L. Fan, X. Feng, *J. Mater. Sci.* **2015**, *50*, 1586-1593.
- [174] D. Dong, Y. Zhang, T. Wang, J. Wang, C. E. Romero, W. Pan, *Mater. Chem. Phys.* **2020**, *252*, 123381.
- [175] J. Hur, B. Hwang, L. Hong, S. J. Yoo, S. E. Chun, *Surfaces and Interfaces* **2023**, *40*, 103127.
- [176] T. Yumak, D. Bragg, E. M. Sabolsky, *Appl. Surf. Sci.* **2019**, *469*, 983-993.
- [177] D. R. Lobato-Peralta, P. U. Okoye, C. Alegre, *J. Power Sources* **2024**, *617*, 235140.
- [178] K. M. Vighnesha, Shruthi, Sandhya, D. N. Sangeetha, M. Selvakumar, *J. Mater. Sci. Mater. Electron.* **2018**, *29*, 914-921.
- [179] S. Kour, S. Tanwar, A. L. Sharma, *J. Alloys Compd.* **2022**, *910*, 164834.
- [180] H. Liao, L. Zhong, H. Zeng, Y. Xiao, B. Cheng, S. Lei, *Carbon* **2024**, *224*, 119080.
- [181] P. Dubey, P. H. Maheshwari, S. Sundriyal, *Energy Fuels* **2022**, *36*, 13218-13228.
- [182] Y. K. Kim, Y. J. Kim, J. Park, S. W. Han, S. M. Kim, *Carbon* **2021**, *173*, 376-383.
- [183] T. Srimani, J. Ding, A. Yu, P. Kanhaiya, C. Lau, R. Ho, J. Humes, C. T. Kingston, P. R. L. Malenfant, M. M. Shulaker, *Adv. Electron. Mater.* **2022**, *8*, 2101377.
- [184] D. K. Yadav, F. S. Omar, M. Yadav, X. L. Ho, M. E. Tessensohn, K. Ramesh, S. Ramesh, R. D. Webster, V. Ganesan, *J. Energy Storage* **2021**, *44*, 103312.
- [185] O. Kwon, J. H. Bae, J. Y. Kim, M. Kim, Y. Ji, J. Kim, S. Y. Lee, D. W. Kim, *Mater. Today Sustain.* **2025**, *31*, 101138.
- [186] M. T. Pettes, L. Shi, *Adv. Funct. Mater.* **2009**, *19*, 3918-3925.
- [187] C. Wang, Y. Li, L. Tong, Q. Song, K. Li, J. Li, Q. Peng, X. He, R. Wang, W. Jiao, S. Du, *Carbon* **2014**, *69*, 239-246.
- [188] P. Avasthi, V. Balakrishnan, *Adv. Mater. Interfaces* **2019**, *6*, 1801842.
- [189] E. Senokos, M. Rana, C. Santos, R. Marcilla, J. J. Vilatela, *Carbon* **2019**,

- 142, 599-609.
- [190] S. Hussain, R. Amade, E. Jover, E. Bertran, *J. Mater. Sci.* **2013**, *48*, 7620-7628.
- [191] P. K. Adusei, S. Gbordzoe, S. N. Kanakaraj, Y. Y. Hsieh, N. T. Alvarez, Y. Fang, K. Johnson, C. McConnell, V. Shanov, *J. Energy Chem.* **2020**, *40*, 120-131.
- [192] K. S. Lee, M. Park, J. M. Ko, J. D. Kim, *Colloids Surfaces A Physicochem. Eng. Asp.* **2016**, *506*, 664-669.
- [193] M. Sivakumar, B. Muthukutty, G. Panomsuwan, V. Veeramani, Z. Jiang, T. Maiyalagan, *Colloids Surfaces A Physicochem. Eng. Asp.* **2022**, *648*, 129188.
- [194] X. Wei, X. Zhou, L. Li, W. Feng, H. Wu, *Appl. Surf. Sci.* **2023**, *613*, 155959.
- [195] D. Thanasamy, D. Jesuraj, V. Avadhanam, K. Chinnadurai, S. K. K. Kannan, *J. Energy Storage* **2022**, *53*, 105087.
- [196] A. C. S. Chandran, J. Schneider, R. Nair, B. Bill, N. Gadegaard, R. Hogg, S. Kumar, L. Manjakkal, *ACS Omega* **2024**, *9*, 33998-34007.
- [197] O. Gorduk, M. Gencten, S. Gorduk, M. Sahin, Y. Sahin, *J. Energy Storage* **2021**, *33*, 102049.
- [198] D. Nechiyil, J. Mor, R. Alexander, S. K. Sharma, K. Dasgupta, J. Prakash, *J. Energy Storage* **2024**, *85*, 111207.
- [199] Z. Pan, M. Liu, J. Yang, Y. Qiu, W. Li, Y. Xu, X. Zhang, Y. Zhang, *Adv. Funct. Mater.* **2017**, *27*, 1701122.
- [200] T. Bordjiba, M. Mohamedi, L. H. Dao, *Adv. Mater.* **2008**, *20*, 815-819.
- [201] Y. Bin Tan, J. M. Lee, *J. Mater. Chem. A* **2013**, *1*, 14814-14843.
- [202] Y. Zhou, X. Xu, B. Shan, Y. Wen, T. Jiang, J. Lu, S. Zhang, D. P. Wilkinson, J. Zhang, Y. Huang, *Energy Storage Mater.* **2015**, *1*, 103-111.
- [203] K. Jitapunkul, K. Deshsorn, K. Payakkachon, T. Chaisrithong, L. Lawtrakul, P. Iamprasertkun, *J. Phys. Chem. C* **2023**, *127*, 18316-18326.
- [204] R. Santhosh, S. R. S. Raman, S. M. Krishna, S. sai Ravuri, V. Sandhya, S. Ghosh, N. K. Sahu, S. Punniyakoti, M. Karthik, P. Kollu, S. K. Jeong, A. N. Grace, *Electrochim. Acta* **2018**, *276*, 284-292.
- [205] P. Mehra, A. Paul, *J. Phys. Chem. C* **2022**, *126*, 6135-6146.
- [206] H. Haridas, A. K. A. Kader, A. Sellathurai, D. P. J. Barz, M. Kontopoulou, *ACS Appl. Mater. Interfaces* **2024**, *16*, 16630-16640.
- [207] Y. Zhuo, E. Prestat, I. A. Kinloch, M. A. Bissett, *ACS Appl. Energy Mater.* **2022**, *5*, 61-70.
- [208] L. Manjakkal, C. G. Núñez, W. Dang, R. Dahiya, *Nano Energy* **2018**, *51*, 604-612.
- [209] L. Zhang, D. DeArmond, N. T. Alvarez, D. Zhao, T. Wang, G. Hou, R. Malik, W. R. Heineman, V. Shanov, *J. Mater. Chem. A* **2016**, *4*, 1876-1886.
- [210] J. S. Shaikh, N. S. Shaikh, Y. K. Mishra, S. S. Pawar, N. Parveen, P. M. Shewale, S. Sabale, P. Kanjanaboos, S. Praserttham, C. D. Lokhande, *Nanotechnology* **2021**, *32*, 362001.
- [211] X. Wang, C. Deng, X. Hong, W. Dong, B. Liang, *J. Energy Storage* **2022**, *55*, 105837.
- [212] M. Zhang, H. Du, Z. Wei, X. Zhang, R. Wang, *ACS Appl. Energy Mater.* **2021**, *4*, 8262-8274.
- [213] C. S. Bongu, M. R. Krishnan, A. Soliman, M. Arsalan, E. H. Alsharaeh, *ACS Omega* **2023**, *8*, 36789-36800.
- [214] M. Dong, Z. Wang, G. Yan, J. Wang, H. Guo, X. Li, *J. Alloys Compd.* **2020**,

- 822, 153645.
- [215] W. Qian, Z. Chen, S. Cottingham, W. A. Merrill, N. A. Swartz, A. M. Goforth, T. L. Clare, J. Jiao, *Green Chem.* **2012**, *14*, 371-377.
- [216] W. Liu, H. Niu, J. Yang, K. Cheng, K. Ye, K. Zhu, G. Wang, D. Cao, J. Yan, *Chem. Mater.* **2018**, *30*, 1055-1068.
- [217] Y. Wang, L. Zhang, H. Hou, W. Xu, G. Duan, S. He, K. Liu, S. Jiang, *J. Mater. Sci.* **2020**, *56*, 173-200.
- [218] S. Palchoudhury, K. Ramasamy, J. Han, P. Chen, A. Gupta, *Nanoscale Adv.* **2023**, *5*, 2724-2742.
- [219] X. Chia, M. Pumera, *Chem. Soc. Rev.* **2018**, *47*, 5602-5613.
- [220] K. Momma, F. Izumi, *J. Appl. Crystallogr.* **2008**, *41*, 653-658.
- [221] M. Sharma, P. K. Mohapatra, *Mater. Today Proc.* **2023**, *78*, 907-910.
- [222] C. S. Tang, X. Yin, Chapter: Two-dimensional transition metal dichalcogenides: A general overview in *Two-Dimensional Transition-Metal Dichalcogenides: Phase Engineering and Applications in Electronics and Optoelectronics* (Ed.: A. Wee, X. Yin, C.S. Tang), Wiley-VCH GmbH, **2023**, 1-59.
- [223] Z. Hong, W. Hong, B. Wang, Q. Cai, X. He, W. Liu, *Chem. Eng. J.* **2023**, *460*, 141858.
- [224] S. Das, G. Swain, K. Parida, *Mater. Chem. Front.* **2021**, *5*, 2143-2172.
- [225] H. Li, X. Yuan, Z. Wei, J. Shi, Q. Jia, D. Ma, Y. Li, Y. Zhang, X. Zhu, *Mater. Today Chem.* **2024**, *37*, 102002.
- [226] N. Thi Xuyen, J. M. Ting, *Chem. - A Eur. J.* **2017**, *23*, 17348-17355.
- [227] B. Zhao, D. Shen, Z. Zhang, P. Lu, M. Hossain, J. Li, B. Li, X. Duan, *Adv. Funct. Mater.* **2021**, *31*, 2105132.
- [228] Y. Li, G. Kuang, Z. Jiao, L. Yao, R. Duan, *Mater. Res. Express* **2022**, *9*, 122001.
- [229] A. Raza, J. Z. Hassan, M. Ikram, S. Ali, U. Farooq, Q. Khan, M. Maqbool, *Adv. Mater. Interfaces* **2021**, *8*, 2002205.
- [230] Á. Coogan, Y. K. Gun'Ko, *Mater. Adv.* **2021**, *2*, 146-164.
- [231] J. Xu, J. Zhang, W. Zhang, C. S. Lee, *Adv. Energy Mater.* **2017**, *7*, 1700571.
- [232] M. S. U. Shah, X. Zuo, A. Shah, S. I. Al-Saeedi, M. Z. U. Shah, E. A. Alabbad, H. Hou, S. A. Ahmad, M. Arif, M. Sajjad, T. U. Haq, *J. Energy Storage* **2023**, *65*, 107267.
- [233] K. D. Ramadhass, C. C. Lin, *Small* **2025**, *Early View*, 2505860.
- [234] X. Y. Yu, L. Yu, X. W. Lou, *Adv. Energy Mater.* **2016**, *6*, 1501333.
- [235] Y. Liu, Z. Che, X. Lu, X. Zhou, M. Han, J. Bao, Z. Dai, *Nanoscale Adv.* **2020**, *2*, 583-604.
- [236] A. Gautam, S. Sk, U. Pal, *Phys. Chem. Chem. Phys.* **2022**, *24*, 20638-20673.
- [237] M. Tobis, M. Elmanzalawy, J. Choi, E. Frąckowiak, S. Fleischmann, *Batter. Supercaps* **2024**, *7*, e202400277.
- [238] S. Rani, M. Tanwar, M. Sharma, L. Bansal, R. Kumar, R. Bhatia, S. Ivaturi, *J. Energy Storage* **2023**, *58*, 106343.
- [239] X. Zheng, Y. Zhu, Y. Sun, Q. Jiao, *J. Power Sources* **2018**, *395*, 318-327.
- [240] C. Falco, J. P. Marco-Lozar, D. Salinas-Torres, E. Morallón, D. Cazorla-Amorós, M. M. Titirici, D. Lozano-Castelló, *Carbon* **2013**, *62*, 346-355.
- [241] X. Su, L. Yu, G. Cheng, H. Zhang, M. Sun, L. Zhang, J. Zhang, *Appl. Energy* **2014**, *134*, 439-445.

- [242] M. Liu, Q. Zhao, H. Liu, J. Yang, X. Chen, L. Yang, Y. Cui, W. Huang, W. Zhao, A. Song, Y. Wang, S. Ding, Y. Song, G. Qian, H. Chen, F. Pan, *Nano Energy* **2019**, *64*, 103942.
- [243] G. A. S. Junior, G. H. M. O. Pinto, N. L. O. Sousa, E. N. D. Araújo, G. J. P. Tonon, I. D. Ferreira, F. S. Medeiros, N. P. G. Lopes, A. Q. Moura, W. A. A. Macedo, P. L. Gastelois, J. P. C. Trigueiro, R. L. Lavall, P. F. R. Ortega, *J. Energy Storage* **2025**, *129*, 117315.
- [244] J. Strachan, A. F. Masters, T. Maschmeyer, *J. Mater. Chem. A* **2021**, *9*, 9451-9461.
- [245] K. Shen, S. Zhai, S. Wang, Q. Ru, X. Hou, K. San Hui, K. Nam Hui, F. Chen, *Batter. Supercaps* **2021**, *4*, 860-880.
- [246] K. Shen, Z. Zhang, S. Wang, Q. Ru, L. Zhao, L. Sun, X. Hou, F. Chen, *Energy Fuels* **2020**, *34*, 8987-8992.
- [247] S. Yuan, X. L. Huang, D. L. Ma, H. G. Wang, F. Z. Meng, X. B. Zhang, *Adv. Mater.* **2014**, *26*, 2273-2279.
- [248] N. U. H. L. Ali, P. Pazhamalai, M. S. M. Saleem, S. J. Kim, *J. Energy Storage* **2024**, *82*, 110423.
- [249] M. Abdullah, S. Khan, K. Jabbour, M. Imran, M. F. Ashiq, P. John, S. Manzoor, T. Munawar, M. N. Ashiq, *Electrochim. Acta* **2023**, *466*, 143020.
- [250] V. K. Mariappan, K. Krishnamoorthy, P. Pazhamalai, S. Sahoo, S. S. Nardekar, S. J. Kim, *Nano Energy* **2019**, *57*, 307-316.
- [251] G. Zhang, W. Li, K. Xie, F. Yu, H. Huang, *Adv. Funct. Mater.* **2013**, *23*, 3675-3681.
- [252] M. Huang, X. L. Zhao, F. Li, L. L. Zhang, Y. X. Zhang, *J. Power Sources* **2015**, *277*, 36-43.
- [253] X. Ren, K. Turcheniuk, D. Lewis, W. Fu, A. Magasinski, M. W. Schauer, G. Yushin, *Small* **2018**, *14*, 1703425.
- [254] Z. Yao, L. Zhou, H. Yin, X. Wang, D. Xie, X. Xia, C. Gu, J. Tu, Z. J. Yao, L. M. Zhou, H. Y. Yin, X. L. Wang, X. H. Xia, C. D. Gu, J. P. Tu, D. Xie, *Small* **2019**, *15*, 1904433.
- [255] P. Pazhamalai, K. Krishnamoorthy, S. Sahoo, V. K. Mariappan, S. J. Kim, *Chem. Eng. J.* **2019**, *359*, 409-418.
- [256] F. Ma, X. Dai, J. Jin, N. Tie, Y. Dai, *Electrochim. Acta* **2020**, *331*, 135459.
- [257] L. G. Bulusheva, G. I. Semushkina, A. D. Fedorenko, *Nanomaterials* **2023**, *13*, 2182.
- [258] K. Le, X. Zhang, Q. Zhao, Y. Liu, P. Yi, S. Xu, W. Liu, *ACS Appl. Mater. Interfaces* **2021**, *13*, 44427-44439.
- [259] S. Zhao, W. Xu, Z. Yang, X. Zhang, Q. Zhang, *Electrochim. Acta* **2020**, *331*, 135265.
- [260] S. Liu, H. Zhang, X. Peng, J. Chen, L. Kang, X. Yin, Y. Yusuke, B. Ding, *ACS Nano* **2025**, *19*, 13591-13636.
- [261] N. Moses Badlyan, N. Pettinger, N. Enderlein, R. Gillen, X. Chen, W. Zhang, K. C. Knirsch, A. Hirsch, J. Maultzsch, *Phys. Rev. B* **2022**, *106*, 104103.
- [262] Y. Yin, P. Miao, Y. Zhang, J. Han, X. Zhang, Y. Gong, L. Gu, C. Xu, T. Yao, P. Xu, Y. Wang, B. Song, S. Jin, *Adv. Funct. Mater.* **2017**, *27*, 1606694.
- [263] J. Huang, X. Pan, X. Liao, M. Yan, B. Dunn, W. Luo, L. Mai, *Nanoscale* **2020**, *12*, 9246-9254.
- [264] S. Roy, A. Joseph, X. Zhang, S. Bhattacharyya, A. B. Puthirath, A. Biswas, C. S. Tiwary, R. Vajtai, P. M. Ajayan, *Chem. Rev.* **2024**, *124*, 9376-9456.

- [265] Y. Guo, D. Sun, B. Ouyang, A. Raja, J. Song, T. F. Heinz, L. E. Brus, *Nano Lett.* **2015**, *15*, 5081-5088.
- [266] Y. Yu, G. H. Nam, Q. He, X. J. Wu, K. Zhang, Z. Yang, J. Chen, Q. Ma, M. Zhao, Z. Liu, F. R. Ran, X. Wang, H. Li, X. Huang, B. Li, Q. Xiong, Q. Zhang, Z. Liu, L. Gu, Y. Du, W. Huang, H. Zhang, *Nat. Chem.* **2018**, *10*, 638-643.
- [267] S. Jiménez Sandoval, D. Yang, R. F. Frindt, J. C. Irwin, *Phys. Rev. B* **1991**, *44*, 3955.
- [268] C. Lee, H. Yan, L. E. Brus, T. F. Heinz, J. Hone, S. Ryu, *ACS Nano* **2010**, *4*, 2695-2700.
- [269] M. Wen, X. Chen, Z. Zheng, S. Deng, Z. Li, W. Wang, H. Chen, *J. Phys. Chem. C* **2021**, *125*, 765-773.
- [270] L. Seguin, M. Figlarz, R. Cavagnat, J. C. Lassègues, *Spectrochim. Acta Part A Mol. Biomol. Spectrosc.* **1995**, *51*, 1323-1344.
- [271] P. A. Spevack, N. S. McIntyre, *J. Phys. Chem* **1992**, *96*, 9029-9035.
- [272] Y. Hanifehpour, M. Abdolmaleki, N. Moradi, A. H. S. Farhood, S. Ahmadiyeh, G. R. Allahgholipour, J. Hosseini, *New J. Chem.* **2022**, *46*, 20932-20939.
- [273] R. Rohith, M. Manuraj, R. Imran Jafri, R. B. Rakhi, *Mater. Today Proc.* **2022**, *50*, 1-6.
- [274] K. Prakash, S. Harish, S. Kamalakannan, T. Logu, M. Shimomura, J. Archana, M. Navaneethan, *J. Energy Chem.* **2023**, *80*, 335-349.
- [275] M. Isacfranklin, L. E. M. Princy, Y. Rathinam, L. Kungumadevi, G. Ravi, A. G. Al-Sehemi, D. Velauthapillai, *Energy and Fuels* **2022**, *36*, 6476-6482.
- [276] J. Shao, Y. Li, M. Zhong, Q. Wang, X. Luo, K. Li, W. Zhao, *Mater. Lett.* **2019**, *252*, 173-177.
- [277] Z. Wang, Y. Liu, Y. Deng, H. Wang, S. Han, Y. Wang, X. Zhang, X. Liu, *Langmuir* **2025**, *41*, 14265-14274.
- [278] M. S. Whittingham, *Science* **1976**, *192*, 1126-1127.
- [279] M. S. Whittingham, *Proc. IEEE* **2012**, *100*, 1518-1534.
- [280] J. B. Cook, T. C. Lin, H. S. Kim, A. Siordia, B. S. Dunn, S. H. Tolbert, *ACS Nano* **2019**, *13*, 1223-1231.
- [281] X. Fang, C. Hua, X. Guo, Y. Hu, Z. Wang, X. Gao, F. Wu, J. Wang, L. Chen, *Electrochim. Acta* **2012**, *81*, 155-160.
- [282] L. Zhang, D. Sun, J. Kang, J. Feng, H. A. Bechtel, L. W. Wang, E. J. Cairns, J. Guo, *Nano Lett.* **2018**, *18*, 1466-1475.
- [283] F. Chen, D. Shi, M. Yang, H. Jiang, Y. Shao, S. Wang, B. Zhang, J. Shen, Y. Wu, X. Hao, *Adv. Funct. Mater.* **2021**, *31*, 2007132.
- [284] S. J. Panchu, K. Raju, H. C. Swart, B. Chokkalingam, M. Maaza, M. Henini, M. K. Moodley, *ACS Omega* **2021**, *6*, 4542-4550.
- [285] H. D. Yoo, Y. Li, Y. Liang, Y. Lan, F. Wang, Y. Yao, *ChemNanoMat* **2016**, *2*, 688-691.
- [286] L. Wang, J. Wu, X. Wang, S. Fu, *J. Alloys Compd.* **2023**, *959*, 170548.
- [287] S. Shanmuganathi, T. Selvam, D. Dhinasekaran, A. K. M. Rajendran, B. Subramanian, A. R. Rajendran, *Appl. Phys. Lett.* **2025**, *126*, 103901.
- [288] Y. Zhuo, I. A. Kinloch, M. A. Bissett, *ACS Appl. Nano Mater.* **2023**, *6*, 18062-18070.
- [289] K. M. Sarode, D. R. Patil, *J. Nanosci. Technol.* **2018**, *4*, 371-373.
- [290] B. A. Ali, A. M. A. Omar, A. S. G. Khalil, N. K. Allam, *ACS Appl. Mater. Interfaces* **2019**, *11*, 33955-33965.
- [291] Z. Liang, C. Zhao, W. Zhao, Y. Zhang, P. Srimuk, V. Presser, G. Feng,

- Energy Environ. Mater.* **2021**, 4, 631-637.
- [292] Y. Gao, H. Zhang, J. Peng, L. Li, Y. Xiao, L. Li, Y. Liu, Y. Qiao, S. L. Chou, *Carbon Energy* **2024**, 6, e464.
- [293] K. M. Abraham, *ACS Energy Lett.* **2020**, 5, 3544-3547.
- [294] J. Y. Hwang, S. T. Myung, Y. K. Sun, *Chem. Soc. Rev.* **2017**, 46, 3529-3614.
- [295] M. Sawicki, L. L. Shaw, *RSC Adv.* **2015**, 5, 53129-53154.
- [296] N. Weber, J. T. Kummer, A Sodium-Sulfur Secondary Battery in *Proc. 21st Power Sources Conference*, PSC Publications, USA, **1967**, 37-39.
- [297] G. H. Newman, L. P. Klemann, *J. Electrochem. Soc.* **1980**, 127, 2097.
- [298] A. S. Nagelberg, W. L. Worrell, *J. Solid State Chem.* **1979**, 29, 345-354.
- [299] D. A. Stevens, J. R. Dahn, *J. Electrochem. Soc.* **2000**, 147, 1271.
- [300] D. A. Stevens, J. R. Dahn, *J. Electrochem. Soc.* **2001**, 148, A803.
- [301] A. Rudola, A. J. R. Rennie, R. Heap, S. S. Meysami, A. Lowbridge, F. Mazzali, R. Sayers, C. J. Wright, J. Barker, *J. Mater. Chem. A* **2021**, 9, 8279-8302.
- [302] R. Rao, L. Chen, J. Su, S. Cai, S. Wang, Z. Chen, *Batter. Energy* **2024**, 3, 20230036.
- [303] L. Zhao, T. Zhang, W. Li, T. Li, L. Zhang, X. Zhang, Z. Wang, *Engineering* **2023**, 24, 172-183.
- [304] K. Sada, J. Darga, A. Manthiram, *Adv. Energy Mater.* **2023**, 13, 2302321.
- [305] N. R. Chodankar, A. K. Nanjundan, D. Losic, D. P. Dubal, J. B. Baek, *Mater. Today Adv.* **2020**, 6, 100053.
- [306] P. K. Nayak, L. Yang, W. Brehm, P. Adelhelm, *Angew. Chemie Int. Ed.* **2018**, 57, 102-120.
- [307] X. Fan, X. Kong, P. Zhang, J. Wang, *Energy Storage Mater.* **2024**, 69, 103386.
- [308] Y. Huang, L. Zhao, L. Li, M. Xie, F. Wu, R. Chen, *Adv. Mater.* **2019**, 31, 1808393.
- [309] K. Vignarooban, R. Kushagra, A. Elango, P. Badami, B. E. Mellander, X. Xu, T. G. Tucker, C. Nam, A. M. Kannan, *Int. J. Hydrogen Energy* **2016**, 41, 2829-2846.
- [310] S. Natarajan, R. M. Bhattarai, M. S. P. Sudhakaran, Y. S. Mok, S. J. Kim, *J. Power Sources* **2023**, 577, 233170.
- [311] J. Ruan, J. Hu, Q. Li, S. Luo, J. Yang, Y. Liu, Y. Song, S. Zheng, D. Sun, F. Fang, F. Wang, *Nat. Sustain.* **2025**, 8, 530-541.
- [312] S. Komaba, T. Ishikawa, N. Yabuuchi, W. Murata, A. Ito, Y. Ohsawa, *ACS Appl. Mater. Interfaces* **2011**, 3, 4165-4168.
- [313] J. F. Peters, A. P. Cruz, M. Weil, *Batteries* **2019**, 5, 10.
- [314] F. Trotta, G. J. Wang, Z. Guo, Z. Xu, M. Crespo Ribadeneyra, H. Au, J. S. Edge, M. M. Titirici, L. Lander, *Adv. Sustain. Syst.* **2022**, 6, 2200047.
- [315] C. Yang, S. Xin, L. Mai, Y. You, *Adv. Energy Mater.* **2021**, 11, 2000974.
- [316] J. B. Robinson, D. P. Finegan, T. M. M. Heenan, K. Smith, E. Kendrick, D. J. L. Brett, P. R. Shearing, *J. Electrochem. Energy Convers. Storage* **2018**, 15, 011010.
- [317] G. G. Eshetu, S. Grugeon, H. Kim, S. Jeong, L. Wu, G. Gachot, S. Laruelle, M. Armand, S. Passerini, *ChemSusChem* **2016**, 9, 462-471.
- [318] X. Xia, J. R. Dahn, *Electrochem. Solid-State Lett.* **2012**, 15, A1.
- [319] Y. Wang, R. Ou, J. Yang, Y. Xin, P. Singh, F. Wu, Y. Qian, H. Gao, *J. Energy Chem.* **2024**, 95, 407-427.

- [320] H. Zhang, Y. Gao, X. Liu, L. Zhou, J. Li, Y. Xiao, J. Peng, J. Wang, S. L. Chou, *Adv. Energy Mater.* **2023**, *13*, 2300149.
- [321] T. Zhang, M. Kamlah, *J. Power Sources* **2021**, *483*, 229187.
- [322] Y. S. Hong, N. Li, H. Chen, P. Wang, W. L. Song, D. Fang, *Energy Storage Mater.* **2018**, *11*, 118-126.
- [323] T. Wei, X. L. Xian, S. X. Dou, W. Chen, S. L. Chou, *Rare Met.* **2024**, *43*, 1343-1349.
- [324] L. Zhang, X. Li, M. Yang, W. Chen, *Energy Storage Mater.* **2021**, *41*, 522-545.
- [325] Z. Xue, D. Zhu, M. Shan, H. Wang, J. Zhang, G. Cui, Z. Hu, K. C. Gordon, G. Xu, M. Zhu, *Nano Today* **2024**, *55*, 102175.
- [326] J. Xu, Y. Qiu, J. Yang, H. Li, P. Han, Y. Jin, H. Liu, B. Sun, G. Wang, *Adv. Funct. Mater.* **2024**, *34*, 2306206.
- [327] Y. Zhao, J. Zhan, X. Liu, H. Wang, Z. Li, G. Xu, W. Zhou, C. Wu, G. Wang, *J. Colloid Interface Sci.* **2024**, *670*, 246-257.
- [328] X. Zhai, X. Sun, M. Zhao, M. Zhang, X. Zhang, H. Li, *J. Energy Storage* **2024**, *101*, 113745.
- [329] V. C. Ho, B. T. D. Nguyen, H. Y. N. Thi, J. F. Kim, J. Mun, *Int. J. Energy Res.* **2022**, *46*, 5177-5188.
- [330] B. Li, Y. Liu, X. Han, Y. Zhou, F. Xiao, W. Xian, Y. Chu, G. Liu, Z. Lu, *Chem. Eng. J.* **2024**, *501*, 157803.
- [331] C. Li, H. Xu, L. Ni, B. Qin, Y. Ma, H. Jiang, G. Xu, J. Zhao, G. Cui, *Adv. Energy Mater.* **2023**, *13*, 2301758.
- [332] Y. Li, F. Wu, Y. Li, M. Liu, X. Feng, Y. Bai, C. Wu, *Chem. Soc. Rev.* **2022**, *51*, 4484-4536.
- [333] S. Lin, Z. Yang, J. Chen, Y. Qiao, L. Li, S. Chou, *Adv. Funct. Mater.* **2024**, *34*, 2400731.
- [334] S. Yang, K. Cheng, Z. Cao, *J. Mater. Chem. A* **2024**, *12*, 13059-13080.
- [335] K. Cui, R. Hou, H. Zhou, S. Guo, *Adv. Funct. Mater.* **2025**, *35*, 2419275.
- [336] Y. Liu, L. Zhu, E. Wang, Y. An, Y. Liu, K. Shen, M. He, Y. Jia, G. Ye, Z. Xiao, Y. Li, Q. Pang, *Adv. Mater.* **2024**, *36*, 2310051.
- [337] M. Wilamowska-Zawłocka, A. Cymann-Sachajdak, Z. Zarach, M. Graczyk-Zajac, Chapter: Cathodes for Sodium-Ion Batteries in *Advanced Technologies for Rechargeable Batteries: Alkaline Metal Ion, Redox Flow, and Metal Sulfur Batteries* (Ed.: P. Raghavan, A. Das, M.J. Jabeen Fatima), CRC Press, **2024**, 110-142.
- [338] H. Zhang, L. Wang, P. Zuo, *J. Mater. Chem. A* **2024**, *12*, 30971-31003.
- [339] H. Wang, H. Chen, Y. Mei, J. Gao, L. Ni, N. Hong, B. Zhang, F. Zhu, J. Huang, K. Wang, W. Deng, D. S. Silvester, C. E. Banks, S. Yasar, B. Song, G. Zou, H. Hou, X. Ji, *ACS Nano* **2024**, *18*, 13150-13163.
- [340] X. Cui, S. Wang, X. Ye, X. Fan, C. Gao, Y. Quan, S. Wen, X. Cai, J. Huang, S. Li, *Energy Storage Mater.* **2022**, *45*, 1153-1164.
- [341] H. Zhao, J. Li, W. Liu, H. Xu, X. Gao, J. Shi, K. Yu, X. Ding, *Electrochim. Acta* **2021**, *388*, 138561.
- [342] Y. Gupta, P. Siwatch, R. Karwasra, K. Sharma, S. K. Tripathi, *Renew. Sustain. Energy Rev.* **2024**, *192*, 114167.
- [343] T. Jin, H. Li, K. Zhu, P. F. Wang, P. Liu, L. Jiao, *Chem. Soc. Rev.* **2020**, *49*, 2342-2377.
- [344] H. Li, M. Xu, Z. Zhang, Y. Lai, J. Ma, *Adv. Funct. Mater.* **2020**, *30*, 2000473.
- [345] Z. Song, R. Liu, W. Di Liu, Y. Chen, W. Hu, *Adv. Energy Sustain. Res.*

- 2023**, 4, 2300102.
- [346] C. Fang, Y. Huang, W. Zhang, J. Han, Z. Deng, Y. Cao, H. Yang, *Adv. Energy Mater.* **2016**, 6, 1501727.
- [347] S. Xu, H. Dong, D. Yang, C. Wu, Y. Yao, X. Rui, S. Chou, Y. Yu, *ACS Cent. Sci.* **2023**, 9, 2012-2035.
- [348] W. R. Brant, R. Younesi, *ECS Meet. Abstr.* **2023**, MA2023-01, 894.
- [349] C. Q. X. Lim, Z. K. Tan, *ACS Appl. Energy Mater.* **2021**, 4, 6214-6220.
- [350] F. M. Maddar, D. Walker, T. W. Chamberlain, J. Compton, A. S. Menon, M. Copley, I. Hasa, *J. Mater. Chem. A* **2023**, 11, 15778-15791.
- [351] S. Qiao, Q. Zhou, M. Ma, H. K. Liu, S. X. Dou, S. Chong, *ACS Nano* **2023**, 17, 11220-11252.
- [352] Z. G. Liu, R. Du, X. X. He, J. C. Wang, Y. Qiao, L. Li, S. L. Chou, *ChemSusChem* **2021**, 14, 3724-3743.
- [353] H. Tan, D. Chen, X. Rui, Y. Yu, *Adv. Funct. Mater.* **2019**, 29, 1808745.
- [354] H. Xu, H. Li, X. Wang, *ChemElectroChem* **2023**, 10, e202201151.
- [355] L. Fang, N. Bahlawane, W. Sun, H. Pan, B. Bin Xu, M. Yan, Y. Jiang, *Small* **2021**, 17, 2101137.
- [356] S. Alvin, D. Yoon, C. Chandra, H. S. Cahyadi, J. H. Park, W. Chang, K. Y. Chung, J. Kim, *Carbon* **2019**, 145, 67-81.
- [357] L. D. Ellis, T. D. Hatchard, M. N. Obrovac, *J. Electrochem. Soc.* **2012**, 159, A1801.
- [358] J. Yang, X. Guo, H. Gao, T. Wang, Z. Liu, Q. Yang, H. Yao, J. Li, C. Wang, G. Wang, *Adv. Energy Mater.* **2023**, 13, 2300351.
- [359] W. Ma, K. Yin, H. Gao, J. Niu, Z. Peng, Z. Zhang, *Nano Energy* **2018**, 54, 349-359.
- [360] R. Shao, Z. Sun, L. Wang, J. Pan, L. Yi, Y. Zhang, J. Han, Z. Yao, J. Li, Z. Wen, S. Chen, S. L. Chou, D. L. Peng, Q. Zhang, *Angew. Chemie - Int. Ed.* **2024**, 63, e202320183.
- [361] J. Zhou, W. Ye, X. Lian, Q. Shi, Y. Liu, X. Yang, L. Liu, D. Wang, J. H. Choi, J. Sun, R. Yang, M. S. Wang, M. H. Rummeli, *Energy Storage Mater.* **2022**, 46, 20-28.
- [362] X. Liu, B. Xiao, A. Daali, X. Zhou, Z. Yu, X. Li, Y. Liu, L. Yin, Z. Yang, C. Zhao, L. Zhu, Y. Ren, L. Cheng, S. Ahmed, Z. Chen, X. Li, G. L. Xu, K. Amine, *ACS Energy Lett.* **2021**, 6, 547-556.
- [363] M. Lao, Y. Zhang, W. Luo, Q. Yan, W. Sun, S. X. Dou, *Adv. Mater.* **2017**, 29, 1700622.
- [364] Q. Wang, C. Zhao, Y. Lu, Y. Li, Y. Zheng, Y. Qi, X. Rong, L. Jiang, X. Qi, Y. Shao, D. Pan, B. Li, Y.-S. Hu, L. Chen, *Small* **2017**, 13, 1701835.
- [365] J. Chen, G. Adit, L. Li, Y. Zhang, D. H. C. Chua, P. S. Lee, *Energy Environ. Mater.* **2023**, 6, e12633.
- [366] P. Ge, M. Fouletier, *Solid State Ionics* **1988**, 28-30, 1172-1175.
- [367] G. Yoon, H. Kim, I. Park, K. Kang, *Adv. Energy Mater.* **2017**, 7, 1601519.
- [368] Z. L. Xu, G. Yoon, K. Y. Park, H. Park, O. Tamwattana, S. Joo Kim, W. M. Seong, K. Kang, *Nat. Commun.* **2019**, 10, 2598.
- [369] W. Deng, H. Yang, H. Huo, Y. Yu, *Adv. Funct. Mater.* **2025**, Early View, 2504168.
- [370] R. Zhao, N. Sun, B. Xu, *Small Struct.* **2021**, 2, 2100132.
- [371] C. Dudding, S. Jankhani, L. Grebener, M. Ali, D. Segets, H. Wiggers, M. A. Pope, *Carbon* **2025**, 244, 120608.
- [372] Z. Tong, C. Lv, G. D. Bai, Z. W. Yin, Y. Zhou, J. T. Li, *Carbon Energy* **2025**,

- 7, e643.
- [373] C. Matei Ghimbeu, A. Beda, B. Réty, H. El Marouazi, A. Vizintin, B. Tratnik, L. Simonin, J. Michel, J. Abou-Rjeily, R. Dominko, *Adv. Energy Mater.* **2024**, *14*, 2303833.
- [374] X. Chen, C. Liu, Y. Fang, X. Ai, F. Zhong, H. Yang, Y. Cao, *Carbon Energy* **2022**, *4*, 1133-1150.
- [375] Y. Cao, L. Xiao, M. L. Sushko, W. Wang, B. Schwenzer, J. Xiao, Z. Nie, L. V. Saraf, Z. Yang, J. Liu, *Nano Lett.* **2012**, *12*, 3783-3787.
- [376] J. Ding, H. Wang, Z. Li, A. Kohandehghan, K. Cui, Z. Xu, B. Zahiri, X. Tan, E. M. Lotfabad, B. C. Olsen, D. Mitlin, *ACS Nano* **2013**, *7*, 11004-11015.
- [377] C. Bommier, T. W. Surta, M. Dolgos, X. Ji, *Nano Lett.* **2015**, *15*, 5888-5892.
- [378] Y. Morikawa, S. ichi Nishimura, R. ichi Hashimoto, M. Ohnuma, A. Yamada, *Adv. Energy Mater.* **2020**, *10*, 1903176.
- [379] M. Olsson, A. Klein, N. Mozhzhukhina, S. Xiong, C. Appel, M. Carlsen, L. Nielsen, L. Rensmo, M. Liebi, A. Matic, *Adv. Sci.* **2025**, *Early View*, e08635.
- [380] L. Kitsu Iglesias, E. N. Antonio, T. D. Martinez, L. Zhang, Z. Zhuo, S. J. Weigand, J. Guo, M. F. Toney, *Adv. Energy Mater.* **2023**, *13*, 2302171.
- [381] X. Chen, J. Tian, P. Li, Y. Fang, Y. Fang, X. Liang, J. Feng, J. Dong, X. Ai, H. Yang, Y. Cao, *Adv. Energy Mater.* **2022**, *12*, 2200886.
- [382] J. M. Stratford, A. K. Kleppe, D. S. Keeble, P. A. Chater, S. S. Meysami, C. J. Wright, J. Barker, M. M. Titirici, P. K. Allan, C. P. Grey, *J. Am. Chem. Soc.* **2021**, *143*, 14274-14286.
- [383] L. Sun, J. Li, L. Wang, E. Li, W. Huang, *J. Power Sources* **2024**, *624*, 235474.
- [384] N. Sun, J. Qiu, B. Xu, *Adv. Energy Mater.* **2022**, *12*, 2200715.
- [385] A. Beda, C. Vaultot, F. Rabuel, M. Morcrette, C. M. Ghimbeu, *Energy Adv.* **2022**, *1*, 185-190.
- [386] M. P. Mercer, M. Nagarathinam, E. M. Gavilán-Arriazu, A. Binjrajka, S. Panda, H. Au, M. Crespo-Ribadeneyra, M. M. Titirici, E. P. M. Leiva, H. E. Hoster, *J. Mater. Chem. A* **2023**, *11*, 6543-6555.
- [387] X. Feng, Y. Li, M. Zhang, Y. Li, Y. Gong, M. Liu, Y. Bai, C. Wu, *ACS Appl. Mater. Interfaces* **2022**, *14*, 50992-51000.
- [388] Y. Yuan, Z. Chen, H. Yu, X. Zhang, T. Liu, M. Xia, R. Zheng, M. Shui, J. Shu, *Energy Storage Mater.* **2020**, *32*, 65-90.
- [389] H. Tonnoir, D. Huo, C. Davoisne, A. Celzard, V. Fierro, D. Saurel, M. El Marssi, M. Benyoussef, P. Meunier, R. Janot, *Carbon* **2023**, *208*, 216-226.
- [390] F. Wu, M. Zhang, Y. Bai, X. Wang, R. Dong, C. Wu, *ACS Appl. Mater. Interfaces* **2019**, *11*, 12554-12561.
- [391] M. Thompson, Q. Xia, Z. Hu, X. S. Zhao, *Mater. Adv.* **2021**, *2*, 5881-5905.
- [392] C. del Mar Saavedra Rios, L. Simonin, C. M. Ghimbeu, C. Vaultot, D. da Silva Perez, C. Dupont, *Fuel Process. Technol.* **2022**, *231*, 107223.
- [393] W. Sun, X. Rui, D. Yang, Z. Sun, B. Li, W. Zhang, Y. Zong, S. Madhavi, S. Dou, Q. Yan, *ACS Nano* **2015**, *9*, 11371-11381.
- [394] X. Liu, K. Zhang, K. Lei, F. Li, Z. Tao, J. Chen, *Nano Res.* **2016**, *9*, 198-206.
- [395] X. M. Lin, J. H. Chen, J. J. Fan, Y. Ma, P. Radjenovic, Q. C. Xu, L. Huang, S. Passerini, Z. Q. Tian, J. F. Li, *Adv. Energy Mater.* **2019**, *9*, 1902312.
- [396] L. bo Tang, B. Zhang, T. Peng, Z. jiang He, C. Yan, J. Mao, K. Dai, X. wen Wu, J. chao Zheng, *Nano Energy* **2021**, *90*, 106568.
- [397] S. H. Choi, Y. C. Kang, *ACS Appl. Mater. Interfaces* **2015**, *7*, 24694-24702.

- [398] S. Dong, C. Li, Z. Li, L. Zhang, L. Yin, S. Dong, C. Li, Z. Li, L. Zhang, L. Yin, *Small* **2018**, *14*, 1704517.
- [399] W. Guo, K. Ding, S. Mei, X. Li, X. Feng, S. Guo, J. Fu, X. Zhang, B. Gao, K. Huo, P. K. Chu, *ChemElectroChem* **2020**, *7*, 914-921.
- [400] S. Zhang, G. Wang, Z. Zhang, B. Wang, J. Bai, H. Wang, *Small* **2019**, *15*, 1900565.
- [401] B. Qu, C. Ma, G. Ji, C. Xu, J. Xu, Y. S. Meng, T. Wang, J. Y. Lee, *Adv. Mater.* **2014**, *26*, 3854-3859.
- [402] Y. Liu, Y. Yang, X. Wang, Y. Dong, Y. Tang, Z. Yu, Z. Zhao, J. Qiu, *ACS Appl. Mater. Interfaces* **2017**, *9*, 15484-15491.
- [403] Y. Jiang, D. Song, J. Wu, Z. Wang, S. Huang, Y. Xu, Z. Chen, B. Zhao, J. Zhang, *ACS Nano* **2019**, *13*, 9100-9111.
- [404] L. Wang, X. Li, Z. Jin, Z. Liang, X. Peng, X. Ren, B. Gao, G. Feng, P. K. Chu, K. Huo, *J. Mater. Chem. A* **2019**, *7*, 27475-27483.
- [405] H. He, D. Sun, Y. Tang, H. Wang, M. Shao, *Energy Storage Mater.* **2019**, *23*, 233-251.
- [406] J. Wang, L. Wang, C. Eng, J. Wang, *Adv. Energy Mater.* **2017**, *7*, 1602706.
- [407] H. Kim, H. Kim, H. Kim, J. Kim, G. Yoon, K. Lim, W. S. Yoon, K. Kang, *Adv. Funct. Mater.* **2016**, *26*, 5042-5050.
- [408] L. Li, R. Jacobs, P. Gao, L. Gan, F. Wang, D. Morgan, S. Jin, *J. Am. Chem. Soc.* **2016**, *138*, 2838-2848.

Chapter II

*The phenomenon of increasing
capacitance induced by 1T/2H–MoS₂
surface modification with Pt particles –
Influence on composition and energy
storage mechanism*

1. Summary of the publication

This study presents a significant contribution to the field of energy storage, specifically addressing the enhancement of supercapacitor performance through novel material modification strategy. It presents an approach to boost the capacitance of molybdenum sulfide-based electrode material, by leveraging platinum surface modification during electrochemical cycling. Unlike conventional methods, this study demonstrates a substantial, sustained increase in capacitance, rather than the typical degradation observed in many MoS₂-based materials over repeated cycles. The paper points into a detailed analysis of the dynamic chemical and structural changes occurring within the electrode material during prolonged electrochemical cycling, especially the progressive exfoliation and transformation into mixed molybdenum oxides with oxygen vacancies.

A critical aspect highlighted in this study is the often-overlooked influence of the counter electrode, particularly platinum, in three-electrode electrochemical measurements. While platinum is widely used due to its excellent electrochemical inertness, electrical conductivity, and mechanical stability, this research demonstrates that it is not truly inert under certain conditions, especially during prolonged cycling in acidic environments.

The paper reveals that platinum can undergo dissolution and subsequent deposition onto the working electrode. This phenomenon, previously discussed in the context of materials studied for application in hydrogen evolution reaction and fuel cells, is shown here to significantly affect the observed electrochemical performance in supercapacitor studies. Notably, the platinum counter electrode was used in the form of a mesh, with a surface area sufficiently large relative to the working electrode to minimize such effects – a standard and reasonable design assumption. Nonetheless, the Pt dissolution and deposition process still occurred. Crucially, this unintended process was not ignored or dismissed as an artifact, but rather deliberately harnessed as a beneficial surface modification strategy that significantly enhanced the electrode's capacitance.

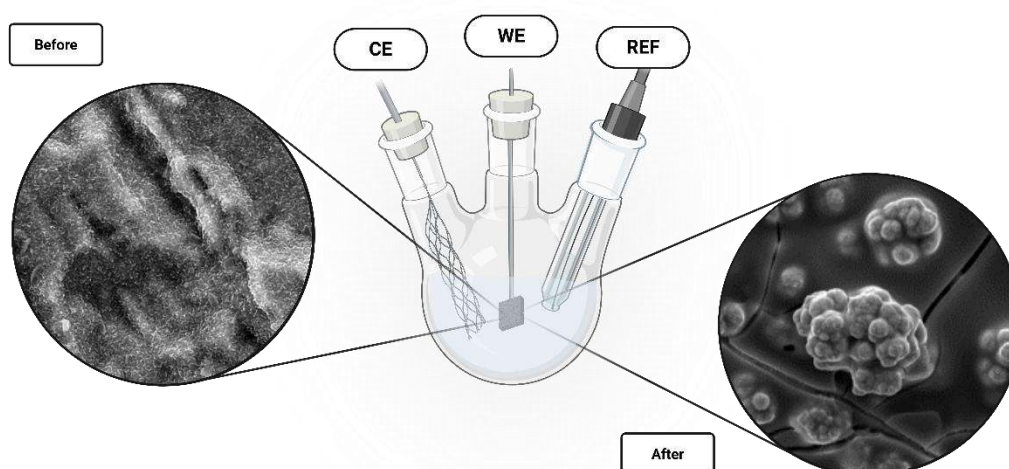


Figure 9. Graphical abstract summarizing Chapter II, created with BioRender.com.

The findings underscore the necessity for caution when interpreting results from 3-electrode measurements, particularly when using Pt counter electrodes. Researchers must consider the potential for Pt dissolution-deposition and its impact on the working electrode's composition and performance, as this can lead to misinterpretations of the material's intrinsic properties and energy storage mechanisms. This paper serves as a vital reminder that dynamic changes introduced by the measurement setup itself must be carefully accounted for to ensure accurate and reliable conclusions about electrode behavior.

2. Publication

Electrochimica Acta 435 (2022) 141389



Contents lists available at ScienceDirect

Electrochimica Acta

journal homepage: www.journals.elsevier.com/electrochimica-acta



The phenomenon of increasing capacitance induced by 1T/2H-MoS₂ surface modification with Pt particles – Influence on composition and energy storage mechanism

Zuzanna Zarach^{a,*}, Mariusz Szkoda^{a,b}, Konrad Trzcinski^{a,b}, Marcin Łapiński^{b,c}, Grzegorz Trykowski^d, Andrzej P. Nowak^{a,b}

^a Department of Chemistry and Technology of Functional Materials, Faculty of Chemistry, Gdańsk University of Technology, Gabriela Narutowicza 11/12, 80-233 Gdańsk, Poland

^b Advanced Materials Center, Gdańsk University of Technology, Gabriela Narutowicza 11/12, 80-233 Gdańsk, Poland

^c Institute of Nanotechnology and Materials Engineering, Faculty of Applied Physics and Mathematics, Gdańsk University of Technology, Narutowicza 11/12, 80-233 Gdańsk, Poland

^d Faculty of Chemistry, Nicolaus Copernicus University in Toruń, Gagarina 7, 87-100, Toruń, Poland

ARTICLE INFO

Keywords:

Molybdenum disulfide
Non-stoichiometric molybdenum oxides
Platinum dissolution-deposition
Supercapacitors
Energy storage

In this paper, several approaches to the synthesis of molybdenum-based electrode materials for supercapacitors are presented, including anodization, hydrothermal process and annealing. For the material prepared via anodization of a molybdenum plate, followed by a hydrothermal process in thiourea aqueous solution, a thorough study of the Pt-surface modification through repetitive cycling in 1 M sulfuric acid with Pt acting as a counter electrode is performed, including X-ray photoelectron spectroscopy analysis and energy storage mechanism contribution. Along with the increasing number of cycles, an increase of the capacitance value is observed up to 1.064 F cm^{-2} after 60 000 cycles, resulting in more than tenfold growth (by over 1 150%). The analysis reveals progressive changes in the electrode material's chemical composition and the increasing pseudocapacitance contribution in energy storage processes, which is strictly caused by the formation of mixed molybdenum oxides with oxygen vacancies. Thus, Pt-surface modification effectively improves the electrochemical performance of the electrode material with excellent coulombic efficiency and capacitance retention. In a symmetric two-electrode configuration with Pt-modified electrode materials, the areal capacitance of 140.5 mF cm^{-2} is obtained after 50 000 cycles (with capacitance retention of 123%) indicating that Pt-surface modification of MoS₂ may provide a novel approach for electrode materials for high-performance supercapacitors.

1. Introduction

Nowadays, the whole world is struggling with environmental problems related to the pollution caused by the use of fossil fuels. These problems do not end with pollution, as it is known that the depletion of these sources could soon lead to an energy crisis. As a consequence, a majority of countries have currently been focusing on the use of renewable energy sources, which can be a solution to this emerging problem. However, it is important to be aware of the limitation of their periodic availability, which is especially noticeable in the case of solar or wind energy. The answer to this problem may be the application of effective and efficient technologies that will enable the storage of energy in order to use it at the most convenient time. Supercapacitors, also known as electrochemical capacitors, are one of energy storage systems

that exhibit higher energy density than conventional capacitors and higher power density than batteries[1,2].

What is more, in energy storage devices such as batteries or supercapacitors, binders are quite often an inherent element, which does not support the energy storage process, but plays role in improving physical contacts. However, their use also contributes to the deterioration of some parameters of the device, causing the reduction of volumetric and gravimetric capacitance. Its presence also may contribute to the occurrence of side reactions during the charging and discharging processes, usually leading to additional costs, and in the case of the binders such as polyvinylidene fluoride, an additional increase in the resistance value may be observed[3,4]. Therefore, the synthesis of the electrode material directly on the current collector is an eminently desirable process in obtaining the superior overall performance of the energy storage device.

* Corresponding author.

E-mail address: zuzanna.zarach@pg.edu.pl (Z. Zarach).

<https://doi.org/10.1016/j.electacta.2022.141389>

Received 25 August 2022; Received in revised form 14 October 2022; Accepted 16 October 2022

Available online 20 October 2022

0013-4686/© 2022 The Author(s). Published by Elsevier Ltd. This is an open access article under the CC BY-NC-ND license (<http://creativecommons.org/licenses/by-nc-nd/4.0/>).

Transition metal dichalcogenides, in particular, are gaining more and more attention in terms of their use as energy storage electrode materials, precisely because of their layered structure and the weak van der Waals bonds between the individual layers [5,6], which enable fast charging and discharging, while maintaining stability comparable to that offered by two-dimensional carbon materials [7–9]. MoS₂ structure consists of three planes in the order of S-Mo-S, with molybdenum sandwiched between two sulfur layers [10] (see Fig. 2a,b). Depending on which phase of MoS₂ is investigated, it is characterized by distinctive features. When it comes to energy storage applications, the most attention is paid to the 1T trigonal and the 2H hexagonal MoS₂ structure. Octahedral 1T phase is a metallic one, which is mainly obtained through the transition from the 2H phase by an electron beam application, laser irradiation, or ion intercalation process [11–13]. Obtaining a 1T phase is particularly desirable and the research is directed toward this one mainly due to its high conductivity, although its stability is still a challenge to face. On the contrary, the 2H phase, which is a trigonal prismatic structure, possesses semiconductive properties and exceeds other polymorphs in terms of stability. Sakar et al. reported molybdenum sulfide electrode material, containing both 1T and 2H phases, that exhibited a volumetric capacitance of 212 F cm⁻³ and even 343 F cm⁻³ when it was combined with reduced graphene oxide [14]. Furthermore, a thin film of MoS₂ obtained by Pujari et al. using low temperature soft chemical synthesis approach was characterized by the volumetric capacitance of 911 F cm⁻³ [15]. MoS₂ synthesis through DC sputtering was also shown to be an effective way to obtain thin, nanostructured films of specific capacitance of 138 F g⁻¹ and the cycling ability of 86% after 5 000 cycles [16]. In another report by Acerce et al. [17], metallic 1T MoS₂ phase exhibited the volumetric capacitance ranging from 400 to 700 F cm⁻³, depending on the aqueous electrolyte that had been used.

When characterizing electrode materials for energy storage, a commonly used counter electrode is platinum, also for materials with other applications, such as electrochemical hydrogen evolution reaction (HER), photoelectrochemical water splitting and amperometric sensors. It is well known that, due to its excellent electrochemical inertness, electrical conductivity and mechanical stability, platinum is considered to be one of the most appropriate materials for use as a counter electrode in electrochemical measurements. However, Cervino et al. were the first to describe that platinum may undergo dissolution at high anodic potentials in an acidic environment [18]. The influence of polarization on the dissolution was also observed by some other authors, as well [19–21]. Apart from that, there are other several factors that may affect the rate of Pt dissolution like temperature, scan rate, and potential range [22–26]. Moreover, some recent reports on the use of a Pt electrode in HER measurements also indicate that the Pt electrode may undergo an electrochemical dissolution-deposition process and thus greatly affect the experimental results [19,27–29]. As a matter of fact, the phenomenon of platinum dissolution has already been widely studied in relation to fuel cells application, and recently the issue has also been raised by Wei et al. questioning its use as a counter electrode in HER measurements [30], but it was also pointed by Jerkiewicz [31] that a great deal of the knowledge regarding platinum electrochemistry is undocumented. Furthermore, many reports not only on MoS₂, but also other transition-metal dichalcogenides, as well as carbon materials indicate that the dissolution-deposition phenomenon of Pt but also the doping itself can be used to improve the properties of an electrode material [20, 21,32–36]. However, most reports on this topic primarily deal with hydrogen evolution reactions and thus, we believe that this is the first time when the phenomena is observed in the electrochemical measurements performed for electrode materials with application for energy storage in supercapacitors.

Furthermore, there are no reports about a change in the chemical composition of the material upon Pt doping and/or repetitive cycling. In the literature, MoS₂ conversion to MoO₃ was reported by Ko et al. [37], using plasma oxidation. The transformation was also obtained by ambient pressure X-ray photoelectron spectroscopy combined with heat

treatment [38]. Recently Hou et al. investigated the phase transition of MoS₂ during sodiation in charge/discharge cycles, indicating that one of the intermediate products is metallic Mo, some of which oxidizes during the charging process, resulting in MoO₃ and oxygen-deficient MoO_x [39]. The presence of molybdenum oxides in electrode materials for energy storage has been extensively considered due to their promising specific capacitance, multiple oxidation states, and environmental friendliness. Especially when it comes to molybdenum oxides with intrinsic oxygen vacancies, they are highly attractive as they are characterized by greatly increased conductivity [40,41] but which was also presented by Dunn et al., oxygen vacancies facilitate faster charge storage kinetics, leading to improved capacitance and cycle life [40]. Furthermore, it is often recognized that molybdenum-based oxides have limited cycle life and poor performance hinders the application for long-term energy storage applications. To increase capacitance retention, several approaches are being introduced. As an example, Cai et al. stated that by introducing K⁺ into the MoO_x structure, it was possible to shift from Mo⁵⁺/Mo⁶⁺ to Mo⁴⁺/Mo⁵⁺ charge storage redox couple. As a consequence, both the conductivity and the overall electrochemical performance were enhanced, altogether with the prolonged cycle life of the supercapacitor [42].

In most of the cases observed with MoS₂-based materials for energy storage applications, the material degrades after repeated charging and discharging cycles, resulting in a decreasing capacitance. The phenomenon of capacitance increase was observed in several literature reports, however, it was temporary and only observed in the initial charge and discharge cycles [43], as generally for MoS₂-based electrode materials it is typical to observe a gradual degradation of specific capacitance with subsequent cycles, which is a major limitation in long-term energy storage applications. The exception is the work presented by Bissett et al., who reported a significant increase in capacitance during the first 3 000 cycles for MoS₂/graphene composite, which was attributed to the progressive exfoliation of the material, associated with ion intercalation/deintercalation [44]. Furthermore, little work has so far analyzed what happens to the material during charge/discharge cycles. Several reports only indicate phase transition occurring during the intercalation and deintercalation of lithium or sodium ions in the materials used in battery applications, including MoS₂-based materials [45–48]. Nonetheless, no detailed investigation of the changes taking place in the material during charge/discharge cycles was performed together with the analysis of the charge storage mechanism, with the simultaneous observation of the phenomenon of a significant increase in specific capacitance.

Therefore, in this work, several approaches to the synthesis of molybdenum-based electrode materials for supercapacitors are shown, including anodization, hydrothermal process, and annealing. Furthermore, we present a complex analysis of the Pt-surface modification during multiple charging and discharging cycles of the electrode material prepared via anodization of a molybdenum plate, followed by a hydrothermal process in thiourea aqueous solution with the energy storage mechanism study. The influence of platinum-surface modification and using platinum as a counter electrode on charge storage performance and charge storage mechanism in studied electrode material is investigated as well. It was shown that the prolonged process of modification of the electrode surface with platinum enhanced the phenomenon of the capacitance increase. After 60 000 cycles, the specific capacitance of the electrode material modified with Pt particles increased to over 1 F cm⁻², whereas the symmetric two-electrode system reached a capacitance of 140 mF cm⁻² and in each case, the coulombic efficiency was above 97% during all the cycles. Furthermore, this study reveals the changes taking place in the composition of the molybdenum disulfide thin layer, presenting the transition to mixed molybdenum oxides. Together with the transition from sulfides to oxides and introduction of oxygen vacancies, the contribution of the pseudocapacitive energy storage mechanism is enhanced. It is also emphasized that when Pt counter electrode is used in the study of energy storage materials,

careful consideration should be given to the investigation due to the dissolution-deposition phenomenon of platinum.

2. Experimental section

Chemicals used: Molybdenum (Mo) foil (0.05 mm thick, 99.95%) (Alfa Aesar) was sonicated in acetone (C_3H_6O) and isopropanol (C_3H_7O) (both obtained from Chempur). The electrolyte for the electrochemical oxidation of titanium foil consisted of ammonium fluoride (NH_4F) p.a., ethylene glycol ($C_2H_6O_2$), phosphoric acid (H_3PO_4), all from Chempur, and distilled water. Thiourea (CH_4N_2S) used in the hydrothermal method and potassium sulfate (K_2SO_4) was purchased from Alfa Aesar and sulfuric acid (H_2SO_4) (p.a. 95%) used for electrochemical characterization was received from POCH.

Anodization of Mo foil: At first, molybdenum foil was cut into pieces, cleaned using ultrasonic treatment in isopropanol:acetone mixture (1:1 v/v) for 10 min, and eventually rinsed with distilled water. In the anodization process, the as-prepared Mo foil constituted an anode and the titanium plate was a cathode. The synthesis was carried out at a constant temperature (23 °C) using a cooling bath thermostat (KISS K6, Huber) with a voltage of 5 V applied for 2 h and the electrolyte was prepared according to the previous report [49].

Hydrothermal synthesis: The final step of electrode preparation was to perform a hydrothermal procedure. For this, an anodized molybdenum plate was placed in a Teflon-lined stainless-steel autoclave (50 mL) with thiourea (1 M) aqueous solution (25 mL). The autoclave was transferred to an oven for 24 h at 200 °C. After that, the autoclave was cooled to room temperature and the obtained plate with deposited molybdenum-based material was washed a few times with ultrapure water.

Different approaches for Mo foil modification: Apart from the electrode material that was obtained as described above, some different approaches of molybdenum foil modification were included, namely, anodic oxidation (A), hydrothermal process (H) and annealing (A450) of modified molybdenum plate were combined in different order and combination, which is accurately presented in Fig. S1. The samples were designated by the letters ascribed to the individual processes in the order in which they were carried out (e.g. Mo(AH) denotes to anodization followed by the hydrothermal process). The annealing process was performed in a tube furnace in an air atmosphere with a heating rate of 2 °C/min for over 3 h and 45 min to 450 °C and eventually hold at this temperature for 2 h.

Electrochemical Pt-surface modification: Electrochemical modification of the surface with platinum particles was carried out in a three-electrode system. The working electrode was a chosen Mo-based material and the Pt electrode was used as a counter electrode. Pt (99.9%) was in the form of a 1 cm x 1 cm mesh with a wire diameter of 0.04 mm and with a nominal aperture 0.12 mm. The modification was based on repetitive cycling in 1 M H_2SO_4 in the potential range from -0.35 V to +0.2 V vs. Ag/AgCl (3 M KCl). Up to 60 000 cycles were carried out to investigate the changes taking place in the structure of the electrode material. For comparative purposes, the material that was not modified with platinum particles was tested in a system in which the working electrode was separated from the counted electrode using an electrolytic key filled with gel electrolyte, which was 0.5 M K_2SO_4 with the addition of gelatin.

Materials Characterization: The morphology of the as prepared materials was investigated using Scanning Electron Microscopy (SEM) (FEI, Quanta 3D FEG) and Transmission Electron Microscopy (TEM) (FEI, Tecnai F20X-Twin). Element identification was performed by energy dispersive X-ray spectrometer (EDS) with energy resolution of 134 eV (EDAX, model RTEM SN9755+). SEM samples were tested directly on the synthesized molybdenum foil without preparation. Samples for TEM, after peeling off the layer from the molybdenum foil, was placed on a copper TEM grid covered with a carbon layer (Lacey type Cu 400 mesh, Plano). Measurement parameters: SEM - voltage 10–20 kV from FEG, Everhart-Thornley detector (ETD), vacuum in the chamber 10^{-4}

Pa; TEM – voltage 200 kV from FEG, imaging in bright field (BF) with CCD camera (Gatan, Orius), vacuum in the chamber 10^{-4} Pa. Moreover, materials were characterized using X-ray Photoelectron Spectroscopy (Escalab 250Xi, Thermo Fisher Scientific) with Al K α radiation and the spectra were analyzed and deconvoluted by an envelope of a Gaussian-Lorentzian sum function using the spectrometer software Advantage (Version 5.973). The vibrational characteristics of the samples were studied using micro-Raman spectrometer (Renishaw InVia) with argon laser emitting at the wavelength of 514 nm and operated at 1% of its total power (50 mW). The determination of crystal structure was performed using a diffractometer (Xpert PRO-MPD) with Cu K α emission (λ = 0.15406 nm).

Electrochemical measurements: At first, they were performed using potentiostat/galvanostat (BioLogic VSP 2078) in three-electrode configuration. The measurements were performed in 1 M H_2SO_4 with the as synthesized electrode materials constituted as a working electrode and Pt mesh and Ag/AgCl (3 M KCl) were used as counter and reference electrode, respectively. Measurements were conducted in 1 M H_2SO_4 aqueous solution, which was used as an electrolyte for a super-capacitor's construction, too. Moreover, electrochemical impedance spectroscopy (EIS) was performed in a frequency range between 20 kHz and 100 mHz with the voltage amplitude of 10 mV. For the chosen material's characterization, various techniques have been applied, e.g. galvanostatic charge-discharge tests (GCD) with current densities ranging from 4.5 to 34 mA cm $^{-2}$, and cyclic voltammetry at 50 mV s $^{-1}$ in order to determine the potential range within which an electrode material is capable of charge storage.

3. Results and discussion

3.1. Characterization of the electrode materials resulted from different Mo foil modifications

Fig. 1 presents images of molybdenum foil before (Fig. 1a–b) and after different modifications, obtained using Scanning Electron Microscopy. In comparison with non-modified molybdenum foil, different morphologies might be observed. In the images obtained at lower magnifications, the initial structure of the molybdenum foil, which is caused by the metal processing, can be observed. Moreover, the anodic oxidation process caused the formation of a rough and rippled surface structure (Fig. 1c–d). The pattern is also clearly visible for the electrodes for which anodization was the first stage of the modification. On the other hand, when Mo foil was subjected to a hydrothermal process, the film that was formed almost uniformly covered the entire surface, and the formation of moss-like nanostructures was observed (Fig. 1e–f). The moss-like covering of the surface is also visible for samples Mo(AH) (Fig. 1g–h) and Mo(AA450H) (Fig. 1i–j). Furthermore, when the annealing process was performed as the last stage, the formation of crystal structure in the form of cuboids and cubes is distinguished (Fig. 1k–l).

X-ray Photoelectron Spectroscopy measurements were also performed for the prepared samples (see Fig. 2c–l). For the anodized sample (Fig. 2c and 2h) spectra show that the material consists of molybdenum oxides of various oxidation states, which is quite common for the anodized molybdenum foils reported in the literature [50,51]. A confirmation may be the signal distinguished in the O1s spectrum at about 530.5 eV, which proves the presence of Mo–O bonds in the sample [52,53]. O1s spectrum reveals the presence of both hydroxide and water in the sample [54–56], which is also observed for the molybdenum foil after anodization and annealing (see Fig. 2f and 2k). The difference between both samples results from the uniformity of the molybdenum oxidation state, namely an almost complete transition to the 6+ oxidation state is observed after annealing. Recorded signals of Mo 3d $_{5/2}$ and 3d $_{3/2}$ at around 233 eV and 233.1 eV may be assigned to the presence of MoO $_3$ [57,58], which was also confirmed by Raman spectroscopy. For the remaining samples, the synthesis of which took into account the

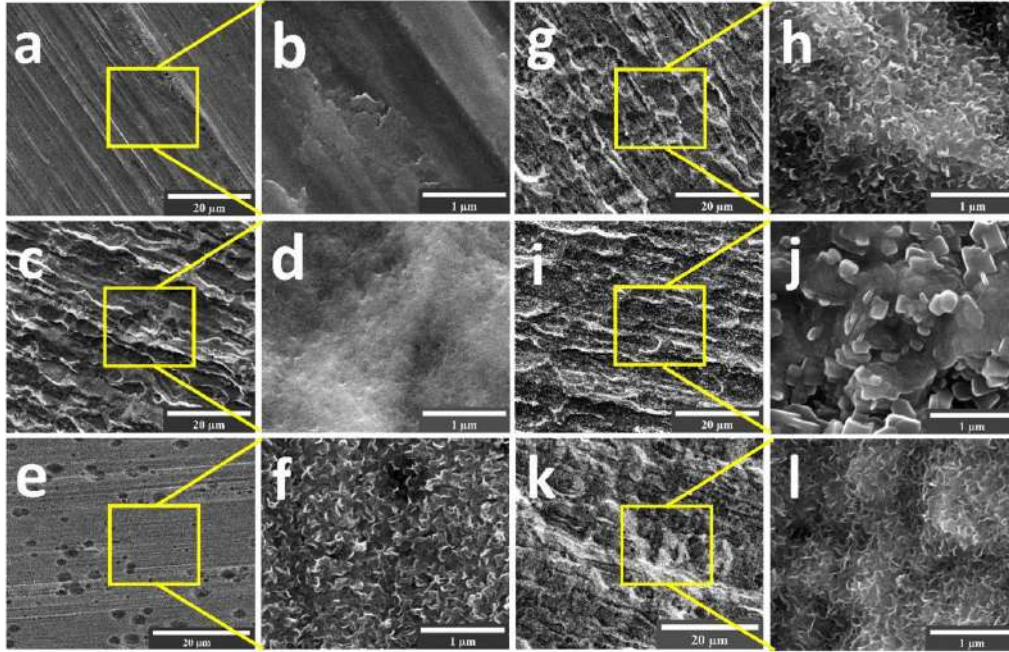


Fig. 1. SEM images for Mo foil before modifications (a-b) and after anodization Mo(A) (c-d), hydrothermal process Mo(H) (e-f), anodization and hydrothermal processes Mo(AH) (g-h), anodization and annealing Mo(AA450) (i-j) and subsequent anodization, annealing and hydrothermal processes Mo(AA450H) (k-l).

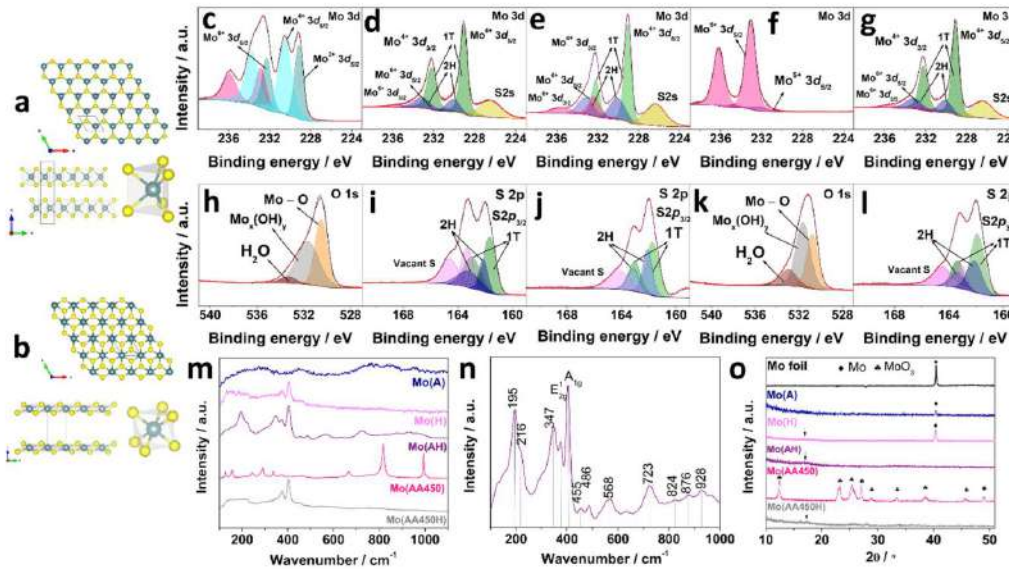


Fig. 2. Top and side views of a) 2H and b) 1T structures of the MoS_2 and the presentation of the trigonal prismatic coordination in 2H- MoS_2 and the octahedral coordination in 1T- MoS_2 for the molybdenum atom (cyan). Crystal structures created with VESTA 3 software[69]. XPS spectra of Mo foil after different modifications: Mo(A) (c,h); Mo(H) (d,i); Mo(AH) (e,j); Mo(AA450) (f,k); Mo(AA450H) (g,l); m) Raman spectra of Mo foil after different modifications with detailed spectrum (n) for the electrode material Mo(A) and Mo(AH); o) XRD spectra of Mo foil after different modifications with the magnification of the area between 10 and 50° .

hydrothermal process, the results clearly indicate that each of them contains mainly MoS₂. This is confirmed by the results presented in the Mo 3d spectra of Mo(H), Mo(AH) and Mo(AA450H) samples (see Fig. 2d, e, g), where two peaks at around 232.2 and 229.0 eV are related to the 1T MoS₂ phase, whereas the signals at 233.2 and 230.1 eV confirm the presence of 2H phase [14,59]. Worth noting is that the shift of 1T phase is about 1 eV from the 2H phase, which is consistent with the literature reports in each case [14,60]. At the same time, the S 2p_{1/2} and 2p_{3/2} signals (Fig. 2i, j, l) from 1T and 2H phases are located at 163.0 and 161.7 eV, and 163.2 and 162.1 eV, respectively [59,61]. Furthermore, the peaks located in the higher binding energy the S 2p spectrum may correspond to the vacant S atoms in both 1T and 2H phases [62,63]. The results also show the signals coming from molybdenum in its oxidized form (Mo⁶⁺), which is present in small amounts in the form of molybdenum oxide [58,61].

The as-modified molybdenum-based electrode materials were also characterized using Raman spectroscopy. As it is shown in the Raman spectrum in Fig. 2m, Mo after anodization (A) is rather amorphous. When molybdenum foil was subjected to both anodization and hydrothermal process (AH), a significant amount of distinct signals can be observed in the Raman spectrum. The two most characteristic peaks at 375 cm⁻¹ and 404 cm⁻¹ can be attributed to the vibrations in thermally stable 2H-MoS₂ molecules, which are ascribed to E_{2g} in-plane and A_{1g} out-plane active modes, respectively [14,59,62,64]. Those signals are also observed for the sample Mo(H), indicating the presence of 2H-MoS₂, as well. Apart from those two prominent signals, some additional peaks at spectrum of Mo(AH) could be distinguished at 195, 216 and 347 cm⁻¹ that indicate the presence of the trigonal phase of MoS₂ in the analyzed sample [14,64–66]. Moreover, weak Raman modes in the range from 445 to 930 cm⁻¹ may suggest that the material contains a minor amount MoO₃ molecules in the intermediate oxidation state, where 2 < x < 3 [67]. In order to present the Raman bands of Mo(AH) more clearly, this spectrum has also been presented in a separate figure (Fig. 2n). After modification in the form of anodization with annealing (AA450), a crystalline MoO₃ was obtained, which was confirmed by the presence of the main band at about 820 cm⁻¹, attributed to the stretching vibrations in Mo–O–Mo [57]. Another characteristic peak at 996 cm⁻¹ is strictly related to the stretching vibration of Mo=O, whereas a maximum at 665 cm⁻¹ refers to a triply coordinated bridging oxygen stretching mode of α-MoO₃. Furthermore, Raman modes that are located below 400 cm⁻¹ are assigned to various bending vibrations and lattice modes of MoO₃[57,68]. For the last sample (AA450H), there are two intense peaks at about 400 cm⁻¹, which are characteristic of vibrations in MoS₂ molecules and are already described above. For samples (H) and (AA450H) the peaks indicating the presence of the trigonal phase of MoS₂ are not clearly seen, probably due to their smaller amount in the sample. Summing up, it can be stated that anodization causes the formation of an amorphous oxide layer, annealing generates crystalline MoO₃, whereas the hydrothermal process allows obtaining MoS₂ (from both the native oxide from anodization and the crystalline one).

The XRD patterns of the studied materials are shown in Fig. S2 (Supplementary Information) and Fig. 2o. Fig. S2 shows the whole pattern in the full range obtained for the prepared samples. Due to the fact that the performed synthesis leads to the deposition of thin layers directly on the surface of the current collector, the recorded signal comes mainly from the molybdenum substrate. However, when the diffractogram area between 10 and 50° is magnified, some signals may be distinguished, especially for the (AA450) sample. The results are consistent with the Raman spectroscopy, namely, the layer consists of MoO₃ [70–72]. Furthermore, for the Mo(A) and Mo(H) samples a signal at 39° from the molybdenum substrate may be identified. However, for the anodized sample, its intensity is relatively lower than for the sample that was not subjected to the anodization process. The reason is that the anodization process and subsequent modifications influence the crystal structure of molybdenum foil and thus the signal from the (110) plane fades [73], which is also visible in the XRD results of the other electrode

materials. It can be simply explained by the growth of the film on the molybdenum surface, suggesting that this plane is privileged and the amorphous MoO₃ film is formed. Furthermore, the other samples seem to be characterized by an amorphous nature as the lack of signals may be observed. It is also worth noting that for the material's modifications that included a hydrothermal process, a weak signal at around 17° may be observed. However, due to the fact that the indicated signal is characterized by very low intensity, the authors note that this may only suggest the presence of MoS₂ as this is the value at which the (002) phase signal of 2H MoS₂ is usually observed [65,74–77]. It may also be stated that the broadening and low intensity are due to the ultrathin dimensions of MoS₂ and low crystallinity [78].

3.2. Electrochemical evaluation of the Mo-based electrode materials

In order to investigate the electrochemical performance of the electrode materials, cyclic voltammetry was applied. It is clearly seen in Fig. 3a that the widest potential range with electrochemical activity and with no occurrence of hydrogen reduction at cathodic scan, as well as the highest current density values were obtained for the Mo(AA450) electrode material, at least during the first few scans. It has to be mentioned that Mo(AA450) exhibits a drastic drop in electrochemical activity at the beginning of electrochemical tests and thus, the experiment performed at different scan rates was performed after several cycles in order to achieve some stability. It has already been reported that under repetitive charging and discharging, MoO₃ undergoes irreversible structure changes and as a result, poor kinetics and fast capacitance fading are observed [79–81]. Moreover, the cathodic limit of system stability is shifted towards more anodic potentials. Similar behavior was already shown and utilized for the modification of MoO₃-based electrodes for HER [82]. Cyclic voltammetry curves recorded at different scan rates for individual electrode materials are included in Supplementary Information (see Fig. S3, Supplementary Information). In order to investigate how the capacitance of each electrode material changes with a scan rate, cyclic voltammetry measurements with scan rates from 2 to 500 mV s⁻¹ was performed, and the results are shown in Fig. 3b. For each material the capacitance was calculated according to Eq. (1) by analyzing the area under the CV curve, which is strictly related to the amount of charge stored by the electrode:

$$C = \frac{\int I(V)dV}{2v \Delta V} \quad (1)$$

Where $\int I(V)dV$ is the total voltammetric charge calculated by integration of positive and negative sweep in the potential window, v is a scan rate and ΔV is the potential window width. For the Mo(AA450) electrode material when increasing the scan rate, a rapid decrease in capacitance is observed, see Fig. 3b. This phenomenon can be due to the decomposition process of the electrode material and therefore its instability, especially observed when increasing the scan rate value. Moreover, at higher scan rates, the slower processes are kinetically hindered and cannot participate in a charge transfer onto or across the electrode/electrolyte interface, which is reflected by lower electrochemical capacitance [83–85]. The capacitance values of Mo (AA450) for the highest scan rates were even lower than for the Mo(AH) electrode material, which was also characterized by high capacitance values, especially in comparison with other molybdenum-based materials. Another advantage of the Mo(AH) may be observed in the EIS spectra, presented in Fig. 3c. Knowing that the reactance (Z'') can be described by Eq. (2):

$$Z'' = -\frac{1}{2\pi fC} \quad (2)$$

where f is the frequency and C is the capacitance value, the Mo(AH) electrode material may offer the most promising capacitive properties. Also, the equivalent series resistance (ESR) is the parameter that may be

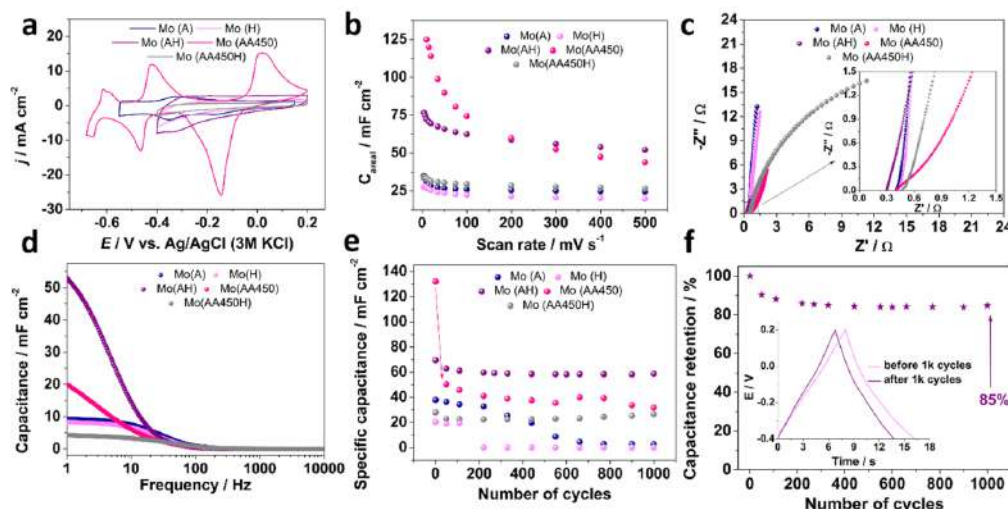


Fig. 3. a) CV curves recorded in 1 M H₂SO₄ ($v = 50 \text{ mV s}^{-1}$) for Mo foil modifications; b) Areal capacitance in a function of a scan rate; c) Nyquist plots in a frequency range from 20 kHz to 100 mHz in 1 M H₂SO₄; d) specific capacitance in the function of applied frequency; e) Changes of specific capacitance during 1 000 cycles and f) changes of specific capacitance retention during 1 000 cycles for the Mo(AH) electrode material; inset: GCD curves before and after 1 000 cycles for the Mo(AH).

described as the intercept with the x-axis and its value depends not only on the electrolyte resistance, but also includes the electrode resistance and the contact resistance between the electrode material and the current collector [86]. Therefore, it may be concluded that the Mo(AH) electrode material is characterized by the lowest value of its internal resistance. Furthermore, a Nyquist plot for both (AA450) and (AA450H) materials in a low-frequency range has a flatter slope and therefore a smaller value of the phase angle, and in the high-frequency range, an appearance of a semi-circle forming might be observed, indicating that the charge transfer resistance arises and hinders the mobility of the ions [87]. A lack of the semicircle in the high-frequency range confirms that there is no ion adsorption/desorption on the electrode material surface coupled with electron transfer to the surface [88]. Moreover, especially in the case of Mo(A), Mo(H), and Mo(AH) electrode materials a line rising up vertically at a low-frequency range may be distinguished, pointing to the capacitive nature of the materials. However, the capacitance value for the Mo(AH) is considerably higher compared to other modifications (Fig. 3d) and the material is characterized by the best charge propagation in the range of very low frequencies, even lower than 1 Hz. Furthermore, capacitance values obtained from the electrochemical impedance spectroscopy measurements also confirm the loss of electrochemical activity of MoO₃ in the Mo(AA450) sample along with subsequent electrochemical measurements.

Initial charge and discharge measurements (GCD) were carried out for each material at different current densities applied (in a 3-electrode system). Prior to the cycling measurements, for each material the most optimal value for the applied current was selected, namely both charge and discharge time should be equal and not exceed 10 to 15 s – exemplary GCD curves are shown in Supplementary Information in Fig. S4 (Supplementary Information). Then, at the selected current values, 1 000 charge and discharge cycles were performed, on the basis of which specific capacitances were calculated and presented in Fig. 3e. The results of GCD measurements are consistent with the cyclic voltammetry results presented above, especially when comparing the capacitance obtained at the 1st cycle with the values in Fig. 3b. The Mo(AA450) electrode material was characterized by the highest specific capacitance value, however, as the charging and discharging cycles progressed, a sharp decrease in capacitance was observed after the first 50 cycles, and

capacitance retention after 1 000 cycles was just about 24%, see Fig. 3e. A rapid drop was also observed in the case of the Mo(H) electrode material (after 100 cycles), which was no longer characterized by capacitive properties. The loss of energy storage capacity is also seen in the case of molybdenum foil after anodization (Mo(A)). The highest capacitance retention was noticed for Mo(AA450H) which was at about 95%. However, for the Mo(AH) the capacitance value was even twice higher, namely 70 mF cm^{-2} , and the capacitance retention was at 85%, which is presented in Fig. 3f. Moreover, the inset in Fig. 3f shows that even after performing 1 000 charge-discharge cycles, a GCD curve preserved its triangular shape, without the increase of the ohmic drop.

With the aim to fully evaluate the electrochemical performance of the Mo(AH) electrode material and investigate the process of Pt-surface modification, an exceedingly large number of galvanostatic charge/discharge tests was performed with an initial value of current density of 4.5 mA cm^{-2} applied in the potential range from +0.2 V to -0.35 V. The cathodic potential limit was adjusted to -0.35 V in order to maintain the coulombic efficiency during cycles at the highest possible level. The resulting areal capacitance is presented in Fig. 4a and the inset shows the galvanostatic charge/discharge profile before (at 4.5 mA cm^{-2}) and after (at 34 mA cm^{-2}) 60 000 cycles. The results obtained up to 1 000 cycles are consistent with the ones presented above, while the phenomenon of a gradual increase in the value of the capacitance is observed during subsequent cycles, which is also confirmed by the inset in Fig. 4a, indicating an increase in both the charging and discharging time, while maintaining a shape that specifies capacitive properties. Due to the phenomenon of increasing capacitance, the value of applied current needed to be adjusted to maintain the appropriate charge/discharge time for supercapacitors, as well as to preserve a high level of coulombic efficiency during the subsequent cycles. Therefore, the current density was changed from 4.5 to 34 mA cm^{-2} which is presented in Fig. 4a. Furthermore, the gradual increase in the capacitance led to an increase in capacitance retention of around 1 000% after 60 000 cycles. Fig. 4b shows the value of coulombic efficiency, which remained at a very high level, averaging 100% during all cycles. The resulting capacitance increase was previously observed in the literature in the case of MoS₂-based electrode materials [43,44] and was e.g. explained by the activation process that takes place and enables the electrolyte

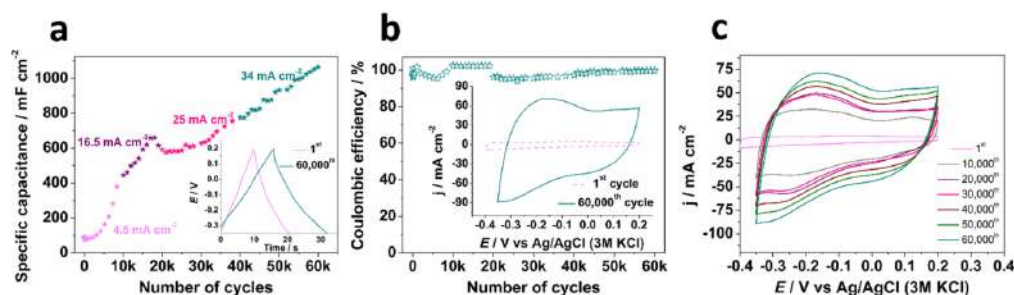


Fig. 4. a) Areal capacitance calculated on the basis of 60 000 GCD cycles for the Mo(AH) with the current adjustment during cycles; inset: GCD curves before and after 60 000 cycles, b) coulombic efficiency during 60 000 cycles; inset: CV curves before and after the measurements, c) CV curves for the Mo(AH) electrode material after subsequent cycles ($v = 50 \text{ mV s}^{-1}$).

diffusion into the interlayers of MoS_2 . Moreover, Fig. 4c presents the cyclic voltammetry curves after subsequent cycles, and it can be seen that the value of the current density increased significantly, especially in the negative potential range. As far as the authors are concerned, this is the highest capacitance value obtained for MoS_2 -based electrode materials, but also one of the highest values for all supercapacitor materials.

3.3. Investigation of the increasing capacitance and the influence of the electrochemical dissolution-deposition process of Pt

In order to determine the cause of the constantly increasing capacitance and to investigate possible changes that took place in the morphology of the electrode material, additional SEM measurements were carried out after 15 000 charging and discharging cycles. As can be seen in Fig. 5a-d, the electrode's morphology after multiple charge/discharge cycles is markedly different from that of the Mo(AH) electrode material (see Fig. 1g-h). SEM images clearly show the delamination of the material, which is in striking contrast to that of the Mo(AH) before electrochemical measurements. In some previous studies [89–92] the electrochemical treatment has been demonstrated to be one of the techniques that leads to the exfoliation of the material. According to the literature, an exfoliated material is said to be characterized by a higher electrochemical capacitance compared to a bulk material [93–97]. Therefore, it may be concluded that the main cause of the increase in

material's capacitance is the exfoliation process that takes place during the charge/discharge cycles. In fact, both of those effects were reported previously by Bissett et al. [44], finding the increase of the capacitance as a result of ion intercalation and partial exfoliation. The fact that the material may change during energy storage should be taken into account especially in the case of materials characterized by a layered structure with Van der Waals interactions, namely graphene and both transition metal oxides and dichalcogenides.

The SEM images obtained at higher magnification (see Fig. 5b-d) show changes that occurred in the electrode material during multiple charge/discharge cycles. In the structure of the material, one can observe particles embedded in the layer that were not present in the as-prepared material. The results of the EDS analysis (see Fig. S5a, Supplementary Information) and mapping results presented in Fig. 5e-h clearly indicate the presence of Pt particles embedded at the surface of the Mo(AH) electrode material. Even though the phenomenon of Pt dissolution-deposition has been discussed in a number of reports, still no universal mechanism describing the phenomenon was presented. Nevertheless, it may be assumed that the crucial parameter is the polarization potential of the Pt counter electrode. During galvanostatic charge/discharge cycles performed in a three-electrode configuration, the working electrode was cycled in the potential range from +0.2 to −0.35 V. Simultaneously, a potential of Pt CE was also recorded and one can see that it was polarized from 1.55 V to around −0.3 V (vs. Ag/AgCl

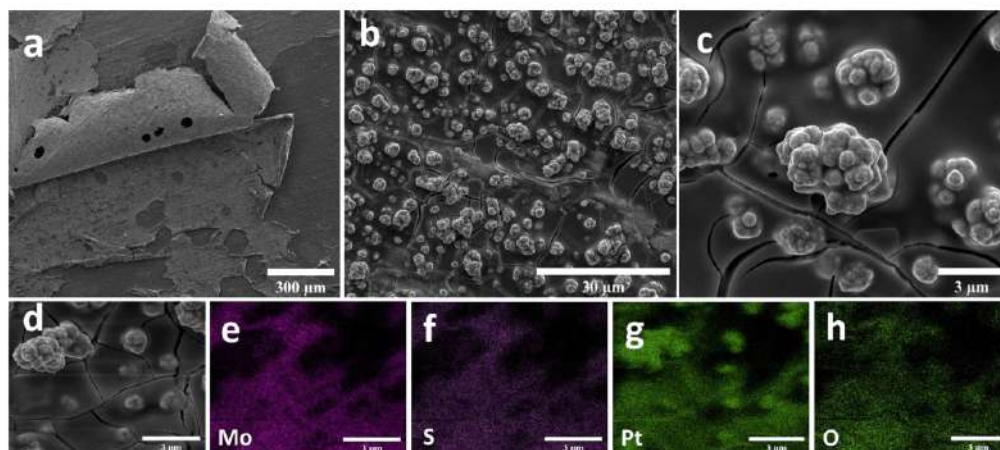
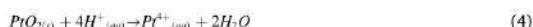
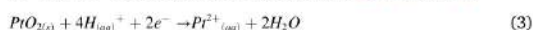


Fig. 5. a-c) SEM images and d-h) EDS mapping results for the Mo(AH) electrode material after 15 000 GCD cycles.

(3 M KCl) (see Fig. S5b, Supplementary Information). According to the literature reports, the oxidation and reduction of platinum occur principally after reaching high potential values during polarization, but the most intensified dissolution and deposition of Pt may occur during reversible cycling within a certain potential range, enabling repetitive oxidation and reduction of Pt [19,20,98]. Topalov et al. [99], proposed that the oxidation of the Pt surface takes place about +1.15 V (vs. RHE) and as the potential value increases, the creation of a sub-surface oxide may occur, as well. The latter's presence is crucial during cathodic sweeping, as it contributes to the weakening of Pt–Pt bonds and as a consequence, during repetitive potential cycling, PtO₂ undergoes subsequent chemical and electrochemical dissolution [29]. Furthermore, oxygen atoms may distort the surface lattice through tunneling into the deeper layers and triggering the dissolution [100,101]. As a result, both Pt²⁺ and Pt⁴⁺ ions are generated, according to Eqs. (3) and (4):



To the best of our knowledge, this is the first time when the phenomenon is observed in the electrochemical measurements performed for electrode materials with the application for energy storage in supercapacitors. The reason for this may be both the fact that, in the case of the analyzed electrode material very high current densities are obtained, as well as the fact that there is little research in the literature on electrode materials for supercapacitors that thoroughly investigate the changes taking place in the material during multiple charge/discharge cycles. Therefore, bearing in mind Wei's et al. critical approach to the use of platinum electrode in HER measurements[30], authors would like to emphasize that when a Pt counter electrode is used in the study of energy storage materials, careful consideration should be given to the investigation, as well. Therefore, in order to make sure whether the incorporation of platinum into the material affects its overall performance, galvanostatic charge/discharge tests were performed with the separation of the working electrode from the counter electrode, and the results are presented in Fig. S6. Based on all the results presented above, the Mo(AH) material with Pt-surface modification was further investigated and from this moment, it was designated as Pt@1T/2H-MoS₂, whereas the electrode material that was not subjected to the Pt-modification was designated as 1T/2H-MoS₂.

The obtained results indicate, that despite the absence of Pt on the surface of the working electrode, an increase in capacitance is still observed, but it is almost two times smaller than in the case of dissolution and deposition of platinum (Fig. S6a). Moreover, no matter how the measurement system was designed, the electrode material still has an almost ideal coulombic efficiency (Fig. S6b), and the GCD curves retain a triangular shape (inset of Fig. S6a). The phenomenon of increasing capacitance is also confirmed by the EIS results presented in Fig. S6c. A slightly increasing slope of the curves indicates an improving capacitive behavior [102], while a gradually decreasing value of the imaginary element of impedance additionally confirms these observations, in accordance with Eq. (2). The absence of platinum on the surface of the electrode material was confirmed by SEM and XPS analysis performed after 15 000 charge-discharge cycles (see Fig. S7, Supplementary Information). The chemical composition of the sample remained almost unchanged, only the presence of traces of SO₄²⁻ was observed. In the case of the morphology of the surface, moss-like nanostructures are still present and visible as before the cycles, but the surface has become more solid with numerous cracks. However, the obtained results may indicate that the process of dissolution-deposition of Pt significantly contributes to the acceleration of the activation process which results in a greater increase in the capacitance. On the other hand, when platinum is not present in the solution and thus the deposition does not occur, the activation process is slower. However, it can undoubtedly be said that Pt-assisted activation of the electrode material is beneficial in the energy

storage process.

For further analysis of the capacitance increase and a more thorough investigation of the Pt-surface modification, XPS analysis was performed in order to investigate the changes occurring in the Pt@1T/2H-MoS₂ electrode material during long-term cycles. As shown in Fig. 6, for the electrode material before cycles (0th) the Mo 3d spectrum shows that it is possible to distinguish two polymorphs of MoS₂, as it was confirmed with Raman spectroscopy results and described in the first part of the manuscript. With subsequent cycles, one can observe more intense peaks coming from Mo⁶⁺ at 233.3 and 236.4 eV [37] and a new pair of doublets coming from Mo⁵⁺ assigned to the peaks at 231.8 and 235.2 eV [39,103,104] (see spectrum after 3 000 cycles). The results indicate a decreasing and finally completely disappearing presence of both 1T and 2H-MoS₂ (see spectrum after 21 000 cycles). The transition of both 1T and 2H-MoS₂ into mixed non-stoichiometric molybdenum oxides also confirms the spectrum recorded for S2p, showing that with the successive cycles, S²⁻ is converted to SO₄²⁻ [39] (see Fig. S8, Supplementary Information). XPS analysis also confirmed the presence of platinum in the electrode material, mainly in the metallic form, but also small amounts of Pt²⁺ and Pt⁴⁺ were observed (see Fig. S8, Supplementary Information). Moreover, in the first part of repetitive cycling, one may see the increase of peaks assigned to Mo⁶⁺. According to the literature reports, a metal/metal oxide interaction should also be taken into consideration as it influences the conductivity and metal oxide's reactivity[103]. Small amounts of Mo⁶⁺ that are present in the sample after synthesis, probably related to the anodization carried out in the first stage of the synthesis, are reduced in contact with the metal substrate, and the metal is oxidized, which may also contribute to the increased amount of metal oxides observed in the material. Furthermore, with the increasing number of repetitive cycles, the amount of molybdenum oxides is increased at the expense of molybdenum sulfide, which is confirmed by XPS results after subsequent cycles as the dominance of molybdenum in the 5+ and 6+ oxidation state can be observed. With the elongation of galvanostatic measurements, the presence of reduced forms of molybdenum is noted – Mo⁴⁺ at 231.2 and 234.5 eV[105], as well as Mo⁶⁺ at 229.5 and 232.6 eV. Mo⁶⁺ relates to the oxidation states 0 < δ < 4 and may be related with the presence of oxygen vacancies in MoO₂ lattice [106,107]. Furthermore, as it was stated by Grainer et al., Mo⁵⁺ cations are also formed as a result of oxygen vacancy defects in MoO₃, and after a certain vacancy concentration is reached, Mo⁴⁺ cations develop [103,104]. Despite the appearance of molybdenum in the 4+ oxidation state, it is not a signal from the original MoS₂ compound, as no signal indicating the presence of sulfur was registered again, which indicates the formation of only oxygen compound of molybdenum (MoO_x) with mixed valence states. Furthermore, on the basis of the Mo-O phase diagram it can be stated that MoO₃ is not expected to equilibrate directly with Mo at Mo/MoO₃ interface, but the equilibrium may be reached between Mo and MoO₂ [108]. There are also several intermediate, non-stoichiometric molybdenum oxides with mixed oxidation states that may be stable in between MoO₃ and Mo. On this basis it may be concluded the results obtained after a major number of cycles are consistent with that, as we observe diminishing intensity of peaks related to Mo⁶⁺ and Mo⁵⁺ at the expense of lower oxidation states. Furthermore, in several reports it was stated that when Mo⁶⁺ is dominant in the sample, a material is characterized by a poorer conductivity, and with its subsequent reduction, the Mo 4d states that were empty are being filled with electrons, resulting in the increased conductivity [40, 42,102,104]. Carrying out subsequent cycles consistently increased the intensity of signals from forms on lower oxidation states, which is in agreement with the continually increasing capacitance.

Furthermore, the morphology of Mo(AH) electrode material before and after repetitive cycles was investigated using transmission electron microscopy and the results are presented in Fig. 7. The results for the sample before cycles (Fig. 7a-c) confirm the morphology observed at SEM images, namely curled nanoflake-like structure may be distinguished that is mainly amorphous. However, the crystalline structure of

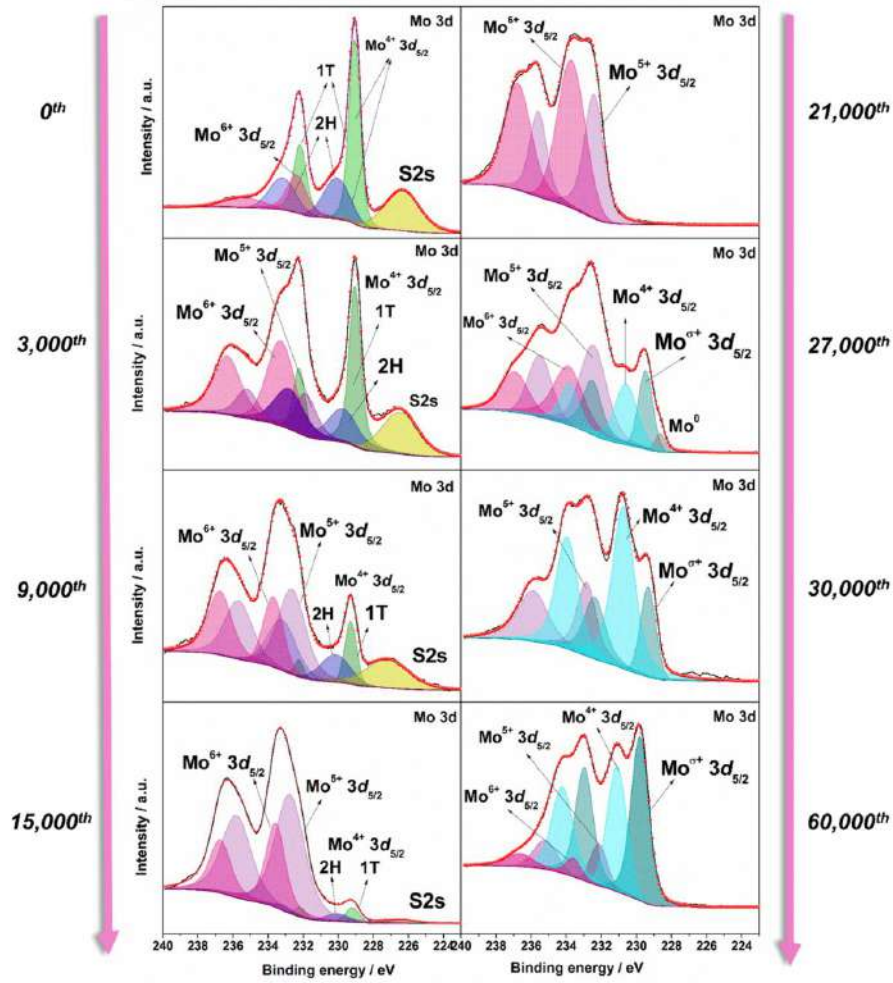


Fig. 6. XPS spectra of Mo 3d for the Pt@1T/2H-MoS₂ electrode material before and after subsequent (3, 9, 15, 21, 27, 30 and 60k) GCD cycles with Pt-surface modification.

MoS₂ may be observed on the edges of the structure, as well. For the Pt@1T/2H-MoS₂ material after 30 000 cycles, the results exhibit the presence of Pt particles in Pt@1T/2H-MoS₂ electrode material occurring as darker spots, which was also confirmed by EDS analysis (see Fig. 7d-f). What is more, when the cycles were performed with the separated WE and CE areas (see Fig. 7g-i), the morphology more closely resembles the one observed before the cycles.

3.4. Charge storage mechanism analysis

In order to properly classify the electrode material being used, it is essential to determine the mechanism through which the charge is being stored. One of the approaches to differentiate capacitances was firstly presented by Conway et al. [109], and followed by its application by Dunn et al. to analyze the charge storage mechanism of nanostructured transition metal oxides [110–112]. This method allows for quantitative

separating the contribution of the surface-confined elements from the diffusion-controlled processes responsible for charge storage by assuming that the total current response at a specified potential ($i(V)$) is the sum of the current related to surface controlled and diffusion-limited processes, according to the following Eq. (5):

$$i(V) = k_1 v + k_2 v^{1/2} \quad (5)$$

where $i(V)$ represents a measured current, k_1 and k_2 are constant values, and v is a scan rate. After transforming Eq. (5) to the form of Eq. (6), the obtained linear dependence with the slope (k_1) and Y-intercept (k_2) values enables to determine the contribution of the outer surface ($k_1 v$) and inner surface ($k_2 v^{1/2}$) to the total charge being stored at a given potential:

$$\frac{i(V)}{v^{1/2}} = k_1 v^{1/2} + k_2 \quad (6)$$

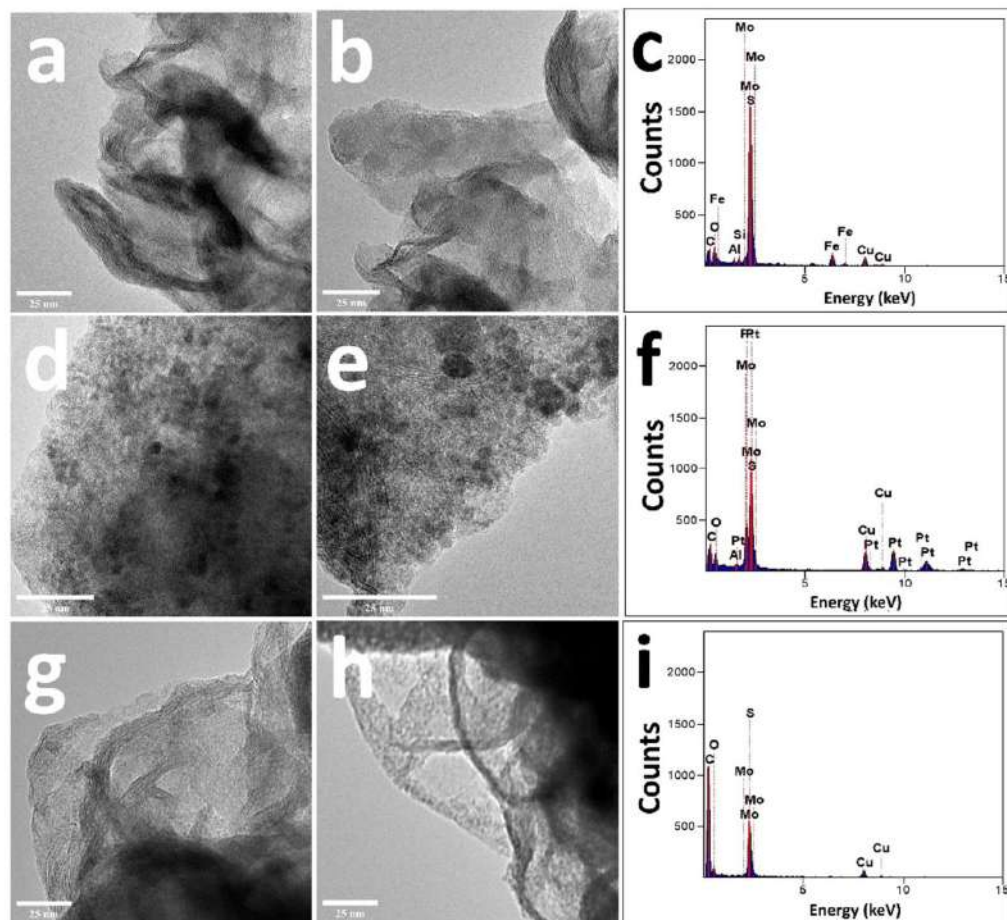


Fig. 7. TEM images and EDS spectra of a-c) Mo(AH), d-f) Pt@1T/2H-MoS₂ after 30 000 cycles and g-i) 1T/2H-MoS₂ after 30 000 cycles.

Fig. S9 shows the results of the Dunn's method application for the analysis of the Mo(AH) charge storage mechanism (before modification with Pt particles), namely cyclic voltammetry curves carried out at different scan rates in the range from 10 to 500 mV s⁻¹ are presented. It can be noticed that when the scan rate value increases, the increase in the surface-controlled contribution is observed and it remains at a high level with the increasing scan rate applied. To analyze in detail how and whether Pt-doping affects the energy storage mechanism, the presented approaches of differentiating capacitances were used for both Pt@1T/2H-MoS₂ and 1T/2H-MoS₂ electrode materials during repetitive cycling.

Another method of differentiating capacitances was proposed by Trasatti and coworkers [113] stating that it is possible to estimate the contribution of diffusion-controlled and surface-controlled charge to the overall charge being stored, according to Eq. (7):

$$q_T = q_i + q_o \quad (7)$$

where q_T is the total amount of charge, q_i represents the charge stored at the "inner" surface and q_o is the charge stored at the "outer" surface. The proposed approach is based on the fact that charge storage at the outer electrode surface is independent of the scanning rate, whereas the

process of charge storage at the inner surface is controlled by diffusion. Performing cyclic voltammetry at different scan rates and evaluating corresponding areal capacitances constitute a base to investigate capacitive contribution from electrical double layer and pseudo-capacitive reactions. Assuming that the diffusion of ions follows a semi-infinite pattern, it should be possible to observe a linear relationship between the reciprocal of the calculated areal capacitance (C^{-1}) and the square root of the scan rate ($v^{1/2}$), according to Eq. (8):

$$C^{-1} = \text{const} \cdot v^{1/2} + C_T^{-1} \quad (8)$$

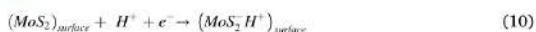
where C_T is a total capacitance, namely the sum of pseudo-capacitance and electric double layer capacitance. Furthermore, plotting the capacitance (C) versus the reciprocal of the scan rate allows to estimate the value of the contributed capacitance of the electrical double layer (C_o), according to Eq. (9):

$$C = \text{const} \cdot v^{-1/2} + C_o \quad (9)$$

Eventually, subtracting C_o from C_T results in a determination of maximum pseudo-capacitance value. The evaluation of the contribution of the Mo(AH) electrode material before galvanostatic charge/discharge

tests is presented in Fig. 8a,b, whereas the final results are compared with Dunn's analysis in Fig. 8c. The values were obtained from a linear fit within the restricted range of the scan rate – the rest of the polarization range was disregarded due to the high ohmic drop caused by the electrode material's internal resistance.

It is clearly seen in Fig. 8c that even though the non-diffusive contribution is higher for the Dunn's analysis, especially for the higher scan rates. The trend towards an increase of surface-controlled contribution may also be observed in the case of the highest scan rates, for which the differentiation of the capacitance was carried out using Dunn's method and the outer surface contribution reaches 94% (see Fig. S9, Supplementary Information). Processes responsible for energy storage reactions can be expressed as shown below in Eq. (10) [114, 115]:



On the other hand, as mentioned above, a layered structure allows ions to intercalate, which results in a contribution of a pseudocapacitance similar to a battery-type one [116], but often wrongly confused with it. According to the literature and both empirical studies and mathematical models presented therein, in the case of 2H-MoS₂ electrode materials, it is necessary to provide a high voltage value that would allow the transfer of electrons through a wide band gap in order to fill the unoccupied states of 2H-MoS₂ and hence contributing to the increasing pseudocapacitance contribution [117]. Therefore, the 2H phase is mainly characterized by EDL capacitive properties, especially in aqueous electrolytes. On the contrary, 1T-MoS₂ is able to store charge using both EDL and pseudocapacitive mechanisms. According to the literature, reversible redox reactions may occur at a large density of states, namely a significant number of d-orbitals of molybdenum atoms above the Fermi level may be observed. For both crystallographic phases, pseudocapacitance's occurrence is mainly due to Mo-edge activity [17,117]. Furthermore, the cyclic voltammetry curves (see Fig. S3, Supplementary Information) clearly show the combination of nearly rectangular shape and pseudocapacitive behavior, and the latter may be depicted as follows in Eq. (11):



For the 1T/2H-MoS₂ electrode material, the results of Dunn's and Trasatti's analysis after 15 000 and 30 000 cycles are presented in Fig. S10 (Supplementary Information, with the CE and WE areas separated). The obtained results indicate that with the successive charging and discharging cycles, we do not observe such significant changes in the energy storage mechanisms. As with the original material, energy is mainly stored through the formation of an electrical double layer. The conclusions are consistent with the previously presented observations that the composition of the material does not change and neither does the energy storage mechanism. On the other hand, for the Pt@1T/2H-MoS₂, as it was stated above, during the repetitive cycling and simultaneous Pt-modification, the change in the chemical composition of electrode material may be observed, and thus a change in the energy storage mechanism. Consequently, with the increasing number of cycles, an increase in the diffusion-controlled contribution is observed (see Fig. 8d,e). The results are consistent with the presented XPS results, which indicate that the material is transformed into mixed molybdenum oxides MoO_x. Transition metal oxides, including molybdenum oxides, are characterized by pseudocapacitive properties and it has been already reported that oxygen-deficient MoO_x with varieties of oxidation states are particularly promising for energy storage applications [40,118,119]. Therefore, due to its enhanced overall electrochemical performance, the Pt@1T/2H-MoS₂ electrode material obtained after 10 000 repetitive charge/discharge cycling was tested in a two-electrode system.

3.5. Two electrode configuration measurements

The results of the two-electrode measurements for the Pt@1T/2H-MoS₂ electrode material obtained after 10 000 repetitive charge/discharge cycling are presented in Fig. 9. The electrode material in the two-electrode configuration was subjected to 50,000 charge/discharge cycles with an applied voltage of 0.6 V and a flowing current of 11.9 mA cm⁻². In Fig. 9a, it can be seen that the capacitance remains stable, and the value of which does not decrease with time. Moreover, a slight

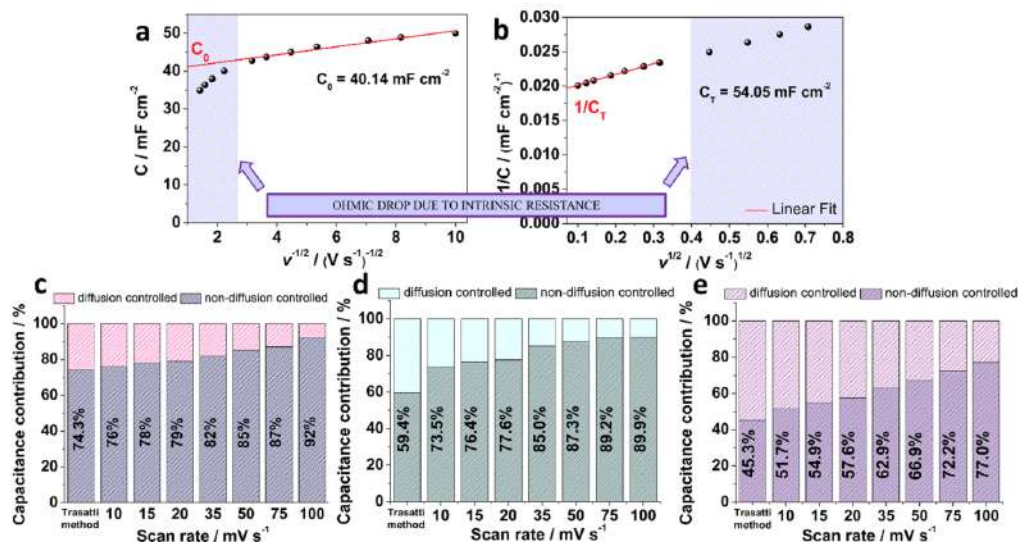


Fig. 8. Determination of a) outer surface capacitance contribution (C_0) and b) total capacitance (C_T) for Mo(AH) before Pt-surface modification, based on Trasatti method; comparison of the results from Trasatti method and Dunn's method c) before Pt-surface modification, d) after 15 000 cycles (Pt@1T/2H-MoS₂) and e) after 30 000 cycles of repetitive cycling (Pt@1T/2H-MoS₂).

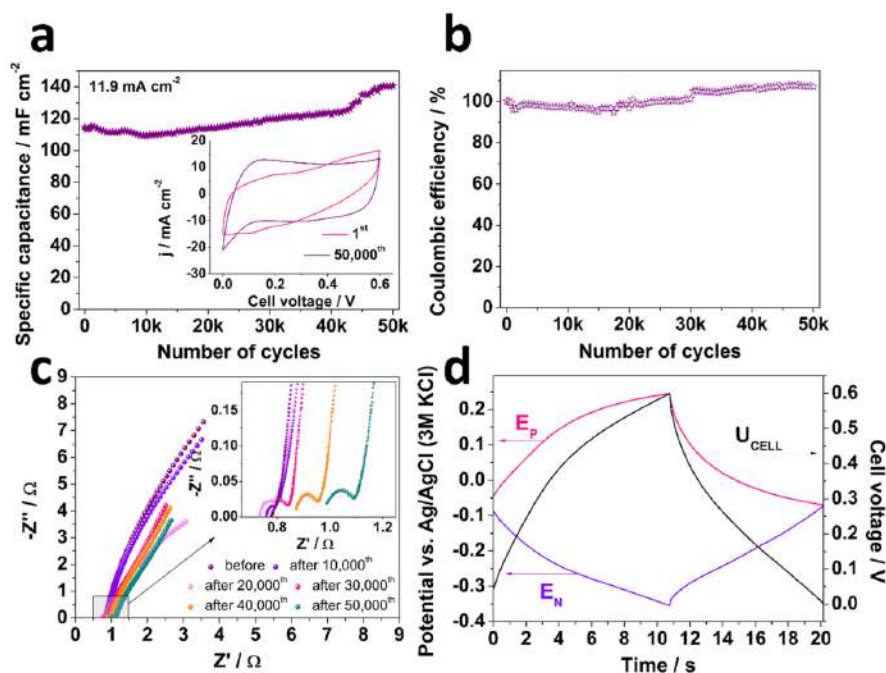


Fig. 9. a) Areal capacitance of the Pt@1T/2H-MoS₂ symmetric supercapacitor calculated on the basis of 50 000 GCD cycles (inset: CV curves before and after 50 000 cycles); b) coulombic efficiency after 50 000 cycles; c) EIS results during subsequent cycles in the frequency range between 20 kHz and 100 mHz; d) galvanostatic charge/discharge profile for the Pt@1T/2H-MoS₂ symmetric supercapacitor.

increase in capacitance was recorded with the increasing number of cycles performed, which is probably due to the still occurring, albeit to a smaller extent, intercalation process and the complementary changes in the electrode material. The increase in capacitance is also visible in the inset provided, showing the recorded voltammetry curves before and after 50 000 cycles. The material in the symmetric supercapacitor system was also characterized by a high-reaching coulombic efficiency during multiple cycles (Fig. 9b) and unprecedented capacitance retention (120% after 50 000 cycles), and it was recorded that by applying a voltage of 0.6 V it is distributed almost symmetrically over both electrode materials (Fig. 9d). Electrochemical impedance spectroscopy analysis was also performed during the repetitive cycling and the results are shown in Fig. 9c. It can be observed that before the measurements, the impedance curve was a straight line, also in the higher frequency range, indicating capacitive properties. Along with the subsequent cycles, in the high-frequency range, a semicircle can be distinguished, pointing to the increasing resistance associated with the charge transfer processes. Furthermore, the appearance of the semicircle in the high-frequency range confirms that an ion adsorption/desorption on the electrode material surface coupled with electron transfer to the surface takes place [88]. There is also a noticeable shift of the intersection with the x-axis value towards higher ones, suggesting an increase in the equivalent series resistance. Nevertheless, at each stage of the repetitive cycling, the overall resistance is small, indicating the good conductivity of the electrode. Moreover, for a comparison, multiple charge/discharge cycles were also performed for the 1T/2H-MoS₂ electrode material without Pt surface modification (see Fig. S11, Supplementary Information). In this case, an increase in the capacitance was also observed, as well as an almost perfect coulombic efficiency, as in the case of materials in a three-electrode configuration cell. However, for the material

that was not modified with Pt particles, the values of the recorded capacitance were much smaller, and therefore the supercapacitor was working at lower current values and the operating voltage value was lower. Nevertheless, Pt@1T/2H-MoS₂ symmetric supercapacitor was primarily characterized by unprecedented capacitance retention, with no significant degradation of the electrode material. A comparison with current literature data on Mo-based electrode materials for supercapacitors is provided in Table S1 (Supplementary Information).

4. Conclusions

The investigation of the different approaches for the synthesis of MoS₂ electrode material was performed, including anodization, hydrothermal process, and annealing, with the results indicating that depending on the processes carried out, amorphous molybdenum oxide, amorphous molybdenum sulfide or crystalline molybdenum oxide is obtained. The electrode material prepared via anodization of a molybdenum plate, followed by a hydrothermal process in thiourea aqueous solution was obtained in a form of a thin layer on metallic molybdenum substrate. The electrode material was characterized by the increasing capacitance during subsequent cycles, which was strictly related to the platinum dissolution-deposition process that occurred during repetitive cycling in 1 M sulfuric acid with Pt acting as a counter electrode. The analysis of the Pt-surface modification during multiple charging and discharging cycles revealed that Pt-surface modification happening simultaneously with the H⁺ ions intercalation resulted in boosting the exfoliation process, and as a result, the increase of capacitance was higher in comparison with non-modified MoS₂. After 60 000 cycles, the specific capacitance of the Pt@1T/2H-MoS₂ electrode material increased to over 1 F cm⁻², with the coulombic efficiency above 97%

during all the cycles. Furthermore, this study revealed that upon Pt-surface modification, the material's composition has been changed. XPS analysis revealed that the transition to mixed molybdenum oxides took place altogether with the introduction of oxygen vacancies into the structure. Altogether with the platinum deposition, significant changes in the energy storage mechanism were observed. Pt-modified electrode material was characterized by a greater contribution of pseudocapacitance in the charge storage processes, which was increasing with the greater number of cycles applied. The phenomenon was strictly related to the presence of mixed molybdenum oxides on the surface and thus, such a modified material was used for the symmetric two-electrode configuration with the capacitance reaching 140 mF cm^{-2} after 60 000 galvanostatic cycles and the coulombic efficiency at around 100% during all cycles.

The authors also believe that the conclusions drawn and the observations presented are a noteworthy and profound insight that provides a novel approach for understanding the ongoing processes taking place in the measurement system, especially when the counter electrode for electrochemical measurements is considered. Furthermore, the authors are of the opinion that paying attention to the constant variability of the material during charge-discharge processes, resulting in electrochemical but also physicochemical changes, can certainly help in gaining in-depth knowledge about the mechanisms underlying energy storage by electrode materials. We also believe that careful consideration should be taken into account when Pt counter electrode is used in the study of energy storage materials due to the dissolution-deposition phenomenon of platinum, which, may have a positive effect on the overall electrochemical performance of the electrode material, should not be ignored regardless of the circumstances. Nevertheless, the results indicate that Pt-surface modification of MoS_2 may provide a novel approach for electrode materials for high-performance supercapacitors.

Credit author statement

Zuzanna Zarach: Conceptualization, Methodology, Validation, Formal analysis, Investigation, Writing - Original Draft, Writing - Review & Editing, Visualization, Project administration; **Mariusz Szkoda:** Conceptualization, Methodology, Validation, Writing - Original Draft, Writing - Review & Editing, Supervision, Project administration, Funding acquisition; **Konrad Trzcinski:** Conceptualization, Methodology, Writing - Review & Editing; **Marcin Lapiński:** Investigation, Resources; **Grzegorz Trykowski:** Investigation, Resources, Writing - Original Draft, Visualization; **Andrzej P. Nowak:** Conceptualization, Validation, Formal analysis, Writing - Review & Editing, Supervision

Declaration of Competing Interest

The authors declare the following financial interests/personal relationships which may be considered as potential competing interests.

Data availability

Data will be made available on request.

Acknowledgments

This work was supported by The National Centre for Research and Development (Grant no LIDER/15/0088/L-10/18/NCBR/2019). We thank K. Jurak for providing the access to the X-ray Photoelectron Spectroscopy apparatus. We would also like to thank M. Gazda for assistance with X-diffraction pattern measurements, and M. Sawczak who provided the access to the micro-Raman spectrometer.

Supplementary materials

Supplementary material associated with this article can be found, in the online version, at [doi:10.1016/j.electacta.2022.141389](https://doi.org/10.1016/j.electacta.2022.141389).

References

- [1] D. Saha, P. Kruse, Editors' choice—review—conductive forms of MoS_2 and their applications in energy storage and conversion, *J. Electrochem. Soc.* 167 (2020), 126517, <https://doi.org/10.1149/1945-7111/AB8348>.
- [2] T. Wang, H.C. Chen, F. Yu, X.S. Zhao, H. Wang, Boosting the cycling stability of transition metal compounds-based supercapacitors, *Energy Storage Mater.* 16 (2019) 545–573, <https://doi.org/10.1016/j.ensm.2018.09.007>.
- [3] D. Kong, H. He, Q. Song, B. Wang, W. Lv, Q.-H. Yang, L. Zhi, Rational design of MoS_2 @graphene nanocables: towards high performance electrode materials for lithium ion batteries, *Energy Environ. Sci.* 7 (2014) 3320–3325, <https://doi.org/10.1039/C4EE02211B>.
- [4] B. Yao, L. Huang, J. Zhang, X. Gao, J. Wu, Y. Cheng, X. Xiao, B. Wang, Y. Li, J. Zhou, Flexible transparent molybdenum trioxide nanopaper for energy storage, *Adv. Mater.* 28 (2016) 6353–6358, <https://doi.org/10.1002/ADMA.201600529>.
- [5] Z. Dai, W. Jin, M. Grady, J.T. Sadowski, J.I. Dadap, R.M. Osgood, K. Pohl, Surface structure of bulk $2\text{H-MoS}_2(0001)$ and exfoliated suspended monolayer MoS_2 : a selected area low energy electron diffraction study, *Surf. Sci.* 660 (2017) 16–21, <https://doi.org/10.1016/j.susc.2017.02.005>.
- [6] W. Xu, C. Sun, K. Zhao, X. Cheng, S. Rawal, Y. Xu, Y. Wang, Defect engineering activating (Boosting) zinc storage capacity of MoS_2 , *Energy Storage Mater.* 16 (2019) 527–534, <https://doi.org/10.1016/j.ensm.2018.09.009>.
- [7] L. Miao, Z. Song, D. Zhu, L. Li, L. Gan, M. Liu, Recent advances in carbon-based supercapacitors, *Mater. Adv.* 1 (2020) 945–966, <https://doi.org/10.1039/D0MA00384K>.
- [8] L. Lin, W. Lei, S. Zhang, Y. Liu, G.G. Wallace, J. Chen, Two-dimensional transition metal dichalcogenides in supercapacitors and secondary batteries, *Energy Storage Mater.* 19 (2019) 408–423, <https://doi.org/10.1016/j.ensm.2019.02.023>.
- [9] H. Liu, X. Liu, S. Wang, H.K. Liu, L. Li, Transition metal based battery-type electrodes in hybrid supercapacitors: a review, *Energy Storage Mater.* 28 (2020) 122–145, <https://doi.org/10.1016/j.ensm.2020.03.003>.
- [10] C. Liu, Y. Bai, Y. Zhao, H. Yao, H. Pang, MoS_2 /graphene composites: fabrication and electrochemical energy storage, *Energy Storage Mater.* 33 (2020) 470–502, <https://doi.org/10.1016/j.ensm.2020.06.020>.
- [11] Y.C. Lin, D.O. Dumcenco, Y.S. Huang, K. Suenaga, Atomic mechanism of the semiconducting-to-metallic phase transition in single-layered MoS_2 , *Nat. Nanotechnol.* 9 (2014) 391–396, <https://doi.org/10.1038/nnano.2014.64>, 2014 95.
- [12] L. Hu, X. Shan, Y. Wu, J. Zhao, X. Lu, Laser thinning and patterning of MoS_2 with layer-by-layer precision, *Sci. Rep.* 7 (2017) 1–9, <https://doi.org/10.1038/s41598-017-15350-4>, 2017 71.
- [13] R. Kappera, D. Voiry, S.E. Yalcin, B. Branch, G. Gupta, A.D. Mohite, M. Chhowalla, Phase-engineered low-resistance contacts for ultrathin MoS_2 transistors, *Nat. Mater.* 13 (2014) 1128–1134, <https://doi.org/10.1038/nmat4080>, 2014 1312.
- [14] D. Sarkar, D. Das, S. Das, A. Kumar, S. Patil, K.K. Nanda, D.D. Sarma, A. Shukla, Expanding interlayer spacing in MoS_2 for realizing an advanced supercapacitor, *ACS Energy Lett.* 4 (2019) 1602–1609, <https://doi.org/10.1021/ACSENERGYLETT.9B00983>, SUPPL_FILE/NZ9B00983_SI_001.PDF.
- [15] R.B. Pujari, A.C. Lokhande, A.R. Shelke, J.H. Kim, C.D. Lokhande, Chemically deposited nano grain composed MoS_2 thin films for supercapacitor application, *J. Colloid Interface Sci.* 496 (2017) 1–7, <https://doi.org/10.1016/j.jcis.2016.11.026>.
- [16] A.S. Neetika, V.K. Malik, R. Chandran, One step sputtered grown MoS_2 nanoworms binder free electrodes for high performance supercapacitor application, *Int. J. Hydrog. Energy* 43 (2018) 11141–11149, <https://doi.org/10.1016/j.ijhydene.2018.05.005>.
- [17] M. Acerce, D. Voiry, M. Chhowalla, Metallic 1T phase MoS_2 nanosheets as supercapacitor electrode materials, *Nat. Nanotechnol.* 10 (2015) 313–318, <https://doi.org/10.1038/nnano.2015.40>, 2015 104.
- [18] R.M. Cervino, W.E. Triaca, A.J. Arvia, Electrochemical preparation and characteristics of platinum electrode surfaces with preferred orientations, *J. Electroanal. Chem. Interfacial Electrochem.* 182 (1985) 51–60, [https://doi.org/10.1016/0368-1874\(85\)85439-3](https://doi.org/10.1016/0368-1874(85)85439-3).
- [19] R. Chen, C. Yang, W. Cai, H.Y. Wang, J. Miao, L. Zhang, S. Chen, B. Liu, Use of platinum as the counter electrode to study the activity of nonprecious metal catalysts for the hydrogen evolution reaction, *ACS Energy Lett.* 2 (2017) 1070–1075, <https://doi.org/10.1021/ACSENERGYLETT.7B00219>.
- [20] D. Li, Y. Li, B. Zhang, Y.H. Lui, S. Mooni, R. Chen, S. Hu, H. Ni, Insertion of platinum nanoparticles into MoS_2 nanoflakes for enhanced hydrogen evolution reaction, *Mater* (2018), <https://doi.org/10.3390/MA11091520>, 2018, Vol. 11, Page 152011520.
- [21] M. Tavakkoli, N. Holmberg, R. Kronberg, H. Jiang, J. Sainio, E.I. Kauppinen, T. Kallio, K. Laasonen, Electrochemical activation of single-walled carbon nanotubes with pseudo-atomic-scale platinum for the hydrogen evolution reaction, *ACS Catal.* 7 (2017) 3121–3130, <https://doi.org/10.1021/ACSCATAL.7B00199>, SUPPL_FILE/CS7B00199_SI_001.PDF.
- [22] L. Kim, C.G. Chung, Y.W. Sung, J.S. Chung, Dissolution and migration of platinum after long-term operation of a polymer electrolyte fuel cell under various

- conditions, *J. Power Sources* 183 (2008) 524–532, <https://doi.org/10.1016/j.jpowsour.2008.05.062>.
- [23] S. Mitsushima, S. Kawahara, K. Ota, N. Kamiya, Consumption rate of Pt under potential cycling, *J. Electrochem. Soc.* 154 (2007) B153, <https://doi.org/10.1149/1.2400596/XML>.
- [24] A. Kawano, S. Imabayashi, Influence of oxygen atmosphere on dissolution of platinum under potential cycling, *J. Electrochem. Soc.* 161 (2014) F67–F71, <https://doi.org/10.1149/2.051401JES/XML>.
- [25] S. Cherevko, A.A. Topalov, A.R. Zeradjanin, G.P. Keeley, K.J.J. Mayrhofer, Temperature-dependent dissolution of polycrystalline platinum in sulfuric acid electrolyte, *Electroanalysis* 5 (2014) 235–240, <https://doi.org/10.1007/s12678-014-0187-9/FIGURES/3>.
- [26] M. Matsumoto, T. Miyazaki, H. Imai, Oxygen-enhanced dissolution of platinum in acidic electrochemical environments, *J. Phys. Chem. C* 115 (2011) 11163–11169, <https://doi.org/10.1021/jp2019594/ASSET/IMAGES/JP2019594.SOCIAL.JPEG.V03>.
- [27] G. Dong, M. Fang, H. Wang, S. Yip, H.Y. Cheung, F. Wang, C.Y. Wong, S.T. Chu, J. C. Ho, Insight into the electrochemical activation of carbon-based cathodes for hydrogen evolution reaction, *J. Mater. Chem. A* 3 (2015) 13080–13086, <https://doi.org/10.1039/C5TA02551F>.
- [28] Z. Shi, K. Nie, Z.J. Shao, B. Gao, H. Lin, H. Zhang, B. Liu, Y. Wang, Y. Zhang, X. Sun, X.M. Cao, P. Hu, Q. Gao, Y. Tang, Phosphorus-Mo 2 C@carbon nanowires toward efficient electrochemical hydrogen evolution: composition, structural and electronic regulation, *Energy Environ. Sci.* 10 (2017) 1262–1271, <https://doi.org/10.1039/C7EE00388A>.
- [29] M. Tian, C. Cousins, D. Beauchemin, Y. Furuya, A. Ohma, G. Jerkiewicz, Influence of the working and counter electrode surface area ratios on the dissolution of platinum under electrochemical conditions, *ACS Catal.* 6 (2016) 5108–5116, <https://doi.org/10.1021/acsatal.6b00200/ASSET/IMAGES/ACSCATAL.6B00200.SOCIAL.JPEG.V03>.
- [30] R. Wei, M. Fang, G. Dong, J.C. Ho, Is platinum a suitable counter electrode material for electrochemical hydrogen evolution reaction?, (2017). <https://doi.org/10.1016/j.sci.2017.06.006>.
- [31] G. Jerkiewicz, Applicability of platinum as a counter-electrode material in electrocatalysis research, *ACS Catal.* 12 (2022) 2661–2670, <https://doi.org/10.1021/acsatal.1c06040/ASSET/IMAGES/LARGE/CS1C06040.0004.JPEG>.
- [32] J. Xie, L. Gao, H. Jiang, X. Zhang, F. Lei, P. Hao, B. Tang, Y. Xie, Platinum nanocrystals decorated on defect-rich MoS₂ nanosheets for pH-universal hydrogen evolution reaction, *Cryst. Growth Des.* 19 (2019) 60–65, https://doi.org/10.1021/ACS.CGD.8B01594/SUPPL_FILE/CG8B01594_SI_001.PDF.
- [33] K. Tang, X. Wang, Q. Li, C. Yan, K. Tang, X. Wang, Q. Li, C. Yan, High edge selectivity of in situ electrochemical Pt deposition on edge-rich layered WS₂ nanosheets, *Adv. Mater.* 30 (2018), 1704779, <https://doi.org/10.1002/adma.201704779>.
- [34] H.Y. Jung, M.J. Chae, J.H. Park, Y. Il Song, J.C. Ro, S.J. Suh, Effects of platinum group metals on MoS₂nanosheets for a high-performance hydrogen evolution reaction catalyst, *ACS Appl. Energy Mater.* 4 (2021) 10748–10755, https://doi.org/10.1021/acsaelm.1c01721/SUPPL_FILE/AE1C01721_SI_001.PDF.
- [35] J. Shao, Y. Li, M. Zhong, Q. Wang, X. Luo, K. Li, W. Zhao, Enhanced-performance flexible supercapacitor based on Pt-deposited MoS₂, *Mater. Lett.* 252 (2019) 173–177, <https://doi.org/10.1016/j.matlet.2019.05.124>.
- [36] X. Jian, T. Li, S. Guo, L. Gao, F. Fu, Y. Tian, Y. Wu, Platinum nanoparticle-electrodeposited Ti3C₂TxMXene as a binder-free electrocatalyst for improved hydrogen evolution, *ACS Appl. Energy Mater.* 5 (2022) 3092–3099, https://doi.org/10.1021/acsaelm.1c03708/SUPPL_FILE/AE1C03708_SI_001.PDF.
- [37] T.Y. Ko, A. Jeong, W. Kim, J. Lee, Y. Kim, J.E. Lee, G.H. Ryu, K. Park, D. Kim, Z. Lee, M.H. Lee, C. Lee, S. Ryu, On-stack two-dimensional conversion of MoS₂ into MoO₃, *2D Mater.* 4 (2016), 014003, <https://doi.org/10.1088/2053-1583/4/1/014003>.
- [38] D. Lee, J. Hyuck Jang, W. Song, J. Moon, Y. Kim, J. Lee, B. Jeong, S. Park, In situ work-function measurement during chemical transformation of MoS₂ to MoO₃ by ambient-pressure x-ray photoelectron spectroscopy, *2D Mater.* 7 (2020), 025014, <https://doi.org/10.1088/2053-1583/AB6780>.
- [39] M. Hou, Y. Qiu, G. Yan, J. Wang, D. Zhan, X. Liu, J. Gao, L. Lai, Aging mechanism of MoS₂ nanosheets confined in N-doped mesoporous carbon spheres for sodium-ion batteries, *Nano Energy* 62 (2019) 299–309, <https://doi.org/10.1016/j.nanoen.2019.05.048>.
- [40] H.S. Kim, J.B. Cook, H. Lin, J.S. Ko, S.H. Tolbert, V. Ozolins, B. Dunn, Oxygen vacancies enhance pseudocapacitive charge storage properties of MoO₃-x, *Nat. Mater.* 16 (2017) 454–462, <https://doi.org/10.1038/NMAT4810>.
- [41] P. Qin, S.Q. Zhang, K.K.L. Yung, Z.F. Huang, B. Gao, Disclosure of charge storage mechanisms in molybdenum oxide nanobelts with enhanced supercapacitive performance induced by oxygen deficiency, *Rare Met.* 40 (2021) 2447–2454, <https://doi.org/10.1007/s12598-021-01722-3/FIGURES/5>.
- [42] X. Cai, X.G. Sang, Y. Song, D. Guo, X.X. Liu, X. Sun, Activating the highly reversible Mo⁴⁺/Mo⁵⁺ redox couple in amorphous molybdenum oxide for high-performance supercapacitors, *ACS Appl. Mater. Interfaces* 12 (2020) 48565–48571, <https://doi.org/10.1021/acsami.0c13692>.
- [43] T. Sun, Z. Li, X. Liu, L. Ma, J. Wang, S. Yang, Facile construction of 3D graphene/MoS₂ composites as advanced electrode materials for supercapacitors, *J. Power Sources* 331 (2016) 180–188, <https://doi.org/10.1016/j.jpowsour.2016.09.036>.
- [44] M.A. Bissett, L.A. Kinloch, R.A.W. Dryfe, Characterization of MoS₂-graphene composites for high-performance coin cell supercapacitors, *ACS Appl. Mater. Interfaces* 7 (2015) 17388–17398, <https://doi.org/10.1021/acsami.5b04672>.
- [45] H. Wang, Z. Lu, S. Xu, D. Kong, J.J. Cha, G. Zheng, P.C. Hsu, K. Yan, D. Bradshaw, F.B. Prinz, Y. Cui, Electrochemical tuning of vertically aligned MoS₂ nanofilms and its application in improving hydrogen evolution reaction, *Proc. Natl. Acad. Sci. U. S. A.* 110 (2013) 19701–19706, <https://doi.org/10.1073/pnas.1316792110>.
- [46] M. Mortazavi, C. Wang, J. Deng, V.B. Shenoy, N.V. Medhekar, Ab initio characterization of layered MoS₂ as anode for sodium-ion batteries, *J. Power Sources* 268 (2014) 279–286, <https://doi.org/10.1016/j.jpowsour.2014.06.049>.
- [47] Z. Hu, L. Wang, K. Zhang, J. Wang, F. Cheng, Z. Tao, J. Chen, MoS₂ nanoflowers with expanded interlayers as high-performance anodes for sodium-ion batteries, *Angew. Chem. Int. Ed.* 53 (2014) 12794–12798, <https://doi.org/10.1002/anie.201407898>.
- [48] Z. Li, K. Jiang, F. Khan, A. Goswami, J. Liu, A. Passian, T. Thundat, Anomalous interfacial stress generation during sodium intercalation/extraction in MoS₂ thin-film anodes, *Sci. Adv.* 5 (2019), https://doi.org/10.1126/SCIADV.AAV2820/SUPPL_FILE/AAV2820_SM.PDF.
- [49] M. Szkoda, K. Trzcinski, K. Siuzdak, A. Lisowska-Oleksiak, Photocatalytic properties of maze-like MoO₃ microstructures prepared by anodization of Mo plate, *Electrochim. Acta* 228 (2017) 139–145, <https://doi.org/10.1016/j.electacta.2017.01.064>.
- [50] M. Ranjba, F. Delalat, H. Salamati, Molybdenum oxide nanosheets prepared by an anodizing-exfoliation process and observation of photochromic properties, *Appl. Surf. Sci.* 396 (2017) 1752–1759, <https://doi.org/10.1016/j.apsusc.2016.11.225>.
- [51] F. Delalat, M. Ranjbar, H. Salamati, Blue colloidal nanoparticles of molybdenum oxide by simple anodizing method: decolorization by PdCl₂ and observation of in-liquid gasochromic coloration, *Sol. Energy Mater. Sol. Cells* 144 (2016) 165–172, <https://doi.org/10.1016/j.solmat.2015.08.038>.
- [52] N. Dukstiene, L. Tatariskinaite, M. Andrulevicius, Characterization of electrochemically deposited thin Mo-O-C-Se film layers, *Mater. Sci.* 28 (2010).
- [53] Y. Mao, W. Li, X. Sun, Y. Ma, J. Xia, Y. Zhao, X. Lu, J. Gan, Z. Liu, J. Chen, P. Liu, Y. Tong, Room-temperature ferromagnetism in hierarchically branched MoO₃ nanostructures, *CrystEngComm* 14 (2012) 1419–1424, <https://doi.org/10.1039/C1CE05700F>.
- [54] H. Komatsu, S. Ozuka, K. Ogura, Cathodic deposition of molybdenum and vanadium mixed oxyhydroxide films from V-substituted polymolybdophosphate, *Electrochim. Acta* 51 (2005) 274–280, <https://doi.org/10.1016/j.electacta.2005.04.025>.
- [55] G.E. Buono-Core, A.H. Klahn, C. Castillo, E. Muñoz, C. Manzur, G. Cabello, B. Chornik, Synthesis and characterization of thin molybdenum oxide films prepared from molybdenum dioxo tropolonate precursors by photochemical metal-organic deposition (PMOD) and its evaluation as ammonia gas sensors, *J. Non Cryst. Solids* 387 (2014) 21–27, <https://doi.org/10.1016/j.jnoncrysol.2013.12.009>.
- [56] J. Gong, Y. Kong, J. Li, X. Wang, Y. Que, Z. Zhang, Z. Ding, X. Xiao, Role of surface microstructure of Mo back contact on alkali atom diffusion and Ga grading in Cu(In,Ga)Se₂ thin film solar cells, *Energy Sci. Eng.* 7 (2019) 754–763, <https://doi.org/10.1002/ese3.304>.
- [57] M. Szkoda, K. Trzcinski, A.P. Nowak, M. Gazda, M. Sawczak, A. Lisowska-Oleksiak, The effect of morphology and crystalline structure of Mo/MoO₃ layers on photocatalytic degradation of water organic pollutants, *Mater. Chem. Phys.* 248 (2020), 122908, <https://doi.org/10.1016/j.matchemphys.2020.122908>.
- [58] W. Wang, X. Zeng, J.H. Warner, Z. Guo, Y. Hu, Y. Zeng, J. Lu, W. Jin, S. Wang, J. Lu, Y. Zeng, Y. Xiao, Photoresponse-bias modulation of a high-performance MoS₂ photodetector with a unique vertically stacked 2H-MoS₂/1T/2H-MoS₂ structure, *ACS Appl. Mater. Interfaces* 12 (2020) 33325–33335, <https://doi.org/10.1021/acsami.0c04048>.
- [59] M. Chen, B. Ji, Z. Dai, X. Du, B. He, G. Chen, D. Liu, S. Chen, K.H. Lo, S. Wang, B. Zhou, H. Pan, Vertically-aligned 1T/2H-MS₂ (M = Mo, W) nanosheets for surface-enhanced Raman scattering with long-term stability and large-scale uniformity, *Appl. Surf. Sci.* 527 (2020), 146769, <https://doi.org/10.1016/j.apsusc.2020.146769>.
- [60] G. Eda, H. Yamaguchi, D. Voiry, T. Fujita, M. Chen, M. Chhowalla, Photoluminescence from chemically exfoliated MoS₂, *Nano Lett.* 11 (2011) 5111–5116, <https://doi.org/10.1021/NL201874W>.
- [61] A. Naujokaitis, P. Gaigalas, C. Bittencourt, S. Mickevicius, A. Jagminas, 1T/2H MoS₂/MoO₃ hybrid assemblies with glycine as highly efficient and stable electrocatalyst for water splitting, *Int. J. Hydrog. Energy* 44 (2019) 24237–24245, <https://doi.org/10.1016/j.ijhydene.2019.07.161>.
- [62] Z. Zhang, Y. Dong, G. Liu, J. Li, H. Sun, H. Luo, S. Liu, The ultrafine monolayer 1 T/2H-MoS₂: preparation, characterization and amazing photocatalytic characteristics, *Colloids Surf. A Physicochem. Eng. Asp.* 589 (2020), 124431, <https://doi.org/10.1016/j.colsurfa.2020.124431>.
- [63] Y. Qi, Q. Xu, Y. Wang, B. Yan, Y. Ren, Z. Chen, CO₂-Induced Phase Engineering: protocol for Enhanced Photoelectrocatalytic Performance of 2D MoS₂ Nanosheets, *ACS Nano* 10 (2016) 2903–2909, https://doi.org/10.1021/acs.nano.6b00001/SUPPL_FILE/NN6B00001_SI_001.PDF.
- [64] C. Zhu, Q. Xian, Q. He, C. Chen, W. Zou, C. Sun, S. Wang, X. Duan, Edge-Rich Bicrystalline 1T/2H-MoS₂ cocatalyst-decorated (110) terminated CeO₂ nanorods for photocatalytic hydrogen evolution, *ACS Appl. Mater. Interfaces* 13 (2021) 35818–35827, <https://doi.org/10.1021/acsami.1c09651>.
- [65] M. Wu, J. Zhan, K. Wu, Z. Li, L. Wang, B. Geng, L. Wang, D. Pan, Metallic 1T MoS₂ nanosheet arrays vertically grown on activated carbon fiber cloth for enhanced Li-ion storage performance, *J. Mater. Chem. A* 5 (2017) 14061–14069, <https://doi.org/10.1039/C7TA03497K>.

- [66] X. Lin, D. Xue, L. Zhao, F. Zong, X. Duan, X. Pan, J. Zhang, Q. Li, In-situ growth of 1T/2H-MoS₂ on carbon fiber cloth and the modification of SnS₂ nanoparticles: a three-dimensional heterostructure for high-performance flexible lithium-ion batteries, *Chem. Eng. J.* 356 (2019) 483–491, <https://doi.org/10.1016/j.cej.2018.08.208>.
- [67] L. Kumari, Y.R. Ma, C.C. Tsai, Y.W. Lin, S.Y. Wu, K.W. Cheng, Y. Liou, X-ray diffraction and Raman scattering studies on large-area array and nanobranched structure of 1D MoO₃ nanorods, *Nanotechnology* 18 (2007), 115717, <https://doi.org/10.1088/0957-4484/18/11/115717>.
- [68] S. Alizadeh, S.A. Hassanzadeh-Tabrizi, MoO₃ fibers and belts: molten salt synthesis, characterization and optical properties, *Ceram. Int.* 41 (2015) 10839–10843, <https://doi.org/10.1016/j.ceramint.2015.05.024>.
- [69] K. Momma, F. Izumi, VESTA3 for three-dimensional visualization of crystal, volumetric and morphology data, *Urn-issn:0021-8988*, 44 (2011) 1272–1276, <https://doi.org/10.1107/S0021898811038970>.
- [70] X. Guan, Y. Ren, S. Chen, J. Yan, G. Wang, H. Zhao, W. Zhao, Z. Zhang, Z. Deng, Y. Zhang, Y. Dai, L. Zou, R. Chen, C. Liu, Charge separation and strong adsorption-enhanced MoO₃ visible light photocatalytic performance, *J. Mater. Sci.* 55 (2020) 5809–5822, <https://doi.org/10.1007/s10853-020-04418-8/FIGURES/12>.
- [71] H. Hu, C. Deng, J. Xu, K. Zhang, M. Sun, Metastable h-MoO₃ and stable α-MoO₃ microstructures: controllable synthesis, growth mechanism and their enhanced photocatalytic activity, *10* (2015) 1336–1346, <https://doi.org/10.1080/17458080.2015.1012654>.
- [72] X. Zhang, X. Zeng, M. Yang, Y. Qi, Investigation of a branchlike MoO₃/polypyrrole hybrid with enhanced electrochemical performance used as an electrode in supercapacitors, *ACS Appl. Mater. Interfaces* 6 (2014) 1125–1130, https://doi.org/10.1021/AM404724U/ASSET/IMAGES/AM404724U.SOCIAL/JPEG_V03.
- [73] J.S. Kang, J. Kim, M.J. Lee, Y.J. Son, D.Y. Chung, S. Park, J. Jeong, J.M. Yoo, H. Shin, H. Choe, H.S. Park, Y.E. Sung, Electrochemically synthesized nanoporous molybdenum carbide as a durable electrocatalyst for hydrogen evolution reaction, *Adv. Sci.* 5 (2018), 1700601, <https://doi.org/10.1002/ADVS.201700601>.
- [74] A.L. Tan, S.S. Ng, H.A. Hassan, Influence of initial sulfur content in precursor solution for the growth of molybdenum disulfide, *J. Phys. Conf. Ser.* 995 (2018), 012060, <https://doi.org/10.1088/1742-6596/995/1/012060>.
- [75] K. Shomalian, M.M. Bagheri-Mohagheghi, M. Ardyanian, Synthesis and characterization of porous nanoparticles of molybdenum sulfide (MoS₂) chalcogenide semiconductor prepared by polymerizing-complexing sol-gel method, *J. Mater. Sci. Mater. Electron.* 28 (2017) 14331–14340, <https://doi.org/10.1007/s10854-017-7293-8/FIGURES/10>.
- [76] Y. Wang, M. Zhen, H. Liu, C. Wang, Interlayer-expanded MoS₂/graphene composites as anode materials for high-performance lithium-ion batteries, *J. Solid State Electrochem.* 22 (2018) 3069–3076, <https://doi.org/10.1007/s10008-018-4018-8/FIGURES/6>.
- [77] X. Zeng, L. Niu, L. Song, X. Wang, X. Shi, J. Yan, Effect of polymer addition on the structure and hydrogen evolution reaction property of nanoflower-like molybdenum disulfide, *Met* 5 (2015) 1829–1844, <https://doi.org/10.3390/MET5041829>, 2015, Vol. 5, Pages 1829–1844.
- [78] H. Liu, X. Chen, L. Deng, M. Ding, J. Li, X. He, Perpendicular growth of few-layered MoS₂ nanosheets on MoO₃ nanowires fabricated by direct anion exchange reactions for high-performance lithium-ion batteries, *J. Mater. Chem. A* 4 (2016) 17764–17772, <https://doi.org/10.1039/C6TA06741G>.
- [79] Y. Dong, X. Xu, S. Li, C. Han, K. Zhao, L. Zhang, C. Niu, Z. Huang, L. Mai, Inhibiting effect of Na⁺ pre-intercalation in MoO₃ nanobelts with enhanced electrochemical performance, *Nano Energy* 15 (2015) 145–152, <https://doi.org/10.1016/j.nanoen.2015.04.015>.
- [80] F. Cheng, Z. Tao, J. Chen, Vapor-transportation preparation and reversible lithium intercalation/deintercalation of α-MoO₃ microrods, *J. Phys. Chem. B* 110 (2006) 119–124, <https://doi.org/10.1021/jp0553784>.
- [81] X.J. Wang, R. Nesper, C. Villavieille, P. Novák, Ammonolyzed MoO₃ Nanobelts as Novel Cathode Material of Rechargeable Li-Ion Batteries, *Adv. Energy Mater.* 3 (2013) 606–614, <https://doi.org/10.1002/AENM.201200692>.
- [82] P. Thangasamy, N. Ilavaraja, D. Jeyakumar, M. Sathish, Electrochemical cycling and beyond: unrevealed activation of MoO₃ for electrochemical hydrogen evolution reactions, *Chem. Commun.* 53 (2017) 2245–2248, <https://doi.org/10.1039/C6CC09187C>.
- [83] H. Wei, X. Yan, S. Wu, Z. Luo, S. Wei, Z. Guo, Electropolymerized Polyaniline Stabilized Tungsten Oxide Nanocomposite Films: electrochromic Behavior and Electrochemical Energy Storage, *J. Phys. Chem. C* 116 (2012) 25052–25064, <https://doi.org/10.1021/jp3090777>.
- [84] M. Nawwar, R. Poon, R. Chen, R.P. Sahu, I.K. Puri, I. Zhitomirsky, High areal capacitance of Fe₃O₄-decorated carbon nanotubes for supercapacitor electrodes, *Carbon Energy* 1 (2019) 124–133, <https://doi.org/10.1002/CEY2.6>.
- [85] R. Yuksel, C. Durucan, H.E. Unalan, Ternary nanocomposite SWNT/WO₃/PANI thin film electrodes for supercapacitors, *J. Alloy. Compd.* 658 (2016) 183–189, <https://doi.org/10.1016/j.jallcom.2015.10.216>.
- [86] B.A. Mei, O. Munteshari, J. Lau, B. Dunn, L. Pilon, Physical Interpretations of Nyquist Plots for EDLC Electrodes and Devices, *J. Phys. Chem. C* 122 (2018) 194–206, https://doi.org/10.1021/ACS.jpcc.7b10582/SUPPL_FILE/JPP7B10582_SI_001.ZIP.
- [87] V. Sunil, B. Pal, I. Izwan Misnon, R. Jose, Characterization of supercapacitive charge storage device using electrochemical impedance spectroscopy, *Mater. Today Proc.* 46 (2021) 1588–1594, <https://doi.org/10.1016/j.matpr.2020.07.248>.
- [88] R. Tatara, P. Karayaylali, Y. Yu, Y. Zhang, L. Giordano, F. Maglia, R. Jung, J. P. Schmidt, I. Lund, Y. Shao-Horn, The Effect of Electrode-Electrolyte Interface on the Electrochemical Impedance Spectra for Positive Electrode in Li-Ion Battery, *J. Electrochem. Soc.* 166 (2019) A5090–A5098, <https://doi.org/10.1149/2.0121903JES/XML>.
- [89] Z.M. Marković, M.D. Budimir, D.P. Kepić, I.D. Holclajner-Antunović, M. T. Marinović-Cincović, M.D. Dramicanin, V.D. Spasojević, D.B. Peruško, Z. Spitalský, M. Micušik, V.B. Pavlović, B.M. Todorović-Marković, Semi-transparent, conductive thin films of electrochemical exfoliated graphene, *RSC Adv.* 6 (2016) 39275–39283, <https://doi.org/10.1039/C6RA04250C>.
- [90] S. García-Dalí, J.I. Paredes, J.M. Munuera, S. Villar-Rodil, A. Adawy, A. Martínez-Alonso, J.M.D. Tascón, Aqueous Cathodic Exfoliation Strategy toward Solution-Processable and Phase-Preserved MoS₂ Nanosheets for Energy Storage and Catalytic Applications, *ACS Appl. Mater. Interfaces* 11 (2019) 36991–37003, https://doi.org/10.1021/ACSAMI.9B13484/SUPPL_FILE/AM9B13484_SI_001.PDF.
- [91] N. Liu, P. Kim, J.H. Kim, J.H. Ye, S. Kim, C.J. Lee, Large-Area Atomically Thin MoS₂ Nanosheets Prepared Using Electrochemical Exfoliation, *ACS Nano* 8 (2014) 6902–6910, <https://doi.org/10.1021/NN5016242>.
- [92] X. You, N. Liu, C.J. Lee, J.J. Pak, An electrochemical route to MoS₂ nanosheets for device applications, *Mater. Lett.* 121 (2014) 31–35, <https://doi.org/10.1016/j.matlet.2014.01.052>.
- [93] S.A. Ansari, H. Fouad, S.G. Ansari, M.P. Sk, M.H. Cho, Mechanically exfoliated MoS₂ sheet coupled with conductive polyaniline as a superior supercapacitor electrode material, *J. Colloid Interface Sci.* 504 (2017) 276–282, <https://doi.org/10.1016/j.jcis.2017.05.064>.
- [94] R.B. Choudhary, M. Majumder, A.K. Thakur, Two-Dimensional Exfoliated MoS₂ Flakes Integrated with Polyindole for Supercapacitor Application, *ChemistrySelect* 4 (2019) 6906–6912, <https://doi.org/10.1002/SLCT.201901558>.
- [95] P. Karthika, N. Rajalakshmi, K.S. Dhathathreyan, Functionalized exfoliated graphene oxide as supercapacitor electrodes, *Soft Nanosci. Lett.* 2012 (2012) 59–66, <https://doi.org/10.4236/SNL.2012.24011>.
- [96] S. Mukherjee, J. Turney, E. Mansfield, J. Holm, D. Soares, L. David, G. Singh, Exfoliated transition metal dichalcogenide nanosheets for supercapacitor and sodium ion battery applications, *R. Soc. Open Sci.* 6 (2019), <https://doi.org/10.1098/RSO.190437>.
- [97] L. Jiang, S. Zhang, S.A. Kulnich, X. Song, J. Zhu, X. Wang, H. Zeng, Optimizing hybridization of 1T and 2H phases in MoS₂ monolayers to improve capacitances of supercapacitors, *Mater. Res. Lett.* 3 (2015) 177–183, https://doi.org/10.1080/21663831.2015.1057654/SUPPL_FILE/TRLR_1057654_SM6377.DOC.
- [98] L. Xing, M.A. Hossain, M. Tian, D. Beauchemin, K.T. Adjemian, G. Jerkiewicz, Platinum electro-dissolution in acidic media upon potential cycling, *Electrocatalysis* 5 (2014) 96–112, <https://doi.org/10.1007/s12678-013-0167-9/FIGURES/11>.
- [99] A.A. Topalov, I. Katsounaros, M. Auzinger, S. Cherevko, J.C. Meier, S.O. Klemm, K. J.J. Mayrhofer, Dissolution of Platinum: limits for the Deployment of Electrochemical Energy Conversion? *Angew. Chemie Int. Ed.* 51 (2012) 12613–12615, <https://doi.org/10.1002/ANGE.201207256>.
- [100] Y. Sugawara, T. Okayasu, A.P. Yadav, A. Nishikata, T. Tsuru, Dissolution mechanism of platinum in sulfuric acid solution, *J. Electrochem. Soc.* 159 (2012) F779–F786, <https://doi.org/10.1149/2.017212JES/XML>.
- [101] H. Imai, K. Izumi, M. Matsumoto, Y. Kubo, K. Kato, Y. Imai, In situ and real-time monitoring of oxide growth in a few monolayers at surfaces of platinum nanoparticles in aqueous media, *J. Am. Chem. Soc.* 131 (2009) 6293–6300, https://doi.org/10.1021/JA810036H/SUPPL_FILE/JA810036H_SI_001.PDF.
- [102] X. Cai, Y. Song, S.Q. Wang, X. Sun, X.X. Liu, Extending the cycle life of high mass loading MoO_x electrode for supercapacitor applications, *Electrochim. Acta* 325 (2019), 134877, <https://doi.org/10.1016/j.electacta.2019.134877>.
- [103] M.T. Greiner, L. Chai, M.G. Helander, W.M. Tang, Z.H. Lu, Metal/Metal-Oxide Interfaces: how Metal Contacts Affect the Work Function and Band Structure of MoO₃, *Adv. Funct. Mater.* 23 (2013) 215–226, <https://doi.org/10.1002/ADFM.201200993>.
- [104] M.T. Greiner, L. Chai, M.G. Helander, W.M. Tang, Z.H. Lu, Transition Metal Oxide Work Functions: the Influence of Cation Oxidation State and Oxygen Vacancies, *Adv. Funct. Mater.* 22 (2012) 4557–4568, <https://doi.org/10.1002/ADFM.201200615>.
- [105] L. Huang, B. Yao, J. Sun, X. Gao, J. Wu, J. Wan, T. Li, Z. Hu, J. Zhou, Highly conductive and flexible molybdenum oxide nanopaper for high volumetric supercapacitor electrode, *J. Mater. Chem. A* 5 (2017) 2897–2903, <https://doi.org/10.1039/C6TA10433A>.
- [106] P. Guha, B. Mohanty, R. Thapa, R.M. Kadam, P.V. Satyam, B.K. Jena, Defect-Engineered MoO₂Nanostructures as an Efficient Electrocatalyst for Oxygen Evolution Reaction, *ACS Appl. Energy Mater.* 3 (2020) 5208–5218, https://doi.org/10.1021/ACSAPM.9B02551/SUPPL_FILE/APS9B02551_SI_001.PDF.
- [107] al - K.-Y. Huang, Y.-H. Luo, H.-M. Cheng, S. Mohammadi, M. Ali Taher, H. Beitollahi, P. Guha, A. Ghosh, A. Sarkar, S. Mandal, S.K. Ray, D.K. Goswami, P. V. Satyam, P-type β-MoO₂ nanostructures on n-Si by hydrogenation process: synthesis and application towards self-biased UV-visible photodetection, *Nanotechnology* 30 (2018), 035204, <https://doi.org/10.1088/1361-6528/AAEADC>.
- [108] L. Brewer, R.H. Lamoreaux, The Mo-O system (Molybdenum-Oxygen), *Bull. Alloy Phase Diagrams* 1 (1980) 85–89, <https://doi.org/10.1007/BF02881199>, 1980 12.
- [109] T.-C. Liu, W.G. Pell, B.E. Conway, S.L. Roberson, Behavior of Molybdenum Nitrides as Materials for Electrochemical Capacitors: comparison with Ruthenium

- Oxide, *J. Electrochem. Soc.* 145 (1998) 1882–1888, <https://doi.org/10.1149/1.1838571/XML>.
- [110] P. Simon, Y. Gogotsi, B. Dunn, Where do batteries end and supercapacitors begin? *Science* 343 (2014) 1210–1211, <https://doi.org/10.1126/science.1249625> (80-).
- [111] K. Brezesinski, J. Wang, J. Haetge, C. Reitz, S.O. Steinmueller, S.H. Tolbert, B. M. Smarsly, B. Dunn, T. Brezesinski, Pseudocapacitive Contributions to Charge Storage in Highly Ordered Mesoporous Group V Transition Metal Oxides with Iso-Oriented Layered Nanocrystalline Domains, *J. Am. Chem. Soc.* 132 (2010) 6982–6990, <https://doi.org/10.1021/JA9106385>.
- [112] V. Augustyn, P. Simon, B. Dunn, Pseudocapacitive oxide materials for high-rate electrochemical energy storage, *Energy Environ. Sci.* 7 (2014) 1597–1614, <https://doi.org/10.1039/C3EE44164D>.
- [113] S. Ardizzone, G. Fregonara, S. Trasatti, Inner and "outer" active surface of RuO₂ electrodes, *Electrochim. Acta.* 35 (1990) 263–267, [https://doi.org/10.1016/0013-4686\(90\)85068-X](https://doi.org/10.1016/0013-4686(90)85068-X).
- [114] Y. Tian, X. Song, J. Liu, L. Zhao, P. Zhang, L. Gao, Y. Tian, X.F. Song, J. Liu, L. Zhao, P. Zhang, L. Gao, Generation of Monolayer MoS₂ with 1T Phase by Spatial-Confinement-Induced Ultrathin PPy Anchoring for High-Performance Supercapacitor, *Adv. Mater. Interfaces.* 6 (2019), 1900162, <https://doi.org/10.1002/ADMI.201900162>.
- [115] H. Ji, C. Liu, T. Wang, J. Chen, Z. Mao, J. Zhao, W. Hou, G. Yang, Porous Hybrid Composites of Few-Layer MoS₂ Nanosheets Embedded in a Carbon Matrix with an Excellent Supercapacitor Electrode Performance, *Small* 11 (2015) 6480–6490, <https://doi.org/10.1002/SMLL.201502355>.
- [116] S. Fleischmann, J.B. Mitchell, R. Wang, C. Zhan, D.E. Jiang, V. Presser, V. Augustyn, Pseudocapacitance: from Fundamental Understanding to High Power Energy Storage Materials, *Chem. Rev.* 120 (2020) 6738–6782, https://doi.org/10.1021/ACS.CHEMREV.0C00170/ASSET/IMAGES/ACS.CHEMREV.0C00170.SOCIAL_IPEG_V03.
- [117] B. Zhang, X. Ji, K. Xu, C. Chen, X. Xiong, J. Xiong, Y. Yao, L. Miao, J. Jiang, Unraveling the different charge storage mechanism in T and H phases of MoS₂, *Electrochim. Acta.* 217 (2016) 1–8, <https://doi.org/10.1016/j.electacta.2016.09.059>.
- [118] B. Saravanakumar, R. Shobana, G. Ravi, V. Ganesh, R. Yuvakkumar, Preparation and electrochemical characterization of Mo₉O₂₆ nanopowders for supercapacitors applications, *Nano-Structures Nano-Objects* 19 (2019), 100340, <https://doi.org/10.1016/j.nanos.2019.100340>.
- [119] J.P. Jégou, H.K. Kim, J.S. Kim, K.B. Kim, One-pot synthesis of mixed-valence MoO_x on carbon nanotube as an anode material for lithium ion batteries, *J. Electroceram.* 31 (2013) 218–223, <https://doi.org/10.1007/s10832-013-9821-0/FIGURES/5>.

Supplementary Material

The Phenomenon of Increasing Capacitance Induced by 1T/2H-MoS₂ Surface Modification with Pt Particles – Influence on Composition and Energy Storage Mechanism

Zuzanna Zarach^{1*}, Mariusz Szkoda^{1,2}, Konrad Trzcinski¹, Marcin Lapiński^{2,3}, Grzegorz Trykowski⁴, Andrzej P. Nowak¹

¹Department of Chemistry and Technology of Functional Materials, Faculty of Chemistry, Gdańsk University of Technology, Gabriela Narutowicza 11/12, 80-233 Gdańsk, Poland

²Advanced Materials Center, Gdańsk University of Technology, Gabriela Narutowicza 11/12, 80-233 Gdańsk, Poland

³Institute of Nanotechnology and Materials Engineering, Faculty of Applied Physics and Mathematics, Gdańsk University of Technology, Narutowicza 11/12, 80-233 Gdańsk, Poland;

⁴Faculty of Chemistry, Nicolaus Copernicus University in Toruń, Gagarina 7, 87-100, Toruń, Poland

Email: zuzanna.zarach@pg.edu.pl

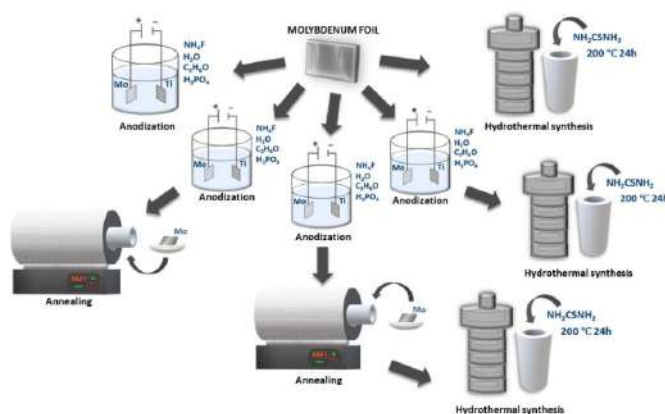


Figure S1. Scheme presenting different approaches for molybdenum foil modifications.

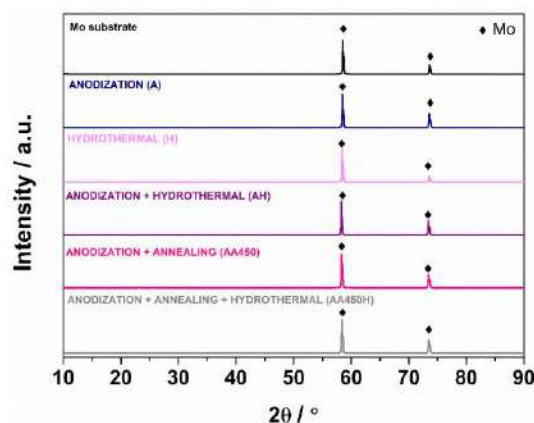


Figure S2. XRD spectra of molybdenum foil after different modifications.

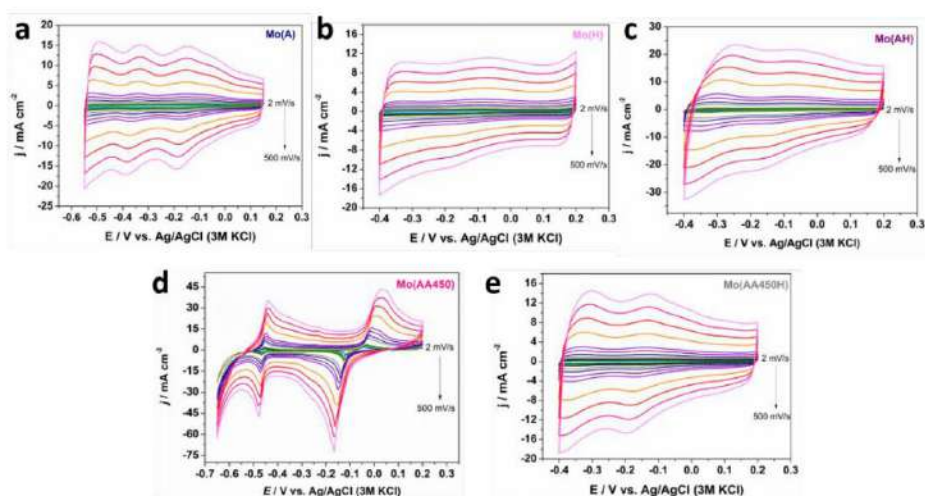


Figure S3. Cyclic voltammetry curves recorded at different scan rates for molybdenum-based electrode materials after different modifications.

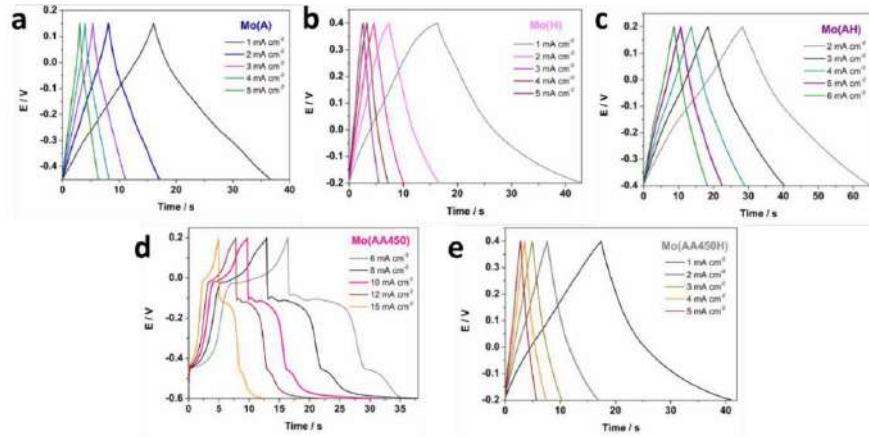


Figure S4. Galvanostatic charge-discharge curves at different current densities applied for electrode materials after different modifications.

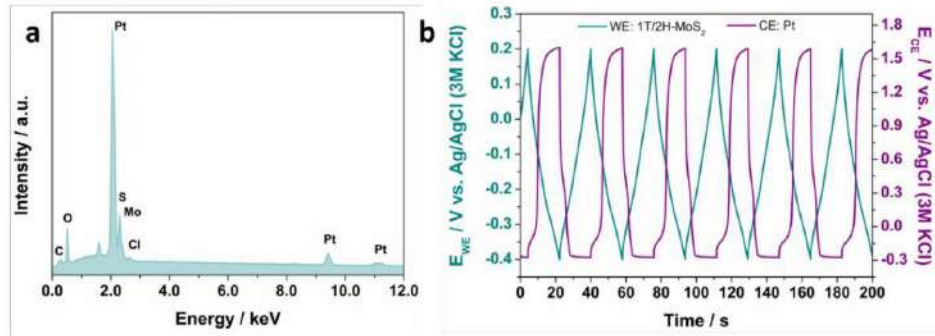


Figure S5. a) EDS results for the Mo(AH) electrode material after 15 000 galvanostatic charge-discharge cycles; b) galvanostatic charge/discharge curves for the WE: Mo(AH) and CE: Pt (performed at 10.5 mA cm⁻²).

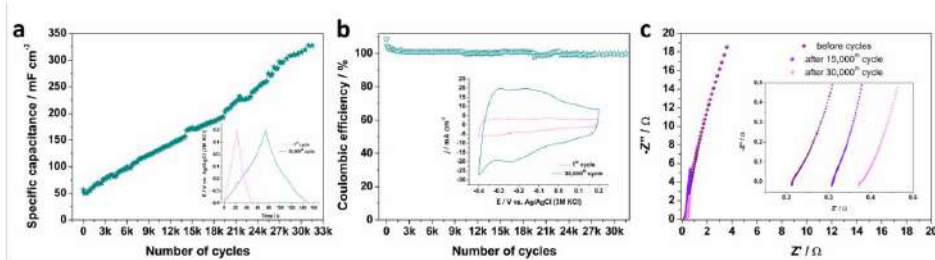


Figure S6. a) Areal capacitance calculated on the basis of 30 000 GCD cycles (inset: GCD curves before and after 30 000 cycles) for the 1T/2H-MoS₂ electrode material; b) coulombic efficiency after 30 000 cycles and CV curves (inset) before and after measurements; c) EIS results during subsequent cycles in the frequency range between 20 kHz and 100 mHz.

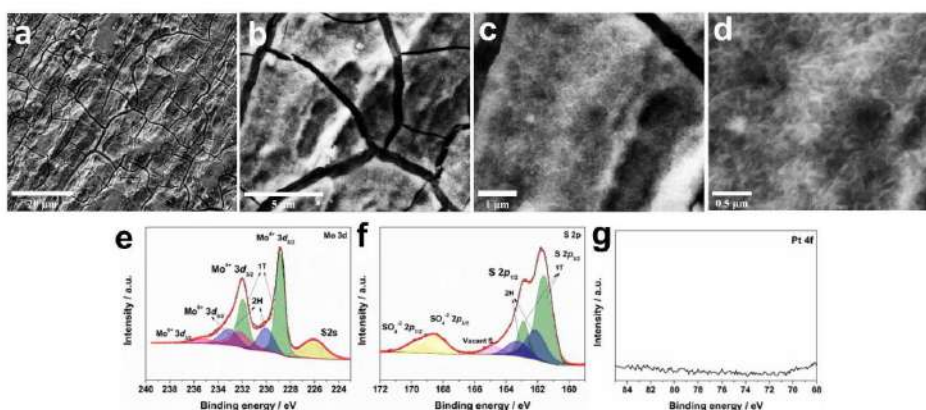


Figure S7. a-d) SEM images taken after 15 000 1T/2H-MoS₂ electrode material with the separation of the WE from the CE during the measurement; e) Mo 3d, f) S 2p and g) Pt 4f X-ray Photoelectron Spectroscopy spectra for the 1T/2H-MoS₂ electrode material after 15 000 charge/discharge cycles.

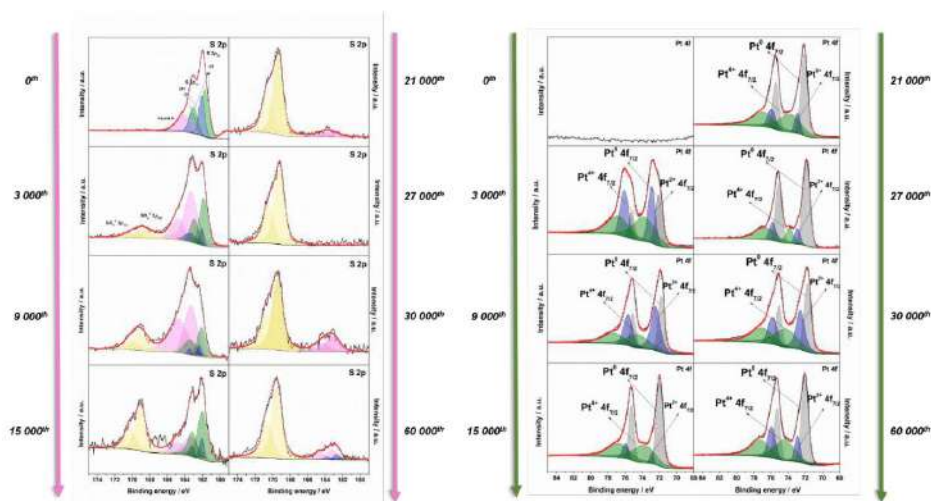


Figure S8. X-ray Photoelectron Spectroscopy spectra of S 2p and Pt 4f for the Pt@1T/2H-MoS₂ electrode material before and after subsequent galvanostatic charge/discharge tests.

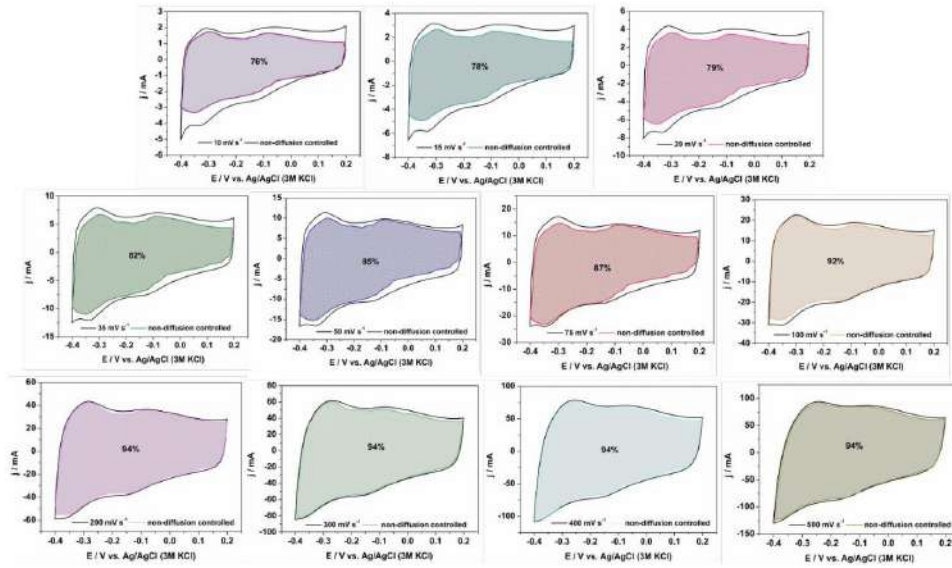


Figure S9. Cyclic voltammetry curves recorded for the Mo(AH) electrode material at different scan rates in the range from 10 to 500 mV s^{-1} with the calculated contribution of non-diffusion processes using Dunn's method.

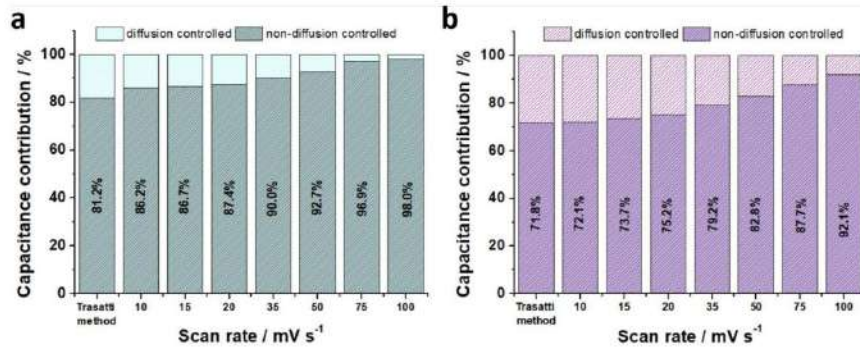


Figure S10. Comparison of the contribution of inner (diffusion controlled) and outer (non-diffusion controlled) capacitance calculated by Trasatti method and Dunn's method for the 1T/2H-MoS₂ a) after 15 000 cycles and b) after 30 000 cycles (with the CE and WE areas separated).

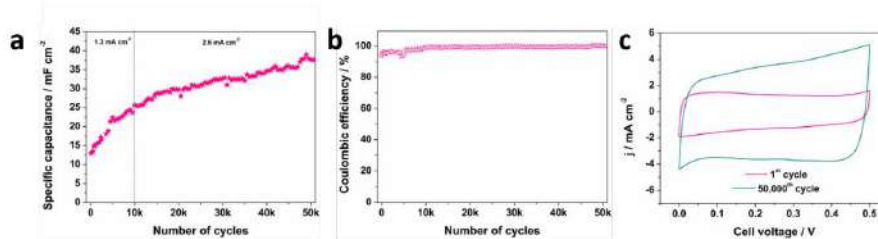


Figure S11. a) Areal capacitance of a symmetric supercapacitor 1T/2H-MoS₂ calculated on the basis of 50 000 GCD cycles; b) coulombic efficiency after 50 000 cycles; c) CV curves before and after 50 000 cycles.

Table S1. Comparison of the literature reports related to Mo-based electrode materials for energy storage applications in supercapacitors.

Electrode material	Conditions	Electrolyte	3 – electrode configuration		2 – electrode configuration		Ref.
			Capacitance [mF cm ⁻²]	Capacitance retention	Capacitance [mF cm ⁻²]	Capacitance retention	
Pt@1T/2H-MoS ₂	GCD: from 4.5 to 34 mA cm ⁻²	1M H ₂ SO ₄	from 100 to 1 000	1 000% (60 000 th)	from 113 to 140	120% (50 000 th)	This work
Core/shell PEDOT@MoS ₂	GCD: 1 and 100 mA cm ⁻²	1M H ₂ SO ₄	2 540	98.5% (5000 th)	-	-	[134]
	GCD: 2 and 100 mA cm ⁻²		-	-	1596.9	100% (5000 th)	
MoS ₂ thin film	CV: 10 mV s ⁻¹	0.5M H ₂ SO ₄	2.079	97% (5 000 th)	-	-	[135]
MoS ₂ Nanosheet/ rGO Hybrid	CV: 5 mV s ⁻¹	1M H ₂ SO ₄	14.09	95% (1 000 th)	-	-	[136]
Thin film α-MoO ₃	CV: 20 mV s ⁻¹	1M H ₂ SO ₄	0.064	100% (720 th)	-	-	[137]
CFP/a-MoS _x	CV: 1 mV s ⁻¹	0.5M H ₂ SO ₄	83.9	600% (4750 th)	41.9 mF cm ⁻²	-	[138]
	GCD: 0.3 mA cm ⁻²		8.76	-	-	-	
MoS ₂ nanowall films	CV: 1 mV s ⁻¹	0.5M H ₂ SO ₄	70	-	-	-	[139]
MoS _x @3D-PE	CV: 10 mV s ⁻¹	1M H ₂ SO ₄	27	-	-	-	[140]
	GCD: 0.13 mA cm ⁻²		11.6	-	-	-	
	GCD: 0.05 mA cm ⁻²	PVA/ H ₂ SO ₄	-	-	4.15	90% (10 000 th)	
Exfoliated MoS ₂	GCD: 1 mA cm ⁻²	1M Na ₂ SO ₄	-	-	1.65	800% (10 000 th)	[54]
	CV: 5 and 20 mV s ⁻¹		from 0.92 to 8.72	-	1.83	-	
MoS ₂ @CNT/RGO	GCD: 0.1 mA cm ⁻²	1M H ₂ SO ₄	129	-	29.7	94.7 % (10 000 th)	[141]
MoO _{3-x} doped MoS ₂ /graphene	GCD: 0.6 mA cm ⁻²	H ₃ PO ₄ / PVA	-	-	121.88	115% (4 000 th)	[142]

References

- [134] Y. Cai, L. Xu, H. Kang, W. Zhou, J. Xu, X. Duan, X. Lu, Q. Xu, *Electrochim. Acta* **2021**, 370, 137791.
- [135] N. Choudhary, M. Patel, Y. H. Ho, N. B. Dahotre, W. Lee, J. Y. Hwang, W. Choi, *J. Mater. Chem. A* **2015**, 3, 24049.
- [136] S. Dutta, S. De, *Mater. Today Proc.* **2018**, 5, 9771.
- [137] B. Mendoza-Sánchez, T. Brousse, C. Ramirez-Castro, V. Nicolosi, P. S. Grant, *Electrochim. Acta* **2013**, 91, 253.
- [138] S. K. Balasingam, A. Thirumurugan, J. S. Lee, Y. Jun, *Nanoscale* **2016**, 8, 11787.
- [139] J. M. Soon, K. P. Loh, *Electrochem. Solid-State Lett.* **2007**, 10, 250.
- [140] K. Ghosh, M. Pumera, *Nanoscale* **2021**, 13, 5744.
- [141] S. Wang, J. Zhu, Y. Shao, W. Li, Y. Wu, L. Zhang, X. Hao, *Chem. – A Eur. J.* **2017**, 23, 3438.
- [142] W. Li, T. Luo, C. Yang, X. Yang, S. Yang, B. Cao, *Electrochim. Acta* **2020**, 332, 135499.

Chapter III

*Influence of hydrochloric acid concentration
and type of nitrogen source
on the electrochemical performance
of TiO₂/N-MoS₂ for energy storage
applications*

1. Summary of the publication

This study presents a straightforward hydrothermal route for the direct growth of nitrogen-doped MoS₂ nanosheets on TiO₂ nanotube arrays, offering a binder-free electrode architecture for high-power supercapacitors. By anodizing titanium foil to form well-ordered TiO₂ nanotubes and then carrying out a single-step hydrothermal reaction in hydrochloric acid medium, an *in situ* formation of MoS₂ with controlled nitrogen incorporation was achieved. Moderate acid concentration (0.5–1 M HCl) is shown to be critical for balanced MoS₂ growth without damaging the TiO₂ scaffold, while the addition of aniline and ammonium persulfate ensures effective nitrogen doping and improved crystallinity.

Electrochemical tests in a three-electrode setup reveal the TiO₂/N-MoS₂ composite prepared in 0.5 M HCl delivers an areal capacitance of 320 mF·cm⁻² and retains 76% of its capacitance over 10 000 cycles, with nearly 100% coulombic efficiency. Moreover, Trasatti–Dunn analysis indicates a shift from surface-confined to diffusion controlled processes upon nitrogen doping, demonstrating deeper ion access and more active sites. In a symmetric supercapacitor configuration, a capacitance of 76 F·g⁻¹ at current density of 3 A·g⁻¹ was achieved, maintaining 84% of capacitance after 15 000 cycles, and reaching energy and power density of 11.1 W·kg⁻¹ and 5 193 Wh·kg⁻¹, respectively.

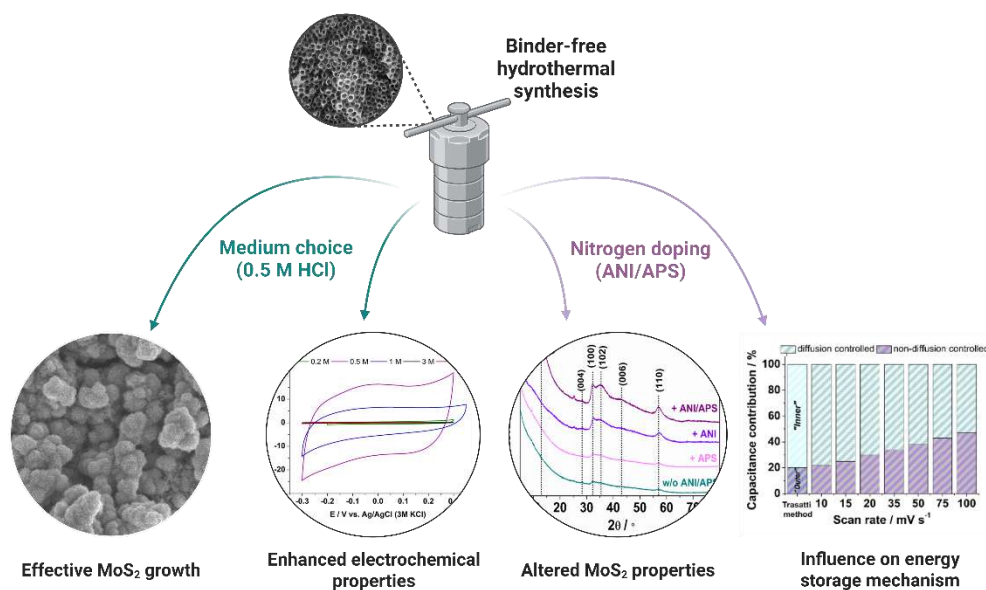


Figure 10. Graphical abstract summarizing Chapter III, created with BioRender.com.

The significance of this work lies in its simplicity: by eliminating polymer binders and leveraging a mild hydrothermal process, robust and high-power electrodes were produced, capable of rapid charge-discharge and long-term stability. The integration of nitrogen doping enhances electronic conductivity and improves the contribution of diffusion-driven capacitance, presenting the TiO₂/N-MoS₂ composite as promising candidate for next-generation energy storage applications.

2. Publication

Applied Surface Science 608 (2023) 155187



Contents lists available at ScienceDirect

Applied Surface Science

journal homepage: www.elsevier.com/locate/apsusc



Full Length Article

Influence of hydrochloric acid concentration and type of nitrogen source on the electrochemical performance of TiO₂/N-MoS₂ for energy storage applications

Z. Zarach^{a,*}, A.P. Nowak^{a,b}, K. Trzciński^{a,b}, G. Gajowiec^c, G. Trykowski^d, M. Sawczak^e, M. Łapiński^{b,f}, M. Szkoda^{a,b}

^a Department of Chemistry and Technology of Functional Materials, Faculty of Chemistry, Gdańsk University of Technology, Narutowicza 11/12, 80-233 Gdańsk, Poland

^b Advanced Materials Center, Gdańsk University of Technology, Gabriela Narutowicza 11/12, 80-233 Gdańsk, Poland

^c Institute of Machine Technology and Materials, Faculty of Mechanical Engineering and Ship Technology, Gdańsk University of Technology, Narutowicza 11/12, 80-233 Gdańsk, Poland

^d Faculty of Chemistry, Nicolaus Copernicus University, Gagarina 7, 87-100, Toruń, Poland

^e Centre for Plasma and Laser Engineering, The Siewalski Institute of Fluid Flow Machinery, Fiszera 14, 80-231 Gdańsk, Poland

^f Institute of Nanotechnology and Materials Engineering, Faculty of Applied Physics and Mathematics, Gdańsk University of Technology, Narutowicza 11/12, 80-233 Gdańsk, Poland

ARTICLE INFO

Keywords:

Molybdenum sulfide
Titanium dioxide nanotubes
Nitrogen doping
Hydrochloric acid
Supercapacitors
Energy storage

ABSTRACT

In this work, nitrogen-doped molybdenum sulfide was directly deposited on titanium dioxide nanotubes substrate (TiO₂/N-MoS₂) during hydrothermal synthesis. The study focuses on the influence of hydrochloric acid concentration used for the synthesis, with the results indicating its essential role in thioacetamide hydrolysis and thus in the effectiveness of the N-MoS₂ deposition. The electrode material itself is characterized by an initial capacitance of 320 mF cm⁻² with 76 % capacitance retention after 10 000 cycles. Moreover, the effect of nitrogen source on the physical and capacitive properties is investigated, revealing that the simultaneous addition of aniline and ammonium persulfate contributes to the improvement of crystallinity and overall electrochemical performance of the electrode material. The analysis of charge storage mechanisms also indicates that the introduction of nitrogen atoms significantly affects the contribution of diffusion-controlled processes. In the construction of a symmetrical device, the specific capacitance of 76 F g⁻¹ and areal capacitance of 70 mF cm⁻² with the superior coulombic efficiency and 84 % of capacitance retention after 15,000 cycles is observed, with 11.1 W kg⁻¹ and 5193.4 Wh kg⁻¹ of energy and power density of the device, respectively.

1. Introduction

Nowadays, supercapacitors, also known as electrochemical capacitors, are one of the key elements of energy management systems, mainly due to their high-power density, but also because of the possibility of integrating them with energy conversion devices [1]. In addition to their ever increasing use in electric vehicles [2,3], they are also attracting attention for their use in portable and wearable electronics [4–6]. Furthermore, in order to constantly improve their properties, primarily related to the improvement of the energy density and the expansion of the device operation voltage, new electrode materials are still being sought, as they are one of the key elements affecting the overall electrochemical performance.

In the case of electrode materials for supercapacitors, the most commonly used are carbonaceous ones, such as graphene, carbon nanotubes and porous carbons of different types [7]. Carbon electrodes store the charge mainly through an electrical double layer (EDL), which is formed when a potential is applied to the electrode and the ions adsorb on the surface. This group of electrode materials is one of the mostly studied, as they possess a high specific surface area and a high porosity which facilitates the diffusion of the charged species [8]. Furthermore, 2D materials like graphene have been receiving a considerable attention, mainly due to its two-dimensional structure and hence the possibility of a large surface area accessibility, as well as its mechanical and electronic properties [8–10]. Especially in the case of both Na- and Li-ion batteries, expanding the spacing between graphene/graphite

* Corresponding author.

E-mail address: zuzanna.zarach@pg.edu.pl (Z. Zarach).

<https://doi.org/10.1016/j.apsusc.2022.155187>

Received 2 August 2022; Received in revised form 26 September 2022; Accepted 30 September 2022

Available online 7 October 2022

0169-4332/© 2022 The Author(s). Published by Elsevier B.V. This is an open access article under the CC BY-NC license (<http://creativecommons.org/licenses/by-nc/4.0/>).

layers enables efficient energy storage [11]. It is the two-dimensional structure that is one of the properties that draws the attention in the relation to energy storage materials. Among these 2D structures, apart from carbon ones, materials such as MXenes [12,13], transition metal oxides and phosphates [14–17], but also transition metal dichalcogenides (TMDs) are of particular interest.

TMDs is a group of layered materials that are characterized by the X–M–X structure, composed of transition metals (M) and chalcogens (X). Materials from this group like MoS₂, WS₂, VS₂ and MoTe₂ [18–21], recently are gaining more and more interest in terms of their application in energy storage, mainly due to their properties such as edge sites, large specific surface area and ease of intercalation [22]. Special attention is paid to MoS₂, which seems to be the most thoroughly studied one, however, due to the variety of synthesis methods and attempts to deposit MoS₂ on various substrates, there is still no systematic knowledge about the correlation between material properties and synthesis parameters, and many other questions related to this arise, for which the answer still remains open. Nowadays, an increasingly widely used approach is hydrothermal synthesis, which offers a fast and low-cost procedure for obtaining nanostructured 2D TMDs. MoS₂ synthesized by hydrothermal method in the form of various structures such as: nanosheets [23], nanospheres [24], nanowires [25], nanorods [26], or hollow nanoparticles [27] has been repeatedly reported in the literature. However, due to the diverse selection of precursors, solvents and additives, as well as the inability to precisely control the processes taking place in the hydrothermal vessel, the MoS₂ crystal growth mechanism and the influence of individual parameters on the final properties of the material are not entirely clear. One of the most frequently chosen solvents in hydrothermal synthesis is deionized water [28–30], but an aqueous solution of hydrochloric acid [31–33] or organic solvents [34,35] are reported, and each of them plays an essential role in the final properties of the material. Therefore, the crucial aspect of hydrothermal synthesis is to understand the importance and the influence of each parameter on material's growth mechanism. However, as far as authors are concerned, so far there was no investigation on the impact of HCl concentration on the physical and electrochemical properties of MoS₂ altogether with its energy storage abilities.

In general, when it comes to electrode materials for energy storage, apart from investigating the influence of individual synthesis parameters, a number of studies are carried out in order to improve the capacitive properties of the materials. Among such solutions, the aim is to synthesize materials in the nanoscale and, above all, to create hybrid electrode materials. TMDs are commonly combined with conductive polymers [36,37], carbon materials [38,39], or MXenes [40], which results in increased energy density and enhanced stability of electrode within charge-discharge cycles. The improvement of electrochemical properties, and in particular the improvement of material's conductivity, is also performed by doping TMDs with various metal atoms, including: nitrogen [28,41,42], cobalt [43], platinum [44], or copper [45]. Moreover, material doping may also lead to imperfections due to atomic rearrangement and thus results in creating more active sites [45].

When it comes to materials used for energy storage, not only should the capacitive properties be considered, but also the material's interaction with the current collector at the interface. The most common practice is the synthesis of materials in the form of powders altogether with the polymer binders application for connecting the active material with the current collector. Unfortunately, binders application contributes to an increase in resistance and reduction of the positive effect caused by the formed nanostructures. Therefore, obtaining materials directly on the conductive substrates is one of the steps to improve the electrochemical performance of energy storage materials. In the case of MoS₂, only few papers have been reported about the synthesis of electrode materials performed in this way [46–49]. However, a major limitation is the fact that most of them require advanced equipment or/and hard synthesis conditions, and thus an efficient, low-cost, and scalable synthesis technique is still being sought.

In this work, we present a facile hydrothermal synthesis of nitrogen-doped molybdenum sulfide (N-MoS₂) performed directly on TiO₂ nanotubes substrate with a thorough investigation of the influence of hydrochloric acid concentration on the physical and electrochemical properties of the electrode material. Furthermore, the effect of the addition of aniline and ammonium persulfate during the synthesis was studied, with the results indicating that their presence significantly enhanced the capacitive properties of the electrode material. The resulted TiO₂/N-MoS₂ electrode material was characterized by the initial capacitance of 320 mF cm⁻², and the improved electrochemical performance was achieved mainly through adjusting concentration of hydrochloric acid and introducing nitrogen atoms into MoS₂ structure. Furthermore, TiO₂/N-MoS₂ material was used to construct a symmetrical device, for which the obtained specific capacitance reached 76F g⁻¹ (C_{areal} = 70 mF cm⁻²), with energy density of 11.1 W kg⁻¹ and superior power density (5193.4 Wh kg⁻¹).

2. Materials and methods

2.1. Materials

In the anodic oxidation process titanium foil (0.127 mm thick, annealed, 99 %), purchased from Alfa Aesar, was used and the synthesis was preceded by a sonication procedure using acetone and isopropanol mixture (Chempur). The electrolyte consisted of reagents from Chempur: ammonium fluoride (NH₄F) pure p.a., ethylene glycol (C₂H₆O₂), phosphoric acid (H₃PO₄), and distilled water. Hydrofluoric acid used for etching was purchased from Fischer Chemical. Reagents used for the hydrothermal process: potassium molybdenum oxide, anhydrous (99.8 % metals basis, Alfa Aesar), thioacetamide (Chemat), ammonium persulfate (APS) (98 %, Sigma-Aldrich), and aniline (ANI) (99.8 % pure, Acros Organics) were all at pure analytical grade. Sulfuric acid (POCH) was used for electrochemical measurements and as an electrolyte in supercapacitor construction. The device was constructed using heat-sealable foil and a fiberglass separator using a vacuum packing machine (CAS CVP-350/MS, Hertogenbosch).

2.2. TiO₂ nanotubes synthesis

Titanium dioxide nanotubes (TiO₂ NTs) were prepared by applying an anodic oxidation procedure according to our previous report [50]. In short, titanium foil was cut into pieces (2 cm × 2 cm), cleaned using ultrasonic treatment in isopropanol: acetone mixture (1:1 v/v) for 20 min, and rinsed with distilled water eventually. The as-prepared Ti foil constituted a working electrode (WE) and another Ti foil as a counter electrode (CE) in a two-electrode configuration in the anodization process. The synthesis was carried out at a constant temperature (23 °C) using a cooling bath thermostat (KISS K6, Huber), with a voltage of 40 V applied for over 2 h. After that, the electrode was rinsed with distilled water and etched by immersing in HF several times. In the final step, the electrode was calcinated in the quartz tube furnace through heating up to 450 °C in 2 h, sintering at this temperature for 2 h and 45 min.

2.3. TiO₂/N-MoS₂ preparation

TiO₂/N-MoS₂ was obtained by hydrothermal synthesis. For this purpose, 0.5 g of potassium molybdate and 1 g of thioacetamide were diluted in 25 ml of 0.5 M HCl and stirred for 10 min. Subsequently, 63 mg of aniline (26 mM) and 153 mg ammonium persulfate (26 mM) were added and stirred for another 20 min. Finally, the mixture was transferred to the Teflon liner altogether with the TiO₂ NTs sample (inside of a stainless steel autoclave) and placed in an oven for 24 h at 200 °C. After the process, the TiO₂/N-MoS₂ electrode was rinsed with distilled water and dried at room temperature. In order to investigate the effect of the hydrochloric acid concentration, it was changed from 0.1 to 5 M, respectively.

2.4. Electrochemical measurements

Electrochemical measurements were performed using potentiostat/galvanostat (BioLogic VSP 2078) in a three-electrode configuration – platinum mesh constituted a counter electrode (CE), Ag/AgCl vs 3 M KCl worked as a reference electrode (REF) and $\text{TiO}_2/\text{N-MoS}_2$ was a working electrode (WE). Measurements were carried out in 1 M sulfuric acid (H_2SO_4) aqueous solution and a number of electrochemical techniques have been applied, e.g. cyclic voltammetry (CV), galvanostatic charge and discharge tests (GCD), and electrochemical impedance spectroscopy (EIS). EIS was performed in a frequency range between 20 kHz and 100 mHz with a voltage amplitude of 10 mV. The impedance of the constant phase element Q used in the model is represented by the Equation below:

$$Z(\omega) = P^{-1}(j\omega)^{-n} \quad (1)$$

In order to investigate the performance in a two-electrode configuration, a symmetric supercapacitor was constructed using two $\text{TiO}_2/\text{N-MoS}_2$ electrodes. The total mass loading in the supercapacitor construction was 1.83 mg. Electrodes were separated using a fiberglass separator soaked in 1 M H_2SO_4 electrolyte and they were encased with a heat-sealable foil using a vacuum packing machine.

2.5. Material characterization

The as-prepared electrode materials were characterized by microscopic techniques, including Scanning Electron Microscopy (SEM) using JSM-7800F (JEOL, Tokyo, Japan) field emission scanning electron microscope. The images were analyzed using a beam accelerating voltage at 5 kV. EDX analysis was performed with a silicon nitride window's detector (OCTANE ELITE model, EDAX company, Mahwah, NJ, USA), and Transmission Electron Microscopy (TEM) (FEI, Tecnai F20X-Twin) with the measurement parameters: voltage 200 kV from FEG, imaging in bright field (BF) with CCD camera (Gatan, Orius), vacuum in the chamber 10^{-4} Pa. Raman spectroscopy measurements were performed with a micro-Raman spectrometer (Renishaw InVia) operating at 1 % of its total power (50 mW), with Ar laser emitting at the wavelength of 514 nm. X-ray Photoelectron Spectroscopy was carried out with an X-ray photoelectron spectrometer (Argus Omicron NanoTechnology) with Mg-K α source of X-ray and anode operated at 15 keV, 300 W. XPS measurements were conducted under ultra-high vacuum at room

temperature, with pressure below 1.1×10^{-8} mbar. XRD analysis was done with a diffractometer (Xpert PRO-MPD) with Cu K α emission ($\lambda = 0.15406$ nm).

3. Results and discussion

3.1. Characterization of the $\text{TiO}_2/\text{N-MoS}_2$ electrode materials prepared with different HCl concentrations

Electrode materials obtained with different hydrochloric acid concentrations were investigated using Scanning Electron Microscopy (SEM) and the results are presented in Fig. 1, indicating that the concentration significantly influenced the morphology of the samples. When the concentration was low (0.1 and 0.2 M), the formation of nanostructures was not observed, whereas, for the highest HCl concentration, nanostructures in a form of cubes and spheres may be distinguished. However, according to the results of Raman spectroscopy and XPS analysis, it may be assumed that the cubes and spheres formation is not due to the MoS_2 synthesis, but is strictly related to the change in the structure of TiO_2 nanotubes, which was caused by the treatment with 5 M HCl. According to some literature reports, treatment of TiO_2 nanotubes with HCl may considerably affect the shape of nanotubes, but the pH value may have some impact on crystallinity and morphology, as well [51–53]. Furthermore, Fan et al. also pointed out that the treatment of carbon nanotubes with hot concentrated HCl led to the formation of closed-capped nanotubes [54]. The closing of TiO_2 NTs was confirmed by the cross-section image and EDS analysis for the 5 M sample (see Figs. S1 and S2a), which clearly shows that the composition is only titanium and oxygen, as well as that the tip of the nanotube has been transformed into a cube, cutting off access to the inside of the nanotubes.

The enhanced signal from titanium was also reported for the sample with 3 M HCl (Fig. S2b), indicating that the synthesis of MoS_2 was also not fully effective. However, one may see that the resulting morphology for 0.5 and 1 M samples of $\text{TiO}_2/\text{N-MoS}_2$ is fairly similar, as the structure of nanosheets may be observed for both of them. Furthermore, for both of them, the EDS analysis confirmed the presence of elemental Mo and S in the deposited layers (see Fig. S2c,d). The SEM results are consistent with the morphology that can be seen in the transmission electron microscopy (TEM) images (see Fig. 2). TEM measurements were performed for the precipitate that was formed during the synthesis. It is impossible to indicate the presence of nanostructures for the samples prepared with 0.1 M and 0.2 M HCl, however, the 0.2 M sample is noticeably more

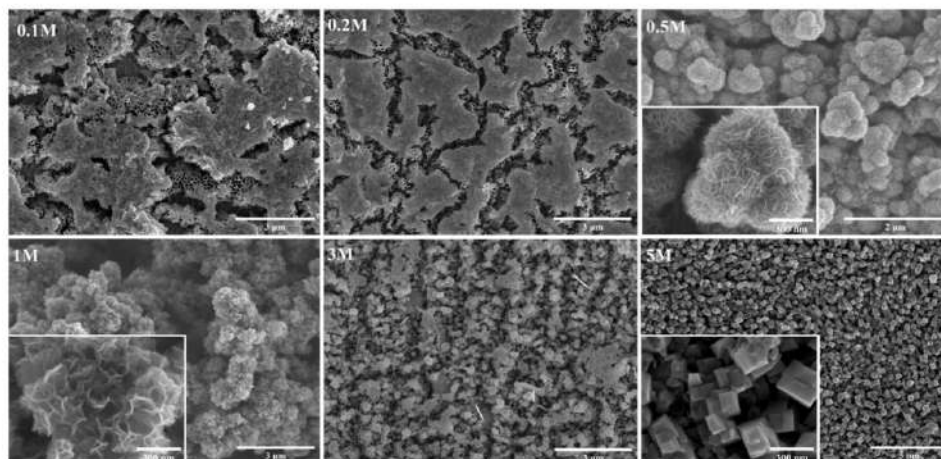


Fig. 1. SEM images of $\text{TiO}_2/\text{N-MoS}_2$ electrode materials obtained after hydrothermal synthesis performed with different hydrochloric acid concentrations.

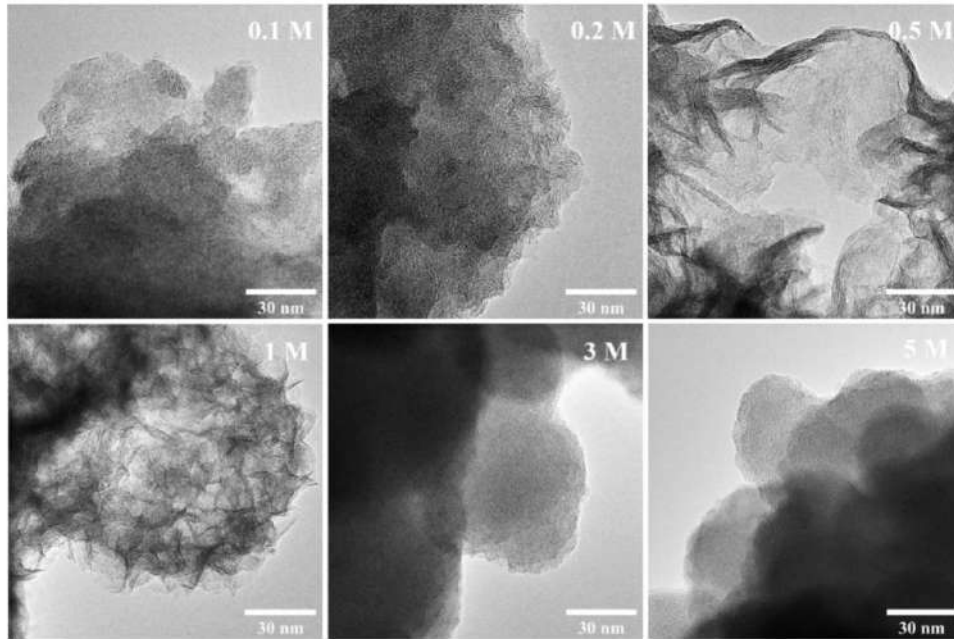


Fig. 2. TEM images of $\text{TiO}_2/\text{N-MoS}_2$ electrode materials obtained after hydrothermal synthesis performed with different hydrochloric acid concentrations.

crystalline. The crystal structure is also clearly distinguishable with 0.5 M and 1 M materials, especially at the edges of the nanosheets, whereas materials prepared with the highest HCl concentration are mostly amorphous. These results were also confirmed by the XRD results, presented in Fig. 3. Despite the fact that the results mainly show signals from Ti/ TiO_2 substrate, it is possible to extract the signals from molybdenum sulfide, as well. Peaks typical for the hexagonal structure of

MoS_2 may be indicated, including ones at 32.48° and 57.31° corresponding to (100) and (110) planes, respectively [55]. However, the signals are visible only for the materials prepared with 0.2 M, 0.5 M, and 1 M hydrochloric acid, with the highest intensities of the peaks recorded for the 0.5 M HCl sample. Among other signals coming from the substrate, one can distinguish signals of titanium at 40.36° and 53.15° for (101) and (102) planes, respectively [56]. Moreover, several signals

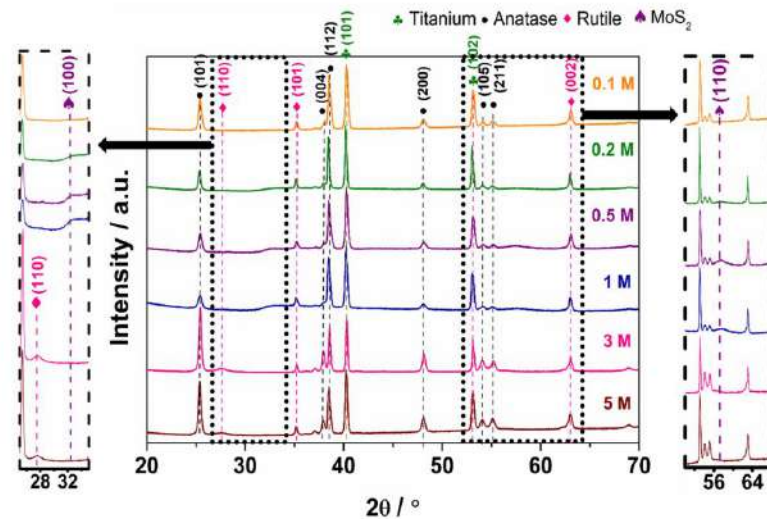


Fig. 3. XRD results for $\text{TiO}_2/\text{N-MoS}_2$ electrode materials obtained after hydrothermal synthesis performed with different hydrochloric acid concentrations.

from the anatase phase of TiO_2 were recorded, including 25.42° , 38.03° , 38.70° , 48.05° , 54.15° , and 55.15° corresponding to (101), (004), (112), (200), (105) and (211) planes, respectively [57]. Also, the presence of a rutile phase was confirmed, especially for the samples treated with high concentration hydrochloric acid. It was shown recently that the HCl environment enhances the anatase to rutile transition [58], which is probably even more triggered when the concentration is increased.

On this basis, it may be concluded that the synthesis of MoS_2 was strictly dependent on the hydrochloric acid concentration, as the deposition was effective only when the concentration was moderate (0.2 – 1 M). The conclusions were also based on Raman spectroscopy results (see Fig. S3a), for which one may see the presence of a hexagonal phase of MoS_2 , confirmed by the presence of peaks at 376 cm^{-1} and 404 cm^{-1} , attributed to the vibrations in 2H-MoS_2 molecules, namely $\text{E}_{2g}^{\text{in-plane}}$ and $\text{A}_{1g}^{\text{out-plane}}$ active modes, respectively [59,60]. However, with both decreased and increased concentration, the synthesis was not effective as only the signals characteristic for TiO_2 may be distinguished. To further verify the presence of the synthesized MoS_2 and the nitrogen dopant, the XPS analysis was applied.

The results of the XPS analysis are presented in Fig. 4. The results indicate, that even for the materials prepared with the lowest and the highest hydrochloric acid concentration, some amount of molybdenum in the form of Mo^{4+} and Mo^{6+} , as well as sulfur, may be detected. However, in the case of the 3 M HCl sample, the signal mainly comes from the trigonal phase of molybdenum sulfide, whereas for the highest HCl concentration, the most intense signal is due to the presence of Mo^{6+} , and stoichiometry does not indicate the presence of molybdenum sulfide. Nevertheless, for the moderate acid concentration, two signals at 227.9 and 231.1 eV suggest the presence of the trigonal phase (1T) of MoS_2 , whereas the existence of the 2H phase is confirmed by the signals recorded at 228.9 and 232.2 eV [59,60]. Analogously, one can distinguish between signals recorded for sulfur – the values of the $\text{S } 2p_{1/2}$ and $2p_{3/2}$ signals from 2H and 1T phases are placed at 161.8 and 163.6 eV, and 161.3 and 163.3 eV, respectively [61,62]. Furthermore, XPS spectra reveal the presence of SO_4^{2-} , which may be related to the presence of

synthesis residues, but also the S^{2-} conversion [63]. For most of the samples, the XPS profile of the N1 s consists of the band at 394.3 eV, assigned to $\text{Mo } 3p_{3/2}$, as well as two bands N1 at 399.5 eV and N2 at 397.0 eV, which resulted from nitrogen presence in the samples. The N1 signal is related to the presence of non-charged nitrogen, ascribed to the N–C bonding. On the other hand, the signal designated as N2 indicates the presence of negatively charged nitrogen resulting from Mo–N bonding [64]. Comparing the results obtained for different HCl concentrations, it may be stated that the 0.5 M and 1 M samples are characterized by the highest nitrogen content, and the difference is particularly clear due to the higher intensity of the N1 signal. The atomic percentage of nitrogen estimated from XPS analysis, % ratio of both N1 to N2 and total N to Mo is presented in Table S1.

3.2. Electrochemical measurements for $\text{TiO}_2/\text{N-MoS}_2$ electrode materials prepared with different HCl concentrations

For the evaluation of the electrochemical properties, electrode materials synthesized with various HCl concentrations were investigated in 3-electrode configuration in 1 M H_2SO_4 . Firstly, using cyclic voltammetry, the potential range within which electrode materials are capable of charge storage was determined and the results are presented in Fig. 5a. It turned out that $\text{TiO}_2/\text{N-MoS}_2$ electrode materials obtained with both 0.5 M and 1 M HCl were characterized by the best capacitive properties, which can be observed in the cyclic voltammetry curves. It was also confirmed during galvanostatic charge and discharge measurements (see Fig. 5b) – the results show that for the $\text{TiO}_2/\text{N-MoS}_2$ electrode material synthesized with 0.5 M HCl, the areal capacitance value was the highest, which was indicated by the initial capacitance of 320 mF cm^{-2} , as well as it was characterized by better capacitance retention after 1000 cycles in comparison with other materials. It is worth mentioning that the deposited MoS_2 layer was not very thick at all, (which could be the cause of such improved capacitance value), and despite its unevenness, it was only up to several micrometers at its thickest point (see Fig. S3b). Therefore, for the $\text{TiO}_2/\text{N-MoS}_2$ electrode material presenting the best capacitive properties, a further study on the

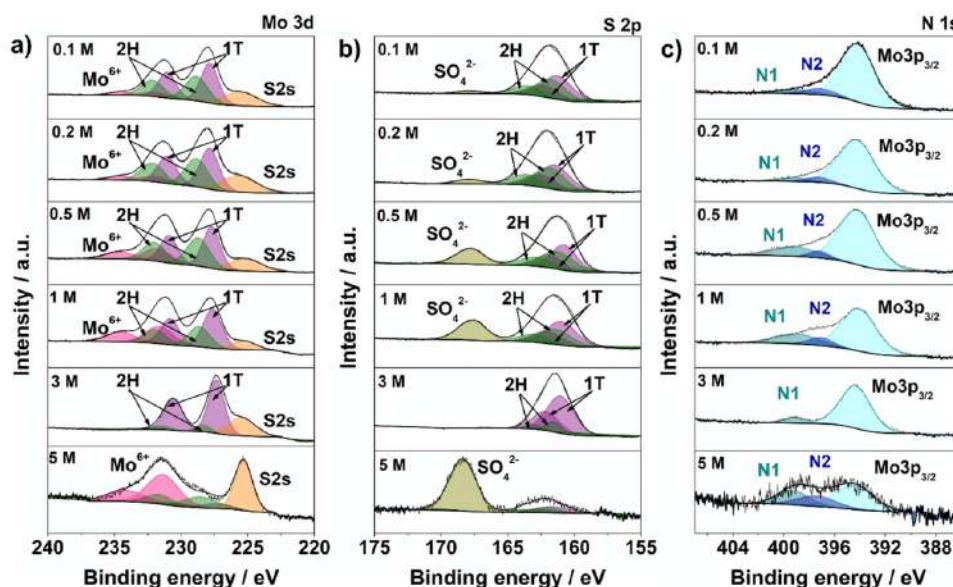


Fig. 4. XPS results for $\text{TiO}_2/\text{N-MoS}_2$ electrode materials obtained after hydrothermal synthesis performed with different hydrochloric acid concentrations.

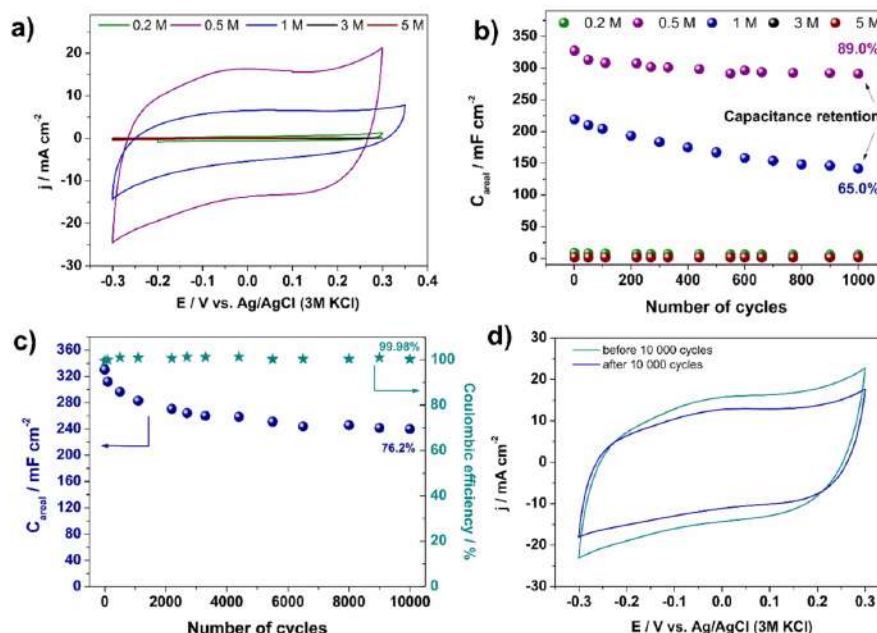


Fig. 5. a) CV curves ($v = 50 \text{ mV s}^{-1}$) recorded in 1 M H_2SO_4 for $\text{TiO}_2/\text{N-MoS}_2$ electrode materials prepared with various HCl concentrations; b) Areal capacitance value during 1000 cycles, calculated on the basis of GCD tests; c) Areal capacitance and coulombic efficiency for $\text{TiO}_2/\text{N-MoS}_2$ (0.5 M) electrode material during 10 000 GCD cycles; d) CV curves for $\text{TiO}_2/\text{N-MoS}_2$ (0.5 M) before and after 10 000 GCD cycles.

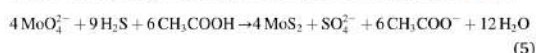
ability of energy storage was conducted. After 10000 galvanostatic charge-discharge cycles, electrode material was characterized by the areal capacitance of 240 mF cm^{-2} , with the coulombic efficiency of around 99.98 % (see Fig. 5c). Moreover, the shape of the cyclic voltammetry curve after galvanostatic tests indicates that despite the loss of some capacitance, the material is still capable of charge storage.

3.3. The influence of HCl concentration on the growth of MoS_2 on TiO_2 nanotubes substrate

MoS_2 synthesis using the hydrothermal method has been repeatedly reported in the literature, however, the mechanism of molybdenum sulfide crystal growth in solution still remains an open question. In order to explore this issue, the influence of hydrochloric acid concentration on the properties of the obtained MoS_2 layer was analyzed, and the possible course of the reaction was proposed. The synthesis of molybdenum sulfide begins with the hydrolysis of thioacetamide, and this process can be efficiently catalyzed and accelerated through the acidic reaction medium [65–67], and the obtained hydrogen sulfide forms the following equilibrium when dissolved in water:



The hydrogen sulfide obtained in the reaction is the main source of sulfur in the further synthesis process, and acts as a reducing agent that reacts with the molybdenum precursor present in the solution [68]:



When hydrochloric acid was not present during the synthesis, no formation of nanostructures was observed, and the electrochemical properties of the material were insufficient (see Figure S4). Similar observations were made for the synthesis with low concentrations of hydrochloric acid, but increasing its concentration to 0.5 M resulted in a significant improvement in the material's capacitive properties, and the formation of nanosheet structures was observed, which is attributed to the increased amount of H_2S , and thus the accelerated reaction of thioacetamide hydrolysis in a more acidic environment. Furthermore, according to the TEM measurements, it may also be concluded that all together with the increasing HCl concentration, the crystallinity of the MoS_2 was improved, and similar observations were reported by Matsui et. al for the ZrO_2 synthesis [69], as well as by Li et al. for the perovskites synthesis [70], with pointing out the fact that the concentration of H^+ ions significantly affects the single particle size. However, no further enhancement in electrochemical properties was observed with increasing acid concentration. The reason for such a phenomenon may be the unfavorable interference of HCl with the substrate material – TiO_2 nanotubes. As the results presented above show, high concentrations of HCl not only changed the surface of the nanotubes but also contributed to the formation of an additional TiO_2 crystal phase (rutile). As a result, it hindered the effective deposition of molybdenum sulfide on the substrate, and the effect was intensified with an increase in the acid concentration.

3.4. The role of aniline (ANI) and ammonium persulfate (APS) in the hydrothermal synthesis of $\text{TiO}_2/\text{N-MoS}_2$

During the simultaneous synthesis and deposition of molybdenum sulfide on TiO_2 substrate by hydrothermal method, apart from precursors of molybdenum and sulfur, aniline and ammonium persulfate were added. According to the literature, the synthesis of molybdenum

sulfide altogether with polyaniline, commonly with the assistance of hydrothermal synthesis, is frequently reported [71–76] and considered successful. The presented synthesis was also initially aimed at obtaining a layer of a hybrid MoS_2/PANI electrode material, deposited on a TiO_2 substrate. However, the results of the solid-state physics analysis do not indicate the presence of polyaniline in the electrode material. Moreover, the results obtained using cyclic voltammetry also do not evidence that polyaniline was effectively deposited on the TiO_2 substrate (see Fig. 5a), as characteristic peaks related to the polyaniline redox reactions [77] can't be distinguished. Unexpectedly, when aniline and ammonium persulfate were excluded from the synthesis, the electrode material lost a significant part of its capacitive properties, which is presented in Fig. 6a. On the basis of the cyclic voltammetry results, it may be concluded that the addition of aniline or ammonium persulfate separately caused a similar effect and the presence of both during synthesis somehow contributes to improved electrochemical performance. In order to investigate the differences between the electrode materials and reveal the reason for the improved charge storage ability with the ANI and APS addition, scanning electron microscopy was used for the morphology study, and the results are presented in Fig. 6b. Each synthesis was conducted with a 0.5 M hydrochloric acid concentration. For the electrodes prepared with aniline and APS, the structure of the nanosheet is observed, but in general, they look quite alike. One may say that the structure of the nanosheets is more developed, especially in the presence of both ANI and APS, and what was pointed out by TEM measurements is that at the edges of these structures a crystalline form is observed in particular. Moreover, although Raman spectroscopy (Fig. 6c) showed no significant changes in the composition, only confirming the presence of the 2H MoS_2 phase in each electrode material, XRD analysis indicated some differences. XRD measurements were performed on the layer scraped off the TiO_2 substrate in order to further analyze the properties of the deposited layer. As presented in Fig. 6d, when ANI and APS were added during the synthesis, some characteristic diffraction peaks at 12.85° , 32.30° , 35.44° , and 57.04° may be distinguished that could be assigned to (002), (100), (102) and (110) planes

oh hexagonal phase of MoS_2 , respectively (JCPDS No. 37–1492). Also, two more diffraction peaks at 28.28° and 43.11° with considerably lower intensities are visible, corresponding to the (004) and (006) planes [55]. However, when the additional reagents were not included in the synthesis, a decrease in the intensity of the diffraction peaks was observed, especially when both of them were not present. The results indicate that the addition of aniline and ammonium persulfate may significantly influence the crystallinity of the MoS_2 layer.

To further evaluate the differences between the electrode materials, XPS analysis was performed with the recorded spectra shown in Fig. 7. The results are consistent with the ones obtained from other techniques, indicating the presence of both hexagonal and trigonal phases of molybdenum sulfide (see Fig. 7a). Moreover, for each sample, a small amount of molybdenum in a 6+ oxidation state was detected, probably related to the sample oxidation upon the air. Sulfur was also identified in each electrode material (see Fig. 7b), with trace amounts of SO_4^{2-} , which can be related both to the presence of synthesis residues, but also the S^{2-} conversion [63]. Most informative are the results for the region of nitrogen binding energy, presented in Fig. 7c. It may be observed that when aniline and ammonium persulfate were not present during the synthesis, the XPS profile of the N1 s mainly consists only of the band at 394.3 eV, assigned to Mo 3p_{3/2}, with a weak signal at 397.0 eV indicating the presence of negatively charged nitrogen resulted from Mo–N bonding. On the other hand, the band at 399.5 eV is only recognizable for the sample with both ANI and APS, indicating that in this case, the doping process was most successful.

The investigation of the influence of both aniline and ammonium persulfate was also evaluated for the impact on the mechanism by which energy storage takes place. Pseudocapacitance is frequently associated with surface redox reactions, however, these reactions usually take place not only at the interface between electrode and electrolyte but also throughout the electrode material, altogether with reversible insertion of charge balancing ions [78]. According to Trasatti's approach [79], it is possible to estimate the contribution of the "outer" and "inner" surface of the electrode in energy storage processes, using Eq. (6):

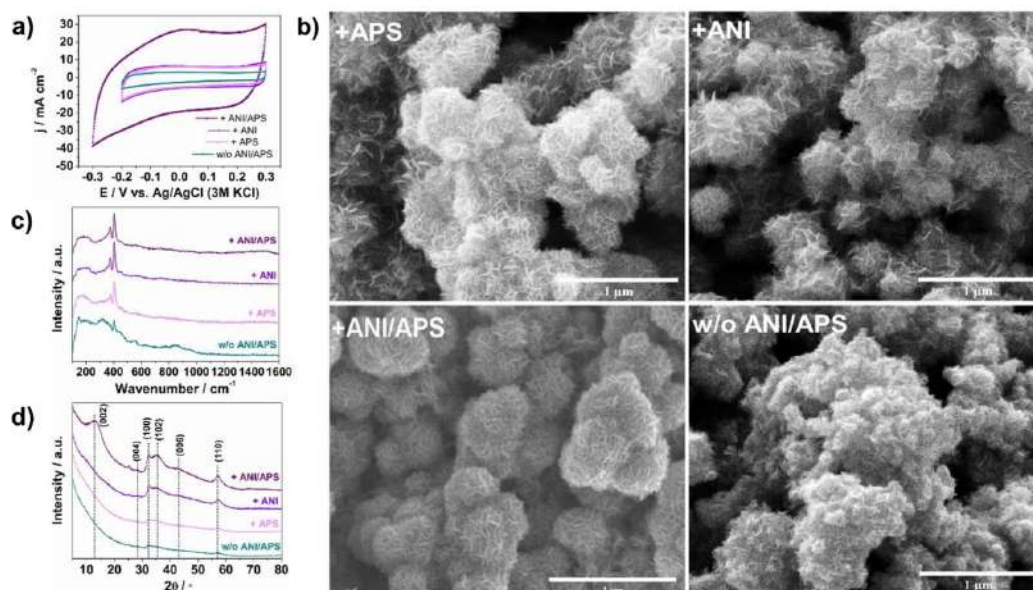


Fig. 6. a) CV curves ($v = 50 \text{ mV s}^{-1}$) recorded in 1 M H_2SO_4 , b) SEM images, c) Raman spectroscopy and d) XRD results for $\text{TiO}_2/\text{N-MoS}_2$ and $\text{TiO}_2/\text{MoS}_2$ electrode materials prepared with and without the addition of aniline and ammonium persulfate during synthesis, respectively (with 0.5 M HCl).

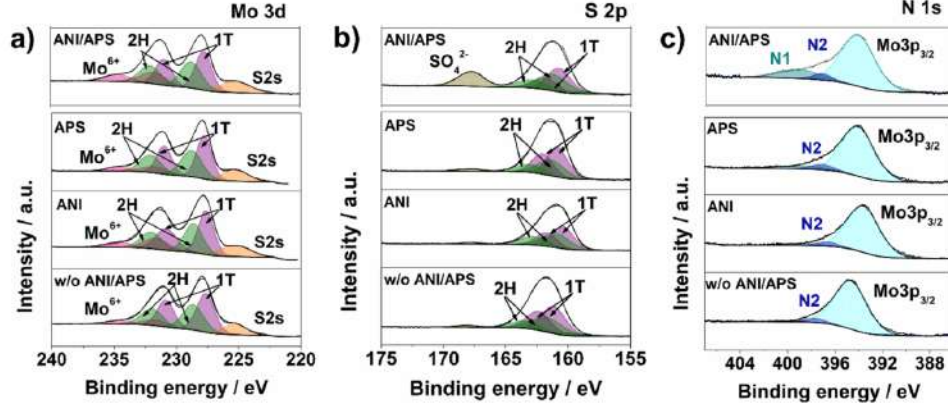


Fig. 7. XPS spectra of a) Mo3d, b) S2p and c) N1s for $\text{TiO}_2/\text{N-MoS}_2$ and $\text{TiO}_2/\text{MoS}_2$ electrode materials prepared with and without the addition of aniline and ammonium persulfate during synthesis (with 0.5 M HCl).

$$q_T = q_i + q_o \quad (6)$$

where q_T represents the total amount of charge, q_i stands for the charge at the inner surface and q_o represents the charge stored at the “inner” surface and q_o is related to the charge stored at the outer surface. After cyclic voltammetry measurements at different scan rates, a linear relationship between the reciprocal of the calculated areal capacitance (C^{-1}) and the square root of the scan rate (see Eq. (7)):

$$\text{C}^{-1} = \text{const} \cdot v^{1/2} + \text{C}_T^{-1} \quad (7)$$

C_T corresponds to the sum of both “outer” and “inner” capacitance. Eventually, the dependence between the capacitance and the reciprocal of the scan rate enables estimating the contribution of the “outer” layer (C_o), according to Eq. (8):

$$\text{C} = \text{const} \cdot v^{-1/2} + \text{C}_o \quad (8)$$

On the other hand, Conway’s approach [80], modified by Dunn et al. for nanostructured transition metal oxides, is based on the statement that the total current response is the sum of the current related to the diffusion-limited and surface-controlled processes:

$$i(V) = k_1 v + k_2 v^{1/2} \quad (9)$$

The linear dependence between the slope (k_1) and Y-intercept (k_2) allows for determining the contribution of both surface-confined and diffusion controlled processes to the total charge being stored:

$$\frac{i(V)}{v^{1/2}} = k_1 v^{1/2} + k_2 \quad (10)$$

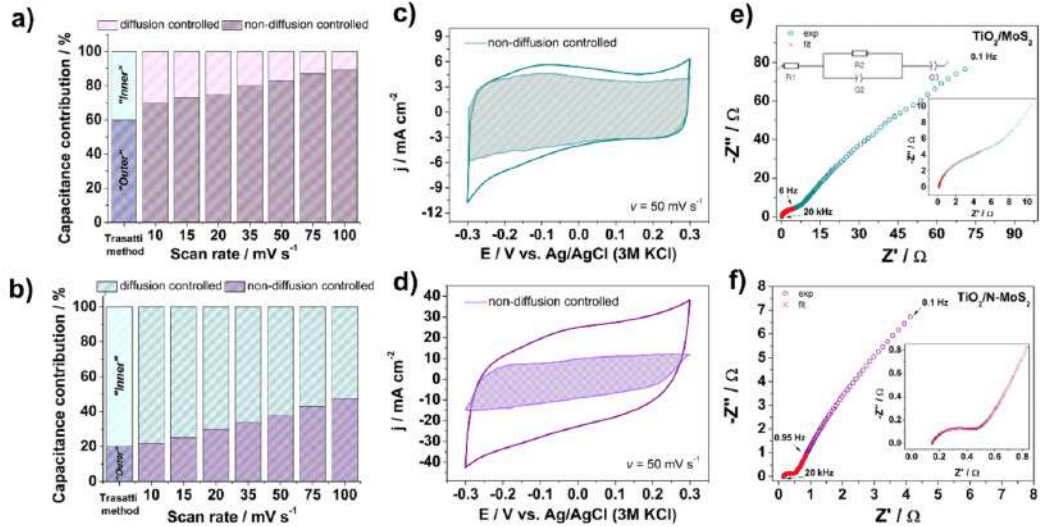


Fig. 8. Comparison of the contribution of the inner surface (and diffusion controlled), an outer surface (and non-diffusion controlled) capacitance calculated by Trasatti and Dunn’s method, respectively, for a) $\text{TiO}_2/\text{MoS}_2$ (without ANI and APS) and b) for $\text{TiO}_2/\text{N-MoS}_2$ (with ANI and APS); CV curves for c) $\text{TiO}_2/\text{MoS}_2$ and d) $\text{TiO}_2/\text{N-MoS}_2$ with non-diffusion controlled capacitance contribution; EIS curves with electrical equivalent circuit used for both e) $\text{TiO}_2/\text{MoS}_2$ and f) $\text{TiO}_2/\text{N-MoS}_2$.

The results for the $\text{TiO}_2/\text{N-MoS}_2$ and $\text{TiO}_2/\text{MoS}_2$ electrode materials are presented in Fig. 8. The values obtained from Conway's analysis show that when ANI and APS were not present during the synthesis, the surface-confined processes have a major contribution to energy storage (Fig. 8a). Furthermore, Trasatti's approach also points out the enhanced contribution of the "outer" layer. On the other hand, when the introduction of nitrogen atoms was performed during the synthesis, mechanisms of energy storage changed significantly. For the $\text{TiO}_2/\text{N-MoS}_2$ electrode material, the "outer" layer contribution decreased to 20 % (according to the Trasatti method), and a similar dependence was observed for the results obtained from Dunn's approach (Fig. 8b), namely the diffusion of ions into the whole body of the material plays a major role in charge storage. An exemplary cyclic voltammetry curves for $\text{TiO}_2/\text{MoS}_2$ and $\text{TiO}_2/\text{N-MoS}_2$ with the calculated non-diffusion controlled processes contribution is presented in Fig. 8c and 8d. Such a transition from surface confinement to diffusion limitation may be observed when the path for ion transport lengthens due to the increase in layer thickness [81]. The comparison of the layers thickness is presented in Figure S5, and the results indicate that when the synthesis was performed with ANI and APS, the thickness of N-MoS₂ layer was increased (which thickness is around 1.8 μm in comparison with 0.6 μm). The electrode materials were also characterized by electrochemical impedance spectroscopy. The spectra of $\text{TiO}_2/\text{MoS}_2$ and $\text{TiO}_2/\text{N-MoS}_2$ are presented in Fig. 8e and 8f. A semicircle may be distinguished in the high-frequency region of the spectra, and their diameter corresponds to the charge transfer resistance R_{ct} (R2). The decreased slope in the low-frequency region may indicate pseudocapacitive behavior [78,82]. Nevertheless, the electrode material that consists of differently obtained MoS₂ on the TiO_2 nanotubes is a very complex system and elaboration of the appropriate model is difficult to achieve. Thus, here the fragmentary analysis that covers only the high-frequency range was performed. The same electrical equivalent circuit (EEC) was applied for all spectra (shown in the inset of Fig. 8e), where Q stands for constant phase element (CPE). The results are shown in Table S2. R_e (R1) values that originate from the electrolyte and cable resistance are the same for both spectra ($\sim 0.147 \Omega$). As could be predicted from the shapes of the spectra, the R_{ct} for N-modified electrode material is lower (0.33 Ω) than for $\text{TiO}_2/\text{MoS}_2$ (5.27 Ω), suggesting that nitrogen atoms in the MoS₂ structure can significantly increase its conductivity [83]. The P value of

CPE that corresponds to the capacitance of electrode material is much higher for $\text{TiO}_2/\text{N-MoS}_2$ which is in good agreement with cyclic voltammetry curves shown in Fig. 8c and 8d. Moreover, the n values are quite close to 1 (~ 0.91) for $\text{TiO}_2/\text{MoS}_2$ thus both CPEs act here almost as capacitors. The values of n for $\text{TiO}_2/\text{N-MoS}_2$ (0.73 and 0.78) suggest that diffusion-related phenomena may contribute to the CPEs used in the analysis which is in line with the results presented in Fig. 8a and 8b.

3.5. Electrochemical measurements of N-MoS₂/TiO₂ electrode material in symmetric supercapacitor (SS)

Finally, the $\text{TiO}_2/\text{N-MoS}_2$ electrode material was investigated in the symmetric two-electrode configuration in "coffee bag" construction. In order to determine the operating voltage window, cyclic voltammetry measurements were applied (see Figure S6). On this basis, the voltage value was fixed at 0.6 V, for which the galvanostatic charge-discharge tests at different current densities were performed. Regardless of the current density, only a small iR drop was observed during the discharge process in Fig. 9a. Moreover, as presented in Fig. 9b, the specific capacitance of 80 F g^{-1} was achieved at 3 A g^{-1} , as well as areal capacitance of 85 mF cm^{-2} at 2.6 mA cm^{-2} . The highest specific capacitance value, 140 F g^{-1} , was observed for the current density of 0.7 A g^{-1} . One of the crucial parameters for supercapacitors, which is long-term cycling stability, was also evaluated for the symmetrical device for the current density of 3 A g^{-1} , as displayed in Fig. 9c. The device was characterized by the initial specific capacitance of 76 F g^{-1} and areal capacitance of 70 mF cm^{-2} , altogether with the capacitance retention of 84 % after 15 000 cycles. Taking SEM images allowed to establish that the electrode morphology did not change significantly, and that the nanostructures retained their spherical shape with nanosheet structures around them (see Figure S7). However, it was also observed that in some places the shell in the form of nanosheets has detached, which may have been one of the reasons for the decrease in capacitance after cycles. The superior electrochemical performance of the device was also confirmed by the coulombic efficiency of almost 100 % throughout the whole long-term cycling test (see Fig. 9d). Moreover, the triangle shape of chronopotentiometry curves before and after the cycles, presented in the inset of Fig. 9d, indicates that even after long-term measurements, the electrode material in the two-electrode configuration was

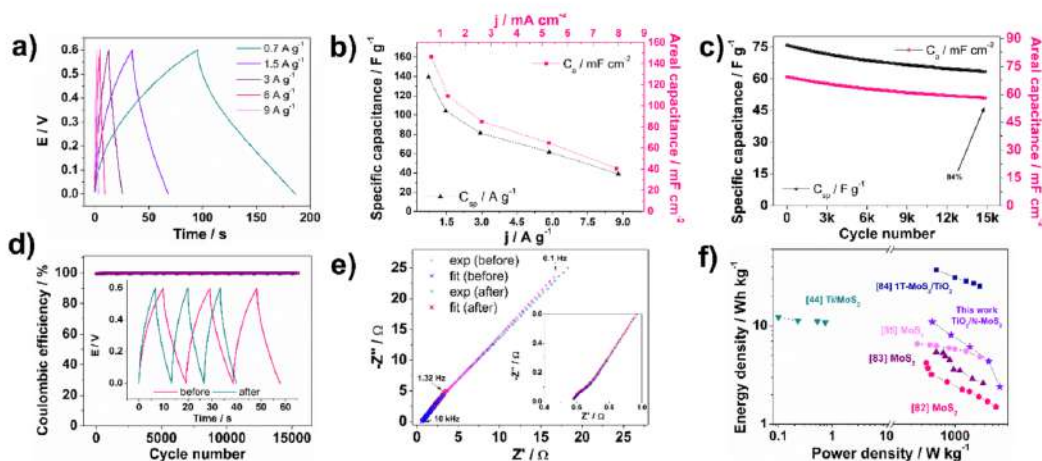


Fig. 9. a) GCD curves for different current densities for $\text{TiO}_2/\text{N-MoS}_2$ SS; b) Specific and areal capacitance the $\text{TiO}_2/\text{N-MoS}_2$ SS as a function of applied current density; c) Long-term cycling testing at 3 A g^{-1} ; d) Coulombic efficiency during long-term cycling with the inset presenting GCD curves for the initial and final cycles at specific current of 3 A g^{-1} ; e) experimental (o) and fitted with EEC (x) EIS data recorded before and after long-term cycling; f) Ragone plot with the results for $\text{TiO}_2/\text{N-MoS}_2$ SS compared with literature reports on MoS₂-based electrode materials.

characterized by capacitive properties, which is also consistent with EIS results (Fig. 9e). The analysis of the high-frequency range was performed using the same EEC as shown in Fig. 8e. The differences between the spectra recorded before and after the charge/discharge test are subtle, however, according to the fitting results a slight increase in charge transfer resistance with a simultaneous decrease in capacitance has been determined. The results are shown in Table S2. As shown in Fig. 9f, $\text{TiO}_2/\text{N-MoS}_2$ SS presented a maximum specific energy of 11.1 W kg^{-1} (at power density of 432.8 Wh kg^{-1}), and the highest specific power of $5193.4 \text{ Wh kg}^{-1}$ (at specific energy of 2.4 W kg^{-1}) at high current density of 9 A g^{-1} , which is much higher in comparison with the literature results obtained for comparable current values [46,84–87]. Despite the fact that higher specific energy has been presented in some literature reports, it is highly likely to achieve such results also with the $\text{TiO}_2/\text{N-MoS}_2$ material, if used in an asymmetric construction.

4. Conclusions

In summary, the study focused on the synthesis of N-MoS_2 directly on a solid substrate of TiO_2 nanotubes using the hydrothermal method. The synthesis procedure was evaluated for the effect of hydrochloric acid, and on the basis of the results it was concluded that higher concentration promoted more effective synthesis of molybdenum sulfide. However, an excessive increase in HCl concentration led to both structure and morphology disruption of the TiO_2 substrate. The $\text{TiO}_2/\text{N-MoS}_2$ electrode material obtained with 0.5 M HCl was characterized by the highest areal capacitance value of 320 mF cm^{-2} and the most appropriate overall electrochemical performance for energy storage applications in general. Moreover, the influence of aniline monomer and ammonium persulfate during the synthesis was investigated. The results indicated that their addition not only significantly increased the crystallinity of the material, but also contributed to the enhanced capacitive properties. The reason for this was the introduction of nitrogen atoms into the structure of MoS_2 , which also led to change in charge storage mechanism – from the surface confinement control, a major contribution was ascribed to diffusion controlled processes related to Faradaic capacitance. Finally, the symmetrical device constructed of two $\text{TiO}_2/\text{N-MoS}_2$ electrodes was characterized by the specific capacitance of specific capacitance of 76 F g^{-1} and areal capacitance of 70 mF cm^{-2} , with the superior coulombic efficiency and 84% of capacitance retention after $15,000$ cycles. Furthermore, the obtained values of energy and power density (11.1 W kg^{-1} and $5193.4 \text{ Wh kg}^{-1}$, respectively) indicate that the presented synthesis of MoS_2 directly on solid substrates may be an effective method for the preparation of electrode materials for high-power applications.

CRedit authorship contribution statement

Z. Zarach: Conceptualization, Data curation, Formal analysis, Investigation, Methodology, Validation, Visualization, Writing – original draft, Writing – review & editing. **A.P. Nowak:** Data curation, Formal analysis, Supervision, Validation, Writing – review & editing. **K. Trzcinski:** Formal analysis, Methodology, Validation, Writing – review & editing. **G. Gajowiec:** Investigation, Resources. **G. Trykowski:** Investigation, Resources. **M. Sawczak:** Investigation, Resources. **M. Łapiński:** Investigation, Resources. **M. Szkoda:** Formal analysis, Funding acquisition, Methodology, Resources, Supervision, Validation, Writing – review & editing.

Declaration of Competing Interest

The authors declare the following financial interests/personal relationships which may be considered as potential competing interests: Mariusz Szkoda reports financial support was provided by National Centre for Research and Development.

Data availability

Data will be made available on request.

Acknowledgments

Funding: This work was supported by The National Centre for Research and Development (Grant no LIDER/15/0088/L-10/18/NCBR/2019).

Appendix A. Supplementary material

Supplementary data to this article can be found online at <https://doi.org/10.1016/j.apsusc.2022.155187>.

References

- [1] C. Li, M.M. Islam, J. Moore, J. Sleppy, C. Morrison, K. Konstantinov, S.X. Dou, C. Renduchintala, J. Thomas, Wearable energy-smart ribbons for synchronous energy harvest and storage, *Nat. Commun.* 2016 71. 7 (2016) 1–10. [10.1038/ncomms13319](https://doi.org/10.1038/ncomms13319).
- [2] T.P. Narins, The battery business: Lithium availability and the growth of the global electric car industry, *Extr. Ind. Soc.* 4 (2017) 321–328, <https://doi.org/10.1016/j.exis.2017.01.013>.
- [3] H. Marzougui, M. Amari, A. Kadri, F. Bacha, J. Ghoul, Energy management of fuel cell/battery/ultracapacitor in electrical hybrid vehicle, *Int. J. Hydrogen Energy*. 42 (2017) 8857–8869, <https://doi.org/10.1016/j.ijhydene.2016.09.190>.
- [4] J. Pablo Esquivel, P. Alday, O.A. Ibrahim, B. Fernández, E. Kjeang, N. Sabaté, J. P. Esquivel, P. Alday, N. Sabaté, O.A. Ibrahim, E. Kjeang, B. Fernández, A Metal-Free and Biologically Degradable Battery for Portable Single-Use Applications, *Adv. Energy Mater.* 7 (2017) 1700275, <https://doi.org/10.1002/AENM.201700275>.
- [5] S.W. Zhang, B.S. Yin, C. Liu, Z.B. Wang, D.M. Gu, A lightweight, compressible and portable sponge-based supercapacitor for future power supply, *Chem. Eng. J.* 349 (2018) 509–521, <https://doi.org/10.1016/j.cej.2018.05.125>.
- [6] A. Scalia, F. Bella, A. Lamberti, S. Bianco, C. Gerbaldi, E. Tresso, C.F. Pirri, A flexible and portable powerpack by solid-state supercapacitor and dye-sensitized solar cell integration, *J. Power Sources*. 359 (2017) 311–321, <https://doi.org/10.1016/j.jpowsour.2017.05.072>.
- [7] S. Lv, L. Ma, X. Shen, H. Tong, Recent design and control of carbon materials for supercapacitors, *J. Mater. Sci.* 56 (2021) 1919–1942, <https://doi.org/10.1007/s10853-020-05351-6/FIGURES/7>.
- [8] D.A.C. Brownson, D.K. Kampouris, C.E. Banks, An overview of graphene in energy production and storage applications, *J. Power Sources*. 196 (2011) 4873–4885, <https://doi.org/10.1016/j.jpowsour.2011.02.022>.
- [9] A.K. Geim, K.S. Novoselov, The rise of graphene, in: *Nanosci. Technol. A Collect. Rev. from Nat. Journals*, World Scientific Publishing Co., 2009, pp. 11–19. [10.1142/9789814287005_0002](https://doi.org/10.1142/9789814287005_0002).
- [10] C.N.R. Rao, A.K. Sood, K.S. Subrahmanyam, A. Govindaraj, Graphene: The New Two-Dimensional Nanomaterial, *Angew. Chemie Int. Ed.* 48 (2009) 7752–7777, <https://doi.org/10.1002/ANGE.200901678>.
- [11] B. Jache, P. Adelhelm, Use of Graphite as a Highly Reversible Electrode with Superior Cycle Life for Sodium-Ion Batteries by Making Use of Co-Intercalation Phenomena, *Angew. Chemie*. 126 (2014) 10333–10337, <https://doi.org/10.1002/ANGE.201403734>.
- [12] Y. Sun, D. Chen, Z. Llang, Two-dimensional MXenes for energy storage and conversion applications, *Mater. Today, Energy*. 5 (2017) 22–36, <https://doi.org/10.1016/j.mtener.2017.04.008>.
- [13] B. Anasori, M.R. Lukatskaya, Y. Gogotsi, 2D metal carbides and nitrides (MXenes) for energy storage, *Nat. Rev. Mater.* 2017 22. 2 (2017) 1–17. [10.1038/natrevmats.2016.98](https://doi.org/10.1038/natrevmats.2016.98).
- [14] H.T. Tan, W. Sun, L. Wang, Q. Yan, 2D Transition Metal Oxides/Hydroxides for Energy-Storage Applications, *ChemNanoMat* 2 (2016) 562–577, <https://doi.org/10.1002/CNMA.201500177>.
- [15] J. Li, Z. Liu, Q. Zhang, Y. Cheng, B. Zhao, S. Dai, H.H. Wu, K. Zhang, D. Ding, Y. Wu, M. Liu, M.S. Wang, Anion and cation substitution in transition-metal oxides nanosheets for high-performance hybrid supercapacitors, *Nano Energy* 57 (2019) 22–33, <https://doi.org/10.1016/j.nanoen.2018.12.011>.
- [16] R. Suresh Babu, R. Vinodh, A.L.F. de Barros, L.M. Samyn, K. Prasanna, M.A. Maier, C.H.F. Alves, H.J. Kim, Asymmetric supercapacitor based on carbon nanofibers as the anode and two-dimensional copper cobalt oxide nanosheets as the cathode, *Chem. Eng. J.* 366 (2019) 390–403, <https://doi.org/10.1016/j.cej.2019.02.108>.
- [17] K.S. Ahn, R. Vinodh, B.G. Pollet, R.S. Babu, V. Ramkumar, S.C. Kim, K. Krishnakumar, H.J. Kim, A high-performance asymmetric supercapacitor consists of binder free electrode materials of bimetallic hydrogen phosphate (MnCo (HPO₄)) hexagonal tubes and graphene ink, *Electrochim. Acta*. 426 (2022), 140763, <https://doi.org/10.1016/j.electacta.2022.140763>.
- [18] G. Zhang, H. Liu, J. Qu, J. Li, Two-dimensional layered MoS₂: rational design, properties and electrochemical applications, *Energy Environ. Sci.* 9 (2016) 1190–1209, <https://doi.org/10.1039/C5EE03761A>.
- [19] D. (David) Xia, F. Gong, X. Pei, W. Wang, H. Li, W. Zeng, M. Wu, D. V. Papavassiliou, Molybdenum and tungsten disulfides-based nanocomposite films for

- energy storage and conversion: A review, *Chem. Eng. J.* 348 (2018) 908–928, [10.1016/j.cej.2018.04.207](https://doi.org/10.1016/j.cej.2018.04.207).
- [20] Q. Ji, C. Li, J. Wang, J. Niu, Y. Gong, Z. Zhang, Q. Fang, Y. Zhang, J. Shi, L. Liao, X. Wu, L. Gu, Z. Liu, Y. Zhang, Metallic vanadium disulfide nanosheets as a platform material for multifunctional electrode applications, *Nano Lett.* 17 (2017) 4908–4916, <https://doi.org/10.1021/ACS.NANO.7B01914>/ASSET/IMAGES/LARGE/NL-2017-01914V_0005.JPEG.
- [21] M. Liu, Z. Wang, J. Liu, G. Wei, J. Du, Y. Li, C. An, J. Zhang, Synthesis of few-layer 1T'-MoTe₂ ultrathin nanosheets for high-performance pseudocapacitors, *J. Mater. Chem. A* 5 (2017) 1035–1042, <https://doi.org/10.1039/C6TA08206H>.
- [22] S. Yuan, S.Y. Pang, J. Hao, 2D transition metal dichalcogenides, carbides, nitrides, and their applications in supercapacitors and electrocatalytic hydrogen evolution reaction, *Appl. Phys. Rev.* 7 (2020), 021304, <https://doi.org/10.1063/5.0005141>.
- [23] S. Liang, J. Zhou, J. Liu, A. Pan, Y. Tang, T. Chen, G. Fang, PVP-assisted synthesis of MoS₂ 2D nanosheets with improved lithium storage properties, *CrystEngComm* 15 (2013) 4998–5002, <https://doi.org/10.1039/C3CE40392K>.
- [24] Y. Zhang, W. Zeng, Y. Li, Hydrothermal synthesis and controlled growth of hierarchical 3D flower-like MoS₂ nanospheres assisted with CTAB and their NO₂ gas sensing properties, *Appl. Surf. Sci.* 455 (2018) 276–282, <https://doi.org/10.1016/j.apsusc.2018.05.224>.
- [25] S. Zhao, G. Wang, J. Liao, S. Lv, Z. Zhu, Z. Li, Vertically aligned MoS₂/ZnO nanowires nanostructures with highly enhanced NO₂ sensing activities, *Appl. Surf. Sci.* 456 (2018) 808–816, <https://doi.org/10.1016/j.apsusc.2018.06.103>.
- [26] C. Zhang, H. Bin Wu, Z. Guo, X.W. Lou, Facile synthesis of carbon-coated MoS₂ nanorods with enhanced lithium storage properties, *Electrochem. Commun.* 20 (2012) 7–10, <https://doi.org/10.1016/j.elecom.2012.03.039>.
- [27] M. Wang, G. Li, H. Xu, Y. Qian, J. Yang, Enhanced lithium storage performances of hierarchical hollow MoS₂ 2D nanoparticles assembled from nanosheets, *ACS Appl. Mater. Interfaces* 5 (2013) 1003–1008, <https://doi.org/10.1021/AM3026954>/SUPPL_FILE/AM3026954_SI_001.PDF.
- [28] M. Li, A. Addad, Y. Zhang, A. Barras, P. Roussel, M.A. Amin, S. Szmerits, R. Boukherroub, Flower-like Nitrogen-co-doped MoS₂@RGO Composites with Excellent Stability for Supercapacitors, *ChemElectroChem* 8 (2021) 2903–2911, <https://doi.org/10.1002/CELC.202100401>.
- [29] Y. Chao, Y. Ge, Z. Chen, X. Cui, C. Zhao, C. Wang, G.G. Wallace, One-Pot Hydrothermal Synthesis of Solution-Processable MoS₂/PEDOT:PSS Composites for High-Performance Supercapacitors, *ACS Appl. Mater. Interfaces* 13 (2021) 7285–7296, <https://doi.org/10.1021/ACSAMI.1C02143>/ASSET/IMAGES/LARGE/AMOC21439_0007.JPEG.
- [30] D. Cao, Q. Wang, S. Zhu, X. Zhang, Y. Li, Y. Cui, Z. Xue, S. Gao, Hydrothermal construction of flower-like MoS₂ on TiO₂ NTs for highly efficient environmental remediation and photocatalytic hydrogen evolution, *Sep. Purif. Technol.* 265 (2021), 118463, <https://doi.org/10.1016/j.seppur.2021.118463>.
- [31] W.J. Li, E.W. Shi, J.M. Ko, Z.Z. Chen, H. Ogino, T. Fukuda, Hydrothermal synthesis of MoS₂ nanowires, *J. Cryst. Growth* 250 (2003) 418–422, [https://doi.org/10.1016/S0022-0248\(02\)02412-0](https://doi.org/10.1016/S0022-0248(02)02412-0).
- [32] W.H. Hu, G.Q. Han, F.N. Dai, Y.R. Liu, X. Shang, B. Dong, Y.M. Chai, Y.Q. Liu, C. G. Liu, Effect of pH on the growth of MoS₂ (002) plane and electrocatalytic activity for HER, *Int. J. Hydrogen Energy* 41 (2016) 294–299, <https://doi.org/10.1016/j.ijhydene.2015.09.076>.
- [33] Z. Xiong, G. Zhu, H. G. Shi, P.-u. Xu, H. Yi, Y. Mao, B. Wang, X. Yu, Hydrochloric Acid-Assisted Synthesis of Highly Dispersed MoS₂ Nanoflowers as the Cathode Material for Mg-Li Batteries, *ACS Appl. Energy Mater.* 5 (5) (2022) 6274–6281.
- [34] P. Wang, H. Sun, Y. Ji, W. Li, X. Wang, P. Wang, Y. Ji, W. Li, X. Wang, H. Sun, Three-Dimensional Assembly of Single-Layered MoS₂, *Adv. Mater.* 26 (2014) 964–969, <https://doi.org/10.1002/ADMA.201304120>.
- [35] F. Huang, R. Meng, Y. Sui, F. Wei, J. Qi, Q. Meng, Y. He, One-step hydrothermal synthesis of a CoS₂@MoS₂ nanocomposite for high-performance supercapacitors, *J. Alloys Compd.* 742 (2018) 844–851, <https://doi.org/10.1016/j.jallcom.2018.01.324>.
- [36] Y. Cai, H. Kang, F. Jiang, L. Xu, Y. He, J. Xu, X. Duan, W. Zhou, X. Lu, Q. Xu, The construction of hierarchical PEDOT@MoS₂ nanocomposite for high-performance supercapacitor, *Appl. Surf. Sci.* 546 (2021), 149088, <https://doi.org/10.1016/j.apsusc.2021.149088>.
- [37] J. Wang, L. Sun, Y. Gong, L. Wu, C. Sun, X. Zhao, X. Shi, Y. Lin, K. Wang, Y. Zhang, A CNT/MoS₂@PPy composite with double electron channels and boosting charge transport for high-rate lithium storage, *Appl. Surf. Sci.* 566 (2021), 150693, <https://doi.org/10.1016/j.apsusc.2021.150693>.
- [38] P. Sun, R. Wang, Q. Wang, H. Wang, X. Wang, Uniform MoS₂ nanolayer with sulfur vacancy on carbon nanotube networks as binder-free electrodes for asymmetrical supercapacitor, *Appl. Surf. Sci.* 475 (2019) 793–802, <https://doi.org/10.1016/j.apsusc.2019.01.007>.
- [39] S. Zhang, R. Hu, P. Dai, X. Yu, Z. Ding, M. Wu, G. Li, Y. Ma, C. Tu, Synthesis of rambutan-like MoS₂/mesoporous carbon spheres nanocomposites with excellent performance for supercapacitors, *Appl. Surf. Sci.* 396 (2017) 994–999, <https://doi.org/10.1016/j.apsusc.2016.11.074>.
- [40] B. Kirubasankar, M. Narayanasamy, J. Yang, M. Han, W. Zhu, Y. Su, S. Angaiah, C. Yan, Construction of heterogeneous 2D layered MoS₂/MXene nanohybrid anode material via interstratification process and its synergistic effect for asymmetric supercapacitors, *Appl. Surf. Sci.* 534 (2020), 147644, <https://doi.org/10.1016/j.apsusc.2020.147644>.
- [41] M.G. Fayed, S.Y. Attia, Y.F. Barakat, E.E. El-Shereafy, M.M. Rashad, S.G. Mohamed, Carbon and nitrogen co-doped MoS₂ nanoflakes as an electrode material for lithium-ion batteries and supercapacitors, *Sustain. Mater. Technol.* 29 (2021) e03036.
- [42] P. Tang, J. Jiao, Q. Fan, X. Wang, V. Agrawal, Q. Xu, Interlayer spacing engineering in N doped MoS₂ for efficient lithium ion storage, *Mater. Chem. Phys.* 261 (2021), 124166, <https://doi.org/10.1016/j.matchemphys.2020.124166>.
- [43] L.T. Bello, K.O. Otun, G. Nyongombe, O. Adedokun, G.L. Kabongo, M.S. Dhlamini, Non-modulated synthesis of cobalt-doped MoS₂ for improved supercapacitor performance, *Int. J. Energy Res.* 46 (2022) 8908–8918, <https://doi.org/10.1002/er.7765>.
- [44] J. Shao, Y. Li, M. Zhong, Q. Wang, X. Luo, K. Li, W. Zhao, Enhanced-performance flexible supercapacitor based on Pt-doped MoS₂, *Mater. Lett.* 252 (2019) 173–177, <https://doi.org/10.1016/j.matlet.2019.05.124>.
- [45] D. Vikraman, S. Hussain, K. Karuppasamy, A. Kathalingam, E.B. Jo, A. Sanmugam, J. Jung, H.S. Kim, Engineering the active sites tuned MoS₂ nanoarray structures by transition metal doping for hydrogen evolution and supercapacitor applications, *J. Alloys Compd.* 893 (2022), 162271, <https://doi.org/10.1016/j.jallcom.2021.162271>.
- [46] L. Wang, Y. Ma, M. Yang, Y. Qi, Titanium plate supported MoS₂ nanosheet arrays for supercapacitor application, *Appl. Surf. Sci.* 396 (2017) 1466–1471, <https://doi.org/10.1016/j.apsusc.2016.11.193>.
- [47] K. Krishnamoorthy, G.K. Veerasubramani, P. Pazhamalai, S.J. Kim, Designing two dimensional nanoarchitected MoS₂ sheets grown on Mo foil as a binder free electrode for supercapacitors, *Electrochim. Acta* 190 (2016) 305–312, <https://doi.org/10.1016/j.electacta.2015.12.148>.
- [48] J.M. Soon, K.P. Loh, Electrochemical double-layer capacitance of MoS₂ nanowall films, *Electrochem. Solid-State Lett.* 10 (2007) 250–254, <https://doi.org/10.1149/1.2778851>/XML.
- [49] N. Choudhary, M. Patel, Y.H. Ho, N.B. Dahotre, W. Lee, J.Y. Hwang, W. Choi, Directly deposited MoS₂ thin film electrodes for high performance supercapacitors, *J. Mater. Chem. A* 3 (2015) 24049–24054, <https://doi.org/10.1039/C5TA08095A>.
- [50] M. Szkoda, K. Siuzdak, A. Lisowska-Oleksiak, Optimization of electrochemical doping approach resulting in highly photoactive iodine-doped titania nanotubes, *J. Solid State Electrochem.* 20 (2016) 563–569, <https://doi.org/10.1007/s10008-015-3081-7>/FIGURES/7.
- [51] G. Woo An, L.K. Dhandole, H. Park, H. Sub Bae, M.A. Mahadik, J. Suk Jang, Enhanced Charge Transfer Process in Morphology Restructured TiO₂ Nanotubes via Hydrochloric Acid Assisted One Step In-Situ Hydrothermal Approach, *ChemCatChem* 11 (2019) 5606–5614, <https://doi.org/10.1002/CCTC.201901177>.
- [52] H. Zhang, P. Zhou, Z. Chen, W. Song, H. Ji, W. Ma, C. Chen, J. Zhao, Hydrogen-Bond Bridged Water Oxidation on 001 Surfaces of Anatase TiO₂, *J. Phys. Chem. C* 121 (2017) 2251–2257, <https://doi.org/10.1021/ACS.JPC.6B11900>/ASSET/IMAGES/LARGE/JP-2016-11900P_0004.JPEG.
- [53] T.D. Nguyen Phan, H.D. Pham, T. Viet Cuong, E. Jung Kim, S. Kim, E. Woo Shin, A simple hydrothermal preparation of TiO₂ nanomaterials using concentrated hydrochloric acid, *J. Cryst. Growth* 312 (2009) 79–85, <https://doi.org/10.1016/j.jcrysgro.2009.09.032>.
- [54] Q.Q. Fan, Z.Y. Qin, X. Liang, L. Li, W.H. Wu, M.F. Zhu, Reducing defects on multi-walled carbon nanotube surfaces induced by low-power ultrasonic-assisted hydrochloric acid treatment, <http://dx.doi.org/10.1080/17458080903536541>, 5 (2010) 337–347, <https://doi.org/10.1080/17458080903536541>.
- [55] G. Feng, A. Wei, Y. Zhao, J. Liu, Synthesis of flower-like MoS₂ nanosheets microspheres by hydrothermal method, *J. Mater. Sci. Mater. Electron.* 26 (2015) 8160–8166, <https://doi.org/10.1007/s10854-015-3476-3>/FIGURES/6.
- [56] K. Trzciński, M. Szkoda, Z. Zarach, M. Sawczak, A.P. Nowak, Towards spectroscopic monitoring of photoelectrodes: In-situ Raman photoelectrochemistry of a TiO₂/prussian blue photoanode, *Electrochim. Acta* 404 (2022), 139774, <https://doi.org/10.1016/j.electacta.2021.139774>.
- [57] M. Wtulić, M. Szkoda, G. Gajowiec, M. Gazda, K. Jurak, M. Sawczak, A. Lisowska-Oleksiak, Hydrothermal Cobalt Doping of Titanium Dioxide Nanotubes towards Photoanode Activity Enhancement, *Mater.* 2021, Vol. 14, Page 1507, 14 (2021) 1507, <https://doi.org/10.3390/MA14061507>.
- [58] N.T. Tung, D.N. Huyen, Effect of HCl on the Formation of TiO₂ Nanocrystallites, *J. Nanomater.* 2016 (2016), <https://doi.org/10.1155/2016/6547271>.
- [59] D. Sarkar, D. Das, S. Das, A. Kumar, S. Patil, K.K. Nanda, D.D. Sarma, A. Shukla, Expanding Interlayer Spacing in MoS₂ for Realizing an Advanced Supercapacitor, *ACS Energy Lett.* 4 (2019) 1602–1609, <https://doi.org/10.1021/ACSENERGYLETT.9B00983>/SUPPL_FILE/NZ9B00983_SI_001.PDF.
- [60] M. Chen, B. Ji, Z. Dai, X. Du, B. He, G. Chen, D. Liu, S. Chen, K.H. Lo, S. Wang, B. Zhou, H. Pan, Vertically-aligned 1T'/2H-MS₂ (M = Mo, W) nanosheets for surface-enhanced Raman scattering with long-term stability and large-scale uniformity, *Appl. Surf. Sci.* 527 (2020), 146769, <https://doi.org/10.1016/j.apsusc.2020.146769>.
- [61] Z. Zhang, Y. Dong, G. Liu, J. Li, H. Sun, H. Luo, S. Liu, The ultrafine monolayer 1T'/2H-MoS₂: Preparation, characterization and amazing photocatalytic characteristics, *Colloids Surfaces A Physicochem. Eng. Asp.* 589 (2020), 124431, <https://doi.org/10.1016/j.colsurfa.2020.124431>.
- [62] Y. Qi, Q. Xu, Y. Wang, B. Yan, Y. Ren, Z. Chen, CO₂-Induced Phase Engineering: Protocol for Enhanced Photoelectrocatalytic Performance of 2D MoS₂ Nanosheets, *ACS Nano* 10 (2016) 2903–2909, <https://doi.org/10.1021/ACS.NANO.5B00001>/SUPPL_FILE/NN6B00001_SI_001.PDF.
- [63] M. Hou, Y. Qiu, G. Yan, J. Wang, D. Zhan, X. Liu, J. Gao, I. Lai, Aging mechanism of MoS₂ nanosheets confined in N-doped mesoporous carbon spheres for sodium-ion batteries, *Nano Energy* 62 (2019) 299–309, <https://doi.org/10.1016/j.nanoen.2019.05.048>.
- [64] L.H. Kwak, L.S. Kwon, H.G. Abbas, J. Seo, G. Jung, Y. Lee, D. Kim, J.P. Ahn, J. Park, H.S. Kang, Intercalated complexes of 1T'-MoS₂ nanosheets with alkylated

- phenylenediamines as excellent catalysts for electrochemical hydrogen evolution, *J. Mater. Chem. A* 7 (2019) 2334–2343, <https://doi.org/10.1039/C8TA11085A>.
- [65] O.M. Peeters, E.A. Butler, D.G. Peters, E.H. Swift, Pathways in thioacetamide hydrolysis in aqueous acid: detection by kinetic analysis, *J. Chem. Soc. Perkin Trans. 2* (1974) 1832–1835, <https://doi.org/10.1039/P29740001832>.
- [66] E.A. Butler, D.G. Peters, E.H. Swift, Hydrolysis Reactions of Thioacetamide in Aqueous Solutions, *Anal. Chem.* 30 (1958) 1379–1383, <https://doi.org/10.1021/AC60140A027>, <https://doi.org/10.1021/ASSET/ACS0140A027.FP.PNG.V03>.
- [67] D. Rosenthal, T.I. Taylor, A Study of the Mechanism and Kinetics of the Thioacetamide Hydrolysis Reaction, *J. Am. Chem. Soc.* 79 (1957) 2684–2690, <https://doi.org/10.1021/JA01568A007>, <https://doi.org/10.1021/ASSET/JA01568A007.FP.PNG.V03>.
- [68] S.M. Senthil Kumar, K. Selvakumar, R. Thangamuthu, A. Karthigai Selvi, S. Ravichandran, G. Sozhan, K. Rajasekar, N. Navasues, S. Irusta, Hydrothermal assisted morphology designed MoS₂ material as alternative cathode catalyst for PEM electrolyser application, *Int. J. Hydrogen Energy* 41 (2016) 13331–13340, <https://doi.org/10.1016/j.ijhydene.2016.05.285>.
- [69] K. Matsui, H. Suzuki, M. Ohgai, H. Arashi, Raman Spectroscopic Studies on the Formation Mechanism of Hydrous-Zirconia Fine Particles, *J. Am. Ceram. Soc.* 78 (1995) 146–152, <https://doi.org/10.1111/j.1151-2916.1995.tb08374.x>.
- [70] Y. Li, H. Li, L. Tian, Q. Wang, F. Wu, F. Zhang, L. Du, Y. Huang, Vertical phase segregation suppression for efficient FA-based quasi-2D perovskite solar cells via HCl additive, *J. Mater. Sci. Mater. Electron.* 31 (2020) 12301–12308, <https://doi.org/10.1007/S10854-020-03775-Z/FIGURES/7>.
- [71] C. Yang, Z. Chen, I. Shaker, Y. Xu, H. Lu, Rational synthesis of carbon shell coated polyaniline/MoS₂ monolayer composites for high-performance supercapacitors, *Nano Res.* 2016 94, 9 (2016) 951–962, [10.1007/S12274-016-0983-3](https://doi.org/10.1007/S12274-016-0983-3).
- [72] J. Chao, L. Yang, J. Liu, R. Hu, M. Zhu, Sandwiched MoS₂/polyaniline nanosheets array vertically aligned on reduced graphene oxide for high performance supercapacitors, *Electrochim. Acta* 270 (2018) 387–394, <https://doi.org/10.1016/j.electacta.2018.03.072>.
- [73] S. Zhang, X. Song, S. Liu, F. Sun, G. Liu, Z. Tan, Template-assisted synthesized MoS₂/polyaniline hollow microsphere electrode for high performance supercapacitors, *Electrochim. Acta* 312 (2019) 1–10, <https://doi.org/10.1016/j.electacta.2019.04.177>.
- [74] E. Ghaleghafi, M.B. Rahmani, Exploring different routes for the synthesis of 2D MoS₂/1D PANI nanocomposites and investigating their electrical properties, *Phys. E Low-Dimensional Syst. Nanostructures* 138 (2022), 115128, <https://doi.org/10.1016/j.physe.2021.115128>.
- [75] J. Dai, S. Zeng, Y. Lv, H. Xie, L. Luo, Y. Xu, L. Dai, A facile strategy for tailoring polyaniline by MoS₂ nanosheets to obtain excellent electrochemical properties, *Electrochim. Acta* 378 (2021), 138149, <https://doi.org/10.1016/j.electacta.2021.138149>.
- [76] H. Ganesha, S. Veeresh, Y.S. Nagaraju, M. Vandana, S.P. Ashokkumar, H. Vijeth, H. Devendrapa, Growth of 3-Dimensional MoS₂-PANI nanofiber for high electrochemical performance, *Mater. Res. Express* 7 (2020), <https://doi.org/10.1088/2053-1591/ab9e30>.
- [77] Z. Zarach, K. Trzcinski, M. Lapiński, A. Lisowska-Oleksiak, M. Szkoda, Improving the Performance of a Graphite Foil/Polyaniline Electrode Material by a Thin PEDOT:PSS Layer for Application in Flexible, High Power Supercapacitors, *Mater.* 2020, Vol. 13, Page 5791, 13 (2020) 5791, [10.3390/MA13245791](https://doi.org/10.3390/MA13245791).
- [78] G.Z. Chen, Linear and non-linear pseudocapacitances with or without diffusion control, *Prog. Nat. Sci. Mater. Int.* 31 (2021) 792–800, <https://doi.org/10.1016/j.pnsci.2021.10.011>.
- [79] S. Ardizzone, G. Fregonara, S. Trasatti, “Inner” and “outer” active surface of RuO₂ electrodes, *Electrochim. Acta* 35 (1990) 263–267, [https://doi.org/10.1016/0013-4686\(90\)85068-X](https://doi.org/10.1016/0013-4686(90)85068-X).
- [80] T.-C. Liu, W.G. Pell, B.E. Conway, S.L. Roberson, Behavior of Molybdenum Nitrides as Materials for Electrochemical Capacitors: Comparison with Ruthenium Oxide, *J. Electrochem. Soc.* 145 (1998) 1882–1888, <https://doi.org/10.1149/1.1838571>, <https://doi.org/10.1149/1.1838571/XML>.
- [81] G.A. Snook, C. Peng, D.J. Fray, G.Z. Chen, Achieving high electrode specific capacitance with materials of low mass specific capacitance: Potentiostatically grown thick micro-nanoporous PEDOT films, *Electrochem. Commun.* 9 (2007) 83–88, <https://doi.org/10.1016/j.elecom.2006.08.037>.
- [82] R. Yuksel, O. Buyukcakir, P.K. Panda, S.H. Lee, Y. Jiang, D. Singh, S. Hansen, R. Adelung, Y.K. Mishra, R. Ahuja, R.S. Ruoff, Necklace-like Nitrogen-Doped Tubular Carbon 3D Frameworks for Electrochemical Energy Storage, *Adv. Funct. Mater.* 30 (2020) 1909725, <https://doi.org/10.1002/ADFM.201909725>.
- [83] C. Lu, L. Yang, B. Yan, L. Sun, P. Zhang, W. Zhang, Z. Sun, C. Lu, L. Yang, B. Yan, P. Zhang, W. Zhang, Z.M. Sun, L. Sun, Nitrogen-Doped Ti3C₂ MXene: Mechanism Investigation and Electrochemical Analysis, *Adv. Funct. Mater.* 30 (2020) 2000852, <https://doi.org/10.1002/ADFM.202000852>.
- [84] B.A. Ali, A.M.A. Omar, A.S.G. Khalil, N.K. Allam, Untapped Potential of Polymorph MoS₂: Tuned Cationic Intercalation for High-Performance Symmetric Supercapacitors, *ACS Appl. Mater. Interfaces* 11 (2019) 33955–33965, <https://doi.org/10.1021/ACSAMI.9B11444>, https://doi.org/10.1021/ACSAMI.9B11444/ASSET/IMAGES/LARGE/AM9B11444_0007.JPEG.
- [85] R.K. Mishra, M. Krishnaih, S.Y. Kim, A.K. Kushwaha, S.H. Jin, Binder-free, scalable hierarchical MoS₂ as electrode materials in symmetric supercapacitors for energy harvesting applications, *Mater. Lett.* 236 (2019) 167–170, <https://doi.org/10.1016/j.matlet.2018.10.009>.
- [86] J. Zhou, M. Guo, L. Wang, Y. Ding, Z. Zhang, Y. Tang, C. Liu, S. Luo, 1T-MoS₂ nanosheets confined among TiO₂ nanotube arrays for high performance supercapacitor, *Chem. Eng. J.* 366 (2019) 163–171, <https://doi.org/10.1016/j.cej.2019.02.079>.
- [87] D. Kesavan, V.K. Mariappan, P. Pazhamalai, K. Krishnamoorthy, S.J. Kim, Topochemically synthesized MoS₂ nanosheets: A high performance electrode for wide-temperature tolerant aqueous supercapacitors, *J. Colloid Interface Sci.* 584 (2021) 714–722, <https://doi.org/10.1016/j.jcis.2020.09.088>.

Supplementary Material

Influence of hydrochloric acid concentration and type of nitrogen source on the electrochemical performance of TiO₂/N-MoS₂ for energy storage applications

Z. Zarach^{1*}, A.P. Nowak^{1,2}, K. Trzcinski^{1,2}, G. Gajowiec³, G. Trykowski⁴, M. Sawczak⁵, M. Lapiński^{2,6}, M. Szkoda^{1,2}

¹*Department of Chemistry and Technology of Functional Materials, Faculty of Chemistry, Gdańsk University of Technology, Narutowicza 11/12, 80-233 Gdańsk, Poland*

²*Advanced Materials Center, Gdańsk University of Technology, Gabriela Narutowicza 11/12, 80-233 Gdańsk, Poland*

³*Institute of Machine Technology and Materials, Faculty of Mechanical Engineering and Ship Technology, Gdansk University of Technology, Narutowicza 11/12, 80-233 Gdansk, Poland*

⁴*Faculty of Chemistry, Nicolaus Copernicus University, Gagarina 7, 87-100, Toruń, Poland*

⁵*Centre for Plasma and Laser Engineering, The Szwalski Institute of Fluid Flow Machinery, Fiszerza 14, 80-231 Gdansk, Poland*

⁶*Institute of Nanotechnology and Materials Engineering, Faculty of Applied Physics and Mathematics, Gdańsk University of Technology, Narutowicza 11/12, 80-233 Gdańsk, Poland*

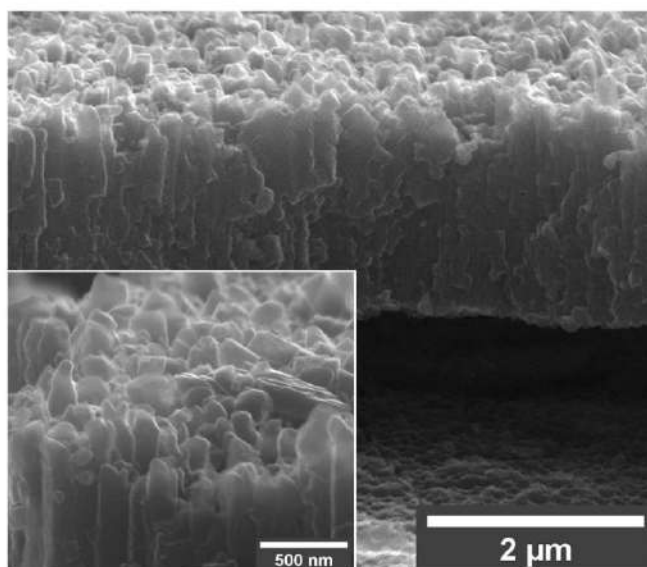


Figure S1. Cross-section images of TiO₂ nanotubes after hydrothermal synthesis performed with 5M HCl.

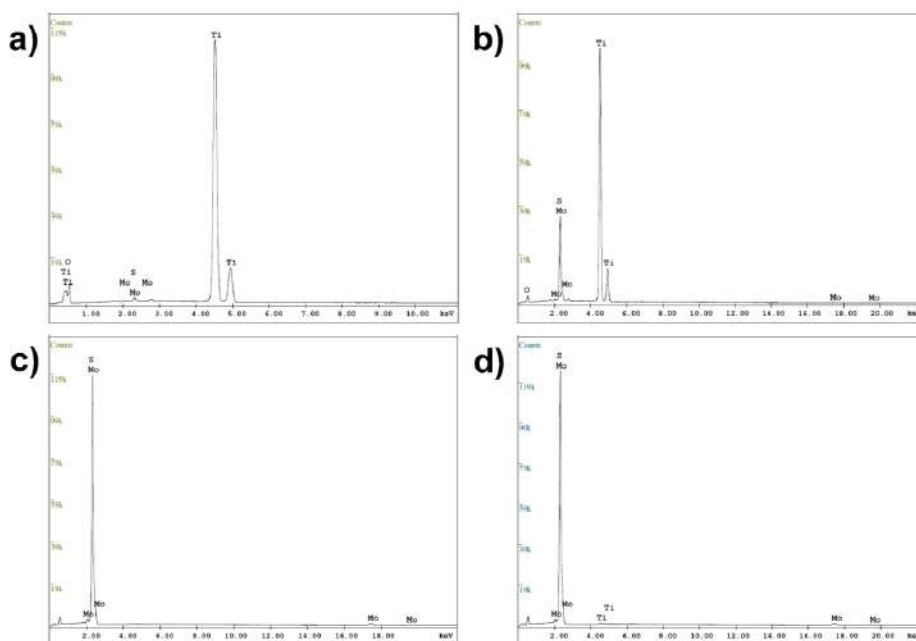


Figure S2. EDS spectra for electrode materials after hydrothermal synthesis performed with a) 5M, b) 3M, c) 1M and d) 0.5M HCl.

Table S1. Atomic % of nitrogen in the $\text{TiO}_2/\text{N-MoS}_2$ electrode materials obtained after hydrothermal synthesis performed with different hydrochloric acid concentrations (calculated from XPS analysis).

Sample designation	at. %N	% ratio	
		N1:N2	N:Mo
0.1 M	2	50:50	14:86
0.2 M	2	50:50	12:88
0.5 M	5	67:33	21:79
1 M	7	70:30	29:71
3 M	2	95:5	10:90
5 M	1	55:45	48:52

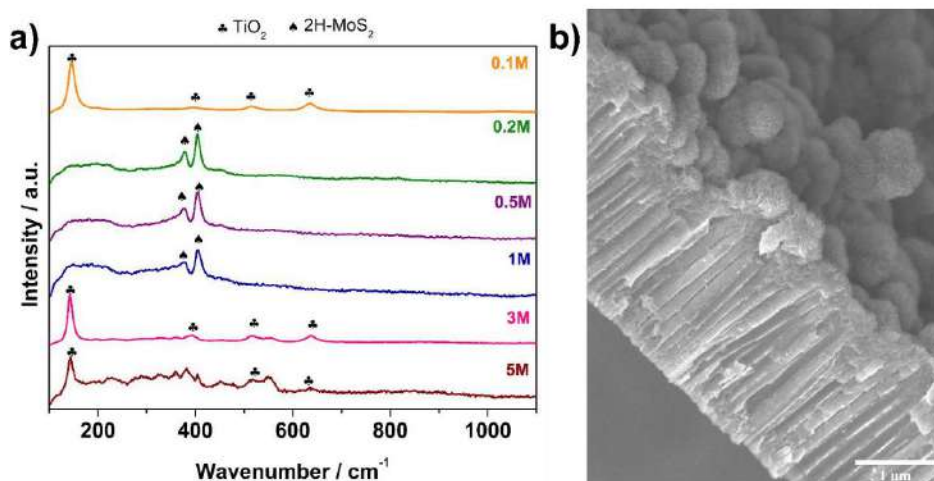


Figure S3. a) Raman spectroscopy results for N-MoS₂/TiO₂ electrode materials obtained after hydrothermal synthesis performed with different HCl concentration; b) Cross-section images of N-MoS₂/TiO₂ after hydrothermal synthesis performed with 0.5M HCl.

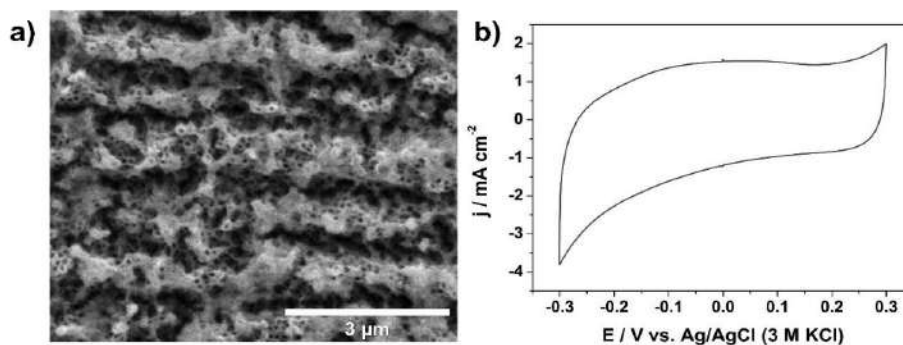


Figure S4. a) SEM image and b) cyclic voltammetry results ($v = 50 \text{ mV s}^{-1}$) of the electrode material prepared by hydrothermal synthesis performed without HCl.

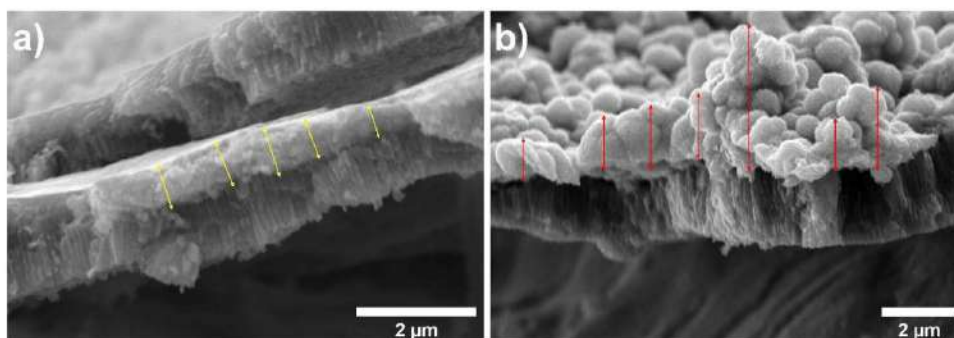


Figure S5. Cross section SEM images of a) TiO₂/MoS₂ and b) TiO₂/N-MoS₂.

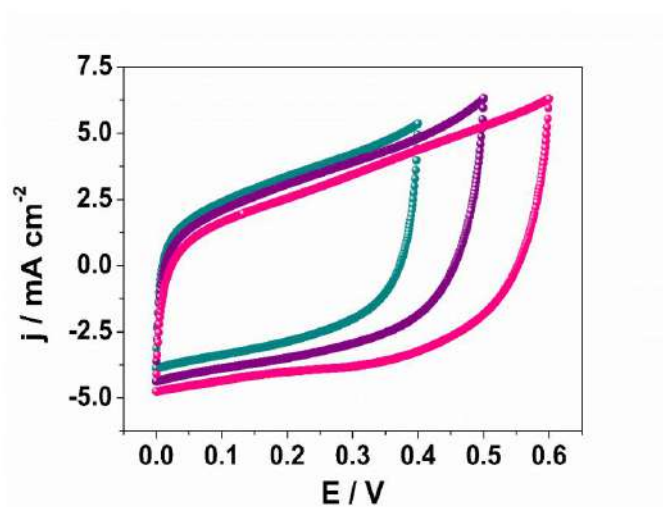


Figure S6. CV curves for TiO₂/N-MoS₂ SS in various operating voltage.

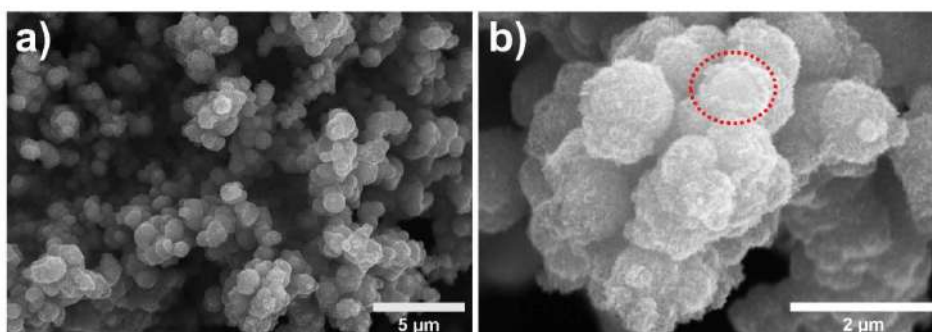


Figure S7. SEM images of TiO₂/N-MoS₂ electrode material after galvanostatic charge-discharge cycles.

Table S2. Electrical equivalent circuit parameters for TiO₂/MoS₂ and TiO₂/N-MoS₂ electrode materials and TiO₂/N-MoS₂ symmetric supercapacitor.

	TiO ₂ /MoS ₂	TiO ₂ /N-MoS ₂	TiO ₂ /N-MoS ₂ SS (before GCD)	TiO ₂ /N-MoS ₂ SS (after GCD)
R1 [Ω]	0.14732	0.14736	0.57711	0.57392
R2 [Ω]	5.2727	0.32672	0.04539	0.0463
P2 [Ω⁻¹ sⁿ]	0.00275	0.01197	0.00273	0.00265
n2	0.91193	0.7774	1	1
P3 [Ω⁻¹ sⁿ]	0.01206	0.27921	0.04537	0.04138
n3	0.91543	0.72595	0.66619	0.66551
χ²	8.99·10 ⁻⁴	4.85·10 ⁻⁵	6.76·10 ⁻⁴	1.56·10 ⁻³

Chapter IV

A Key to Material's Stability: Tuning Pyrolysis Temperature in SnS_x@C Anodes for Sodium-Ion Batteries

1. Summary of the publication

This study presents a comprehensive exploration of how thermal treatment during synthesis critically shapes the structure and performance of $\text{SnS}_x@\text{C}$ composite anodes for sodium-ion batteries. It identifies pyrolysis temperature as a decisive factor in tuning the chemical composition, defect density, porosity, and ultimately the electrochemical behavior of the material. Specifically, pyrolysis at 800 °C was found to optimize the sulfur release and transformation of SnS_2 into SnS , while simultaneously generating a stable yet defect-rich carbon matrix that facilitates reversible sodiation-desodiation cycles. This material exhibited a capacity of $\sim 500 \text{ mAh g}^{-1}$ and demonstrated significantly improved cycling stability especially compared to sample annealed at lower (600 °C) temperature. A key insight from the paper is that incomplete sulfur removal at lower pyrolysis temperature leads to residual sulfur trapped in the carbon matrix, which impairs full SnS conversion and hinders ion transport. On the other hand, excessive pyrolysis temperature degrades the chalcogenide component entirely, leading to a mostly carbonaceous structure with increased porosity but diminished electrochemical activity.

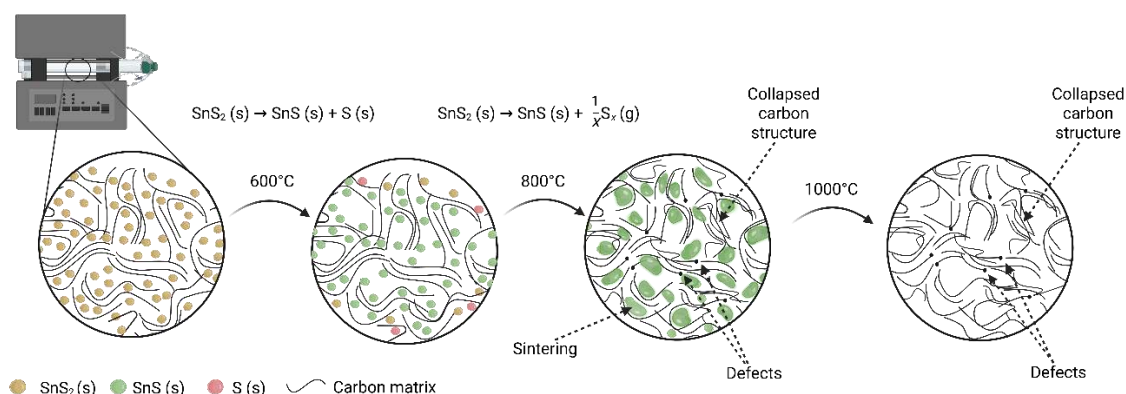


Figure 11. Graphical abstract presenting active materials' changes and summarizing Chapter IV, created with BioRender.com.

A particularly important contribution of this study lies in its use of *operando* Raman spectroscopy, which enables real-time observation of structural evolution during electrochemical cycling. These measurements provided clear evidence of reversible SnS transformations and stability under optimal pyrolysis conditions, confirming the material's ability to maintain active participation in sodium storage reactions. Importantly, they also enabled the distinction between the degradation of sodium storage mechanisms associated with the SnS phase and those related to carbon intercalation. By comparing with the low-temperature sample, it became evident that the loss of capacity followed different pathways – an early fading in the SnS phase at lower temperature pyrolysis was observed, while the optimally treated material maintained both contributions (SnS conversion-alloying and carbon intercalation) over extended cycling.

In parallel, XPS depth profiling was employed to examine surface composition and SEI development across two anode materials. This revealed that only

the 800 °C-treated sample showed a favorable chemical gradient with limited sulfur residues and stable SEI formation, directly linking surface chemistry to improved performance. Together, these advanced techniques offered a deeper understanding of interfacial processes, underlining their value in guiding the rational design of high-performance anodes for sodium-ion batteries. Overall, the findings from the research also emphasize that the presence of a carbon matrix, while often assumed to mitigate mechanical degradation in conversion-alloying type anodes, does not universally guarantee structural or electrochemical stability unless its structure is carefully optimized. This highlights the non-trivial nature of carbon's buffering role and the need for precise synthesis control.

2. Publication



RESEARCH ARTICLE



A Key to Material's Stability: Tuning Pyrolysis Temperature in $\text{SnS}_x\text{@C}$ Anodes for Sodium-Ion Batteries

Zuzanna Zarach,* Mirosław Sawczak, Carsten Dosche, Konrad Trzciński, Mariusz Szkoda, Magdalena Graczyk-Zajac, Ralf Riedel, Gunther Wittstock, and Andrzej P. Nowak

Developing robust and efficient anodes is essential for advancing sodium-ion battery technology. Herein, a systematic investigation of $\text{SnS}_x\text{@C}$ composites prepared at different pyrolysis temperatures to elucidate how their structural, surface, and electrochemical properties govern sodium-ion storage is reported. The study reveals that a lower synthesis temperature traps extra sulfur within the carbon matrix, which hampers the complete SnS conversion reaction and Na^+ intercalation processes. In contrast, pyrolysis at 800 °C facilitates more thorough sulfur release, yielding a defect-rich but stable carbon matrix that supports enhanced sodiation/desodiation reversibility. *Operando* Raman spectroscopy and X-ray photoelectron spectroscopy depth profiling confirm that the pyrolysis temperature strongly affects the formation and stability of the solid electrolyte interphase. The $\text{SnS}_x\text{@C}$ material pyrolyzed at 800 °C not only possesses superior ion transport characteristics but also delivers enhanced electrochemical performance, maintaining a stable capacity of $\approx 500 \text{ mAh g}^{-1}$ at C/10 and retaining a substantial fraction of its capacity over 100 cycles, in contrast to the rapidly decaying capacity of the material pyrolyzed at 600 °C.

1. Introduction

In today's world, the rapidly growing demand for electrical energy and the increasing electrification of various sectors require continuous advancements in energy storage technologies. This demand spans from large-scale, stationary energy storage systems to portable devices, including electric vehicles (EVs), where the performance of batteries is paramount. The need for longer driving ranges, faster charging, and higher overall energy density in EVs has driven scientific research and innovation in advanced battery systems. While significant progress has been made in lithium-ion batteries (LIBs) technology over the past decade,^[1] the limited supply of lithium, along with financial concerns, has led to increased scrutiny of this technology's long-term viability.^[2,3]

Lithium's scarcity arises from its low elemental abundance in the Earth's crust and

the geographically concentrated nature of its reserves. As demand grows, particularly due to the exponential uptake of electric vehicles and portable electronics, the price of lithium has surged, prompting the exploration of alternative energy storage solutions. Sodium-ion batteries (SIBs) have emerged as a promising contender due to the abundant availability of sodium, which is two to three orders of magnitude more plentiful than lithium, both on land and in the oceans.^[4,5] Although early research into sodium-based battery technology dates back to the 1970s, LIBs gained traction due to several key breakthroughs^[6–8] resulting in a slowdown of sodium-ion research. However, given the increasing disparity between lithium supply and demand, SIBs are now being revisited as a cost-effective alternative for large-scale energy storage.^[9,10] Yet, several challenges are to be faced when SIBs are compared to their lithium-ion counterparts, particularly in terms of energy density. Sodium ions are larger (1.02 Å vs 0.76 Å for Li^+) and heavier (23 g mol⁻¹ vs 6.9 g mol⁻¹ for Li^+), which impede the achievement of high volumetric and gravimetric energy densities.^[11] Commercial anode materials like graphite, which are well-suited for LIBs, do not perform optimally with sodium ions due to significant structural mismatches, resulting in poorer capacity retention during long-term cycling.^[12–14] Nevertheless, SIBs offer several advantages that make them attractive alternatives. For instance, SIBs utilize aluminum current collectors, which do not form alloys with sodium,

Z. Zarach, K. Trzciński, M. Szkoda, A. P. Nowak
Faculty of Chemistry
Gdansk University of Technology
Gdansk 80-233, Poland
E-mail: zuzanna.zarach@pg.edu.pl

M. Sawczak
Centre of Plasma and Laser Engineering
The Szwalski Institute of Fluid-Flow Machinery of Polish Academy of Sciences
Gdansk 80-231, Poland
C. Dosche, G. Wittstock
Institute of Chemistry
Carl von Ossietzky University of Oldenburg
26111 Oldenburg, Germany
M. Graczyk-Zajac, R. Riedel
Institute of Materials Science
Darmstadt University of Technology
64287 Darmstadt, Germany
M. Graczyk-Zajac
EnBW Energie Baden-Württemberg AG
76131 Karlsruhe, Germany

The ORCID identification number(s) for the author(s) of this article can be found under <https://doi.org/10.1002/sml.202504485>

© 2025 The Author(s). Small published by Wiley-VCH GmbH. This is an open access article under the terms of the Creative Commons Attribution License, which permits use, distribution and reproduction in any medium, provided the original work is properly cited.

DOI: 10.1002/sml.202504485

Small 2025, e04485

e04485 (1 of 17)

© 2025 The Author(s). Small published by Wiley-VCH GmbH

improving their safety profile compared to LIBs. Moreover, the slightly smaller Stokes radius of sodium ions (e.g., in propylene carbonate (PC): Na^+ (4.6 Å) < Li^+ (4.8 Å)) improves their diffusion kinetics at the solid-electrolyte interphase (SEI), leading to enhanced ionic conductivity.^[15] This can help mitigate some of the performance drawbacks associated with the larger ionic size and mass of sodium, offering potential for further improvements in energy efficiency and cycle life.^[16] Furthermore, many SIBs designs employ stable insertion-based or carbon-based anodes that limit dendritic plating, thereby enhancing their inherent safety and suitability for large-scale applications.^[17,18] However, dendrite formation remains inevitable when metallic sodium is used directly as the anode material, and thus, the search for suitable anode materials continues to be a key challenge in improving the performance and safety of SIBs.

Within the spectrum of emerging anodes, metal sulfides (MeS_x) have attracted attention due to their favorable electrochemical properties relative to their oxide counterparts. The inherent features of MeS_x , including tunable crystal structures, layered architectures, and flexible valence states, contribute to their higher electronic conductivity and relatively faster sodium storage kinetics in comparison with the corresponding oxides.^[19–21] This faster kinetic profile is attributed to the smaller Me–S bond energy in MeS_x , which facilitates a swifter conversion reaction than is possible with Me–O bonds in metal oxides.^[22,23] As such, many metal sulfides, including those based on Mo, W, Fe, and Sn, exhibit multiple reaction mechanisms for sodium storage, including intercalation, conversion and alloying reactions, which together support enhanced charge capacity and extended cycle life. Within the MeS_x group, tin-based sulfides stand out due to their exceptional theoretical capacities. Tin(II) sulfide, for instance, exhibits a high theoretical capacity of 1022 mAh g^{−1}, resulting from a sequence of sodium storage reactions that involve initial Na^+ ion intercalation, followed by conversion to Na_2S and eventual alloying with Na to produce $\text{Na}_{3.75}\text{Sn}$.^[24] These multiple reaction pathways contribute to its impressive energy density but also lead to notable challenges, primarily associated with structural integrity over repeated cycles. During the sodiation/desodiation process, SnS may experience substantial volume changes as bonds between Sn and S are repeatedly formed and broken. This causes electrode expansion, pulverization, and degradation, which can result in reduced cycling stability.^[25]

A key determinant of battery performance and lifespan is the formation and stability of an SEI. In carbon-based anodes, such as hard carbon, the SEI is governed by the material's porosity, surface functionalities, and defect structures, which can store sodium via multiple mechanisms—ranging from surface adsorption at defect sites to intercalation between the domains and pore filling at low voltages^[26–29]—making the SEI structure equally complex and dynamic. On the other hand, metal sulfide anodes undergo repeated conversion and alloying reactions that continuously reshape the electrode–electrolyte interface. This restructuring, with repeated structural expansion and contraction, can fracture the SEI, triggering persistent electrolyte decomposition, an increase in charge transfer resistance, and subsequent capacity fading.^[21,25,30] Recent studies have highlighted the importance of designing anodes with controlled porosity and tailored surface chemistry to promote the formation of

an inorganic-rich, uniform, and stable SEI, which can mitigate these effects.^[29,31,32] Especially, SEI layers with a well-structured inorganic composition—such as NaF , Na_2O , or Na_2S —have demonstrated improved stability and better Na^+ transport kinetics, effectively reducing side reactions and enhancing long-term performance.^[33] Thus, designing SnS -based composite anodes in which carbon phases mitigate volume changes, while promoting stable SEI formation, is one of the most viable approaches to achieving better cycling longevity and rate capability.

Understanding and controlling the SEI formation, as well as degradation mechanisms responsible for capacity loss, is therefore essential to advancing the stability of SIBs. Advanced *in situ* and *operando* techniques, including Raman spectroscopy, have proven invaluable for real-time monitoring of the dynamic processes occurring during charge–discharge cycles. These methods provide crucial insights into the formation stability of the SEI, but also for optimizing material design and electrolyte composition.^[34,35] Gan et al.^[36] employed *operando* Raman spectroscopy to investigate a nitrogen-doped hard carbon anode for SIBs, revealing the presence of C–C• and C–N• radicals that significantly contributed to additional sodium storage sites. Raman measurements enabled the identification of reversible radical evolution during sodiation and desodiation, which was directly linked to the enhanced capacity and long-term cycling stability.^[36] Similarly, Weaving et al.^[37] used *operando* Raman spectroscopy to elucidate the sodiation mechanism in commercial hard carbon and demonstrated how changes in the I_G and I_{D1} Raman bands corresponded to sodium intercalation between turbostratic nanodomains (TNDs). The findings showed that sodium occupation of edge sites and interlayer defects drives the sloping voltage profile, while pore filling dominates at low potentials. Importantly, the study emphasized the necessity of *operando* techniques, as *ex situ* measurements often fail to capture critical transient states, such as those associated with SEI formation or sodium reversibility.^[37]

Thus, in this work, SnS_x/C composites for sodium-ion battery anode material are investigated, using *operando* Raman spectroscopy, thereby unveiling the differences that emerge during intercalation processes within the carbon material. The study also explores the impact of pyrolysis temperature on the material's surface properties, porosity, and structural features, which collectively influence the efficiency of sodium-ion storage and stability of chalcogenide-based anode materials. Furthermore, X-ray photoelectron spectroscopy depth profiling is employed to elucidate how synthesis protocols and thermal treatments affect the electrochemical performance. Overall, the findings provide critical insights into tuning the SnS_x/C electrode architectures for high-performance sodium-ion anodes and emphasize the role of advanced spectroscopic techniques in guiding the design of energy storage materials.

2. Results and Discussion

Regardless of the temperature applied during the annealing process, the SEM images reveal a distinct irregularity within the morphology, accompanied by a similarity in particle sizes (Figure 1). In addition, the observations indicate a tendency of the materials to form agglomerates, suggesting that the thermal treatment influences the degree of particle clustering. However,

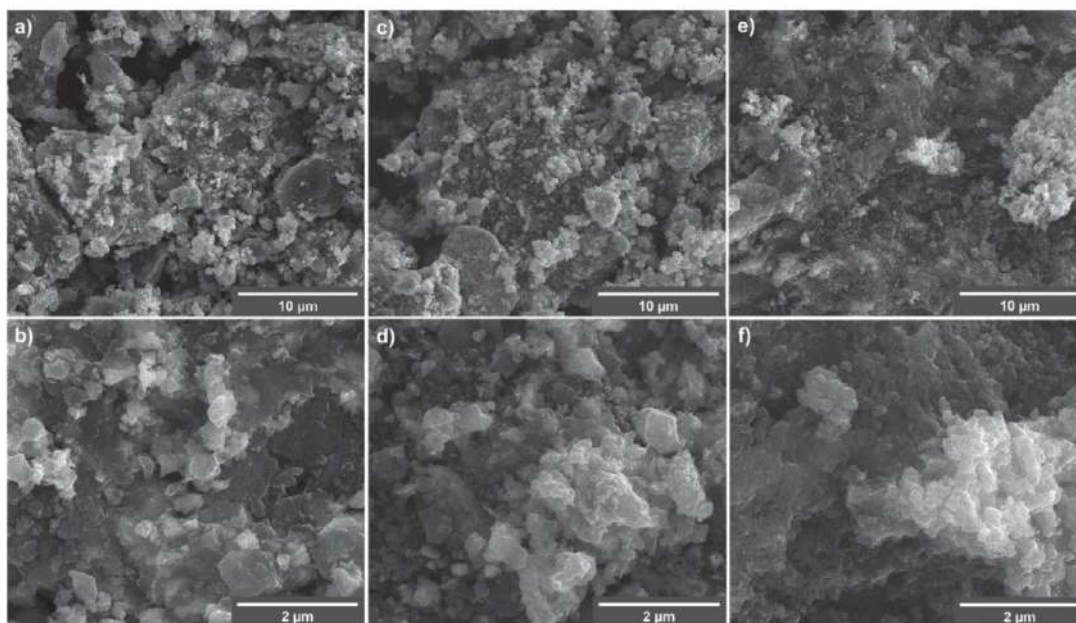


Figure 1. Scanning electron microscopy images of a,b) $\text{SnS}_x\text{@C}_{-600}$, c,d) $\text{SnS}_x\text{@C}_{-800}$, and e,f) $\text{SnS}_x\text{@C}_{-1000}$ materials.

the measurements conducted with the energy-dispersive X-ray spectroscopy (EDX) show a change in stoichiometry of the tin-sulfide compound (Tables S1–S4, Supporting Information). The sulfur-to-tin ratio changed from 2:1 for the untreated sample ($\text{SnS}_x\text{@C}$), to a 1:0.92 ratio for $\text{SnS}_x\text{@C}_{-600}$ and a 1:0.95 ratio for $\text{SnS}_x\text{@C}_{-800}$. Also, a significant loss of both sulfur and tin is found for $\text{SnS}_x\text{@C}_{-1000}$, indicating the upper practical limit for the thermal stability of tin-sulfide compounds.

The EDX results, confirming the presence of Sn and S atoms at different stoichiometries, were consistent with the X-ray diffraction (XRD) data—the obtained patterns are presented in Figure 2a. The hydrothermal synthesis resulted in the synthesis of the pure, single-phase SnS_2 (see Figure S2, Supporting Information, ICDD-PDF 00-001-1010). This is confirmed by the diffraction peaks registered at 28.7° , 32.9° , 50.3° , and 52.9° that correspond to the (100), (101), (110), and (111) planes of the hexagonal SnS_2 , respectively.^[38] Since it is impossible to distinguish the reflection from the (001) plane at 15.0° , it is likely that the adsorption of carbon species on this plane suppresses its detection in the XRD pattern.^[39]

The thermal treatment of the $\text{SnS}_2\text{@C}$ material in Ar atmosphere at elevated temperatures reaching 800°C led to the conversion of tin(IV) sulfide to tin(II) sulfide. For both $\text{SnS}_x\text{@C}_{-600}$ and $\text{SnS}_x\text{@C}_{-800}$, the XRD patterns indicate the formation of orthorhombic SnS (ICDD-PDF 00-033-1375).^[40] No reflections attributable to SnS_2 , Sn_2S_3 , or metallic Sn are present after pyrolysis. However, the treatment at 1000°C resulted in losing the chalcogenide-based part of the composite with the increased contribution of an amorphous-type carbon structure, since the pattern shows only the broad carbon (002) reflex at 24° . On the basis

of the obtained results, the crystallite size was calculated by utilization of Scherrer's equation:

$$D = \frac{K\lambda}{\beta \cos \theta} \quad (1)$$

where D represents the crystallite size, K is a constant (0.94), λ is the X-ray wavelength, β is the width at half maximum of the peak, and θ is the Bragg angle. The (111) reflection of SnS at 31.6° narrows from 0.78 to 0.72° (FWHM) when the pyrolysis temperature is raised from 600 to 800°C , corresponding Scherrer sizes of 110.3 and 120.3 Å , respectively. High-resolution transmission electron microscopy (TEM) supports these X-ray calculations. In the $\text{SnS}_x\text{@C}_{-600}$ sample, individual SnS particles are visible in the carbon matrix (Figure 2e). The small difference in size is expected since TEM images include a thin carbon shell and can show two overlapping crystals as one. Moreover, at 800°C , SnS is still present as nanodomains (Figure 2f and Figure S3a, Supporting Information), but fewer particles are seen: at this temperature, tin and sulfur start to evaporate, and neighboring grains start to sinter, so their edges are less distinct. In the $\text{SnS}_x\text{@C}_{-1000}$, no SnS particles are detected—TEM shows only the porous carbon framework (Figure S3b, Supporting Information), which is consistent with XRD results. Also, some differences were revealed by Raman spectroscopy analysis, the results of which are presented in Figure 2b (with a narrow range shown in Figure S4a, Supporting Information), revealing four main carbon-related bands—D1, D3, D4, and the G band—across all samples.^[41] All spectral parameters obtained from the deconvoluted Raman spectra are listed in Table S5

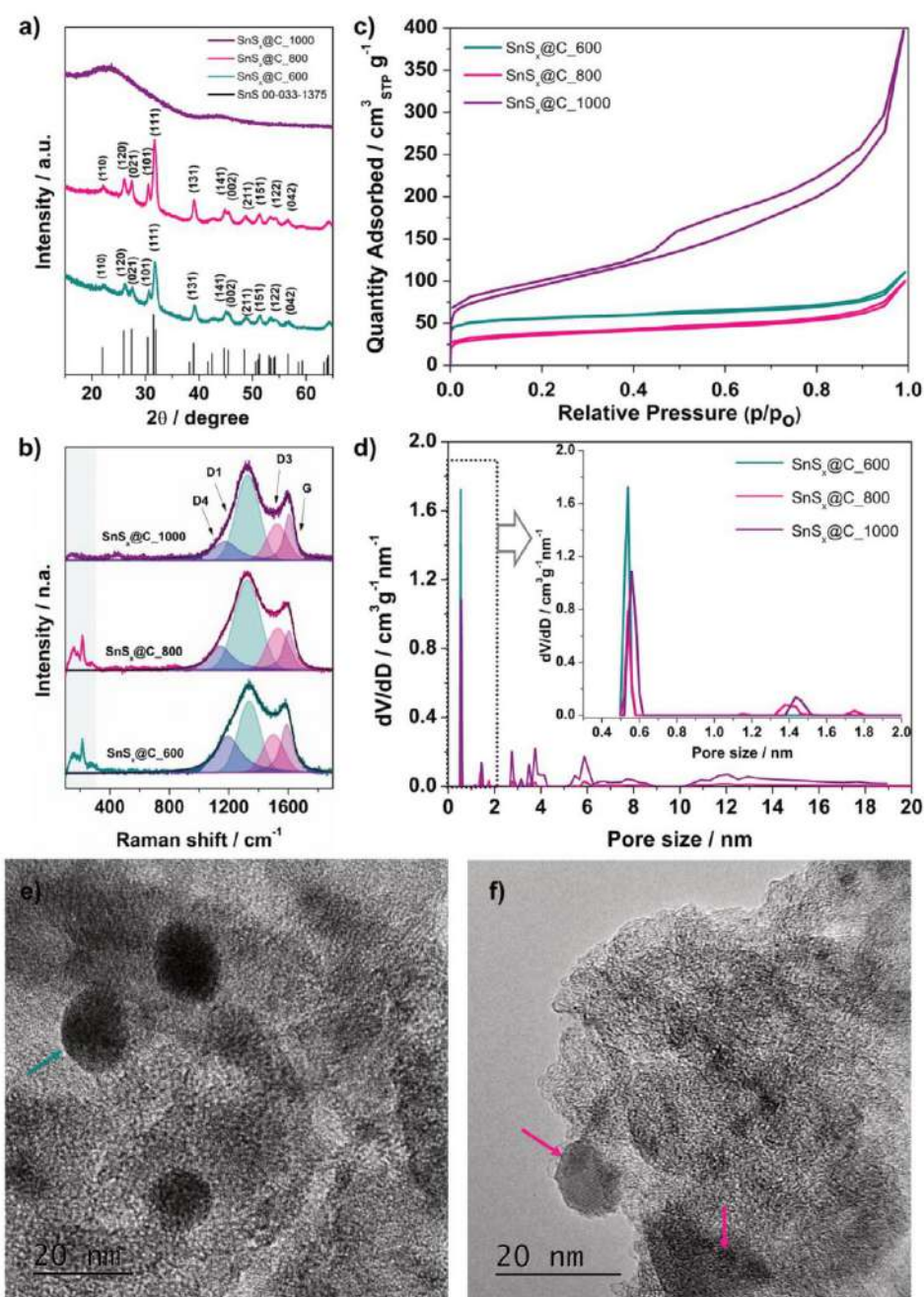


Figure 2. a) XRD patterns, b) Raman spectra, c) nitrogen adsorption-desorption isotherms, and d) pore size distribution calculated from N₂ adsorption isotherms based on the DFT method for SnS_x@C materials; TEM images for e) SnS_x@C₆₀₀ and f) SnS_x@C₈₀₀.

(Supporting Information). The G band ($1590\text{--}1605\text{ cm}^{-1}$) is typically assigned to the in-plane stretching between sp^2 carbon atoms, whereas the D1 band ($1324\text{--}1337\text{ cm}^{-1}$) arises from disordered, defect-activated modes and the vibration of graphene layer edges.^[27] Two additional disorder-related features, D3 ($1500\text{--}1525\text{ cm}^{-1}$) and D4 ($1170\text{--}1195\text{ cm}^{-1}$), were also deconvoluted. For the $\text{SnS}_x\text{@C}_{1000}$ sample, only these four carbon bands are visible, indicating the almost complete loss of chalcogenide-based phases at this temperature, which is in agreement with the XRD data.

In contrast, both $\text{SnS}_x\text{@C}_{600}$ and $\text{SnS}_x\text{@C}_{800}$ show additional bands at ≈ 158.7 , 181.2 , and 217.7 cm^{-1} , corresponding to the B_{3g} , B_{2g} , and A_g vibrational modes of SnS, respectively.^[42] Notably, the intensities of these SnS bands can vary substantially with the laser excitation wavelength owing to resonance effects in chalcogenide-based materials.^[43] Here, an excitation of 785 nm ($\approx 1.6\text{ eV}$) closely matches the direct bandgap of SnS ($\approx 1.5\text{ eV}$), enhancing those vibrational features.^[44] Despite the usual expectation that higher-temperature annealing produces more ordered carbon (i.e., lower $I_{\text{D1}}/I_{\text{G}}$ ratio), the $I_{\text{D1}}/I_{\text{G}}$ ratio (see Table S5, Supporting Information) actually increases from 1.44 for $\text{SnS}_x\text{@C}_{600}$ to 2.07 for $\text{SnS}_x\text{@C}_{800}$, before dropping slightly to 1.84 for $\text{SnS}_x\text{@C}_{1000}$. Although it is not a common phenomenon, a similar trend was also reported by Li et al.^[45] and Simone et al.^[32] for hard carbons with SIBs application. The higher $I_{\text{D1}}/I_{\text{G}}$ ratio at 800°C suggests that sulfur released during pyrolysis may disrupt the carbon structure, generating additional defects. In contrast, at 600°C , more sulfur appears to remain within the matrix, reducing new defect formation and thus yielding a lower $I_{\text{D1}}/I_{\text{G}}$ ratio. By the time the temperature reaches 1000°C , most sulfur-containing species have sublimated, leaving predominantly carbon (the $I_{\text{D1}}/I_{\text{G}}$ ratio of 1.84). The moderate decrease in the $I_{\text{D1}}/I_{\text{G}}$ ratio compared to $\text{SnS}_x\text{@C}_{800}$ suggests a partial reorganization of the carbon framework, likely driven by the high-temperature annealing process. At the same time, the G-band width narrows steadily, from 50 cm^{-1} for $\text{SnS}_x\text{@C}_{600}$, 45 cm^{-1} for $\text{SnS}_x\text{@C}_{800}$ to 37 cm^{-1} for $\text{SnS}_x\text{@C}_{1000}$ (Table S5, Supporting Information). According to the Ferrari–Robertson amorphization model, a narrower G band signals larger and more ordered sp^2 domains.^[46,47] Thus, the observed values confirm that the overall graphitization degree still increases with temperature even though the $I_{\text{D1}}/I_{\text{G}}$ ratio is highest for $\text{SnS}_x\text{@C}_{800}$. The blue shift of the G band towards the graphite value (1600 cm^{-1}) in the $\text{SnS}_x\text{@C}_{1000}$ further supports this conclusion. Nonetheless, the removal of sulfur at elevated temperatures can also impact the overall electrochemical properties by altering the number and nature of carbon defects available for sodium storage.

Further investigation included N_2 adsorption measurements, for which the adsorption–desorption isotherms were obtained and are presented in Figure 2c. The isotherms for the $\text{SnS}_x\text{@C}_{600}$ and $\text{SnS}_x\text{@C}_{800}$ exhibit a type-I behavior, according to IUPAC classification, indicative of a predominantly microporous structure. When the pyrolysis temperature is increased to 1000°C , a type-IV isotherm is recorded with a pronounced hysteresis (see $\text{SnS}_x\text{@C}_{1000}$), characteristic of micro- and mesoporous carbons. The pore size distribution in Figure 2d indicates that at 800 and 1000°C , the pore size is in the range of ≈ 1 to $\approx 4\text{ nm}$ (see also Figure S4b, Supporting Information), con-

Table 1. Specific surface area calculated with BET theory, total pore volume determined with the DFT method, and crystallite size obtained from the Scherrer equation for $\text{SnS}_x\text{@C}$ materials.

Sample	S_{BET} [$\text{m}^2\text{ g}^{-1}$]	V_t [$\text{cm}^3\text{ g}^{-1}$]
$\text{SnS}_x\text{@C}_{600}$	212	0.17
$\text{SnS}_x\text{@C}_{800}$	128	0.15
$\text{SnS}_x\text{@C}_{1000}$	321	0.62

firming the formation of micro-mesoporous structure, whereas the $\text{SnS}_x\text{@C}_{600}$ sample remains primarily microporous (pores around 0.5 nm). Interestingly, both the total pore volume (V_t) and surface area (S_{BET}) in Table 1 decrease when a substantial SnS fraction is present. This effect is most pronounced for $\text{SnS}_x\text{@C}_{800}$, which shows $V_t = 0.15\text{ cm}^3\text{ g}^{-1}$, compared to $0.17\text{ cm}^3\text{ g}^{-1}$ for $\text{SnS}_x\text{@C}_{600}$. A likely explanation is that partial sintering and more thorough decomposition of SnS_2 to SnS cause pore collapse and a reduced overall pore volume at 800°C . By contrast, pyrolysis to 1000°C (where tin sulfide largely decomposes and evaporates) leads to a predominantly carbon-based structure with significantly higher pore volume of $0.62\text{ cm}^3\text{ g}^{-1}$ and a broader size distribution of mesopores.

To further compare the $\text{SnS}_x\text{@C}_{600}$ and $\text{SnS}_x\text{@C}_{800}$ electrode materials, an X-ray photoelectron spectroscopy (XPS) analysis was performed for layered materials, as shown in Figure 3. Table S6 (Supporting Information) summarizes the corresponding relative elemental composition, revealing that the surface of both materials is dominated by carbon, but the Sn content is significantly lower for $\text{SnS}_x\text{@C}_{800}$ (0.64% compared to 1.34% for $\text{SnS}_x\text{@C}_{600}$), indicating that SnS starts to evaporate from the sample surface already at 800°C . These results are in contrast to the EDX results with higher Sn and S contents, reflecting the surface-sensitive nature of XPS versus the more bulk-sensitive EDX. For $\text{SnS}_x\text{@C}_{600}$, in the Sn 3d region (Figure 3a), two main contributions at 487.1 and 495.6 eV were deconvoluted into two lines, indicating the presence of Sn^{2+} and Sn^{4+} .^[48] In both $\text{SnS}_x\text{@C}_{600}$ and $\text{SnS}_x\text{@C}_{800}$ samples, Sn^{4+} is the predominant oxidation state near the surface—an effect commonly observed due to the material's exposure to air.^[49] In the Sn 3d spectrum of $\text{SnS}_x\text{@C}_{800}$, a minor shoulder is observed at $\approx 497\text{ eV}$. A survey scan of the same electrode (see Figure S5a, Supporting Information) reveals Na 1s and Na 2s signals together with the Cu 2p peak from the current collector and weak O 1s and N 1s contributions from surface adsorbates. The shoulder at 497 eV is therefore assigned to the Na KLL Auger emission and not to an additional Sn oxidation state. Depth-profiling experiments (see Figure S5b,c, Supporting Information) confirm a stronger Sn^{2+} signal beneath the surface, consistent with the presence of tin sulfide. Notably, the relative molar Sn content at the surface is almost twice as high in $\text{SnS}_x\text{@C}_{600}$ compared to $\text{SnS}_x\text{@C}_{800}$. In the S 2p region (Figure 3b), the first main $2p_{3/2}$ line at 161.5 eV indicates the presence of Sn–S bonds.^[50,51] Additional peaks at 163.7 and 164.9 eV correspond to C–S bonding, indicating interactions between the carbon matrix and sulfur species.^[52] It is worth noting that the carbon black additive ($5\text{ wt}\%$) can also contain traces of sulfur, thus potentially contributing to the S 2p signals in minor amounts. In addition, a weak feature at 168.2

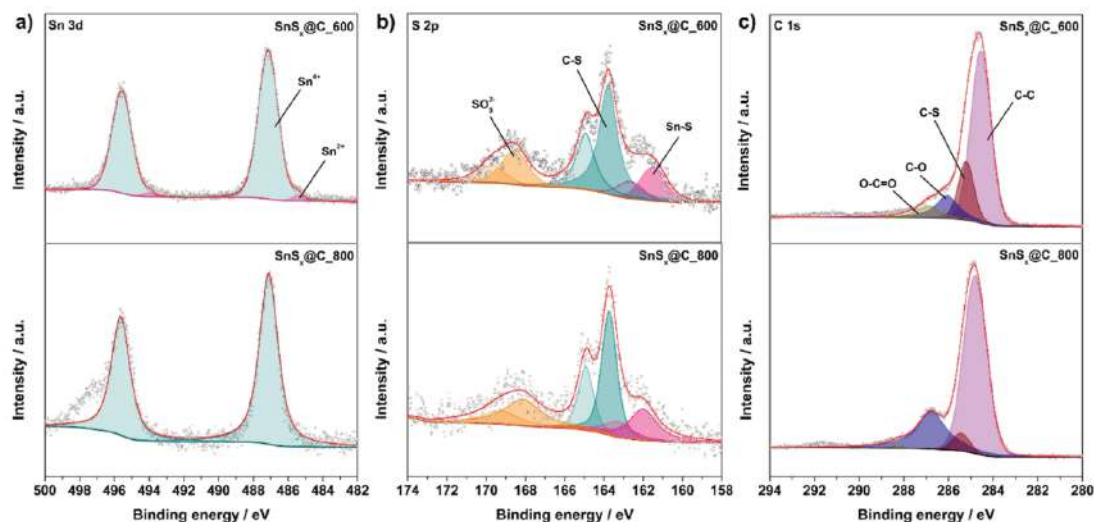


Figure 3. XPS spectra of a) Sn 3d, b) S 2p, and c) C 1s regions for the $\text{SnS}_x\text{@C}_{600}$ and $\text{SnS}_x\text{@C}_{800}$ electrodes.

eV is assigned to the presence of sulfates(VI), likely formed by partial oxidation of the sulfur species when exposed to air. The C 1s spectra region (Figure 3c) shows the principal component at 284.6 eV, ascribed to sp^3 and sp^2 C atoms without electronegative substituents. Peaks at higher binding energies are deconvoluted into contributions from $\text{C}-\text{S}$ and $\text{C}-\text{O}$, whereas signals at 287 eV can be linked to $\text{O}-\text{C}=\text{O}$ groups (carboxyl/ester functionalities). In addition, the line with an energy of 290.8 eV can be ascribed to the shake-up excitation originating from sp^2 carbon, which is an additional confirmation of the extended π -electron system in the material.^[53]

Thus, we propose that during the pyrolysis at 600 °C, most of the SnS_2 is converted to SnS , but the lower temperature may hamper the complete release of sulfur, which instead remains partly retained or trapped within the carbon matrix (see

Figure 4). This aligns with the XPS findings (Table S6, Supporting Information), which show comparatively higher surface contents of tin and sulfur for $\text{SnS}_x\text{@C}_{600}$. Some of this residual sulfur may also bond with or become immobilized in the carbon framework. The overall lower temperature likely preserves more micropores and minimizes sintering – an effect consistent with the higher surface area ($212 \text{ m}^2 \text{ g}^{-1}$) for $\text{SnS}_x\text{@C}_{600}$, measured by BET. In Raman spectroscopy, the $I_{\text{D1}}/I_{\text{G}}$ ratio for $\text{SnS}_x\text{@C}_{600}$ is 1.44, which is unexpectedly lower than the 2.07 ratio for $\text{SnS}_x\text{@C}_{800}$. Although higher pyrolysis temperatures typically yield more graphitic (and thus lower-defect) carbon, the vigorous loss of sulfur at 800 °C is considered to locally perturb the carbon structure and create additional defects, thereby raising the measured $I_{\text{D1}}/I_{\text{G}}$ ratio. By 800 °C, the release of sulfur is more effective, consistent with lower Sn and S levels at the

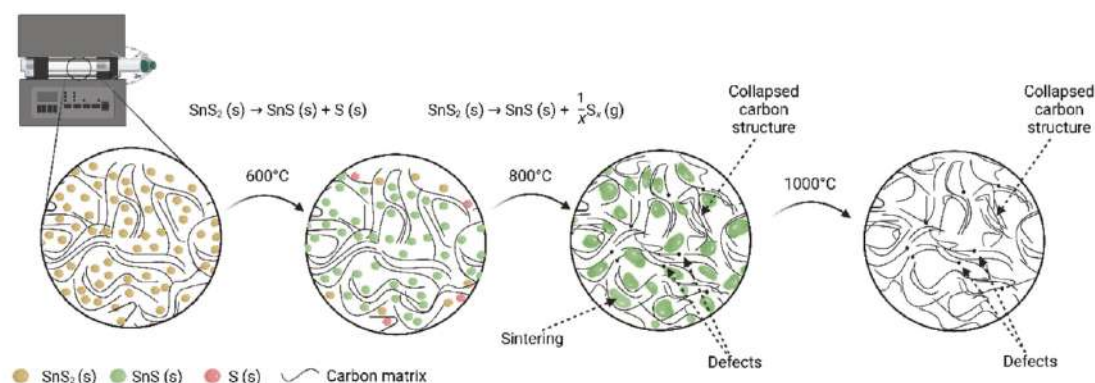


Figure 4. Schematic illustration of the structural and chemical evolution of $\text{SnS}_2\text{@C}$ during pyrolysis at 600, 800, and 1000 °C.

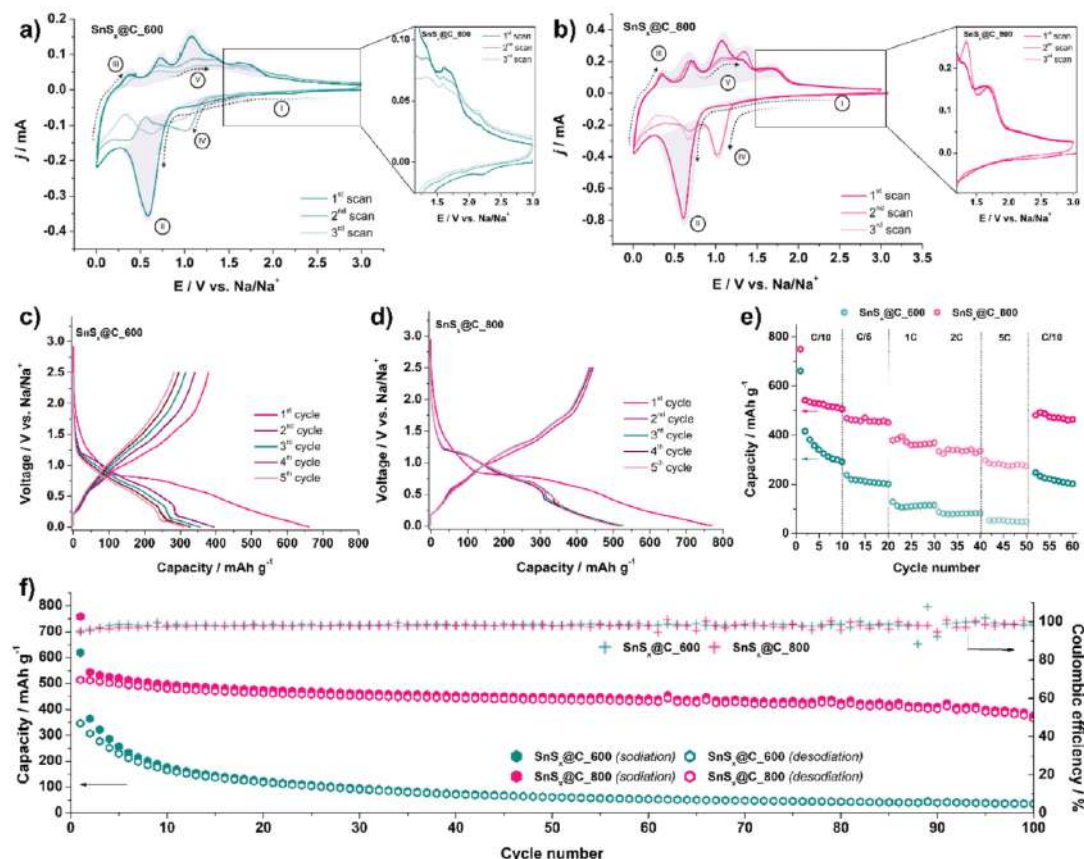


Figure 5. Cyclic voltammograms recorded in 1 M NaPF₆ in EC:DEC (30:70) + 5% FEC electrolyte ($\nu = 100 \mu\text{V s}^{-1}$) for half-cells with the a) SnS_x@C₆₀₀ and b) SnS_x@C₈₀₀ anode materials; galvanostatic charge-discharge curves recorded in 1 M NaPF₆ in EC:DEC (30:70) + 5% FEC at current density of C/10 for the c) SnS_x@C₆₀₀ and d) SnS_x@C₈₀₀; e) rate capability tests; f) cycling performance at current density of C/10 for the SnS_x@C₆₀₀ and SnS_x@C₈₀₀ anode materials.

electrode surface, yet the ensuing partial sintering and structural rearrangement reduce the surface area ($128 \text{ m}^2 \text{ g}^{-1}$). Overall, the SnS_x@C₈₀₀ sample undergoes more thorough sulfur evolution and develops a defect-rich but compact carbon framework, while SnS_x@C₆₀₀ retains extra sulfur in the matrix and consequently exhibits a higher surface area but fewer carbon defects. On the other hand, nearly all residual Sn-S species volatilize at 1000°C , leaving behind pores that coalesce into an open micro/mesoporous network. Although the carbon backbone undergoes partial graphitization and “collapses,” the newly created voids contribute to the increased surface area of $321 \text{ m}^2 \text{ g}^{-1}$ and the pore volume of $0.62 \text{ cm}^3 \text{ g}^{-1}$. Raman data support this picture: the G band sharpens (HWHM 37 cm^{-1} vs 45 cm^{-1} at 800°C) and upshifts to 1605 cm^{-1} , indicating increased ordering. However, the $I_{\text{D1}}/I_{\text{G}}$ ratio only falls from 2.07 to 1.84 (still being higher than the 1.44 value at 600°C) because the newly exposed pore walls introduce fresh edge defects.

The composites and their behavior during sodium-ion storage were investigated via cycling voltammetry in 1 M NaPF₆ in ethyl carbonate:diethyl carbonate (EC:DEC) (30:70) + 5% FEC. The CV curves for the SnS_x@C₁₀₀₀ material (see Figure S6a, Supporting Information) do not show reactions associated with tin sulfide, which is in line with the characterization results that showed the loss of tin sulfide. For the SnS_x@C₆₀₀ material (Figure 5a), distinct yet subtle peaks are found that are not discernible for the materials annealed at higher temperatures. In region I of the first cathodic scan, a small reduction signal at $\approx 2.2 \text{ V}$ is followed by an anodic peak at $\approx 1.6 \text{ V}$ in the reverse scan. Given the XPS results showing residual sulfur species and the Raman data indicating SnS and C–S interactions, these peaks likely correspond to redox processes of surface-confined sulfur species. The initial cathodic signal suggests the reduction of surface sulfur species, forming sulfur intermediates. The subsequent anodic peak indicates their re-oxidation. Since these signals are absent in the SnS_x@C₈₀₀

material (see Figure 5b), it is reasonable to assume that sulfur sublimation occurs more efficiently at 800 °C, reducing the available amount of the component, causing the redox process. For both $\text{SnS}_x/\text{C}_600$ and $\text{SnS}_x/\text{C}_800$, an intense peak is distinguished at around 0.56 V during the first negative scan at region II, indicating the conversion of SnS to Na_2S and metallic Sn , the electrolyte reduction, and the formation of a SEI.^[39,54] The peak is only observed in the first potential cycle. In the reverse scan and the region III, multiple peaks were registered, including anodic ones at 0.36, 0.72, 1.06, and 1.34 V, with the corresponding reduction peaks in cathodic scan at 0.27, 0.69, and 1.01 V, attributed to the Na-Sn alloying/dealloying reactions.^[39,55] For $\text{SnS}_x/\text{C}_600$, continuous changes and a decrease in current over successive cycles indicate material degradation. For $\text{SnS}_x/\text{C}_800$, the anodic peak at 1.7 V indicates a reversible conversion reaction of Na_2S back to SnS ,^[56] which is clearly visible and remains stable over cycles. However, in $\text{SnS}_x/\text{C}_600$, this peak appears only in the first cycle and diminishes thereafter, reflecting a progressive loss of reversibility and electrochemical activity (see the inset for both Figure 5a,b). Differences in electrochemical performance are further evident in the galvanostatic charge–discharge curves. For $\text{SnS}_x/\text{C}_600$ (Figure 5c), a clear decrease in capacity is observed with each cycle, highlighting its limited cycling stability. In contrast, $\text{SnS}_x/\text{C}_800$ (Figure 5d) maintains a stable capacity, with the initial coulombic efficiency (ICE) of 68%. On the other hand, the ICE is 56% for $\text{SnS}_x/\text{C}_600$ and 35% for $\text{SnS}_x/\text{C}_1000$ (see Figure S6b, Supporting Information) confirms an unusually large irreversible capacity centered above 0.6 V, exactly where extensive SEI formation is expected. This drop in ICE correlates with the BET analysis: the surface area exhibits a step-increase from 128 $\text{m}^2 \text{g}^{-1}$ at 800 °C to 321 $\text{m}^2 \text{g}^{-1}$ at 1000 °C, while the pore volume increases from 0.15 to 0.62 $\text{cm}^3 \text{g}^{-1}$, providing an enhanced carbon/electrolyte interface that consumes Na^+ irreversibly in the first cycle. Regarding the effect of pyrolysis temperature on ICE, Li et al.^[57] have reviewed temperature-induced graphitization in hard carbons and concluded that raising the carbonization temperature from ≈600 to 1400 °C steadily closes open pores, lowers surface area, and therefore increases ICE. A typical example is paulownia-derived hard carbon, where the ICE increased from 76.8% at 1000 °C to 85.9% at 1400 °C as the pore volume collapsed and the graphitization degree rose.^[58] Furthermore, it is generally stated that higher defect density lowers the ICE, because vacancies, edge sites and sp^3 domains may trap Na^+ irreversibly. An example is the work by Yang et al.^[59] focusing on wheat-starch hard carbon and graphene-induced graphitized carbons, where lowering the I_D/I_G ratio and the BET area pushed the ICE up to 90%–94%. Yet, contrary to most of the presented research, it seems that chemically engineered defects can overturn this trend, which was discussed by Wang et al.^[60] Defect-rich long-range graphene nanoribbons were synthesized by forcing N/S heteroatoms to escape at increased pyrolysis temperature. The resulting hard carbon delivered 284.5 mAh g^{-1} with an ICE of 85.9% (doped material), which was significantly lower for the less-defective sample (ICE: 72.7%, pristine material).^[60] Density-functional calculations showed that the presence of vacancies lowers the Na-adsorption energy and cuts the interlayer diffusion barrier from 0.69 to 0.51 eV, while the same high-temperature step decreases the BET area, thus lim-

iting SEI formation.^[60] A similar “beneficial-defect” pattern was observed for the $\text{SnS}_x/\text{C}_800$ electrode material in this study: sulfur volatilization at 800 °C increases the I_D/I_G ratio to 2.07 (compared to 1.44 at 600 °C) yet simultaneously lowers the surface area by ≈40% and removes sulfur from the matrix. The surface-area and defect formation effects therefore outweigh the possible Na-trapping by those additional defects, indicating that the ICE is governed by the balance between defect chemistry and electrolyte interface, and that controlled heteroatom escape is a viable route to enhanced Na-ion kinetics and higher first-cycle efficiency in both hard carbon and chalcogenide–carbon composites. Rate capability tests, illustrated in Figure 5e, confirm this trend, showing a continuous capacity decay for $\text{SnS}_x/\text{C}_600$ across increasing current densities. On the other hand, $\text{SnS}_x/\text{C}_800$ demonstrates superior rate performance, maintaining a capacity of ≈500 mAh g^{-1} at a current density of $C/10$, underscoring the ability of the material to sustain its electrochemical activity, even under varying charge–discharge conditions. Finally, long-term cycling results, shown in Figure 5f, further emphasize the significant stability advantage of the $\text{SnS}_x/\text{C}_800$ material. Over 100 cycles, it retains 73% of its initial capacity, demonstrating robust performance and structural integrity. In contrast, the $\text{SnS}_x/\text{C}_600$ material exhibits rapid capacity loss, with a loss of over 82% of its initial capacity within the first 50 cycles. Moreover, average-voltage hysteresis (ΔV , see Table S7, Supporting Information), which was calculated based on the hysteresis curves (see Figure S6c–e, Supporting Information), further confirms the differences between the materials. $\text{SnS}_x/\text{C}_800$ delivers the highest reversible capacity, with a low average charge voltage (1.21 V) and a small hysteresis (0.53 V). In contrast, $\text{SnS}_x/\text{C}_600$ is characterized by a higher \bar{V}_{chg} of up to 1.30 V, further increasing upon cycling, and rising hysteresis, which points to impedance growth and sluggish desodiation process.^[61,62] Literature reports suggest that this may be the effect of a continuously growing SEI, which is also consistent with decreased reversibility.^[63,64] However, it still needs to be borne in mind that in comparison with materials for SIBs, like hard carbons^[65] or polyanion-type materials,^[66] conversion-alloying materials suffer from high average voltages and hysteresis that still need improvement.^[67]

Electrochemical impedance spectroscopy was conducted in staircase potentiostatic mode. The full-range frequency response is presented in Figure S7 (Supporting Information). The Nyquist plots obtained during the second sodiation and desodiation cycles in a narrower frequency range reveal clear differences between the $\text{SnS}_x/\text{C}_600$ (Figure 6a,b) and $\text{SnS}_x/\text{C}_800$ (Figure 6c,d) electrodes, providing insight into their charge transfer resistance, sodium-ion diffusion behavior, and interfacial stability. Each spectrum consists of a high-to-medium frequency semicircle, attributed to charge transfer resistance (R_{ct}) and SEI characteristics, followed by a low-frequency Warburg-type linear region, corresponding to sodium-ion diffusion kinetics. In a Nyquist plot, a Warburg element appears as an inclined line with a 45° slope and is typically described as follows:

$$Z_W(\omega) = \sigma \omega^{-1/2} (1 - j) \quad (2)$$

where ω is the angular frequency and σ is the Warburg coefficient. To determine σ , the real part of the impedance was plotted against $\omega^{-1/2}$ in the low-frequency region, and the slope of the

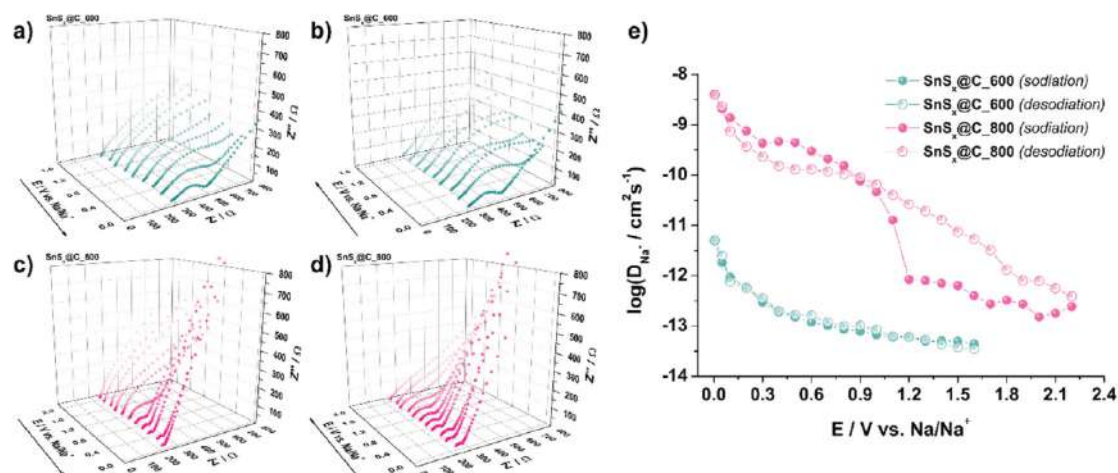


Figure 6. Staircase potentiometric-EIS results for a,b) $\text{SnS}_x\text{@C}_{600}$ and c,d) $\text{SnS}_x\text{@C}_{800}$ half-cells for sodiation (a, c) during desodiation (b, d), focusing on the impedance range up to 800 Ω , and e) calculated diffusion coefficient values in a frequency range of 20 kHz to 1 mHz.

linear fit was calculated. Eventually, the diffusion coefficient D of the mobile ions can be estimated using:

$$D = \left(\frac{RT}{An^2 F^2 c \sigma} \right)^2 \quad (3)$$

where R is the gas constant, T the absolute temperature, A the electrode area, n the charge transferred per ion, F the Faraday constant, and c the concentration of the diffusing species. In this analysis, the low-frequency Warburg impedance was attributed primarily to electrolyte diffusion within the electrode pores (rather than solid-state ion transport in the active material). Consequently, the bulk electrolyte concentration was used in the diffusion coefficient calculations. It should be noted, however, that the actual in-pore concentration can deviate from the nominal bulk value due to partial depletion and local mass transport effects; hence, the resulting diffusion coefficient reflects an effective or apparent value for electrolyte infiltration under these experimental conditions. Nyquist spectra were fitted with the equivalent circuit (Figure S8, Supporting Information), and the fitted data for every potential step during desodiation for both $\text{SnS}_x\text{@C}_{600}$ and $\text{SnS}_x\text{@C}_{800}$ are presented in Tables S8 and S9 (Supporting Information), respectively. During desodiation, R_{SEI} fluctuates between 50 and 100 Ω for $\text{SnS}_x\text{@C}_{600}$, indicating a less stable SEI that continuously reforms.^[68,69] On the other hand, R_{SEI} only rises from 13 to 81 Ω for $\text{SnS}_x\text{@C}_{800}$, evidencing a thinner and more stable interphase.^[49,70,71] R_{ct} is an order of magnitude lower (see Figure S9, Supporting Information) for $\text{SnS}_x\text{@C}_{800}$ (20–80 Ω) than for $\text{SnS}_x\text{@C}_{600}$ (100–1100 Ω), which is the consequence of a more conductive carbon matrix formed at 800 °C. Moreover, the tenfold smaller Warburg coefficient (12 vs 123 $\Omega \text{ s}^{-1/2}$) indicates faster Na^+ transport through the partially closed, mesoporous matrix. Calculated sodium-ion diffusion coefficients further highlight the superior ion transport in $\text{SnS}_x\text{@C}_{800}$ (see Figure 6e). At the beginning of sodiation, the diffusion coefficient for $\text{SnS}_x\text{@C}_{800}$ is 4.0

$\times 10^{-13} \text{ cm}^2 \text{ s}^{-1}$, which is an order of magnitude higher than in $\text{SnS}_x\text{@C}_{600}$ ($4.5 \times 10^{-14} \text{ cm}^2 \text{ s}^{-1}$). As the sodiation process continues, the diffusion coefficients increase, reaching $4.0 \times 10^{-9} \text{ cm}^2 \text{ s}^{-1}$ at 0.005 V for $\text{SnS}_x\text{@C}_{800}$, compared to $4.9 \times 10^{-12} \text{ cm}^2 \text{ s}^{-1}$ for $\text{SnS}_x\text{@C}_{600}$ —a difference of nearly three orders of magnitude. According to the calculated D_{Na^+} , sodium extraction is also kinetically significantly more favorable in the $\text{SnS}_x\text{@C}_{800}$ matrix than for $\text{SnS}_x\text{@C}_{600}$. This result suggests that sodium-ion insertion and deintercalation is much more efficient for $\text{SnS}_x\text{@C}_{800}$, due to its higher electronic conductivity as a direct consequence of the higher pyrolysis temperature. The striking difference in EIS response between $\text{SnS}_x\text{@C}_{600}$ and $\text{SnS}_x\text{@C}_{800}$ can also be linked directly to their pore architecture. BET analysis shows that $\text{SnS}_x\text{@C}_{600}$ is dominated by open micropores ($\approx 0.5 \text{ nm}$), giving a high external surface area. When electrolyte penetrates this network, SEI is forced to grow throughout it, and the ICE is limited to 56%. However, raising the pyrolysis temperature to 800 °C results in partial sintering while also introducing a moderate 1–4 nm mesopore fraction (see Figure S4b, Supporting Information), with an exposed surface area reduced to 128 $\text{m}^2 \text{ g}^{-1}$ and an improved ICE (68%). These new mesopores also shorten Na^+ diffusion paths, explaining the order-of-magnitude higher D_{Na^+} . When the pyrolysis temperature was increased to 1000 °C, the volatilized SnS generates an extensive micro/mesoporous network. Although the transport may be kinetically favored, significantly larger electrode/electrolyte interface area results in a thicker SEI and the ICE falls to 35%, limiting its practical application. This is consistent with recent reports indicating that closed micropores enhance ICE, a moderate mesopore fraction may facilitate ion transport, and excessive mesoporosity results in suppressed ICE despite the enhanced kinetics.^[72–75]

To gain insight into the behavior of these electrode materials during repeated charge–discharge (sodiation–desodiation) cycles, *operando* Raman spectroscopy measurements were carried out on both samples. The second cycle was examined in

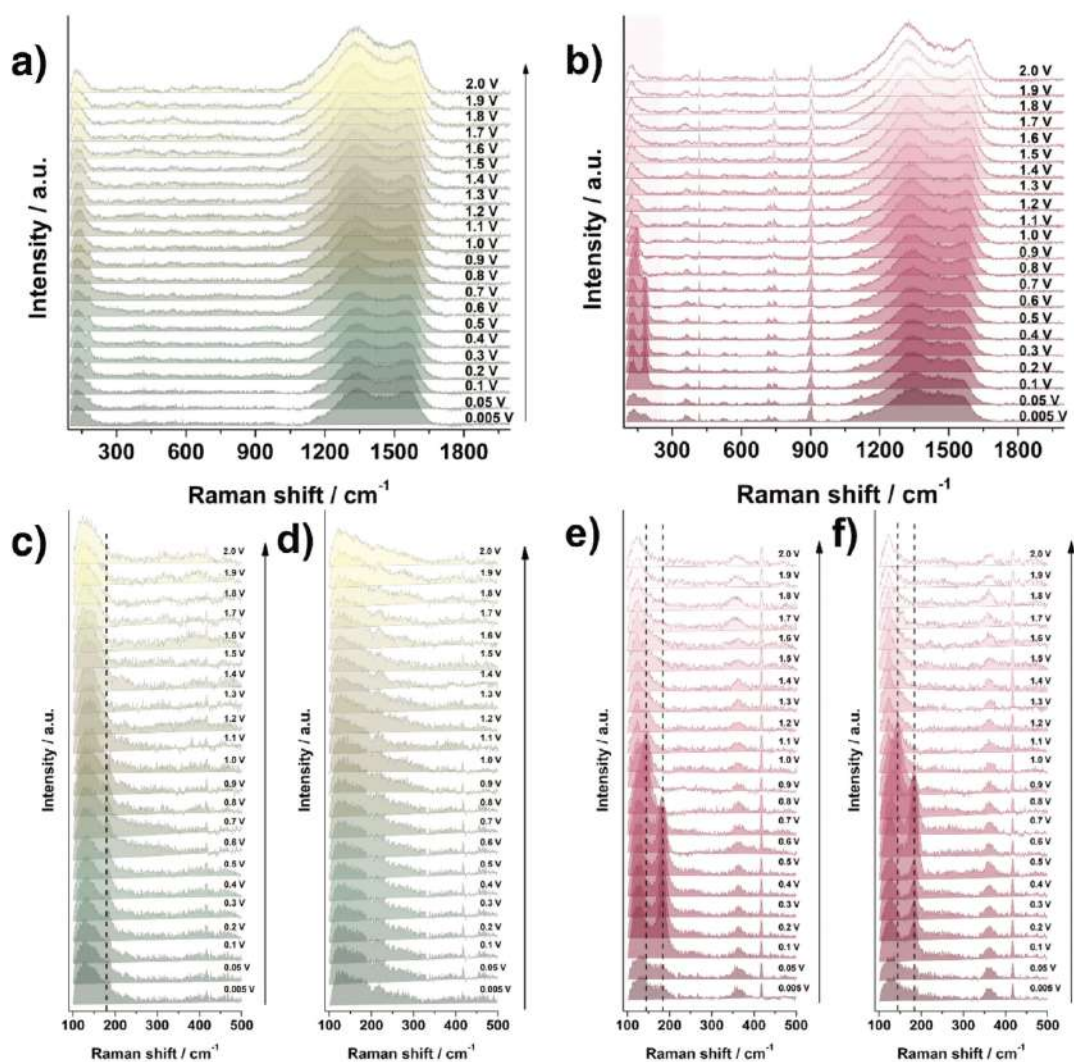


Figure 7. Raman spectra in a full range recorded during desodiation for a) $\text{SnS}_x/\text{C}_{600}$ (2nd cycle) and b) $\text{SnS}_x/\text{C}_{800}$ (2nd cycle); 100–500 cm^{-1} range for c) $\text{SnS}_x/\text{C}_{600}$ (2nd cycle), d) $\text{SnS}_x/\text{C}_{600}$ (20th cycle), e) $\text{SnS}_x/\text{C}_{800}$ (2nd cycle), and f) $\text{SnS}_x/\text{C}_{800}$ (20th cycle).

detail, along with the 20th cycle, to assess any long-term changes. The analysis focused on spectral regions indicative of tin sulfide phases and the carbon matrix within the composite. In addition to the main features discussed in this section, several bands in the Raman spectra can be attributed to the electrolyte, e.g., the signals at ≈ 715 and 892 cm^{-1} , corresponding to the $\text{O}=\text{C}$ ring bending mode and a symmetric ring breathing mode of EC, respectively. The CH_2-O stretching of DEC is represented by the band at $\approx 900\text{ cm}^{-1}$, while the band at 742 cm^{-1} describes the symmetric vibration of PF_6^- ions,^[76] with a weaker band at 417 cm^{-1} , typically associated with one of the bending or deforma-

tion modes of PF_6^- . Representative Raman spectra for the desodiation process in the second scan are presented in Figure 7a,b (full-range sodiation spectra are provided in Figure S10a,b, Supporting Information).

2.1. Second Scan: Tin Sulfide Evolution during Cycling

At 2.0 V, before sodiation, both electrodes show a band at $\approx 217\text{ cm}^{-1}$, attributed to the presence of tin sulfide (see Figure S10c,e, Supporting Information). Upon sodiation, this band weakens,

indicating structural modifications as Na^+ intercalates. For the $\text{SnS}_x/\text{C}_800$ sample, an additional band emerges near $\approx 180 \text{ cm}^{-1}$, which becomes more pronounced at low potentials, confirming the formation of a more sodiated phase (likely Na_2S , Sn , or Na_xSn phases). Notably, this 180 cm^{-1} band is absent in $\text{SnS}_x/\text{C}_600$, suggesting an incomplete conversion reaction—an observation consistent with the weaker electrochemical response in this voltage range, as seen in cyclic voltammetry. During the second desodiation scan, the SnS band at 180 cm^{-1} can be distinguished (Figure 7c,e), especially for $\text{SnS}_x/\text{C}_800$, for which an additional feature at $\approx 150 \text{ cm}^{-1}$ also appears transiently. This sequential band behavior suggests the formation of multiple partially sodiated tin sulfide intermediates, indicating a more complex reaction pathway compared to $\text{SnS}_x/\text{C}_600$. Moreover, in $\text{SnS}_x/\text{C}_800$, this low-energy band persists over a broader voltage range during desodiation compared to sodiation, whereas for $\text{SnS}_x/\text{C}_600$, the signal is much weaker, indicating the process is not as effective, leading to a more irreversible reaction mechanism.

2.2. Second Scan: Carbon Matrix Evolution: $I_{\text{D1}}/I_{\text{G}}$ Ratio and Band Shifts

In the higher-wavenumber region associated with the carbon matrix, at first, both samples exhibit shifts in the D1 and G bands upon sodiation, together with variations in band intensity ratio, indicating sodium intercalation into the carbon structure.^[77] In $\text{SnS}_x/\text{C}_600$, the $I_{\text{D1}}/I_{\text{G}}$ ratio increases from 1.74 at 2.0 V to 1.94 at 0.005 V (Figure 8a and Table S10, Supporting Information), before reversing to 1.71 upon desodiation (Figure 8b and Table S10, Supporting Information). Simultaneously, the G band downshifts from 1585 cm^{-1} at 2.0 V to 1574 cm^{-1} at 0.005 V, then returns to 1579.43 cm^{-1} during desodiation, indicating that Na^+ intercalation modifies the local bonding environment (reflected by shifts in vibrational modes of the carbon), although the process is largely reversible upon desodiation. For $\text{SnS}_x/\text{C}_800$, the spectral shifts are even more pronounced. The $I_{\text{D1}}/I_{\text{G}}$ ratio increases from 1.82 (2.0 V) to 2.68 (0.005 V) (Figure 8e and Table S11, Supporting Information), before dropping back to 1.65 upon desodiation (Figure 8f and Table S11, Supporting Information). The G band follows a similar trend, shifting from 1592 cm^{-1} (2.0 V) to 1569 cm^{-1} (0.005 V), then restoring to 1592 cm^{-1} after full desodiation. The $I_{\text{D1}}/I_{\text{G}}$ ratio, which points to edge defects and vacancies, and the ratios $I_{\text{D3}}/I_{\text{G}}$ and $I_{\text{D4}}/I_{\text{G}}$, indicating chemical or sp^3 -type defects, all rise in $\text{SnS}_x/\text{C}_800$, but change only modestly (or even fall) in $\text{SnS}_x/\text{C}_600$. The large, fully reversible increases in $I_{\text{D3}}/I_{\text{G}}$ and $I_{\text{D4}}/I_{\text{G}}$ for the $\text{SnS}_x/\text{C}_800$ point to reversible sp^2 to sp^3 re-hybridization, while the smaller response for $\text{SnS}_x/\text{C}_600$ indicates that Na^+ mainly dopes preexisting defects without creating new ones. The greater extent of the shifts for $\text{SnS}_x/\text{C}_800$ suggests a more defective carbon structure, which allows stronger interactions with Na^+ . This aligns with previous Raman and BET findings, where higher pyrolysis temperature resulted in more carbon disorder (higher $I_{\text{D1}}/I_{\text{G}}$ ratio) and a lower surface area, making the carbon more electrochemically active. In contrast, the more microporous, less defective structure of $\text{SnS}_x/\text{C}_600$ appears to moderate these interactions, resulting in less intense spectral shifts. Notably, in this wavenumber

region, at ≈ 1115 and 1459 cm^{-1} , one or two additional bands are observed, which can be ascribed to signals arising from the EC and DEC vibrations.^[78,79]

2.3. Long-Term Evolution: 20th Cycle Changes

After 20 charge–discharge cycles, the Raman spectra of $\text{SnS}_x/\text{C}_800$ remain largely unchanged, retaining clear signals associated with tin sulfide transformations. The SnS -related band at $\approx 180 \text{ cm}^{-1}$ is still present before sodiation (Figure S10f, Supporting Information). In addition, the transient 150 cm^{-1} feature, which appeared in the second desodiation cycle, persists (Figure 7f), reinforcing the stepwise, controlled nature of Na^+ insertion and removal. This suggests that $\text{SnS}_x/\text{C}_800$ continues to maintain its well-defined reaction mechanism, supporting its superior electrochemical performance over prolonged cycling. In contrast, significant changes emerge for $\text{SnS}_x/\text{C}_600$. The sodiated SnS -related signals at ≈ 180 and 150 cm^{-1} become unidentifiable (Figure S10d, Supporting Information), suggesting that sodiation remains incomplete. There is only a broadened, weakened signal at $\approx 217 \text{ cm}^{-1}$, showing the tin sulfide is still there, but does not participate in the sodiation process, and the desodiation spectra are almost identical (Figure 7d), confirming that energy storage is not ongoing.

Moreover, sodium intercalation/deintercalation into the carbon framework also remains active in $\text{SnS}_x/\text{C}_800$, reflecting the behavior observed in earlier cycles. The G band shift from 1591 cm^{-1} at 2.0 V to 1565 cm^{-1} at 0.005 V remains significant (Figure 8g and Table S13, Supporting Information), and the back-shift during deintercalation is repetitive (Figure 8h and Table S13, Supporting Information), confirming that Na^+ interaction with the carbon matrix remains effective even after prolonged cycling. The graphitization contrast established above persists after 20 cycles. $\text{SnS}_x/\text{C}_800$ keeps a G-band width of $43\text{--}45 \text{ cm}^{-1}$ and still shows reversible swings in the intensity ratios $I_{\text{D1}}/I_{\text{G}}$, $I_{\text{D3}}/I_{\text{G}}$, and $I_{\text{D4}}/I_{\text{G}}$, confirming that the material is a more ordered sp^2 framework that continues to intercalate Na^+ between the layers. In $\text{SnS}_x/\text{C}_600$, the G band remains broad and all D band ratios vary insignificantly, indicating that the carbon matrix has become electrochemically inert and Na^+ storage is now limited to surface sites. These consistent structural changes suggest that $\text{SnS}_x/\text{C}_800$ maintains its defect-rich carbon framework, ensuring long-term Na^+ storage capability and structural resilience. Conversely, in $\text{SnS}_x/\text{C}_600$, the shifts in D1 and G bands become negligible for both sodiation (Figure 8c and Table S12, Supporting Information) and desodiation (Figure 8d and Table S12, Supporting Information) processes, indicating that the carbon phase is no longer an active participant in the electrochemical process. The $I_{\text{D1}}/I_{\text{G}}$ ratio undergoes only minimal variation, sharply contrasting the greater response in $\text{SnS}_x/\text{C}_800$, suggesting that the carbon network in $\text{SnS}_x/\text{C}_600$ has undergone irreversible transformations, limiting its ability to accommodate Na^+ .

All the findings above can be attributed to distinct SEI formation mechanisms, influenced by both the electrode surface composition and its specific surface area. In $\text{SnS}_x/\text{C}_600$, the higher tin and sulfur content at the electrode surface and the increased specific surface area ($212 \text{ m}^2 \text{ g}^{-1}$) appear to prevent the

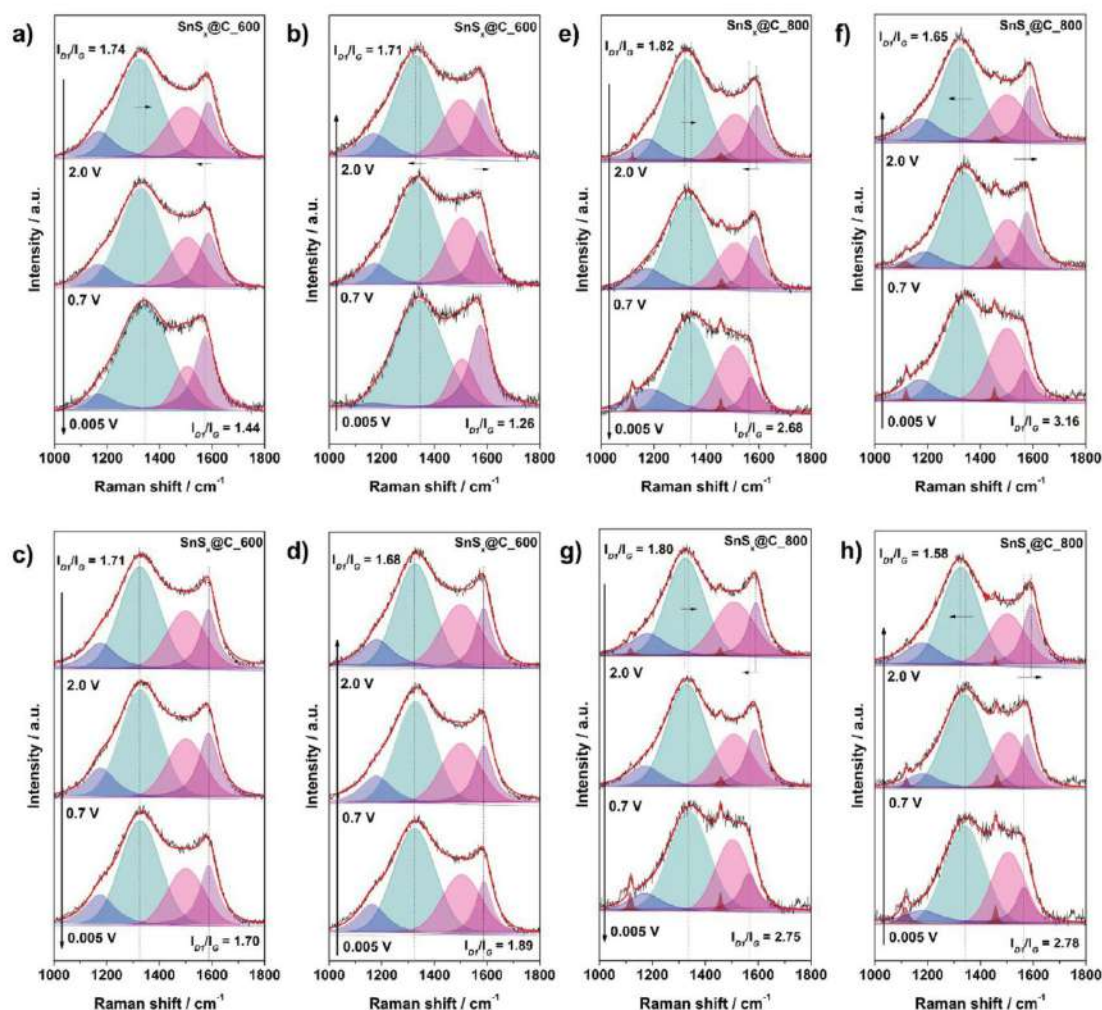


Figure 8. Raman spectra deconvolution for a–d) $\text{SnS}_x\text{@C}_{600}$ and e–h) $\text{SnS}_x\text{@C}_{800}$, spectra recorded *operando* during 2nd sodiation (a,e), 2nd desodiation (b,f), 20th sodiation (c,g), and 20th desodiation (d,h).

establishment of a stable, uniform SEI layer. As repeated sodiation-desodiation induces volume changes in the tin sulfide, the SEI undergoes partial breakdown and reformation, leading to continuous electrolyte consumption. This ongoing process is amplified by the larger surface area, which provides more active sites for side reactions, accelerating capacity loss and overall degradation. The pronounced decrease in the intensity of electrolyte-derived Raman signals for $\text{SnS}_x\text{@C}_{600}$ further supports this, as it indicates continuous electrolyte decomposition and incomplete SEI reformation. By contrast, $\text{SnS}_x\text{@C}_{800}$, where the surface area is lower ($128 \text{ m}^2 \text{ g}^{-1}$) and the carbon framework is more defective but structurally stable, a more coherent SEI layer likely forms, effectively passivating the electrode and preventing excessive electrolyte consumption. This allows

$\text{SnS}_x\text{@C}_{800}$ to retain distinct tin sulfide signals in Raman spectra even after prolonged cycling, indicating better preservation of the chalcogenide-based phase. Moreover, the sustained D1/G-band shifts confirm that its carbon matrix remains electrochemically active, supporting a more stable and reversible Na^+ storage process.

Electrodes were analyzed using XPS depth profiling after 20 charge–discharge cycles, studied in the desodiated state. By examining the surface and subsurface regions (Figure 9a–c for $\text{SnS}_x\text{@C}_{600}$ and Figure 9e–g for $\text{SnS}_x\text{@C}_{800}$), the spectra were obtained before (0 s) and after 90 and 180 s sputtering time. Additional spectral regions (O 1s, F 1s, and S 2p) are displayed in Figure S11 (Supporting Information). The goal was to identify changes in chemical composition and potential interfacial

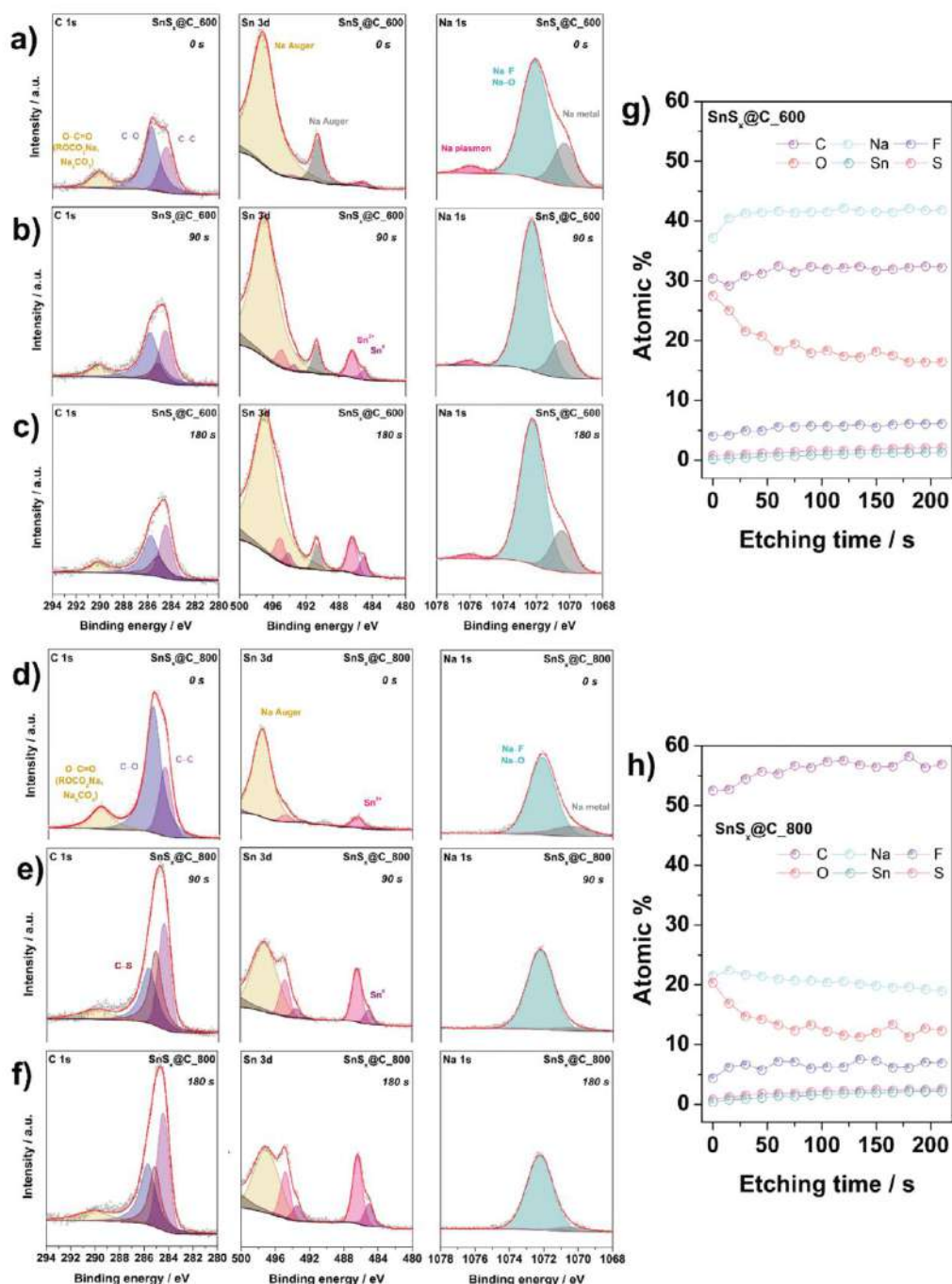


Figure 9. XPS depth-profiling results for a-c) $\text{SnS}_x@\text{C}_{600}$ and d-f) $\text{SnS}_x@\text{C}_{800}$ at (a,d) 0 s, (b,e) 90 s, and (c,f) 180 s of Ar^+ ion sputtering with the corresponding relative elemental composition profiles for g) $\text{SnS}_x@\text{C}_{600}$ and h) $\text{SnS}_x@\text{C}_{800}$.

reactions occurring during cycling. Prior to depth profiling, electrodes were washed to remove residual electrolyte salts.

Initially (before sputtering, designated as 0 s), both $\text{SnS}_x@\text{C}_600$ and $\text{SnS}_x@\text{C}_800$ display pronounced peaks at 285.7 and 290.1 eV in the C 1s region, corresponding to C=O and O—C=O species, respectively (Figure 9a,e). These features are commonly associated with inorganic carbonates (Na_2CO_3) and sodium alkyl carbonates (ROCO_2Na , O—C), indicating a surface SEI layer rich in oxygen-containing compounds.^[80] After sputtering (90 and 180 s), the relative intensities from these oxygenated species significantly decrease, while the C—C peak at 284.4 eV grows (Figure 9b,c,f,g). The simultaneous drop in the O 1s signal at 532.2 eV (Figure S11, Supporting Information) further confirms that a major portion of the organic or carbonate-based SEI is etched away, exposing a higher fraction of the underlying carbonaceous matrix. In this region, a distinct peak is also observed at ≈ 528 eV, which corresponds to the shifted Na KLL Auger signal, typically expected around 533 eV.

Interestingly, $\text{SnS}_x@\text{C}_800$ retains ≈ 50 at% carbon at deeper sputtering levels, whereas $\text{SnS}_x@\text{C}_600$ shows only ≈ 30 at% C. In addition, a C—S component—which had been observed in the pristine electrodes—is visible, suggesting a preservation of the carbon—chalcogen framework.^[52] Analysis of the Sn 3d region reveals a larger fraction of metallic Sn and Sn^{2+} in $\text{SnS}_x@\text{C}_800$, while in $\text{SnS}_x@\text{C}_600$, a peak at ≈ 489.9 eV is also observed, which corresponds to a shifted Na KLL Auger signal from metallic sodium. In addition, a Na 1s signal at ≈ 1070.3 eV is detected, which also indicates the presence of metallic sodium,^[81,82] hinting at more pronounced sodium incorporation and conversion reaction that is not fully reversible. Furthermore, the Na 1s peak at around 1072.1 eV, typically attributed to Na^+ salts, indicated the presence of sodium fluoride or related fluoride-based species in both samples,^[83] which is in agreement with the F 1s signal at 685 eV (Figure S11, Supporting Information). Both Na and F content increase with the etching time, which is consistent with the established multilayer SEI model, where the outer layer is predominantly composed of various organic species (e.g., ROCO_2Na) generated by electrode instability and degradation during cycling, while the inner layer mainly contains inorganic compounds such as NaF .^[83,84] Also, the overall sodium content is nearly twice as high in the $\text{SnS}_x@\text{C}_600$ electrode, even after 180 s of sputtering. This aligns with more extensive irreversible Na trapping or side reactions in the $\text{SnS}_x@\text{C}_600$ material. Such observations corroborate the *operando* Raman findings, where $\text{SnS}_x@\text{C}_800$ showed more effective and reversible sodiation. The XPS data imply that a thicker, more heterogeneous SEI is formed on $\text{SnS}_x@\text{C}_600$, with a higher proportion of organic byproducts and residual Na^+ . In contrast, $\text{SnS}_x@\text{C}_800$ exhibits a relatively thinner and more carbon-dominated near-surface region. Moreover, although bulk-averaged EDS (Tables S1–S4, Supporting Information) confirms the near-stoichiometric Sn/S ratio of both $\text{SnS}_x@\text{C}_600$ and $\text{SnS}_x@\text{C}_800$, the surface-sensitive XPS data reveal that $\text{SnS}_x@\text{C}_600$ exposes more S sites than $\text{SnS}_x@\text{C}_800$. This surface enrichment promotes a thicker SEI and the higher R_{SEI} observed by EIS, whereas the lower coverage in $\text{SnS}_x@\text{C}_800$ favors a thinner, more stable interphase and improved cycling stability. A thicker or more heterogeneous SEI (as implied for $\text{SnS}_x@\text{C}_600$) can lead to irreversible capacity losses and compromised ion transport.^[85] Altogether, the XPS

depth profiling clarifies why the $\text{SnS}_x@\text{C}_800$ electrode exhibits greater stability and reversibility: its near surface region contains fewer irreversibly bound sodium species, a more robust carbon—sulfur framework signal, and a higher fraction of stable inorganic Sn-containing phases—all of which promote a more favorable electrode—electrolyte interface during prolonged cycling.

3. Conclusion

In summary, this work demonstrates the pivotal influence of pyrolysis temperature on the structure, interfacial chemistry, and electrochemical performance of $\text{SnS}_x@\text{C}$ anodes for sodium-ion batteries. By systematically comparing samples carbonized at 600, 800, and 1000 °C, it was shown that the pyrolysis at 800 °C promotes more effective sulfur release from SnS_2 and yields a defect-rich yet robust carbon matrix, resulting in a stable electrode—electrolyte interface. *Operando* Raman spectroscopy revealed that $\text{SnS}_x@\text{C}_800$ maintains reversible Sn—S redox processes and Na^+ intercalation throughout extended cycling, whereas the $\text{SnS}_x@\text{C}_600$ sample retains extra sulfur in the matrix, hindering complete conversion reactions and leading to capacity decay. XPS depth profiling further confirms that the 800 °C composite forms a thinner SEI layer with fewer irreversibly bound Na species. As a result, $\text{SnS}_x@\text{C}_800$ achieves a stable capacity of ≈ 500 mAh g^{−1} at C/10 and retains a substantial fraction of this capacity over 100 cycles, significantly outperforming its lower-temperature counterpart. These findings highlight the crucial balance between carbon defects, surface area, and SEI formation for optimizing Na^+ storage performance. Overall, the *operando* spectroscopic insights gained here underscore the importance of tailoring thermal treatments to design stable chalcogenide-carbon anodes, paving the way toward high-performance sodium-ion batteries.

4. Experimental Section

$\text{SnS}_x@\text{C}$ Synthesis: The $\text{SnS}_x@\text{C}$ electrode materials were prepared as follows: 4.72 g of starch ($(\text{C}_6\text{H}_{10}\text{O}_5)_n$, Sigma-Aldrich, USA) and 2.98 g of thioacetamide ($\text{C}_2\text{H}_5\text{NS}$, Chemat, Poland) were mixed with 100 mL of ethylene glycol ($\text{C}_2\text{H}_6\text{O}_2$, POCH, Poland) under continuous stirring. Subsequently, 3.4 mL of tin(IV) chloride (POCH, Poland) was added to the mixture, and finally, the solution was placed in the Teflon-lined autoclave at 150 °C for 20 h. The resulting suspension was centrifuged at 9000 rpm with acetone (POCH, Poland) until clear phase separation was achieved. The as-obtained solid fraction was preliminarily dried at 60 °C for 24 h, and then subjected to annealing under an Ar atmosphere in a quartz tube furnace with a vacuum system. Powders were heated from room temperature to the target pyrolysis temperature at a heating rate of ≈ 1.7 °C min^{−1}, with a holding time of 4 h at the final temperature. Pyrolysis temperatures of 600, 800, and 1000 °C were selected to probe three distinct regions: below the onset of significant Sn/S volatilization, the region where SnS does not yet sublime intensively, and an upper limit where SnS reaches a high vapor pressure and is effectively removed. For brevity, the samples are named as $\text{SnS}_x@\text{C}_600$, $\text{SnS}_x@\text{C}_800$, and $\text{SnS}_x@\text{C}_{1000}$ depending on the pyrolysis temperature applied. The obtained samples were ground in a mortar and subsequently in a ball mill (Rocker Mill MM 400, Retsch, Germany), with a final step of sieving down to <40 μm . The scheme of materials preparation is presented in Figure S1 (Supporting Information).

Electrode Preparation: Electrodes for electrochemical testing were prepared by mixing the active material with styrene-butadiene rubber (SBR, Zeon, Japan), carboxymethylcellulose (CMC, Sigma-Aldrich, USA), and carbon black (CB, TIMCAL Super P Conductive, Switzerland) in the

Table 2. SnS_x@C-based slurry composition used for electrode printing.

Material	Wt%	Composition
SnS _x @C	85	Powder
Styrene-butadiene rubber	5	40 wt% in H ₂ O/EtOH (vol. 3:7)
Carboxymethylcellulose	5	5 wt% in H ₂ O
Carbon Black	5	Powder

composition presented in **Table 2**. The chemicals were mixed with water using an Ultra Turrax (IKA-Werke, GmbH, Germany). After that, the electrodes were printed on a copper foil using a doctor blade technique (gap distance 120 µm) and dried at 40 °C for 24 h. Finally, the round-shaped electrodes with a diameter of 10 mm were cut with a cutter and dried in a vacuum oven (B-585 BUCHI Glass Oven, Switzerland) at 80 °C for 24 h. The weight of the materials on individual electrodes was 2.15 ± 0.35 mg cm⁻².

Materials Characterization: Scanning electron microscopy (SEM) was applied for morphological analysis of powders with an accelerating voltage of 30 kV (type 1430 VP, LEO Electron Microscopy Ltd., equipped with EDX). High-resolution TEM images were recorded using a JEOL JEM-21000F field-emission microscope.

N₂ sorption analysis was performed using ASAP2020 Plus (Micromeritics) after outgassing in a vacuum at 200 °C for 24 h. The specific surface area (S_{BET}) value was obtained through calculations by the Brunauer–Emmett–Teller equation, whereas the density functional theory (DFT) method was applied to determine the pore size distribution. The total pore volume (V_t) was measured at a single point at the maximum relative pressure (p/p_0).

XRD patterns were recorded for powders with the diffractometer (Philips X'Pert) equipped with Cu K α radiation detector (X'Celerator Scientific, $\lambda = 0.15406$ nm).

Raman measurements were performed *operando* by means of Micro-Raman spectrometer (Renishaw InVia) equipped with a 785 nm diode laser (100 mW). Spectra were recorded through a quartz window of an electrochemical cell using a 50x objective lens. Raman spectra were recorded in two regimes by measuring the entire spectra in the range 120–3200 cm⁻¹ and by fast measurement in a narrow spectral range, which enabled shortening the recording time of a single spectrum during electrochemical analysis.

XPS analysis was performed with an ESCALAB 250Xi spectrometer (ThermoFisher, GB), equipped with a monochromized Al K α source ($E_{h\nu} = 1486.68$ eV) set to 650 µm spot size. The standard lens mode was used with a pass energy of 100 eV for survey and 10 eV for high-resolution spectra. In-lens charge compensation was applied for samples with insulating SEI. For depth profiling, samples were etched with a MAGCIS Ar ion source (ThermoFisher, GB) in ion mode set at 3 keV and 1.5 mm spot size in cycles of 15 s. Prior to XPS depth profiling, the cycled electrodes were washed to remove residual electrolyte salts. The washing procedure involved immersing each electrode in fresh dimethyl carbonate (DMC, anhydrous, ≥99%, Sigma-Aldrich, USA) for 5 min. This step was repeated two additional times with fresh portions of DMC, for a total of three washing cycles. To remove remains of organic solvents, electrochemically modified samples were pretreated by etching with the MAGCIS Ar ion source in cluster mode four times for 15 s at 6 keV. For data analysis, Advantage 5.9931 was used.

For *operando* measurements, the ECC-Opto-10 cell (EL-Cell GmbH, Germany), allowing for side-by-side arrangements of the electrodes, was used with a galvanostat/potentiostat BioLogic SP-150. Apart from *operando* Raman analysis, electrochemical measurements were performed in a two-electrode Swagelok configuration, in 1 M NaPF₆ in EC/DEC (3:7 by wt%) supplemented with 5 wt% fluoroethylene carbonate (FEC) addition (E-Lyte, Germany). The prepared materials were used as a working electrode, and a sodium disc (AOT, China) was used as a combined counter and reference electrode, separated by a glass fiber separator (Schleicher&Schill, Germany). The galvanostatic charge/discharge was

performed in the potential range from 0.005 to 2.5 V versus Na/Na⁺ with a current density based on the theoretical capacity of graphite, i.e., 1 C = 372 mA g⁻¹ (fully charged/discharged in 1 h), e.g., C/10 = 37.2 mA g⁻¹. Staircase potentiostatic electrochemical impedance spectroscopy (SPEIS) was conducted in a three-electrode Swagelok cell with two sodium discs working as counter and reference electrodes, with an amplitude of 10 mV in a frequency range of 20 kHz to 1 mHz. SPEIS measurements were performed at a series of 100 mV potential increments during the charging and discharging of the material. Prior to each impedance measurement, a stabilization period of 4 h was employed to ensure that the system reached steady-state current conditions, minimizing transient effects and enabling accurate impedance data acquisition. All experiments were performed using the galvanostat/potentiostat BioLogic VMP3 and BioLogic VSP 2078.

Supporting Information

Supporting Information is available from the Wiley Online Library or from the author.

Acknowledgements

Z.Z. and A.P.N. acknowledge the financial support provided by the National Science Centre, Poland, under PRELUDIUM Grant No. UMO-2023/49/N/ST5/01794 and Polish National Agency for Academic Exchange, Poland, within the STER programme, under Grant No. PPI/STE/2020/00023/U/00001. The authors acknowledge the Electron and Light Microscopy Service Unit of the School of Mathematics and Science of the Carl von Ossietzky University for the use of the imaging facilities. The authors would also like to acknowledge A. Ilnicka for SEM and BET measurements.

Conflict of Interest

The authors declare no conflict of interest.

Data Availability Statement

The data that support the findings of this study are available from the corresponding author upon reasonable request.

Keywords

anode materials, metal chalcogenides, *operando* Raman spectroscopy, sodium-ion batteries, tin sulfide

Received: April 10, 2025

Revised: July 4, 2025

Published online:

- [5] X. M. Lin, X. T. Yang, H. N. Chen, Y. L. Deng, W. H. Chen, J. C. Dong, Y. M. Wei, J. F. Li, *J. Energy Chem.* **2023**, *76*, 146.
- [6] A. H. Thompson, M. S. Whittingham, *Mater. Res. Bull.* **1977**, *12*, 741.
- [7] A. Yoshino, K. Sanekihika, T. Nakajima, U.S. Patent 4,669,595, **1987**.
- [8] K. Mizushima, P. C. Jones, P. J. Wiseman, J. B. Goodenough, *Mater. Res. Bull.* **1980**, *15*, 783.
- [9] X. Cai, Y. Yue, Z. Yi, J. Liu, Y. Sheng, Y. Lu, *Nano Energy* **2024**, *129*, 110052.
- [10] Y. Yang, C. Wu, X.-X. He, J. Zhao, Z. Yang, L. Li, X. Wu, L. Li, S. L. Chou, *Adv. Funct. Mater.* **2024**, *34*, 2302277.
- [11] S. Komaba, T. Hasegawa, M. Dahbi, K. Kubota, *Electrochem. Commun.* **2015**, *60*, 172.
- [12] E. J. Kim, P. R. Kumar, Z. T. Gossage, K. Kubota, T. Hosaka, R. Tatara, S. Komaba, *Chem. Sci.* **2022**, *13*, 6121.
- [13] C. Zhao, Q. Wang, Z. Yao, J. Wang, B. Sánchez-Lengeling, F. Ding, X. Qi, Y. Lu, X. Bai, B. Li, H. Li, A. Aspuru-Guzik, X. Huang, C. Delmas, M. Wagemaker, L. Chen, Y. S. Hu, *Science* **2020**, *370*, 708.
- [14] K. M. Abraham, *ACS Energy Lett.* **2020**, *5*, 3544.
- [15] H. Lei, J. Li, X. Zhang, L. Ma, Z. Ji, Z. Wang, L. Pan, S. Tan, W. Mai, *InfoMat* **2022**, *4*, 12272.
- [16] Y. Matsuda, H. Nakashima, M. Morita, Y. Takasu, *J. Electrochem. Soc.* **1981**, *128*, 2552.
- [17] K. Sada, J. Darga, A. Manthiram, *Adv. Energy Mater.* **2023**, *13*, 2302321.
- [18] A. Rudola, C. J. Wright, J. Barker, *Energy Mater. Adv.* **2021**, *2021*, 9798460.
- [19] X. Y. Yu, X. W. Lou, *Adv. Energy Mater.* **2018**, *8*, 1701592.
- [20] X. Y. Yu, L. Yu, X. W. Lou, *Adv. Energy Mater.* **2016**, *6*, 1501333.
- [21] S. Dai, L. Wang, M. Cao, Z. Zhong, Y. Shen, M. Wang, *Mater. Today Energy* **2019**, *12*, 114.
- [22] Y. Fang, D. Luan, X. W. Lou, *Adv. Mater.* **2020**, *32*, 2002976.
- [23] X. Xia, C. Zhu, J. Luo, Z. Zeng, C. Guan, C. F. Ng, H. Zhang, H. J. Fan, *Small* **2014**, *10*, 766.
- [24] Y. Xiao, S. H. Lee, Y. K. Sun, *Adv. Energy Mater.* **2017**, *7*, 1601329.
- [25] J. Wu, M. Ihsan-Ul-Haq, F. Ciucci, B. Huang, J. K. Kim, *Energy Storage Mater.* **2021**, *34*, 582.
- [26] G. Huang, H. Zhang, F. Gao, D. Zhang, Z. Zhang, Y. Liu, Z. Shang, C. Gao, L. Luo, M. Terrones, Y. Wang, *Carbon* **2024**, *228*, 119354.
- [27] A. Gomez-Martin, J. Martinez-Fernandez, M. Ruttter, M. Winter, T. Placke, J. Ramirez-Rico, *Chem. Mater.* **2019**, *31*, 7288.
- [28] L. Liu, L. Xiao, Z. Sun, S. Bashir, R. Kasi, Y. Gu, R. Subramaniam, *J. Energy Chem.* **2024**, *94*, 414.
- [29] A. Beda, C. Vaulot, F. Rabuel, M. Morcrette, C. M. Ghimbeu, *Energy Adv.* **2022**, *1*, 185.
- [30] X. Yue, B. Qiao, J. Wang, Z. Xie, Z. Liu, Z. Yang, A. Abudula, G. Guan, *Renewable Sustainable Energy Rev.* **2023**, *185*, 113592.
- [31] E. Olsson, J. Cottom, H. Alptekin, H. Au, M. Crespo-Ribadeneyra, M.-M. Titirici, Q. Cai, *Small* **2022**, *18*, 2200177.
- [32] V. Simone, A. Boulineau, A. de Geyer, D. Rouchon, L. Simonin, S. Martinet, *J. Energy Chem.* **2016**, *25*, 761.
- [33] T. Wang, D. Legut, Y. Fan, J. Qin, X. Li, Q. Zhang, *Nano Lett.* **2020**, *20*, 6199.
- [34] X. Q. Cheng, H. J. Li, Z. X. Zhao, Y. Z. Wang, X. M. Wang, *New Carbon Mater.* **2021**, *36*, 93.
- [35] C. Meng, P. Das, X. Shi, Q. Fu, K. Müllen, Z. S. Wu, *Small Sci.* **2021**, *1*, 2000076.
- [36] Q. Gan, N. Qin, S. Gu, Z. Wang, Z. Li, K. Liao, K. Zhang, L. Lu, Z. Xu, Z. Lu, *Small Methods* **2021**, *5*, 2100580.
- [37] J. S. Weaving, A. Lim, J. Millichamp, T. P. Neville, D. Ledwoch, E. Kendrick, P. F. McMillan, P. R. Shearing, C. A. Howard, D. J. L. Brett, *ACS Appl. Energy Mater.* **2020**, *3*, 3474.
- [38] M. Sathish, S. Mitani, T. Tormai, I. Honma, *J. Phys. Chem. C* **2012**, *116*, 12475.
- [39] T. Zhou, W. K. Pang, C. Zhang, J. Yang, Z. Chen, H. K. Liu, Z. Guo, *ACS Nano* **2014**, *8*, 8323.
- [40] A. P. Nowak, A. Rokicińska, Z. Wang, M. Przeźniak-Welenc, Z. Zarach, K. Tao, D. Roda, M. Szkoda, K. Trzciński, J. Li, P. Kuśtrowski, *Sci. Rep.* **2024**, *14*, 31212.
- [41] A. Sadezky, H. Muckenhuber, H. Grothe, R. Niessner, U. Pöschl, *Carbon* **2005**, *43*, 1731.
- [42] Y. Zheng, T. Zhou, C. Zhang, J. Mao, H. Liu, Z. Guo, *Angew. Chem., Int. Ed.* **2016**, *55*, 3408.
- [43] M. Guc, J. Andrade-Arvizu, I. Y. Ahmet, F. Oliva, M. Placidi, X. Alcobé, E. Saucedo, A. Pérez-Rodríguez, A. L. Johnson, V. Izquierdo-Roca, *Acta Mater.* **2020**, *183*, 1.
- [44] R. E. Banai, L. A. Burton, S. G. Choi, F. Hofherr, T. Sorgenfrei, A. Walsh, B. To, A. Cröll, J. R. S. Brownson, *J. Appl. Phys.* **2014**, *116*, 013511.
- [45] Y. Li, S. Xu, X. Wu, J. Yu, Y. Wang, Y. S. Hu, H. Li, L. Chen, X. Huang, *J. Mater. Chem. A* **2014**, *3*, 71.
- [46] A. C. Ferrari, J. Robertson, *Philos. Trans. R. Soc., A* **2004**, *362*, 2477.
- [47] A. Ferrari, J. Robertson, *Phys. Rev. B* **2000**, *61*, 14095.
- [48] B. Zhao, D. Song, Y. Ding, J. Wu, Z. Wang, Z. Chen, Y. Jiang, J. Zhang, *Nanoscale* **2020**, *12*, 3941.
- [49] J. Lee, C. Choi, H. Lee, S. Ma, J. Tan, G. Jang, S. G. Shim, Y. S. Park, J. Yun, D. W. Kim, J. Moon, *Adv. Energy Mater.* **2022**, *12*, 2103138.
- [50] J. Song, X. Zu, W. Jian, Y. Sun, W. Zhang, X. Qiu, *Chem. Eng. Sci.* **2024**, *300*, 120670.
- [51] Z. Dang, W. Meng, J. Han, D. Li, L. Jiang, *J. Alloys Compd.* **2022**, *891*, 162051.
- [52] T. H. T. Luu, D. L. Duong, T. H. Lee, D. T. Pham, R. Sahoo, G. Han, Y. M. Kim, Y. H. Lee, *J. Mater. Chem. A* **2020**, *8*, 7861.
- [53] D. Li, L. Dai, X. Ren, F. Ji, Q. Sun, Y. Zhang, L. Ci, *Energy Environ. Sci.* **2021**, *14*, 424.
- [54] C. Xia, F. Zhang, H. Liang, H. N. Alshareef, *Nano Res.* **2017**, *10*, 4368.
- [55] L. Wang, X. Li, Z. Jin, Z. Liang, X. Peng, X. Ren, B. Gao, G. Feng, P. K. Chu, K. Huo, *J. Mater. Chem. A* **2019**, *7*, 27475.
- [56] D. Chao, C. Zhu, P. Yang, X. Xia, J. Liu, J. Wang, X. Fan, S. V. Savilov, J. Lin, H. J. Fan, Z. X. Shen, *Nat. Commun.* **2016**, *7*, 12122.
- [57] S. Li, J. Liu, Y. Chen, S. Li, P. Tang, Y. Xie, S. Xie, Z. Miao, J. Zhu, X. Yan, *Adv. Funct. Mater.* **2025**, <https://doi.org/10.1002/adfm.202424629>.
- [58] J. Xu, B. Chen, B. Hu, Y. Gu, X. Li, Y. Liu, D. Sha, J. Zhang, S. Huang, *J. Energy Storage* **2024**, *81*, 110306.
- [59] B. Yang, J. Wang, Y. Zhu, K. Ji, C. Wang, D. Ruan, Y. Xia, *J. Power Sources* **2021**, *492*, 229656.
- [60] Y. Wang, M. Li, Y. Zhang, N. Zhang, *Chem. Eng. J.* **2024**, *499*, 156115.
- [61] J. E. Harlow, S. L. Glazier, J. Li, J. R. Dahn, *J. Electrochem. Soc.* **2018**, *165*, A3595.
- [62] C. P. Aiken, J. E. Harlow, R. Tingley, T. Hynes, E. R. Logan, S. L. Glazier, A. S. Keefe, J. R. Dahn, *J. Electrochem. Soc.* **2020**, *167*, 130541.
- [63] J. Plotek, A. Kalka, A. Maximenko, Ł. Kondracki, S. Trabesinger, M. Moździerz, P. Czaja, J. Molenda, *Energy Storage Mater.* **2024**, *72*, 103780.
- [64] J. Qian, Y. Chen, L. Wu, Y. Cao, X. Ai, H. Yang, *Chem. Commun.* **2012**, *48*, 7070.
- [65] A. Kamiyama, K. Kubota, D. Igarashi, Y. Youn, Y. Tateyama, H. Ando, K. Gotoh, S. Komaba, *Angew. Chem., Int. Ed.* **2021**, *60*, 5114.
- [66] C. Wu, S.-X. Dou, Y. Yu, *Small* **2018**, *14*, 1703671.
- [67] L. Fang, N. Bahlawane, W. Sun, H. Pan, B. Bin Xu, M. Yan, Y. Jiang, *Small* **2021**, *17*, 2101137.
- [68] R. Tripathi, G. Yesilbas, X. Lamprecht, P. Gandharapu, A. S. Bandarenka, R. O. Dusan, A. Mukhopadhyay, *J. Electrochem. Soc.* **2023**, *170*, 090544.
- [69] S. Waluś, C. Barchasz, R. Bouchet, F. Alloin, *Electrochim. Acta* **2020**, *359*, 136944.
- [70] Z. Wang, H. Yang, Y. Liu, Y. Bai, G. Chen, Y. Li, X. Wang, H. Xu, C. Wu, J. Lu, *Small* **2020**, *16*, 2003268.

- [71] J. Choi, N. R. Kim, K. Lim, K. Ku, H. J. Yoon, J. G. Kang, K. Kang, P. V. Braun, H. J. Jin, Y. S. Yun, *Small* **2017**, *13*, 1700767.
- [72] C. Wen, M. Huang, C. Feng, N. Kong, K. Hou, R. Xie, Z. Shao, R. Tan, F. Han, *Carbon* **2024**, *230*, 119702.
- [73] Z. Tang, R. Zhang, H. Wang, S. Zhou, Z. Pan, Y. Huang, D. Sun, Y. Tang, X. Ji, K. Amine, M. Shao, *Nat. Commun.* **2023**, *14*, 6024.
- [74] A. Rützler, J. Büttner, J. Oechsler, S. E. Balaghi, S. Küspert, N. Ortlieb, A. Fischer, *Adv. Funct. Mater.* **2024**, *34*, 2401188.
- [75] W. Luo, C. Bommier, Z. Jian, X. Li, R. Carter, S. Vail, Y. Lu, J. J. Lee, X. Ji, *ACS Appl. Mater. Interfaces* **2015**, *7*, 2626.
- [76] D. Chao, P. Liang, Z. Chen, L. Bai, H. Shen, X. Liu, X. Xia, Y. Zhao, S. V. Savilov, J. Lin, Z. X. Shen, *ACS Nano* **2016**, *10*, 10211.
- [77] Y. Aniskevich, J. H. Yu, J. Y. Kim, S. Komaba, S. T. Myung, *Adv. Energy Mater.* **2024**, *14*, 2304300.
- [78] P. Lanz, P. Novák, *J. Electrochem. Soc.* **2014**, *161*, A1555.
- [79] M. Melzi d'Eril, A. Kempf, D. M. De Carolis, M. J. Graczyk-Zajac, G. Mera, R. Riedel, *Batteries Supercaps* **2024**, *7*, 202400029.
- [80] X. Zheng, H. Fu, C. Hu, H. Xu, Y. Huang, J. Wen, H. Sun, W. Luo, Y. Huang, *J. Phys. Chem. Lett.* **2019**, *10*, 707.
- [81] L. E. Goodwin, P. Till, M. Bhardwaj, N. Nazer, P. Adelhelm, F. Tietz, W. G. Zeier, F. H. Richter, J. Janek, *ACS Appl. Mater. Interfaces* **2023**, *15*, 50457.
- [82] V. Kumar, A. Y. S. Eng, Y. Wang, D. T. Nguyen, M. F. Ng, Z. W. Seh, *Energy Storage Mater.* **2020**, *29*, 1.
- [83] Z. Tang, H. Wang, P. F. Wu, S. Y. Zhou, Y. C. Huang, R. Zhang, D. Sun, Y. G. Tang, H. Y. Wang, *Angew. Chem., Int. Ed.* **2022**, *61*, 202200475.
- [84] J. Zhang, D. W. Wang, W. Lv, S. Zhang, Q. Liang, D. Zheng, F. Kang, Q. H. Yang, *Energy Environ. Sci.* **2017**, *10*, 370.
- [85] M. Ma, H. Cai, C. Xu, R. Huang, S. Wang, H. Pan, Y.-S. Hu, *Adv. Funct. Mater.* **2021**, *31*, 2100278.

Supporting Information

A Key to Material's Stability: Tuning Pyrolysis Temperature in $\text{SnS}_x\text{@C}$ Anodes for Sodium-Ion Batteries

Zuzanna Zarach^{*}, Mirosław Sawczak, Carsten Dosche, Konrad Trzcinski, Mariusz Szkoda, Magdalena Graczyk-Zajac, Ralf Riedel, Gunther Wittstock, Andrzej P. Nowak

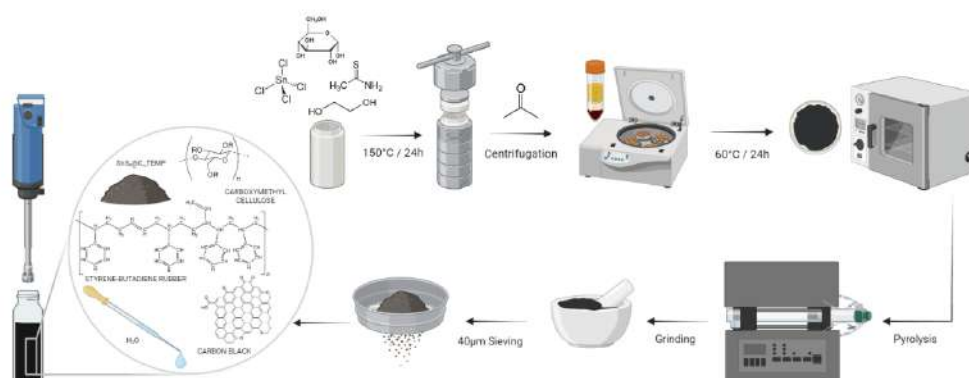


Figure S1. Scheme of the $\text{SnS}_x\text{@C}$ electrode materials preparation.

Table S1. EDS analysis for the $\text{SnS}_x\text{@C-600}$ powder

$\text{SnS}_x\text{@C-600}$	Mass fraction (%)					
Spectrum	C	O	Al	S	Cl	Sn
Mean Value	10.75	47.75	1.80	8.93	0.13	30.55
Sigma	1.38	1.32	0.47	0.53	0.01	1.71
Sigma mean	0.69	0.66	0.23	0.27	0.00	0.85
Relative elemental composition (%)						
Value	19.95	66.53	1.49	6.21	0.08	5.74

Table S2. EDS analysis for the $\text{SnS}_x\text{@C-800}$ powder

$\text{SnS}_x\text{@C-800}$	Mass fraction (%)				
Spectrum	C	O	Al	S	Sn
Mean Value	7.50	41.85	2.14	10.72	37.79
Sigma	4.72	13.61	0.54	3.07	14.71
Sigma mean	2.36	6.80	0.27	1.53	7.36
Relative elemental composition (%)					
Value	15.72	65.85	2.00	8.42	8.01

Table S3. EDS analysis for the $\text{SnS}_x\text{@C-1000}$ powder

$\text{SnS}_x\text{@C-1000}$	Mass fraction (%)					
Spectrum	C	O	Al	Si	S	Sn
Mean Value	40.98	51.43	1.18	0.20	4.30	1.90
Sigma	1.46	1.38	0.10	0.01	0.06	0.09
Sigma mean	0.73	0.69	0.05	0.01	0.03	0.05
Relative elemental composition (%)						
Value	49.97	47.08	0.64	0.11	1.97	0.23

Table S4. EDS analysis for the $\text{SnS}_x\text{@C}$ powder

$\text{SnS}_x\text{@C}$	Mass fraction (%)					
Spectrum	C	O	Al	S	Cl	Sn
Mean Value	17.72	58.76	0.76	8.00	2.37	12.39
Sigma	8.01	6.76	0.22	4.76	0.96	9.56
Sigma mean	3.27	2.76	0.09	1.94	0.39	3.90
Relative elemental composition (%)						
Value	26.36	65.62	0.51	4.46	1.19	1.86

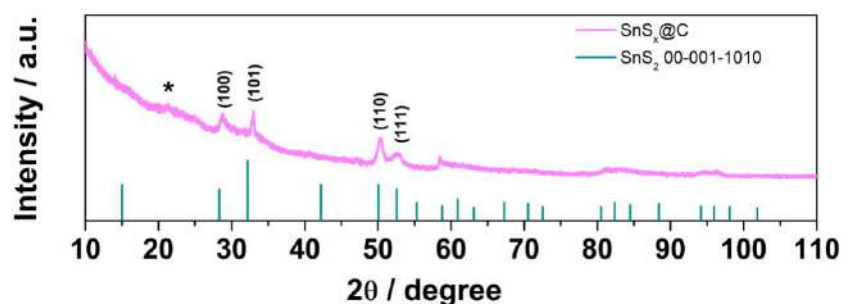


Figure S2. XRD patterns for the $\text{SnS}_x\text{@C}$ powder (without pyrolysis) in the full range.

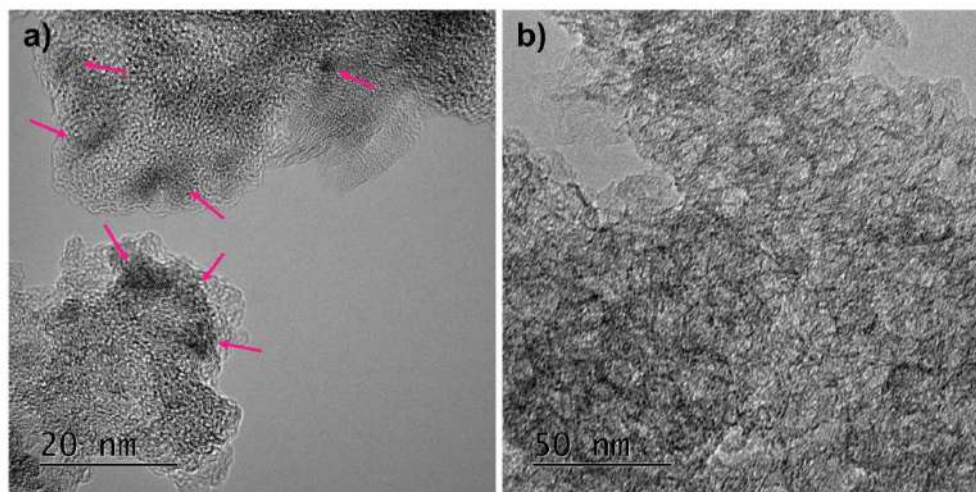


Figure S3. TEM images recorded for a) $\text{SnS}_x\text{@C}_800$ and b) $\text{SnS}_x\text{@C}_1000$.

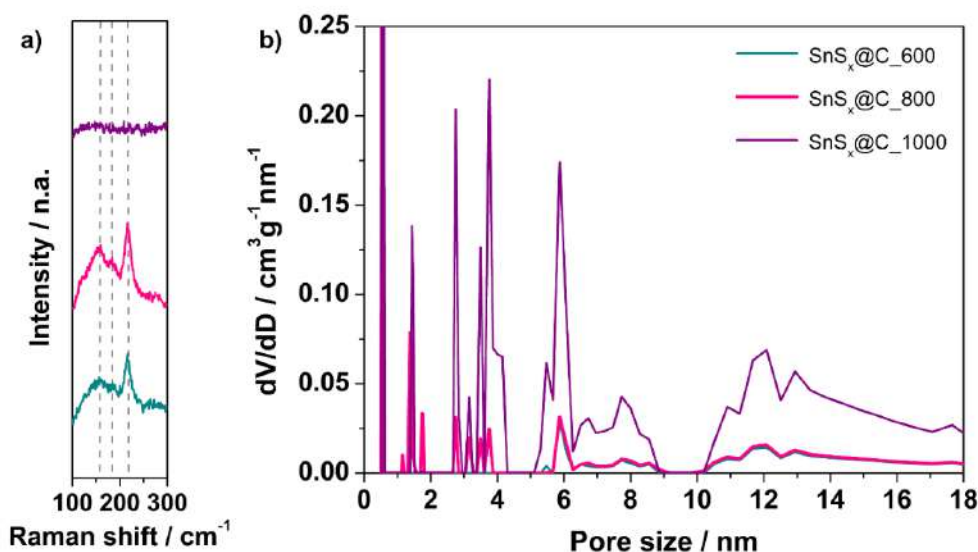


Figure S4. a) Raman spectroscopy (short range) for the SnS_x@C powders (pyrolyzed at different temperature) and b) pore size distribution calculated from N₂ adsorption isotherms based on DFT method for SnS_x@C materials.

Table S5. Spectral parameters for the first-order Raman bands of SnS_x@C_600, SnS_x@C_800 and SnS_x@C_1000 electrode materials: band position (Stokes Raman Shift), half width at half maximum (HWHM), and **peak intensity ratios** relative to the G band.

Band	Spectral parameter	SnS _x @C_600	SnS _x @C_800	SnS _x @C_1000
G	Position (cm ⁻¹)	1590.28	1601.51	1605.29
	HWHM (cm ⁻¹)	50.16	45.13	37.12
D1	Position (cm ⁻¹)	1337.57	1324.55	1327.01
	HWHM (cm ⁻¹)	87.13	87.42	92.01
	I_{D1}/I_G	1.44	2.07	1.84
D3	Position (cm ⁻¹)	1500.33	1510.76	1525.13
	HWHM (cm ⁻¹)	83.62	95.99	79.87
	I_{D3}/I_G	0.77	1.11	0.77
D4	Position (cm ⁻¹)	1194.39	1172.27	1173.77
	HWHM (cm ⁻¹)	101.02	90.76	105.01
	I_{D4}/I_G	0.74	0.86	0.42

Table S6. Elemental composition (atomic %) of the SnS_x@C_600 and SnS_x@C_800 electrodes' surfaces (before cycling) determined by XPS.

Element	Sn	S	C	O	N
Atomic %					
SnS _x @C_600	1.34	1.77	80.47	13.79	2.64
SnS _x @C_800	0.64	1.08	79.16	17.75	1.36

Impurities analysis

EDS (Table S1–S4) and XPS spectra (Figure 3, Figure S5 and Table S6) provide both bulk- and surface-sensitive information. Before pyrolysis, the precursor composite (SnS₂@C) contained ~ 1.2 % Cl, originating from the tin(IV) chloride used as tin precursor. After pyrolysis

at 600 °C, the chloride signal drops by more than one order of magnitude ($\sim 0.08\%$), and is already below the XPS detection limit (and was not detected in the other samples). Al was also detected in EDS analysis for every sample, but does not show up in the corresponding XPS survey, even after mild Ar^+ sputtering, indicating that it originates from the aluminum SEM table and is not incorporated into the powder itself. Finally, a weak Si signal (0.11%), detected in EDS for the $\text{SnS}_x\text{@C}_{1000}$ material originate from the quartz boat contamination at the highest temperature. None of these elements forms a crystalline phase detectable by XRD, none participates in the electrochemical reactions followed in the paper, and their summed concentration never exceeds $0.3\text{ at.}\%$ in the samples that were thoroughly evaluated ($\text{SnS}_x\text{@C}_{600}$ and $\text{SnS}_x\text{@C}_{800}$).

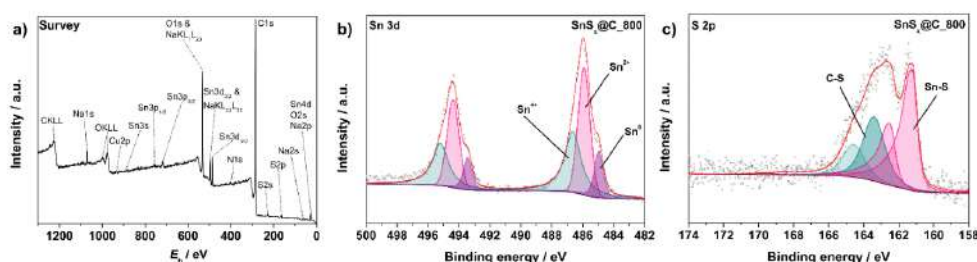


Figure S5. XPS (a) survey spectra of $\text{SnS}_x\text{@C}_{800}$ electrode; (b) high-resolution spectrum of Sn 3d and (c) high-resolution spectrum of the S 2p regions for the $\text{SnS}_x\text{@C}_{800}$ electrode materials after 60 s etching with Ar^+ .

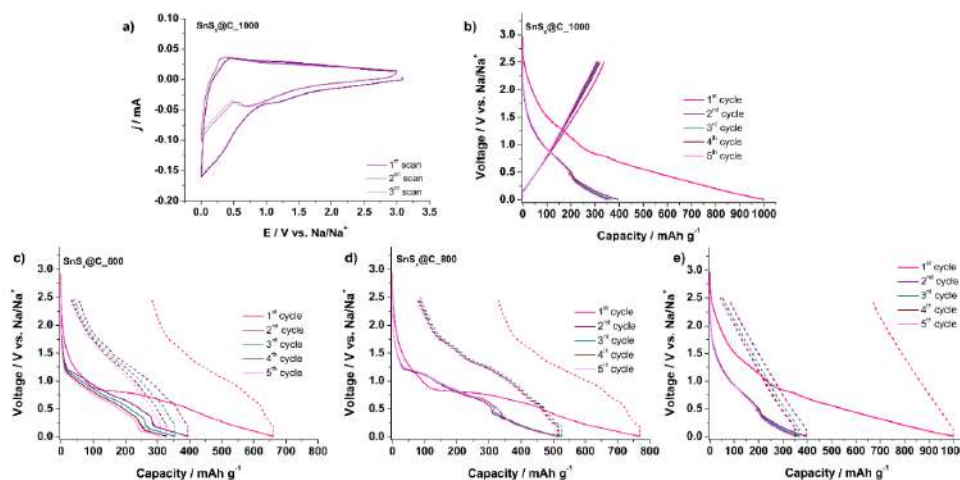


Figure S6. (a) Cyclic voltammetry curves recorded in 1 M NaPF_6 in EC:DEC (30:70) + 5% FEC electrolyte ($\nu = 100\text{ }\mu\text{V s}^{-1}$) for half-cells with the $\text{SnS}_x\text{@C}_{1000}$ electrode material; (b) galvanostatic charge-discharge curves recorded in 1 M NaPF_6 in EC:DEC (30:70) + 5% FEC at current density of $C/10$ for the $\text{SnS}_x\text{@C}_{1000}$; galvanostatic charge-discharge curves exhibiting voltage hysteresis for (c) $\text{SnS}_x\text{@C}_{600}$, (d) $\text{SnS}_x\text{@C}_{800}$ and (e) $\text{SnS}_x\text{@C}_{1000}$.

Table S7. Average charge and discharge voltages, with average voltage hysteresis calculated for $\text{SnS}_x\text{@C}_600$, $\text{SnS}_x\text{@C}_800$ and $\text{SnS}_x\text{@C}_{1000}$ based on the charge/discharge curves in Figure S6.

	Cycle no.	$\bar{V}_{\text{sod}} / \text{V}$	$\bar{V}_{\text{des}} / \text{V}$	$\Delta \bar{V} / \text{V}$
$\text{SnS}_x\text{@C}_600$	1	0.61	1.19	0.58
	2	0.63	1.23	0.61
	3	0.61	1.26	0.65
	4	0.59	1.28	0.69
	5	0.58	1.30	0.72
$\text{SnS}_x\text{@C}_800$	1	0.62	1.18	0.56
	2	0.65	1.20	0.55
	3	0.66	1.21	0.55
	4	0.67	1.21	0.53
	5	0.68	1.21	0.53
$\text{SnS}_x\text{@C}_{1000}$	1	0.69	1.24	0.55
	2	0.60	1.25	0.65
	3	0.64	1.25	0.61
	4	0.66	1.25	0.60
	5	0.66	1.25	0.59

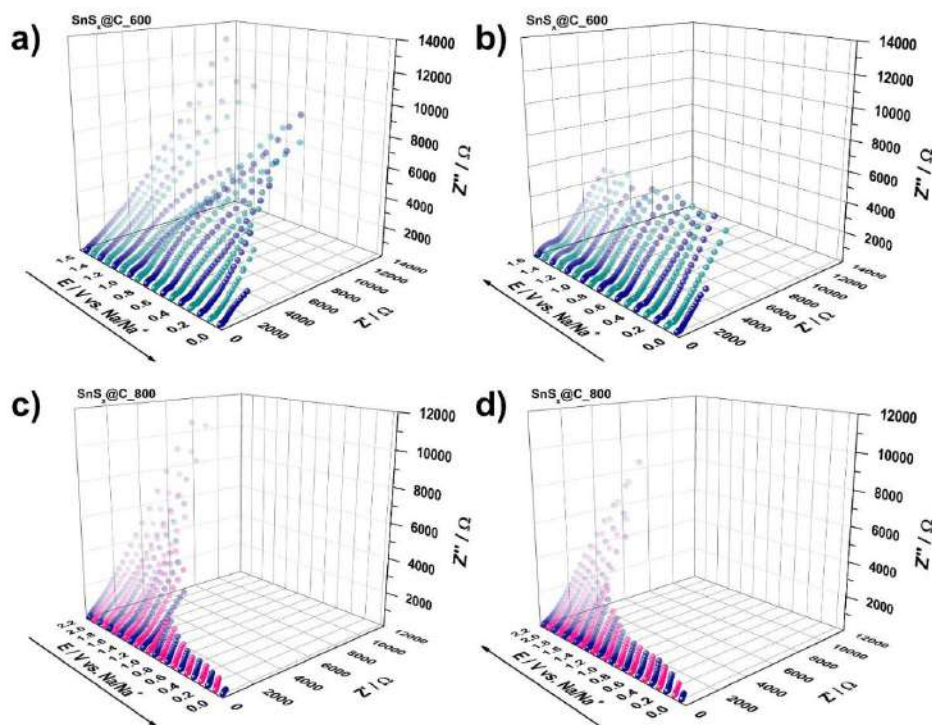


Figure S7. Staircase potentiostatic EIS results for (a-b) $\text{SnS}_x\text{@C}_600$ and (c-d) $\text{SnS}_x\text{@C}_800$ half-cells during sodiation (a, c) and desodiation (b, d), measured in the frequency range from 20 kHz to 1 mHz.

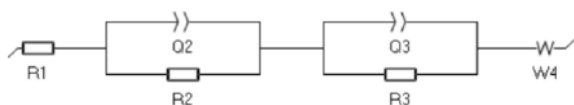


Figure S8. Electrical equivalent circuit used for Nyquist spectra fitting: R1 is the electrolyte resistance, R2/Q2 stands for the resistance (R_{SEI}) and capacitance origination from SEI, R3/Q3 corresponds to the charge transfer (R_{ct}) resistance and double layer capacitance, and W4 is a semi-infinite-length Warburg element that models Na^+ diffusion.

Table S8. Impedance fitting data for $SnS_x@C_{600}$ during desodiation cycle.

E / V	Desodiation				
	R_{SEI} / Ω	R_{ct} / Ω	$W_{coeff} / \Omega s^{-1/2}$	R^2 (parametric)	R^2 (amplitude)
0.1	99.58	106.28	123.35	1.51e-4	1.83e-05
0.2	42.82	397.32	297.20	6.47e-4	6.22e-05
0.4	25.79	411.43	448.99	7.27e-4	8.04e-05
0.6	59.81	434.52	722.60	1.30e-4	2.92e-05
0.8	82.67	499.89	873.78	2.16e-4	7.24e-05
1.0	55.35	543.08	942.39	8.35e-5	1.59e-05
1.2	52.37	852.99	1099.60	1.86e-6	3.31e-05
1.4	50.95	803.81	1265.00	5.43e-5	1.13e-05
1.6	52.50	1085.30	1384.5	5.03e-5	1.27e-05

Table S9. Impedance fitting data for $SnS_x@C_{800}$ during desodiation cycle.

E / V	Desodiation				
	R_{SEI} / Ω	R_{ct} / Ω	$W_{coeff} / \Omega s^{-1/2}$	R^2 (parametric)	R^2 (amplitude)
0.1	12.61	20.77	12.17	2.49e-2	9.33e-06
0.2	17.91	19.96	17.33	2.50e-2	1.10e-05
0.4	25.38	23.22	27.36	3.13e-2	1.56e-05
0.6	24.21	25.73	29.52	2.40e-2	1.81e-05
0.8	30.76	34.86	32.29	2.42e-2	1.36e-05
1.0	33.38	29.90	40.14	2.07e-2	1.14e-05
1.2	40.92	56.83	59.89	1.59e-2	7.20e-06
1.4	52.30	61.01	82.67	1.34e-2	5.60e-06
1.6	80.86	76.68	119.32	1.38e-2	6.22e-06

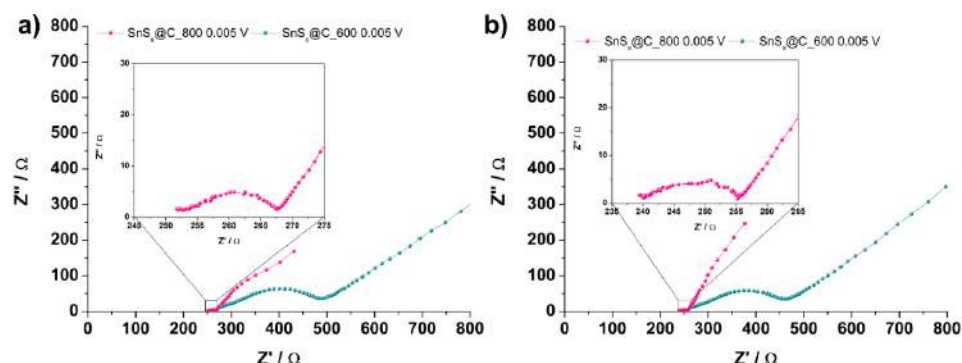


Figure S9. Nyquist plots for $\text{SnS}_x\text{@C}_{600}$ and $\text{SnS}_x\text{@C}_{800}$ recorded during a) sodiation and b) desodiation cycle at 0.005 V in the frequency range from 20 kHz to 1 mHz.

Table S10. Spectral parameters for the first-order Raman bands of $\text{SnS}_x\text{@C}_{600}$ electrode material recorder during 2nd charge/discharge test: band position (Stokes Raman Shift), half width at half maximum (HWHM), and **peak intensity ratios** relative to the G band.

Band	Spectral parameter	Sodiation – 2 nd scan			Desodiation – 2 nd scan		
		2.0 V	0.7 V	0.005 V	0.005 V	0.7 V	2.0 V
G	Position (cm^{-1})	1585.18	1585.38	1573.751	1573.751	1577.01	1579.43
	HWHM (cm^{-1})	42.14	45.54	48.62	48.62	39.41	42.22
D1	Position (cm^{-1})	1322.8	1329.03	1340.51	1340.51	1331.37	1328.27
	HWHM (cm^{-1})	92.25	96.55	110.84	110.84	95.13	93.74
	I_{D1}/I_G	1.74	1.79	1.44	1.26	1.92	1.71
D3	Position (cm^{-1})	1500.12	1505.39	1505.52	1505.52	1505.67	1500.12
	HWHM (cm^{-1})	91.46	79.71	55.52	55.52	77.95	81.04
	I_{D3}/I_G	0.89	0.90	0.58	0.56	1.22	0.96
D4	Position (cm^{-1})	1169.25	1166.23	1166.23	1166.23	1171.77	1169.25
	HWHM (cm^{-1})	70.45	78.94	78.92	78.94	78.95	91.52
	I_{D4}/I_G	0.49	0.47	0.22	0.04	0.45	0.49

WILEY-VCH

Table S11. Spectral parameters for the first-order Raman bands of SnS_x@C_800 electrode material recorder during 2nd charge/discharge test: band position (Stokes Raman Shift), half width at half maximum (HWHM), and **peak intensity ratios** relative to the G band.

Band	Spectral parameter	Sodiation – 2 nd scan			Desodiation – 2 nd scan		
		2.0 V	0.7 V	0.005 V	0.005 V	0.7 V	2.0 V
G	Position (cm ⁻¹)	1592.25	1586.89	1569.47	1568.88	1577.35	1592.53
	HWHM (cm ⁻¹)	45.13	38.13	33.61	32.63	41.77	39.23
D1	Position (cm ⁻¹)	1323.49	1329.29	1339.53	1334.73	1339.49	1323.37
	HWHM (cm ⁻¹)	88.72	88.32	88.56	86.94	89.34	85.15
	I_{D1}/I_G	1.82	2.12	2.68	3.16	1.64	1.65
D3	Position (cm ⁻¹)	1509.59	1509.47	1502.46	1502.01	1506.08	1501.86
	HWHM (cm ⁻¹)	81.06	80.33	77.02	78.73	71.95	84.44
	I_{D3}/I_G	0.83	0.84	1.96	2.33	0.85	0.83
D4	Position (cm ⁻¹)	1176.15	1177.01	1186.01	1171.27	1189.84	1178.03
	HWHM (cm ⁻¹)	74.77	91.28	108.39	81.20	82.15	84.73
	I_{D4}/I_G	0.43	0.45	0.77	0.77	0.32	0.46

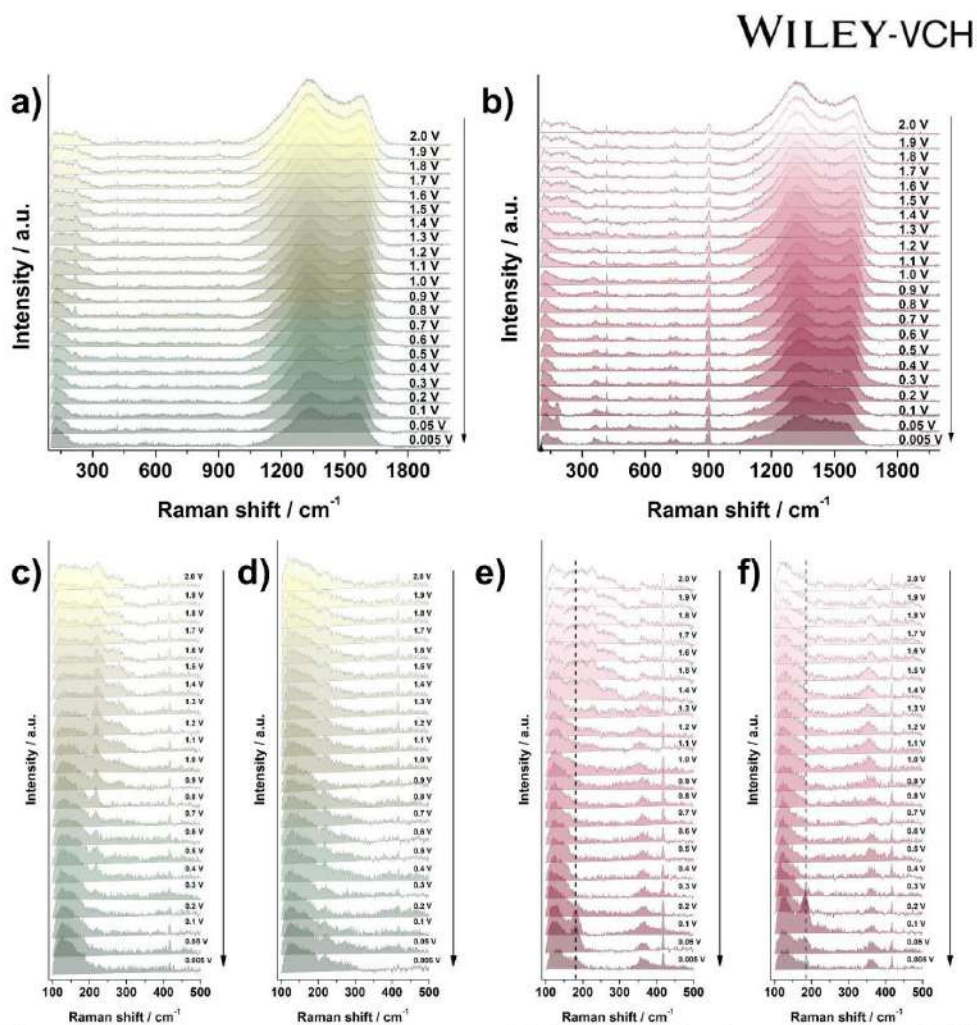


Figure S10. Raman spectra in a full range recorded during sodiation for (a) $\text{SnS}_x\text{@C}_{600}$ (2nd cycle) and (b) $\text{SnS}_x\text{@C}_{800}$ (2nd cycle); 100 – 800 cm^{-1} range for (c) $\text{SnS}_x\text{@C}_{600}$ (2nd cycle), (d) $\text{SnS}_x\text{@C}_{600}$ (20th cycle), (e) $\text{SnS}_x\text{@C}_{800}$ (2nd cycle), (f) $\text{SnS}_x\text{@C}_{800}$ (20th cycle).

Table S12. Spectral parameters for the first-order Raman bands of SnS_x@C_600 electrode material recorder during 20th charge/discharge test: band position (Stokes Raman Shift), half width at half maximum (HWHM), and **peak intensity ratios** relative to the G band.

Band	Spectral parameter	Sodiation – 20 th scan			Desodiation – 20 th scan		
		2.0 V	0.7 V	0.005 V	0.005 V	0.7 V	2.0 V
G	Position (cm ⁻¹)	1587.09	1587.27	1587.68	1588.10	1587.99	1587.74
	HWHM (cm ⁻¹)	38.79	45.43	42.38	39.46	40.85	39.92
D1	Position (cm ⁻¹)	1325.48	1328.46	1327.75	1324.32	1328.10	1326.16
	HWHM (cm ⁻¹)	88.97	90.35	88.30	93.06	88.17	86.48
	I_{D1}/I_G	1.71	1.63	1.70	1.89	1.75	1.68
D3	Position (cm ⁻¹)	1500.12	1500.51	1500.48	1503.51	1501.03	1500.03
	HWHM (cm ⁻¹)	85.71	81.98	82.40	85.90	87.36	87.96
	I_{D3}/I_G	0.96	0.89	0.93	1.03	1.03	0.99
D4	Position (cm ⁻¹)	1176.65	1176.65	1174.33	1162.344	1179.42	1181.14
	HWHM (cm ⁻¹)	71.46	71.43	71.40	71.46	78.09	75.53
	I_{D4}/I_G	0.47	0.49	0.53	0.59	0.53	0.48

Table S13. Spectral parameters for the first-order Raman bands of SnS_x@C_800 electrode material recorder during 20th charge/discharge test: band position (Stokes Raman Shift), half width at half maximum (HWHM), and **peak intensity ratios** relative to the G band.

Band	Spectral parameter	Sodiation – 20 th scan			Desodiation – 20 th scan		
		2.0 V	0.7 V	0.005 V	0.005 V	0.7 V	2.0 V
G	Position (cm ⁻¹)	1591.15	1587.34	1564.32	1565.09	1577.46	1592.04
	HWHM (cm ⁻¹)	34.32	38.65	35.75	35.74	37.05	37.68
D1	Position (cm ⁻¹)	1324.41	1324.41	1338.72	1339.78	1339.83	1324.81
	HWHM (cm ⁻¹)	83.66	86.43	89.17	90.86	89.12	83.98
	I_{D1}/I_G	1.80	1.77	2.75	2.78	1.73	1.58
D3	Position (cm ⁻¹)	1508.40	1507.57	1502.30	1505.69	1508.25	1501.67
	HWHM (cm ⁻¹)	89.14	82.40	73.63	73.62	71.26	79.57
	I_{D3}/I_G	0.99	0.91	1.98	2.00	1.02	0.81
D4	Position (cm ⁻¹)	1182.23	1171.21	1171.37	1178.99	1180.06	1178.97
	HWHM (cm ⁻¹)	88.06	83.83	80.14	80.06	78.64	88.55
	I_{D4}/I_G	0.47	0.42	0.54	0.36	0.31	0.42

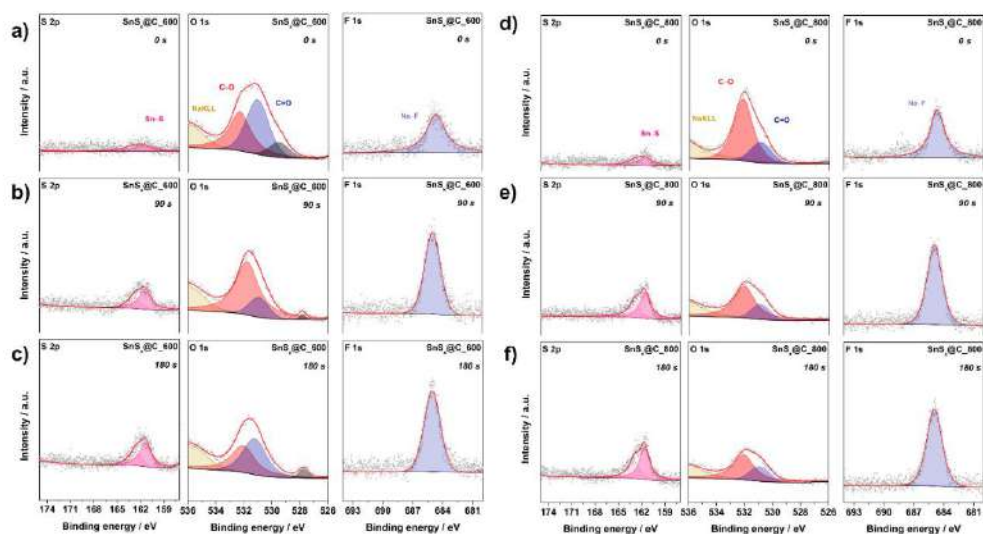


Figure S11. XPS depth-profiling results for (a-c) $\text{SnS}_x@\text{C}_{600}$ and (d-f) $\text{SnS}_x@\text{C}_{800}$ at (a, d) 0 s, (b, e) 90 s, (c, f) 180 s of Ar^+ sputtering.

General conclusions

This dissertation investigated the electrochemical behavior and structure-property relationships of metal chalcogenide-based electrodes for supercapacitors and sodium-ion batteries, with emphasis on MoS₂ and SnS_x composites. The studies showed that targeted synthesis control and structural engineering can improve charge storage properties, while also demonstrating the importance of careful interpretation of electrochemical measurements and the value of operando diagnostics. By combining material synthesis, electrochemical testing and real-time spectroscopic observation, the work provides new insights into the mechanisms governing energy storage in these materials.

The first part of the work focused on MoS₂-based electrodes for supercapacitors. It was demonstrated that platinum dissolution and redeposition from the counter electrode can substantially influence the electrochemical response. Rather than treating this as an artifact, the process was studied in detail and shown to act as a surface modification that enhanced capacitance due to material's exfoliation. The results highlight that electrode behavior is not determined only by intrinsic properties of the material, but also can be affected by the electrochemical environment and test configuration. This emphasizes the need for careful consideration of counter electrode effects in supercapacitor studies, particularly when using platinum in acidic electrolytes.

The second study developed a binder-free electrode architecture by integrating nitrogen-doped MoS₂ nanosheets with TiO₂ nanotube arrays through a hydrothermal synthesis. The optimization of acid concentration and nitrogen sources enabled controlled growth of crystalline, conductive MoS₂ structures. Electrochemical testing confirmed high capacitance, long-term cycling stability and favorable charge storage kinetics. The results show that nitrogen doping and nanoscale integration with TiO₂ scaffolds can significantly improve both the conductivity and ion accessibility of MoS₂, making this approach a practical strategy for high-power supercapacitors.

The third part of the dissertation focused on SnS_x@C composites as anodes for sodium-ion batteries. It was shown that pyrolysis temperature is the key factor controlling composition, carbon structure, and electrochemical behavior. Treatment at 800 °C produced a material with stable cycling performance, high reversible capacity, and favorable surface chemistry. *Operando* Raman spectroscopy revealed reversible SnS transformations, while XPS analysis confirmed stable SEI formation. The results indicate that the role of the carbon matrix is not universally beneficial, but strongly dependent on synthesis conditions and structural optimization. This study also demonstrated the effectiveness of *operando* Raman as a diagnostic tool for monitoring structural changes during electrochemical cycling.

Overall, the findings of this dissertation contribute to the understanding and development of metal chalcogenide electrodes for energy storage. For supercapacitors, the results underline the need for caution when interpreting stability under measurement conditions and point to the potential of surface

modification and nanoscale design for improving performance. For sodium-ion batteries, the results highlight that stability, initial coulombic efficiency and hysteresis remain critical challenges for practical application, yet they can be improved when synthesis optimization is taken into account. The integration of *operando* Raman technique proved essential for correlating electrochemical behavior with material transformations and degradation, and such approaches should be further developed and applied more widely.

In conclusion, this dissertation has shown that through controlled synthesis, careful evaluation of measurement effects, and advanced diagnostics, it is possible to improve both performance and understanding of chalcogenide-based electrodes. The results provide not only material-specific guidelines for MoS₂ and SnS_x electrodes but also general insights that are relevant for the design and evaluation of future electrochemical energy storage materials.

Scientific achievements

Publication record

Publications Constituting the Core of the Doctoral Thesis

1. **Z. Zarach***, M. Sawczak, C. Dosche, K. Trzciński, M. Szkoda, M. Graczyk-Zajac, R. Riedel, G. Wittstock, A.P. Nowak, A Key to Material's Stability: Tuning Pyrolysis Temperature in SnS_x@C Anodes for Sodium-Ion Batteries, *Small* **2025**, *Early View*, e04485.
<https://doi.org/10.1002/sml.202504485>

IF₂₀₂₄: 12.1; MNiSW: 200

2. **Z. Zarach***, A.P. Nowak, K. Trzciński, G. Gajowiec, G. Trykowski, M. Sawczak, M. Łapiński, M. Szkoda, Influence of hydrochloric acid concentration and type of nitrogen source on the electrochemical performance of TiO₂/N-MoS₂ for energy storage applications, *Appl. Surf. Sci.* **2023**, 608, 155187.
<https://doi.org/10.1016/j.apsusc.2022.155187>

IF₂₀₂₄: 6.9; MNiSW: 140

3. **Z. Zarach***, M. Szkoda, K. Trzciński, M. Łapiński, G. Trykowski, A.P. Nowak, Phenomenon of Increasing Capacitance Induced by 1T/2H-MoS₂ Surface Modification with Pt Particles – Influence on Composition and Energy Storage Mechanism, *Electrochim. Acta* **2022**, 435, 141389.
<https://doi.org/10.1016/j.electacta.2022.141389>

IF₂₀₂₄: 5.6; MNiSW: 100

Other Contributions to the Autor's Publication Record

4. A.P. Nowak, A. Rokicińska, Z. Wang, M. Przeźniak-Welenc, **Z. Zarach**, K. Tao, D. Roda, M. Szkoda, K. Trzciński, J. Li, P. Kuśtrowski, Experimental and computational analysis of SnS_x encapsulated into carbonized chitosan as electrode material for potassium ion batteries, *Sci. Rep.* **2024**, 14, 31212.
<https://doi.org/10.1038/s41598-024-82588-0>

IF₂₀₂₄: 3.9; MNiSW: 140

5. M. Szkoda, A. Ilnicka, K. Trzciński, **Z. Zarach**, D. Roda, A.P. Nowak, Synthesis and characterization of MoS₂-carbon based materials for enhanced energy storage applications, *Sci. Rep.* **2024**, 14, 26128.
<https://doi.org/10.1038/s41598-024-77545-w>

IF₂₀₂₄: 3.9; MNiSW: 140

6. K. Trzciński, **Z. Zarach**, M. Szkoda, A.P. Nowak, K. Berent, M. Sawczak, Controlling crystallites orientation and facet exposure for enhanced electrochemical properties of polycrystalline MoO₃ films, *Sci. Rep.* **2023**, 13, 16668.
<https://doi.org/10.1038/s41598-023-43800-9>

IF₂₀₂₄: 3.9; MNiSW: 140

7. M. Szkoda, A. Ilnicka, **Z. Zarach**, D. Roda, A.P. Nowak, K. Trzciński, Ti-Fe₂O₃/In₂O₃ as photoactive material: The role of the substrate in photoelectrochemical water oxidation, *J. Alloys Compd.* **2023**, 960, 170924.
<https://doi.org/10.1016/j.jallcom.2023.170924>
IF₂₀₂₄: 6.3; MNiSW: 100

8. A. Ilnicka, M. Skorupska, M. Szkoda, **Z. Zarach**, J.P. Łukaszewicz, N-doped hybrid carbon materials as electrodes for highly stable supercapacitors, *Mater. Res. Lett.* **2023**, 11(3), 213-221.
<https://doi.org/10.1080/21663831.2022.2139163>
IF₂₀₂₄: 7.9; MNiSW: 140

9. A. Nowak, K. Trzciński, **Z. Zarach**, J. Li, D. Roda, M. Szkoda, Poly(Hydroxybutyrate-Co-Hydroxyvalerate) as a Biodegradable Binder in a Negative Electrode Material for Lithium-Ion Batteries, *App. Surf. Sci.* **2022**, 606, 154933.
<https://doi.org/10.1016/j.apsusc.2022.154933>
IF₂₀₂₄: 6.9; MNiSW: 140

10. M. Szkoda, **Z. Zarach**, M. Nadolska, G. Trykowski, K. Trzciński, SnO₂ nanoparticles embedded onto MoS₂ nanoflakes – An efficient catalyst for photodegradation of methylene blue and photoreduction of hexavalent chromium, *Electrochim. Acta* **2022**, 404, 140173.
<https://doi.org/10.1016/j.electacta.2022.140173>
IF₂₀₂₄: 5.6; MNiSW: 100

11. K. Trzciński, M. Szkoda, **Z. Zarach**, M. Sawczak, A.P. Nowak, Towards spectroscopic monitoring of photoelectrodes: In-situ Raman photoelectrochemistry of a TiO₂/Prussian blue photoanode, *Electrochim. Acta* **2022**, 404, 139774.
<https://doi.org/10.1016/j.electacta.2021.139774>
IF₂₀₂₄: 5.6; MNiSW: 100

12. M. Szkoda, K. Trzciński, **Z. Zarach**, D. Roda, M. Łapiński, A.P. Nowak, Scaling Up the Process of Titanium Dioxide Nanotube Synthesis and Its Effect on Photoelectrochemical Properties, *Materials* **2021**, 14(19), 5686.
<https://doi.org/10.3390/ma14195686>
IF₂₀₂₄: 3.2; MNiSW: 140

13. A. Ilnicka, M. Skorupska, M. Szkoda, **Z. Zarach**, P. Kamedulski, W. Zieliński, J.P. Łukaszewicz, Combined effect of nitrogen-doped functional groups and porosity of porous carbons on electrochemical performance of supercapacitors, *Sci. Rep.* **2021**, 11, 18387.
<https://doi.org/10.1038/s41598-021-97932-x>

IF₂₀₂₄: 3.9; MNiSW: 140

14. A.P. Nowak, M. Gazda, M. Łapiński, **Z. Zarach**, K. Trzciński, M. Szkoda, S. Mania, J. Li, R. Tylingo, Tin oxide encapsulated into pyrolysed chitosan as a negative electrode for lithium-ion batteries, *Materials* **2021**, 14(5), 1156.
<https://doi.org/10.3390/ma14051156>

IF₂₀₂₄: 3.2; MNiSW: 140

15. M. Szkoda, **Z. Zarach**, K. Trzciński, A.P. Nowak, An Aqueous Exfoliation of WO₃ as a Route for Counterions Fabrication – Improved Photocatalytic and Capacitive Properties of Polyaniline/WO₃ Composite, *Materials* **2020**, 13(24), 5781.
<https://doi.org/10.3390/ma13245781>

IF₂₀₂₄: 3.2; MNiSW: 140

16. M. Szkoda, **Z. Zarach**, K. Trzciński, G. Trykowski, A.P. Nowak, An easy and ecological method of obtaining hydrated and non-crystalline WO_{3-x} for application in supercapacitors, *Materials* **2020**, 13(8), 1925.
<https://doi.org/10.3390/ma13081925>

IF₂₀₂₄: 3.2; MNiSW: 140

17. **Z. Zarach**^{*}, K. Trzciński, M. Łapiński, A. Lisowska-Oleksiak, M. Szkoda, Improving the Performance of a Graphite Foil/Polyaniline Electrode Material by a Thin PEDOT:PSS Layer for Application in Flexible, High Power Supercapacitors, *Materials* **2020**, 13(24), 5791.
<https://doi.org/10.3390/ma13245791>

IF₂₀₂₄: 3.2; MNiSW: 140

Total Impact Factor (2024): 88.5

Total MNiSW points: 2280

Book chapters

1. M. Wilamowska-Zawłocka, A. Cymann-Sachajdak, **Z. Zarach**, M. Graczyk-Zajac, Chapter 9: Cathodes for Sodium-ion Batteries, Book: *Advanced Technologies for Rechargeable Batteries: Alkaline Metal Ion, Redox Flow, and Metal Sulfur Batteries*, 1st Edition, **2024**, CRC Press, Taylor and Francis Group.

Patents

1. **Z. Zarach**, K. Trzciński, M. Szkoda, (**2022**), Method of obtaining electrode material and electrode material (**Polish Patent No. 246601B1**, Polish Patent Office).
2. K. Trzciński, M. Sawczak, **Z. Zarach**, Szkoda, (**2023**), Method of producing crystal layers of molybdenum trioxide (**Polish Patent No. 247166B1**, Polish Patent Office).

Patent applications

1. M. Szkoda, K. Trzciński, **Z. Zarach**, D. Roda, (**2023**), Method for obtaining an integrated photoelectrochemical capacitor and integrated photoelectrochemical capacitor (**Polish Patent Application No. 444790A1**, Polish Patent Office; **European Patent Application No. 24460020.1A**, European Patent Office).

Oral presentations

1. **Z. Zarach***, M. Szkoda, A. Kempf, M. Graczyk-Zajac, K. Trzciński, R. Riedel, A.P. Nowak, *Exploring the Electrochemical Performance of SnS_x@C Composites for Sodium-Ion Battery Anodes: Insights from operando Raman Spectroscopy*, 66th Scientific Congress of the Polish Chemical Society (Poznań, Poland, 15.09 – 20.09.2024).
2. **Z. Zarach***, M. Szkoda, K. Trzciński, A.P. Nowak, *Tlenki metali przejściowych jako materiały elektrodowe do magazynowania energii*, 5th Interdisciplinary Conference Nano&Biomaterials – from Theory to Applications NaBioMat V, (Toruń, Poland, 14.06–16.06.2023).
3. **Z. Zarach***, M. Szkoda, K. Trzciński, M. Łapiński, G. Trykowski, A.P. Nowak, *The influence of Pt Counter Electrode on the Electrochemical Properties, Composition, and Energy Storage Mechanism of 1T/2H-MoS₂ electrode material*, Regional Meeting of the International Society of Electrochemistry (Prague, Czech Republic, 15.08–19.08.2022).

4. **Z. Zarach***, M. Szkoda, K. Trzeciński, G. Gajowiec, A.P. Nowak, *Binder-free TiO₂ nanotubes/MoS₂ electrode material for energy storage applications: surface design and electrochemical performance*, 5th International Conference on Applied Surface Science (Mallorca, Spain, 25.04–28.04.2022).
5. **Z. Zarach***, K. Trzeciński, G. Gajowiec, M. Szkoda, *Hydrothermal binder-free MoS₂/PANI/TiO₂ NTs electrode material for asymmetric supercapacitors: surface design and electrochemical performance*, 63rd Scientific Congress of the Polish Chemical Society (Łódź, Poland, 13.09–17.09.2021).
6. **Z. Zarach***, K. Trzeciński, M. Szkoda, *Investigation of different approaches for the synthesis of MoS₂-based material and its application as a binder-free cathode material for asymmetric supercapacitors*, 6th International Symposium on Surface Imaging/Spectroscopy at the Solid/Liquid Interface (Kraków, Poland, 06.06–09.06.2021).

Poster presentations

1. **Z. Zarach***, M. Sawczak, C. Dosche, K. Trzeciński, M. Szkoda, R. Riedel, G. Wittstock, A.P. Nowak, *Wpływ temperatury pirolizy na stabilność materiałów anodowych SnS_x@C w bateriach sodowo-jonowych*, 7th Interdisciplinary Conference Nano&Biomaterials – from Theory to Applications NaBioMat VII (Toruń, Poland, 11.06–13.06.2025).
2. **Z. Zarach***, K. Trzeciński, A.P. Nowak, M. Szkoda, *MoS₂-based electrochemical capacitor: effect of doping and synthesis route*, 15th International Symposium on Systems with Fast Ionic Transport ISSFIT15 (Dubrovnik, Croatia, 18.04–22.04.2023).
3. **Z. Zarach***, M. Szkoda, K. Trzeciński, M. Łapiński, G. Trykowski, A.P. Nowak, *The phenomenon of the increasing capacitance of 1T/2H-MoS₂ induced by surface modification with Pt particles and its influence on composition and energy storage mechanism*, International Symposium on Enhanced Electrochemical Capacitors ISEECap (Bologna, Italy, 11.07–15.07.2022).

Scientific projects

- 1. SONATA 19**, (UMO-2023/51/D/ST4/00297), *“Can photointercalation negatively affect the efficiency of photoanodes? Exploring effective methods to mitigate the adverse impact of photointercalation in layered materials”*, National Science Centre (NCN)
Principal Investigator: Ph.D., Asst. Prof. Mariusz Szkoda
Role: Young Scientist (10.2024 – present)
- 2. PRELUDIUM 22** (UMO-2023/49/N/ST5/01794), *“Beyond MoS₂: Unraveling Charge Storage Mechanisms in Transition Metal Dichalcogenides as Anode Materials for Sodium-Ion Batteries through In-situ Raman Measurements”*, National Science Centre (NCN)
Role: Principal Investigator (07.2024 – present)
- 3. BEETHOVEN 3** (2018/31/G/ST5/02056), *“Beyond Li-ion Batteries: Novel, Efficient Electrode Materials for Sodium Ion Storage”*, National Science Centre (NCN)
Principal Investigator: Ph.D., D. Sc., Assoc. Prof. Monika Wilamowska-Zawłocka
Role: Young Scientist (11.2020 – 11.2023)
- 4. ARGENTUM** Triggering Research Grant, *“One-electrode system for simultaneous conversion and storage of solar Energy”*, Excellence Initiative – Research University (IDUB)
Principal Investigator: Ph.D., Asst. Prof. Konrad Trzciński
Role: Young Scientist (02.2021 – 04.2023)
- 5. LIDER X** (LIDER/15/0088/L-10/18/NCBR/2019), *“Integrated prototype of a photo-supercapacitor for energy storage obtained as a result of solar radiation conversion”*, National Centre for Research and Development (NCBR)
Principal Investigator: Ph.D., Asst. Prof. Mariusz Szkoda
Role: Young Scientist (06.2020 – 12.2022)
- 6. URANIUM** Supporting Cooperation with High Schools, *“Chemia bez granic – warsztaty fizykochemiczne dla uczniów szkół średnich”*, Excellence Initiative – Research University (IDUB)
Principal Investigator: Prof. Ewa Wagner-Wysiecka
Role: Young Scientist (06.2022 – 12.2022)
- 7. FIRST TEAM** (POIR.04.04.00-00-42E9/17-00), *“Nanocrystalline Ceramic Materials for Efficient Electrochemical Energy Conversion”*, Foundation for Polish Science (FNP)
Principal Investigator: Ph.D, D. Sc., Assoc. Prof. Sebastian Molin
Role: Young Scientist (10.2018 – 01.2019)

Statutory grants (Faculty of Chemistry, GUT)

8. **Mini-grant** subsidy from the fund supporting the development of young academics in 2021 at Gdansk University of Technology, *“Electrode materials based on conductive polymers and transition metal dichalcogenides for energy storage in asymmetric supercapacitors”*
9. **Mini-grant** subsidy from the fund supporting the development of young academics in 2022 at Gdansk University of Technology, *“Study of the structure-electrochemical activity correlation of molybdenum telluride (MoTe₂): analysis of the influence of synthesis parameters on capacitive properties and energy storage mechanism”*
10. **Mini-grant** subsidy from the fund supporting the development of young academics in 2023 at Gdansk University of Technology, *“Tungsten sulfide as anode material for sodium-ion batteries: influence of synthesis parameters on structural properties and electrochemical efficiency”*
11. **Mini-grant** subsidy from the fund supporting the development of young academics in 2024 at Gdansk University of Technology, *“Mangosteen as carbon source for enhancing the performance of metal chalcogenide-based sodium-ion battery anodes”*

Short-term scientific internships

1. Research stay and training in X-ray Photoelectron Microscopy (XPS) at Prof. Gunther Wittstock's research group at **Carl von Ossietzky University in Oldenburg, Germany**
19.01.2025 – 24.01.2025
2. Research internship co-financed by Polish National Agency for Academic Exchange (NAWA) under mobility STER programme at Prof. Ralf Riedel's research group at **Technical University of Darmstadt (TUD), Germany**
01.09.2023 – 01.12.2023
3. Research stay and training in Scanning Electrochemical Microscopy (SECM) at PhD Wojciech Nogala's research group at **Institute of Physical Chemistry (Polish Academy of Sciences), Poland**
03.01.2021 – 17.01.2021

Awards and Distinctions

- 1. Honorable Mention – Poster Competition for Young Scientists**
Conference *“Nano(&)BioMaterials – from Theory to Application”*
Toruń, Poland, 11.06-13.06.2025
Awarded for the poster titled *“Effect of Pyrolysis Temperature on the Stability of SnSx@C Anode Materials in Sodium-Ion Batteries”*
- 2. NAWA Scholarship for the best PhD students carrying out PhD projects in international cooperation**, Polish National Agency for Academic Exchange (NAWA), 2023
Awarded as part of the *“Gdańsk Tech Doctoral School Closer to Europe”* program, co-financed by NAWA
- 3. FRANCIIUM** Supporting Outstanding Doctoral Candidates, *Excellence Initiative – Research University (IDUB)*
Awarded 3 times (10.2021-09.2022, 10.2022-09.2023, 10.2023-09.2024)
- 4. Best Master’s Thesis Award – Faculty of Chemistry**
Polish Chemical Society (PTChem), 2021
Distinction in the competition for the best master’s thesis defended at the Faculty of Chemistry, GUT, in the academic year 2019/2020
Thesis title: *“Electrode Materials for Photo-Supercapacitors”*
- 5. XXX Edition of Prof. Jerzy I. Skowroński Award**
Polish Committee for Electrotechnical Materials Association, Polish Electrical Engineers (SEP), 2020
First prize for the best thesis in electrical engineering, high voltage and electrical engineering materials, Thesis title: *“Electrode Materials for Photo-Supercapacitors”*
- 6. Graduate Student Symposium on Advantageous Electrochemistry**
Institute of Physical Chemistry, Polish Academy of Sciences (PAN), 2020
First award for the presentation of master’s thesis results *“Electrode Materials for Photo-Supercapacitors”*
- 7. Competition for Best Engineering and Master’s Thesis in Technical Sciences Area**
Pomeranian Council of the Federation of Scientific and Technical Associations of the Supreme Technical Organization (FSNT NOT), 2019
First prize for best engineering thesis *“Glucose Sensor Based on Titanium Dioxide Nanotubes with Gold Nanoparticles”*

Other scientific activities

Membership and Roles in Scientific Societies

- 1. Treasurer – RedOx Scientific Club, Gdańsk Tech Student Chapter affiliated with the Electrochemical Society (ECS)**
Gdansk University of Technology
Coordination of student activities and events; responsible for budget management and funding resources
- 2. Member of The Electrochemical Society (ECS)**
- 3. Member of The International Society of Electrochemistry (ISE)**

Events co-organization

- 4. Knowledge Transfer Lecture Series (RedOx Scientific Club)**
Gdańsk University of Technology, Gdańsk
Organization of open academic lectures with invited speakers
- 5. Baltic Science Festival**
Gdańsk University of Technology, Gdańsk
Hands-on educational workshops on energy storage for schools
- 6. Gdańsk Tech Open Days**
Gdańsk University of Technology, Gdańsk
Design and coordination of educational workshops on battery technologies
- 7. Materials Engineering Days (RedOx Scientific Club)**
Gdańsk University of Technology, Gdańsk

Engagement in interactive demonstrations for visitors and students
- 8. “Sustainable Energy” Outreach Program (RedOx Scientific Club)**
Fahrenheit Universities Association
Workshops and science shows for primary and secondary school students

Teaching and Academic Involvement

Academic Employment

Research and Teaching Assistant

Department of Corrosion and Electrochemistry, Faculty of Chemistry, Gdańsk
University of Technology
10.2024 – present

Teaching Activities

1. **Course:** Chemia
Field of Study: Fizyka Techniczna (WFTIMS PG)
2. **Course:** Chemiczne Źródła Prądu
Field of Study: Fizyka Techniczna, Inżynieria Odnawialnych Źródeł
Energii (WFTIMS PG)
3. **Course:** Metody Elektrochemiczne w Zastosowaniach Biomedycznych
Field of Study: Inżynieria Biomedyczna (WCh PG)
4. **Course:** Materiały Biozgodne i Specjalnego Przeznaczenia
Field of Study: Inżynieria Biomedyczna (WCh PG)
5. **Course:** Nanoskopia Powierzchni
Field of Study: Korozja (WCh PG)
6. **Course:** Techniki Spektroskopowe w Analizie Korozyjnej
Field of Study: Korozja (WCh PG)
7. **Course:** Elektrochemiczne Źródła Energii
Field of Study: Technologie Wodorowe i Elektromobilność (WEIA PG)
8. **Course:** Elektrochemiczne Źródła Energii
Field of Study: Technologia Chemiczna, Technologie Energii
Odnawialnych (WCh PG)
9. **Course:** Elektrochemia Techniczna
Field of Study: Technologie Wodorowe i Elektromobilność (WEIA PG)
10. **Course:** Korozja Materiałów Konstrukcyjnych
Field of Study: Technologie Wodorowe i Elektromobilność (WEIA PG)
11. **Course:** Korozja w Przemysle Spożywczym
Field of Study: Korozja (WCh PG)
12. **Course:** Metody Badań Degradacji Materiałów
Field of Study: Technologia Chemiczna, Technologie Energii
Odnawialnych (WCh PG)

Author Contribution Statements



FACULTY OF
CHEMISTRY

Gdańsk, 21.07.2025

Co-author Contribution Declaration

As the co-author of the following paper, I hereby declare that my contribution to this work was as stated below.

Article: Phenomenon of Increasing Capacitance Induced by 1T/2H-MoS₂ Surface Modification with Pt Particles – Influence on Composition and Energy Storage Mechanism

Authors: Z. Zarach, M. Szkoda, K. Trzciński, M. Łapiński, G. Trykowski, A.P. Nowak

Published: *Electrochimica Acta* **2022**, 435, 141389

DOI: <https://doi.org/10.1016/j.electacta.2022.141389>

Contribution: Conceptualization, Methodology, Validation, Formal analysis, Investigation, Writing – original draft, Writing – review & editing, Visualization, Project administration


Signature

GDAŃSK UNIVERSITY
OF TECHNOLOGY
G. Narutowicza 11/12
80-233 Gdańsk, Poland

tel +48 58 348 64 34
e-mail: zuzanna.zarach@pg.edu.pl
www.pg.edu.pl





Gdańsk, 21.07.2025

Co-author Contribution Declaration

As the co-author of the following paper, I hereby declare that my contribution to this work was as stated below. I acknowledge that Zuzanna Zarach was the lead author of this work.

Article: Phenomenon of Increasing Capacitance Induced by 1T/2H-MoS₂ Surface Modification with Pt Particles – Influence on Composition and Energy Storage Mechanism

Authors: Z. Zarach, M. Szkoda, K. Trzciński, M. Łapiński, G. Trykowski, A.P. Nowak

Published: *Electrochimica Acta* 2022, 435, 141389

DOI: <https://doi.org/10.1016/j.electacta.2022.141389>

Contribution: Conceptualization, Methodology, Validation, Writing – original draft, Writing – review & editing, Supervision, Project administration, Funding Acquisition


Signature

GDAŃSK UNIVERSITY
OF TECHNOLOGY
G. Narutowicza 11/12
80-233 Gdańsk, Poland

tel +48 58 348 64 34
e-mail: mariusz.szkoda@pg.edu.pl
www.pg.edu.pl





FACULTY OF
CHEMISTRY

Gdańsk, 21.07.2025

Co-author Contribution Declaration

As the co-author of the following paper, I hereby declare that my contribution to this work was as stated below. I acknowledge that Zuzanna Zarach was the lead author of this work.

Article: Phenomenon of Increasing Capacitance Induced by 1T/2H-MoS₂ Surface Modification with Pt Particles – Influence on Composition and Energy Storage Mechanism

Authors: Z. Zarach, M. Szkoda, K. Trzciński, M. Łapiński, G. Trykowski, A.P. Nowak

Published: *Electrochimica Acta* **2022**, 435, 141389

DOI: <https://doi.org/10.1016/j.electacta.2022.141389>

Contribution: Conceptualization, Methodology, Writing – review & editing


Signature

GDAŃSK UNIVERSITY
OF TECHNOLOGY
G. Narutowicza 11/12
80-233 Gdańsk, Poland

tel +48 58 348 64 34
e-mail: kontrzci@pg.edu.pl
www.pg.edu.pl





FACULTY OF APPLIED
PHYSICS AND MATHEMATICS

Gdańsk, 22.07.2025

Co-author Contribution Declaration

As the co-author of the following paper, I hereby declare that my contribution to this work was as stated below. I acknowledge that Zuzanna Zarach was the lead author of this work.

Article: Phenomenon of Increasing Capacitance Induced by 1T/2H-MoS₂ Surface Modification with Pt Particles – Influence on Composition and Energy Storage Mechanism

Authors: Z. Zarach, M. Szkoda, K. Trzeciński, M. Łapiński, G. Trykowski, A.P. Nowak

Published: *Electrochimica Acta* **2022**, 435, 141389

DOI: <https://doi.org/10.1016/j.electacta.2022.141389>

Contribution: Investigation, Resources

Zastępca Dyrektora
ds. infrastruktury badawczej

dr hab. inż. Marcin Łapiński, prof. PG
INSTYTUT TECHNOLOGII
I INŻYNIERII MATERIAŁOWEJ

Signature

GDAŃSK UNIVERSITY
OF TECHNOLOGY
G. Narutowicza 11/12
80-233 Gdańsk, Poland

tel +48 58 348 66 16
e-mail: marcin.lapinski@pg.edu.pl
www.pg.edu.pl





NICOLAUS COPERNICUS
UNIVERSITY
IN TORUŃ
Faculty of Chemistry



RESEARCH
UNIVERSITY
EXCELLENCE INITIATIVE

Gdańsk, 22.07.2025

Co-author Contribution Declaration

As the co-author of the following paper, I hereby declare that my contribution to this work was as stated below. I acknowledge that Zuzanna Zarach was the lead author of this work.

Article: Phenomenon of Increasing Capacitance Induced by 1T/2H-MoS₂ Surface Modification with Pt Particles – Influence on Composition and Energy Storage Mechanism

Authors: Z. Zarach, M. Szkoda, K. Trzeciński, M. Łapiński, **G. Trykowski**, A.P. Nowak

Published: *Electrochimica Acta* **2022**, 435, 141389

DOI: <https://doi.org/10.1016/j.electacta.2022.141389>

Contribution: Investigation, Resources, Writing – original draft, Visualization



PODPIS ZAUFANY
GRZEGORZ
TRYKOWSKI
29.07.2025 13:06:43 (GMT+2)
Dokument podpisany elektronicznie
podpisem zaufanym

Signature



FACULTY OF
CHEMISTRY

Gdańsk, 21.07.2025

Co-author Contribution Declaration

As the co-author of the following paper, I hereby declare that my contribution to this work was as stated below. I acknowledge that Zuzanna Zarach was the lead author of this work.

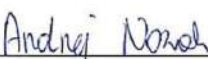
Article: Phenomenon of Increasing Capacitance Induced by 1T/2H-MoS₂ Surface Modification with Pt Particles – Influence on Composition and Energy Storage Mechanism

Authors: Z. Zarach, M. Szkoda, K. Trzciński, M. Łapiński, G. Trykowski, A.P. Nowak

Published: *Electrochimica Acta* **2022**, 435, 141389

DOI: <https://doi.org/10.1016/j.electacta.2022.141389>

Contribution: Conceptualization, Validation, Formal analysis, Writing – review & editing, Supervision


Signature

GDAŃSK UNIVERSITY
OF TECHNOLOGY
G. Narutowicza 11/12
80-233 Gdańsk, Poland

tel +48 58 348 64 34
e-mail: andnowak@pg.edu.pl
www.pg.edu.pl





FACULTY OF
CHEMISTRY

Gdańsk, 21.07.2025

Co-author Contribution Declaration

As the co-author of the following paper, I hereby declare that my contribution to this work was as stated below.

Article: Influence of hydrochloric acid concentration and type of nitrogen source on the electrochemical performance of $\text{TiO}_2/\text{N-MoS}_2$ for energy storage applications

Authors: Z. Zarach, A.P. Nowak, K. Trzciński, G. Gajowiec, G. Trykowski, M. Sawczak, M. Łapiński, M. Szkoda

Published: *Applied Surface Science* **2023**, 608, 155187

DOI: <https://doi.org/10.1016/j.apsusc.2022.155187>

Contribution: Conceptualization, Data curation, Formal analysis, Investigation, Methodology, Validation, Visualization, Writing – original draft, Writing – review & editing


Signature

GDAŃSK UNIVERSITY
OF TECHNOLOGY
G. Narutowicza 11/12
80-233 Gdańsk, Poland

tel +48 58 348 64 34
e-mail: zuzanna.zarach@pg.edu.pl
www.pg.edu.pl





Gdańsk, 21.07.2025

Co-author Contribution Declaration

As the co-author of the following paper, I hereby declare that my contribution to this work was as stated below. I acknowledge that Zuzanna Zarach was the lead author of this work.

Article: Influence of hydrochloric acid concentration and type of nitrogen source on the electrochemical performance of TiO₂/N-MoS₂ for energy storage applications

Authors: Z. Zarach, A.P. Nowak, K. Trzciński, G. Gajowiec, G. Trykowski, M. Sawczak, M. Łapiński, M. Szkoda

Published: *Applied Surface Science* **2023**, 608, 155187

DOI: <https://doi.org/10.1016/j.apsusc.2022.155187>

Contribution: Data curation, Formal analysis, Supervision, Validation, Writing – review & editing


Signature

GDANSK UNIVERSITY
OF TECHNOLOGY
G. Narutowicza 11/12
80-233 Gdańsk, Poland

tel +48 58 348 64 34
e-mail: andnowak@pg.edu.pl
www.pg.edu.pl





FACULTY OF
CHEMISTRY

Gdańsk, 21.07.2025

Co-author Contribution Declaration

As the co-author of the following paper, I hereby declare that my contribution to this work was as stated below. I acknowledge that Zuzanna Zarach was the lead author of this work.

Article: Influence of hydrochloric acid concentration and type of nitrogen source on the electrochemical performance of $\text{TiO}_2/\text{N-MoS}_2$ for energy storage applications

Authors: Z. Zarach, A.P. Nowak, K. Trzciński, G. Gajowiec, G. Trykowski, M. Sawczak, M. Łapiński, M. Szkoda

Published: *Applied Surface Science* **2023**, 608, 155187

DOI: <https://doi.org/10.1016/j.apsusc.2022.155187>

Contribution: Formal analysis, Methodology, Validation, Writing – review & editing


Signature

GDAŃSK UNIVERSITY
OF TECHNOLOGY
G. Narutowicza 11/12
80-233 Gdańsk, Poland

tel +48 58 348 64 34
e-mail: kontrzc@pg.edu.pl
www.pg.edu.pl





FACULTY OF
MECHANICAL ENGINEERING
AND SHIP TECHNOLOGY

Gdańsk, 22.07.2025

Co-author Contribution Declaration

As the co-author of the following paper, I hereby declare that my contribution to this work was as stated below. I acknowledge that Zuzanna Zarach was the lead author of this work.

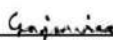
Article: Influence of hydrochloric acid concentration and type of nitrogen source on the electrochemical performance of $\text{TiO}_2/\text{N-MoS}_2$ for energy storage applications

Authors: Z. Zarach, A.P. Nowak, K. Trzeciński, G. Gajowiec, G. Trykowski, M. Sawczak, M. Łapiński, M. Szkoda

Published: *Applied Surface Science* **2023**, 608, 155187

DOI: <https://doi.org/10.1016/j.apsusc.2022.155187>

Contribution: Investigation, Resources


Signature

GDANSK UNIVERSITY
OF TECHNOLOGY
G. Narutowicza 11/12
80-233 Gdańsk, Poland

tel +48 58 347 16 01
e-mail: grzgajow@pg.edu.pl
www.pg.edu.pl





NICOLAUS COPERNICUS
UNIVERSITY
IN TORUŃ
Faculty of Chemistry



RESEARCH
UNIVERSITY
EXCELLENCE INITIATIVE

Gdańsk, 22.07.2025

Co-author Contribution Declaration

As the co-author of the following paper, I hereby declare that my contribution to this work was as stated below. I acknowledge that Zuzanna Zarach was the lead author of this work.

Article: Influence of hydrochloric acid concentration and type of nitrogen source on the electrochemical performance of $\text{TiO}_2/\text{N-MoS}_2$ for energy storage applications

Authors: Z. Zarach, A.P. Nowak, K. Trzeciński, G. Gajowiec, **G. Trykowski**, M. Sawczak, M. Łapiński, M. Szkoda

Published: *Applied Surface Science* **2023**, 608, 155187

DOI: <https://doi.org/10.1016/j.apsusc.2022.155187>

Contribution: Investigation, Resources



Signature



The Szewalski
INSTITUTE OF FLUID-FLOW MACHINERY
POLISH ACADEMY OF SCIENCES
80-231 Gdansk J. Fiszer 14 Poland

Tel.(operator): +48 58 3460881
Tel.(office): +48 58 3416071

Fax: +48 58 3416144

e-mail: imp@imp.gda.pl
www.imp.gda.pl

Gdańsk, 15.07.2025

Co-author Contribution Declaration

As the co-author of the following paper, I hereby declare that my contribution to this work was as stated below.

Article: Influence of hydrochloric acid concentration and type of nitrogen source on the electrochemical performance of $\text{TiO}_2/\text{N-MoS}_2$ for energy storage applications
Authors: Z. Zarach, A.P. Nowak, K. Trzciński, G. Gajowiec, G. Trykowski, **M. Sawczak**, M. Łapiński, M. Szkoda
Published: *Applied Surface Science* **2023**, 608, 155187
DOI: <https://doi.org/10.1016/j.apsusc.2022.155187>
Contribution: Investigation, Resources

Mirosław Sawczak

Signature



REGON: 000326121

NIP: 584-035-78-82

POLTAX VAT-5UE: PL5840357882

NATO Commercial and Government Entity Code NCAGE: 0409H



FACULTY OF APPLIED
PHYSICS AND MATHEMATICS

Gdańsk, 22.07.2025

Co-author Contribution Declaration

As the co-author of the following paper, I hereby declare that my contribution to this work was as stated below. I acknowledge that Zuzanna Zarach was the lead author of this work.

Article: Influence of hydrochloric acid concentration and type of nitrogen source on the electrochemical performance of $\text{TiO}_2/\text{N-MoS}_2$ for energy storage applications

Authors: Z. Zarach, A.P. Nowak, K. Trzciński, G. Gajowiec, G. Trykowski, M. Sawczak, M. Łapiński, M. Szkoda

Published: *Applied Surface Science* **2023**, 608, 155187

DOI: <https://doi.org/10.1016/j.apsusc.2022.155187>

Contribution: Investigation, Resources

Zastępca Dyrektora
ds. infrastruktury badawczej

dr hab. inż. Marcin Łapiński, prof. PŁ,
INSTYTUT NANOTECHNOLOGII
I INŻYNIERII MATERIAŁOWEJ

Signature

GDAŃSK UNIVERSITY
OF TECHNOLOGY
G. Narutowicza 11/12
80-233 Gdańsk, Poland

tel +48 58 348 66 16
e-mail: marcin.lapinski@pg.edu.pl
www.pg.edu.pl





FACULTY OF
CHEMISTRY

Gdańsk, 21.07.2025

Co-author Contribution Declaration

As the co-author of the following paper, I hereby declare that my contribution to this work was as stated below. I acknowledge that Zuzanna Zarach was the lead author of this work.

Article: Influence of hydrochloric acid concentration and type of nitrogen source on the electrochemical performance of TiO₂/N-MoS₂ for energy storage applications

Authors: Z. Zarach, A.P. Nowak, K. Trzciński, G. Gajowiec, G. Trykowski, M. Sawczak, M. Łapiński, M. Szkoda

Published: *Applied Surface Science* **2023**, 608, 155187

DOI: <https://doi.org/10.1016/j.apsusc.2022.155187>

Contribution: Formal analysis, Funding acquisition, Methodology, Resources, Supervision, Validation, Writing – review & editing

Mariusz Szkoda
Signature

GDANSK UNIVERSITY
OF TECHNOLOGY
G. Narutowicza 11/12
80-233 Gdańsk, Poland

tel +48 58 348 64 34
e-mail: mariusz.szkoda@pg.edu.pl
www.pg.edu.pl





FACULTY OF
CHEMISTRY

Gdańsk, 01.08.2025

Co-author Contribution Declaration

As the co-author of the following paper, I hereby declare that my contribution to this work was as stated below.

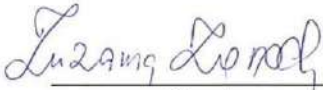
Article: A Key to Material's Stability: Tuning Pyrolysis Temperature in SnS_x/C Anodes for Sodium-Ion Batteries

Authors: Z. Zarach, M. Sawczak, C. Dosche, K. Trzciński, M. Szkoda, M. Graczyk-Zajac, R. Riedel, G. Wittstock, A.P. Nowak

Published: *Small* **2025**, e04485

DOI: <https://doi.org/10.1002/sml.202504485>

Contribution: Conceptualization, Data curation, Formal analysis, Funding acquisition, Investigation, Methodology, Project administration, Resources, Validation, Visualization, Writing – original draft, Writing – review & editing


Signature

GDANSK UNIVERSITY
OF TECHNOLOGY
G. Narutowicza 11/12
80-233 Gdańsk, Poland

tel +48 58 348 64 34
e-mail: zuzanna.zarach@pg.edu.pl
www.pg.edu.pl





The Szewalski
INSTITUTE OF FLUID-FLOW MACHINERY
POLISH ACADEMY OF SCIENCES
80-231 Gdansk J. Fiszer 14 Poland

Tel.(operator): +48 58 3460881
Tel.(office): +48 58 3416071

Fax: +48 58 3416144

e-mail: imp@imp.gda.pl
www.imp.gda.pl

Gdańsk, 01.08.2025

Co-author Contribution Declaration

As the co-author of the following paper, I hereby declare that my contribution to this work was as stated below. I acknowledge that Zuzanna Zarach was the lead author of this work.

Article: A Key to Material's Stability: Tuning Pyrolysis Temperature in SnS_x@C Anodes for Sodium-Ion Batteries
Authors: Z. Zarach, M. Sawczak, C. Dosche, K. Trzciński, M. Szkoda, M. Graczyk-Zajac, R. Riedel, G. Wittstock, A.P. Nowak
Published: *Small* **2025**, e04485
DOI: <https://doi.org/10.1002/sml.202504485>
Contribution: Investigation, Methodology, Resources, Writing – review & editing

Miroslaw Sawczak

Signature



REGON: 000326121

NIP: 584-035-78-82

POLTAX VAT-5UE: PL5840357882

NATO Commercial and Government Entity Code NCAGE: 0409H

Oldenburg, 01.08.2025

Co-author Contribution Declaration

As the co-author of the following paper, I hereby declare that my contribution to this work was as stated below. I acknowledge that Zuzanna Zarach was the lead author of this work.

Article: A Key to Material's Stability: Tuning Pyrolysis Temperature in SnS_x@C Anodes for Sodium-Ion Batteries

Authors: Z. Zarach, M. Sawczak, **C. Dosche**, K. Trzcinski, M. Szkoda, M. Graczyk-Zajac, R. Riedel, G. Wittstock, A.P. Nowak

Published: *Small* **2025**, e04485

DOI: <https://doi.org/10.1002/sml.202504485>

Contribution: Investigation, Methodology, Writing – review & editing



Signature



FACULTY OF
CHEMISTRY

Gdańsk, 01.08.2025

Co-author Contribution Declaration

As the co-author of the following paper, I hereby declare that my contribution to this work was as stated below. I acknowledge that Zuzanna Zarach was the lead author of this work.

Article: A Key to Material's Stability: Tuning Pyrolysis Temperature in SnS_x/C Anodes for Sodium-Ion Batteries

Authors: Z. Zarach, M. Sawczak, C. Dosche, K. Trzciński, M. Szkoda, M. Graczyk-Zajac, R. Riedel, G. Wittstock, A.P. Nowak

Published: *Small* 2025, e04485

DOI: <https://doi.org/10.1002/sml.202504485>

Contribution: Conceptualization, Formal analysis, Methodology, Writing – review & editing


Signature

GDAŃSK UNIVERSITY
OF TECHNOLOGY
G. Narutowicza 11/12
80-233 Gdańsk, Poland

tel +48 58 348 64 34
e-mail: kontrzc@pg.edu.pl
www.pg.edu.pl





FACULTY OF
CHEMISTRY

Gdańsk, 01.08.2025

Co-author Contribution Declaration

As the co-author of the following paper, I hereby declare that my contribution to this work was as stated below. I acknowledge that Zuzanna Zarach was the lead author of this work.

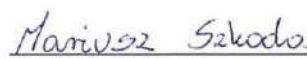
Article: A Key to Material's Stability: Tuning Pyrolysis Temperature in SnS_x/C Anodes for Sodium-Ion Batteries

Authors: Z. Zarach, M. Sawczak, C. Dosche, K. Trzcíński, M. Szkoda, M. Graczyk-Zajac, R. Riedel, G. Wittstock, A.P. Nowak

Published: *Small* 2025, e04485

DOI: <https://doi.org/10.1002/sml.202504485>

Contribution: Conceptualization, Methodology, Resources, Supervision, Writing – review & editing


Signature

GDANSK UNIVERSITY
OF TECHNOLOGY
G. Narutowicza 11/12
80-233 Gdańsk, Poland

tel +48 58 348 64 34
e-mail: mariusz.szkoda@pg.edu.pl
www.pg.edu.pl



EnBW
Energie Baden-Württemberg AG

EnBW Energie Baden-Württemberg AG · Großkunden-PLZ: 76180 Karlsruhe



Durlacher Allee 93
76131 Karlsruhe
Großkunden-PLZ: 76180 Karlsruhe
Telefon +49 721 63-06
Telefax +49 721 63-12725
www.enbw.com

Name: Dr. Magdalena Graczyk-Zajac
Bereich: Forschung
Telefon: +49 1516 7162319
Telefax: +49 721 63-17888
E-Mail: m.graczyk-zajac@enbw.com

August 7th 2025

Co-author Contribution Declaration

As the co-author of the following paper, I hereby declare that my contribution to this work was as stated below. I acknowledge that Zuzanna Zarach was the lead author of this work.

Article: A Key to Material's Stability: Tuning Pyrolysis Temperature in SnS_x@C Anodes for Sodium-Ion Batteries
Authors: Z. Zarach, M. Sawczak, C. Dosche, K. Trzciński, M. Szkoda, M. Graczyk-Zajac, R. Riedel, G. Wittstock, A.P. Nowak
Published: Small 2025, e04485
DOI: <https://doi.org/10.1002/sml.202504485>
Contribution: Resources, Supervision, Writing – review & editing

Dr. Magdalena Graczyk-Zajac
R&D Project Leader

EnBW Energie Baden-Württemberg AG

Sitz der Gesellschaft: Karlsruhe
Amtsgericht Mannheim
HRB Nr. 107956
Steuer-Nr. 35001/01075

Vorsitzender des Aufsichtsrats:
Lutz Feldmann

Vorstand:

Dr. Georg Stamatelopoulos
[Vorsitzender]
Thomas Kusterer [Stv. Vorsitzender]
Dirk Güsewell
Peter Heydecker
Colette Rückert-Hennen



TECHNISCHE
UNIVERSITÄT
DARMSTADT

Institut für
Materialwissenschaft
FG Materials & Resources



Co-Author Contribution Declaration

As the co-author of the following paper, I hereby declare that my contribution to this work was as stated below. I acknowledge that Zuzanna Zarach was the lead author of this work.

Article: A Key to Material's Stability: Tuning Pyrolysis Temperature in SnSx@C Anodes for Sodium-Ion Batteries

Authors: Z. Zarach, M. Sawczak, C. Dosche, K. Trzciński, M. Szkoda, M. Graczyk-Zajac, R. Riedel, G. Wittstock, A.P. Nowak

Published: Small 2025, e04485
DOI: <https://doi.org/10.1002/sml.202504485>

Contribution: Resources, Supervision, Writing – review & editing


(Prof. Dr. Dr. h. c. R. Riedel)

Prof. Dr. Dr. h. c.
Ralf Riedel

Otto-Berndt-Str. 3
64287 Darmstadt

Tel. +49 6151 16 - 21624
Fax +49 6151 16 - 21623
ralf.riedel@tu-darmstadt.de

Datum
01.08.2025

Ihre Nachricht

Unser Zeichen

Sparkasse Darmstadt
BLZ: 508 501 50
Kto. Nr. 704 300
IBAN:
DE 36 5085 0150 0000 7043 00
BIC: HELADEF1DAS

Carl von Ossietzky Universität Oldenburg / 26111 Oldenburg

Ms Zuzanna Zarach
Faculty of Chemistry
Gdansk University of Technology
Gdansk 80-233
Poland

electronic transmission to
zuzanna.zarach@pg.edu.pl

Dear Ms. Zarach,

I am happy to formally declare the contribution to our joint paper for the purpose of the PhD process.

Co-author Contribution Declaration

As the co-author of the following paper, I hereby declare that my contribution to this work was as stated below. I acknowledge that Zuzanna Zarach was the lead author of this work.

Article: A Key to Material's Stability: Tuning Pyrolysis Temperature in SnS_x/C Anodes for Sodium-Ion Batteries
Authors: Z. Zarach, M. Sawczak, C. Dosche, K. Trzciński, M. Szkoda, M. Graczyk-Zajac, R. Riedel, G. Wittstock, A.P. Nowak
Published: Small **2025**, e04485
DOI: <https://doi.org/10.1002/sml.202504485>
Contribution: Conceptualization, Formal analysis, Resources, Supervision, Writing – review & editing

Kind regards



(Gunther Wittstock)

Carl von Ossietzky
Universität
Oldenburg

Fakultät V - Mathematik
und Naturwissenschaften
Institut für Chemie



Arbeitsgruppe Elektrochemie und
Grenzflächen kondensierter Systeme
Prof. Dr. Gunther Wittstock
Tel.: 0441 798 - 3971
wittstock@uol.de

Sekretariat
Heike Hillmer
Tel. 0441 798 - 3970
Fax: 0441 798 - 3979
heike.hillmer@uol.de

Oldenburg, den 03.08.2025

Standort
Campus Wechloy, Raum W03 1-105
Carl-von-Ossietzky-Str. 9-11
26129 Oldenburg

Postanschrift
26111 Oldenburg

Paketanschrift
Ammerländer Heerstraße 114-118
26129 Oldenburg

Bankverbindung
Landessparkasse zu Oldenburg
IBAN DE46 2805 0100 0001 9881 12
BIC SLZODE22

Steuernummer
6422008701



FACULTY OF
CHEMISTRY

Gdańsk, 01.08.2025

Co-author Contribution Declaration

As the co-author of the following paper, I hereby declare that my contribution to this work was as stated below. I acknowledge that Zuzanna Zarach was the lead author of this work.

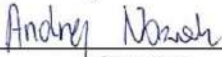
Article: A Key to Material's Stability: Tuning Pyrolysis Temperature in $\text{SnS}_x\text{@C}$ Anodes for Sodium-Ion Batteries

Authors: Z. Zarach, M. Sawczak, C. Dosche, K. Trzciński, M. Szkoda, M. Graczyk-Zajac, R. Riedel, G. Wittstock, **A.P. Nowak**

Published: *Small* 2025, e04485

DOI: <https://doi.org/10.1002/sml.202504485>

Contribution: Conceptualization, Formal analysis, Funding acquisition; Investigation; Methodology, Resources, Supervision, Writing – review & editing


Signature

GDANSK UNIVERSITY
OF TECHNOLOGY
G. Narutowicza 11/12
80-233 Gdańsk, Poland

tel +48 58 348 64 34
e-mail: andnowak@pg.edu.pl
www.pg.edu.pl



Copyrights

Article: Phenomenon of Increasing Capacitance Induced by 1T/2H-MoS₂ Surface Modification with Pt Particles – Influence on Composition and Energy Storage Mechanism

Authors: Z. Zarach*, M. Szkoda, K. Trzciński, M. Łapiński, G. Trykowski, A.P. Nowak

Journal: *Electrochimica Acta* **2022**, 435, 141389

DOI: <https://doi.org/10.1016/j.electacta.2022.141389>

License: The content is available under CC-BY-NC-ND

Copyrights statement: Available



The phenomenon of increasing capacitance induced by 1T/2H-MoS₂ surface modification with Pt particles – Influence on composition and energy storage mechanism

Author:

Zuzanna Zarach, Mariusz Szkoda, Konrad Trzciński, Marcin Łapiński, Grzegorz Trykowski, Andrzej P. Nowak

Publication: Electrochimica Acta

Publisher: Elsevier

Date: 10 December 2022

© 2022 The Author(s). Published by Elsevier Ltd.

Welcome to RightsLink

Elsevier has partnered with Copyright Clearance Center's RightsLink service to offer a variety of options for reusing this content:

Note: This article is available under the [Creative Commons CC-BY-NC-ND](#) license and permits non-commercial use of the work as published, without adaptation or alteration provided the work is fully attributed.

For commercial reuse, permission must be requested below.

I would like to... ?

make a selection



To request permission for a type of use not listed, please contact [Elsevier](#) Global Rights Department.

Are you the [author](#) of this Elsevier journal article?

Article: Influence of hydrochloric acid concentration and type of nitrogen source on the electrochemical performance of TiO₂/N-MoS₂ for energy storage applications

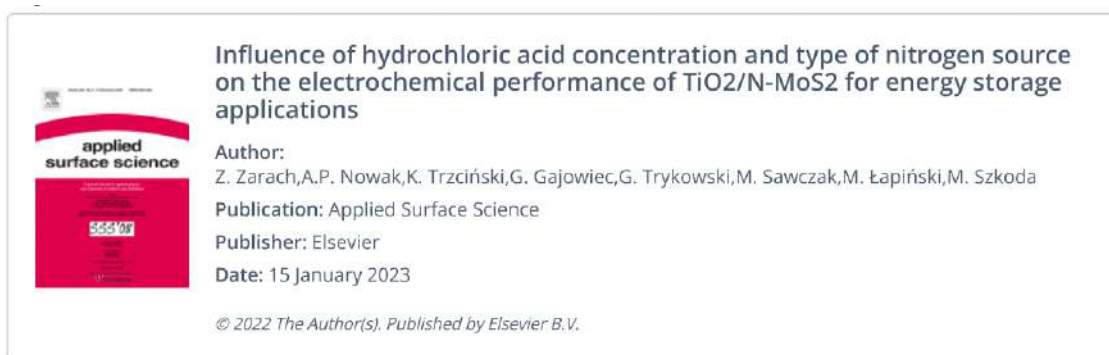
Authors: Z. Zarach*, A.P. Nowak, K. Trzciński, G. Gajowiec, G. Trykowski, M. Sawczak, M. Łapiński, M. Szkoda

Published: *Applied Surface Science* **2023**, 608, 155187

DOI: <https://doi.org/10.1016/j.apsusc.2022.155187>

License: The content is available under CC-BY-NC

Copyrights statement: Available




Welcome to RightsLink

Elsevier has partnered with Copyright Clearance Center's RightsLink service to offer a variety of options for reusing this content.

Note: This article is available under the [Creative Commons CC-BY-NC](#) license and permits non-commercial use, distribution and reproduction in any medium, provided the original work is properly cited.

For commercial reuse, permission must be requested below.

I would like to... 

To request permission for a type of use not listed, please contact [Elsevier](#) Global Rights Department.

Are you the [author](#) of this Elsevier journal article?

Article: A Key to Material's Stability: Tuning Pyrolysis Temperature in SnS_x@C Anodes for Sodium-Ion Batteries

Authors: Z. Zarach*, M. Sawczak, C. Dosche, K. Trzciński, M. Szkoda, M. Graczyk-Zajac, R. Riedel, G. Wittstock, A.P.Nowak

Published: *Small* **2025**, e04485

DOI: <https://doi.org/10.1002/smll.202504485>

License: The content is available under CC-BY

Copyrights statement: Available



A Key to Material's Stability: Tuning Pyrolysis Temperature in SnS_x@C Anodes for Sodium-Ion Batteries

Author: Andrzej P. Nowak, Gunther Wittstock, Ralf Riedel, et al

Publication: Small

Publisher: John Wiley and Sons

Date: Jul 31, 2025

© 2025 The Author(s). Small published by Wiley-VCH GmbH

Open Access Article

This is an open access article distributed under the terms of the [Creative Commons CC BY](#) license, which permits unrestricted use, distribution, and reproduction in any medium, provided the original work is properly cited.

You are not required to obtain permission to reuse this article.

For an understanding of what is meant by the terms of the Creative Commons License, please refer to [Wiley's Open Access Terms and Conditions](#).

Permission is not required for this type of reuse.

Wiley offers a professional reprint service for high quality reproduction of articles from over 1400 scientific and medical journals. Wiley's reprint service offers:

- Peer reviewed research or reviews
- Tailored collections of articles
- A professional high quality finish
- Glossy journal style color covers
- Company or brand customisation
- Language translations
- Prompt turnaround times and delivery directly to your office, warehouse or congress.

Please contact our Reprints department for a quotation. Email corporatesaleseurope@wiley.com or corporatesalesusa@wiley.com or corporatesalesDE@wiley.com.